E. E. Zubov,
E. S. Zhitlukhina

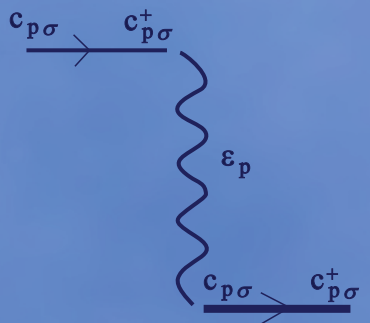# EFFECTIVE FIELD APPROACH TO TRANSITION-METAL OXIDE SYSTEMS: MAGNETISM, TRANSPORT AND SPECTRAL PROPERTIES

$$\underrightarrow{c_{p\sigma} \quad c_{p\sigma}^+} = \underrightarrow{c_{p\sigma} \quad c_{p\sigma}^+} + \underrightarrow{c_{p\sigma} \quad c_{p\sigma}^+} \quad \varepsilon_p \quad \underrightarrow{c_{p\sigma} \quad c_{p\sigma}^+}$$

Е. Є. Зубов, О. С. Житлухіна

МЕТОД ЕФЕКТИВНОГО ПОЛЯ В СИСТЕМАХ НА ОСНОВІ ОКСИДІВ ПЕРЕХІДНИХ МЕТАЛІВ: МАГНЕТИЗМ, ТРАНСПОРТНІ І СПЕКТРАЛЬНІ ВЛАСТИВОСТІ

*Рекомендовано до друку Вченою радою ДонНУ імені Василя Стуса
(протокол № 11 від 29.05.2019 р.)*

Рецензенти:

В. Ф. Русаков, доктор фіз.-мат. наук, проф., зав. кафедрою Донецького національного університету імені Василя Стуса, Вінниця;

В. Є. Шатернік, доктор фіз.-мат. наук, провідний науковий співробітник Інституту металофізики імені Г. В. Курдюмова, Національна академія наук України, Київ;

В. І. Шнирков, доктор фіз.-мат. наук, проф., старший науковий співробітник Київського академічного університету, Київ.

Зубов Е. Є., Житлухіна О. С.

Метою цієї монографії є аналіз багаточастинкового та складного характеру низки проблем, пов'язаних із метал-оксидними гетероструктурами, а також огляд останніх теоретичних результатів, отриманих авторами в цій галузі. Запропоновано концепцію самоузгодженого поля, яка базується на діаграмному методі залежної від часу теорії збурень, розглянуто такі аспекти застосування цієї теорії: фазовий перехід метал-ізолятора для напівзаповненої електронної смуги; вплив електрон-фононної взаємодії на спектр збуджень і затухання у вузькосмуговій електронній підсистемі; можливий механізм високотемпературної надпровідності в купратах і специфічні магнітні і резистивні властивості манганітів, зарядовий транспорт та ефект резистивних біполярних перемикань в оксидних гетероструктурах.

Для наукових співробітників, які працюють в галузі фізики твердих тіл, аспірантів і магістрантів фізичних факультетів університетів та науково-дослідних інститутів.

УДК 538.915

E. E. Zubov, E. S. Zhitlukhina

EFFECTIVE FIELD APPROACH TO TRANSITION-METAL OXIDE SYSTEMS: MAGNETISM, TRANSPORT AND SPECTRAL PROPERTIES

Reviewers:

V. F. Rusakov, Dr. Sci., Prof., Head of the Department, Vasyl' Stus Donetsk National University, Vinnytsia.

V. E. Shaternik, Dr. Sci., Leading Research Associate, G.V. Kurdyumov Institute for Metal Physics, National Academy of Sciences of Ukraine, Kyiv.

V. I. Shnyrkov, Dr. Sci., Prof., Senior Researcher, Kyiv Academic University, Kyiv.

E. E. Zubov, E. S. Zhitlukhina

Effective field approach to transition-metal oxide systems: Magnetism, transport and spectral properties, монографія. Vinnytsia: Vasyl' Stus DonNU, 2019. – 164 p.

The goal of this monograph is to highlight the many-body and complex character of some metal-oxide heterostructure problems and to discuss recent theoretical advances in this field achieved by the authors. The concept of a self-consistent field based on the diagram method of the time-dependent perturbation theory is introduced and the following aspects of the theory applications are discussed: metal-insulator phase transition for a half-filled electron band; impact of the electron-phonon interaction on the excitation spectrum and damping in a narrow-band electron subsystem; possible mechanism of the high-temperature superconductivity in cuprates and specific magnetic and resistive properties of manganites, charge transport and resistive bipolar switching phenomenon in oxide-based heterostructures.

For researchers working in the field of solid-state physics, PhD and master's students at physical faculties of universities and research institutions.

UDC 538.915

PREFACE

Metal oxides have been a subject to enormous research activities in recent years due to their wealth of interesting properties and applications in a diverse range of areas from electronic devices, components for catalysts, novel energy materials, and sensors. Among them, transition-metal oxides form a special class with very different electrical properties from metals, superconductors, semiconductors and insulators. Their magnetic characteristics are exciting as well. To understand the most basic physics of transition-metal oxides and the recent progress in this field was our aim in writing this book.

More than a hundred years has been passed from the time when P.-E. Weiss formulated a hypothesis of the self-consistent molecular field for magnetic materials that remains to be a useful tool for studying basic properties of systems with localized magnetic moments. Moreover, having an unperturbed Hamiltonian with selected order parameters, there appears possibility to account correlation effects for describing various fluctuation phenomena. Unfortunately, in the systems with collectivized electrons the situation is not so simple because a kinematic part of the corresponding total Hamiltonians does not allow correct selection of the basic order parameters that form an effective self-consistent field. The urgency of the problem has increased after discovery of metal-dielectric phase transitions in metal oxides, high-temperature superconductivity, as well as non-trivial features of the magnetic structure and conductivity in multiferroics, magnetic semiconductors and other multifunctional materials. In this book, we develop the effective field theory applying it to the condensed matter and hybrid structures on the base of diagram methods of the time-dependent perturbation theory. In this case, the main concern is with the correct account for both charge and spin degrees of freedom. One can say that the method of extracting an effective field to some extent is related to the well-known Dyson equation for Green's functions that generalizes infinite series of similar diagrams. In the simplest case, the mass operator is considered as the simplest interaction line, which is determined by the perturbation Hamiltonian. If such approximation is not acceptable as for the Hubbard model, the first non-vanishing approximation is used to take into account the one-loop diagrams.

Effective field approach to transition-metal oxide systems: Magnetism, transport and spectral properties covers theoretical aspects related to transport and magnetic properties of heterostructures based on metal oxides. The book concludes with the current research carried out by the authors within the Fundamental Research Programme funded by the Ministry of Education and Science of Ukraine, Project "Spectral and transport properties of metal-oxide compounds with transition-group elements" No. 0117U002360 as well as future prospective applications of these materials.

We express our sincere thanks to all colleagues who contributed to our joint results used in the book, in particular, Ivan Fita, Vladimir Dyakonov, Henryk Szymczak, Andrej Plecenik, and Peter Kúš. Thanks are due to Mikhail Belogolovskii for his suggestions and improvements. We are grateful to all colleagues from the Vasyl' Stus Donetsk National University for their great help during the book preparation.

Vinnytsia, May 2019   *Eduard Zubov*
                                                                     Elena Zhitlukhina

ABBREVIATIONS – SHORT LIST

AFM – antiferromagnetic
ARPES – angle-resolved photoemission spectroscopy
BCS – Bardeen, Copper, and Schrieffer theory of superconductivity
BTK – Blonder-Tinkham-Klapwijk theory
CPA – coherent potential approximation
DE – double-exchange
DMF – dynamic mean-field approximation
FM – ferromagnetic
HR – high resistance
HTSC – high-temperature superconductivity
LR – low resistance
PM – paramagnetic
ReRAM – resistive random access memory
YBCO – $YBa_2Cu_3O_{7-\delta}$

CONTENTS

FOREWORD

Transition-metal oxides are known as a very challenging problem in condensed matter physics and materials chemistry [1]. The delicate balance between itinerancy and localization of electrons stemming from partially-filled *d*-orbitals in the compounds creates many intriguing phenomena, among them different electronic phases, namely, conventional (normal) metal, superconductor, band insulator and Mott insulator, which demonstrate different forms of transport and magnetism [2]. The identification of high-temperature superconductivity (HTSC) in CuO_2-based systems [3], eventually well above the liquid-nitrogen temperature, still marks the most impressive finding in this group of compounds.

To explain a rich variety of bulk transition-metal oxides with a weakly screened local Coulomb interaction and so vast variety of physical characteristics was and remain to be a difficult theoretical task. Restriction to a conventional single-particle scheme valid for ordinary metals often misses key oxide features such as local-moment formation or the many-body concept of Hubbard bands. Therefore, density functional theory in the Kohn-Sham representation, which is a standard first-principles tool of materials science, is not sufficient for oxides. Realistic methods beyond conventional approaches that take into account importance of strong local Coulomb interactions together with many-body electron states are nowadays routinely applicable to the correlated electronic structure of bulk oxides.

Some of transition-metal oxides exhibit significant amount of complexity. As an example, we can mention perovskites, complex oxides with a cubic structure and the general formula ABX_3, see Fig. I.1 where the A-site ion is usually an alkaline earth or rare earth element, the B-site ions can be $3d$, $4d$, and $5d$ transition-metal elements and form an octahedral BX_6 with the X ion. The most popular perovskites contain oxygen at the X-ion cites and the most known ones are the HTSC compounds. A few other perovskites are formed with X = B, C, F, or Ni. The recent demonstration of high power conversion up to 22 % in photovoltaic films of complex hybrid halides with X = I, Br, or Cl made these materials widespread. The symmetry breaking under the influence of pressure, temperature or doping can lead to tetragonal, orthorhombic or rhombohedral structures. When additional sheets are inserted in the basic materials, various layered structures can be realized with novel properties, as for example, it was shown by J. G. Bednorz and K. A. Müller in 1986 for cuprates exhibiting high-temperature superconductivity effect.
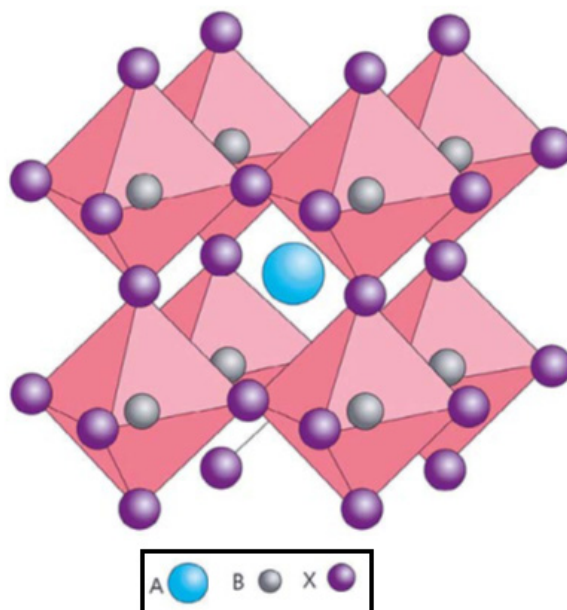

Fig. 1. Cubic perovskite structure of ABX_3 type

In the transition-metal oxides, the key many-body aspects reside within the electronic subsystem. The Pauli principle and the mutual Coulomb interaction among the electrons give rise to an intricate many-particle wave function. While the former exchange physics, in its pure appearance, may be cast into a Slater determinant, the explicit interaction leads to more intriguing modifications of the wave function. Electronic correlations, as defined from quantum chemistry, are routed in the latter. Though the Coulomb interaction is long-ranged, screening processes in the solid restrict in most cases its actual relevant range to rather short distances. To a good approximation for many systems, a sole local interaction appears sufficient to describe the dominant physics. Given that viewpoint, the Hubbard model stands out as the seminal picturing of the competition between localization and itinerancy among interacting condensed matter electrons, i.e.

$$H_{\text{Hubbard}} = -t \sum_{i,j,s} \left(\hat{c}_{is}^+ \hat{c}_{js} + \text{h.c.} \right) + U \sum_i \hat{n}_{i\uparrow} \hat{n}_{i\downarrow}$$

with i and j, site indices, $s = \uparrow$ and $\downarrow$, spin projection and $\hat{n}_{is} = \hat{c}_{is}^+ \hat{c}_{is}$. The nearest-neighbor hopping t describes the tendency of an electron to delocalize on the lattice, giving rise to the noninteracting band structure while the Hubbard U value originates from the local Coulomb interaction. The given basic Hamiltonian is appropriate and effective for dealing with a one-band problem whereas the case of multi-band systems needs an addition of the local Hund's physics described by the Hund's exchange J_H. Depending on the ratio of the two parameters U and t the Hubbard model provides very different solutions. For small U/t ratios the system is a very good metal, close to a Fermi gas, with a maximum spectral weight at the Fermi level E_F. On the contrary for large U/t ratios, the lattice is in an insulating state, since the electrons localize in the real space due to the strong Coulomb repulsion. In spectral terms, removing or adding an electron is associated with states in the lower or upper Hubbard bands, respectively. This Mott-insulating state strongly differs from a conventional band insulator which arises due to complete band filling in reciprocal space. When U and t are of the same order, i.e., between the limits discussed above, the system is in the most interesting regime of a correlated metal when it is balancing between the emerging Hubbard bands and the coherent quasiparticle peak close to the Fermi energy.

A new stage of the oxides research activities started in the early 2000s, when systematic studies of oxide heterostructures appeared [4]. Ever since, that topical field belongs to a key focus in condensed matter and materials science, see e.g. the references [5–7] for reviews). Important advancements in scaling down heterostructures and having an improved interface quality together with atomically-thin two-dimensional materials allow researchers to design novel oxide materials which do not exist in nature. Before it, creation of novel materials, especially in the case of semiconductors, was based on the doping effect. However, such techniques often lead to unintended materials changes. A radically new approach for tailoring oxides with desired properties has recently emerged from proximity effects which can transform a given material through its adjacent regions to become magnetic, or superconducting, or topologically nontrivial. The paradigm of proximitized materials may be very important for future technological applications providing a ubiquitous path for modifying a wide class of materials that could overcome limitations inherent to doping and functionalization. Hybrid heterostructures, made of two non-alloying materials with different and even mutually exclusive properties, have recently come at the forefront of materials research [8]. Strong mutual interaction between two subsystems at their interface may dramatically modify main characteristics of the proximitized films. This trend becomes dominant in determining composite

functionalities when it takes place at the nanoscale. In particular, the combination of different properties from the constituent materials has attracted an ever growing interest for thermal management or energy harvesting applications [9]. Another example is van der Waals heterostructures where constituent monolayers which display the dominance of interfacial over bulk behavior, providing an ideal setting to tailor and test proximitized materials. The two examples, which certainly open new avenues for practical applications, can and (in some cases) have been already realized in oxide-based heterostructures.

Returning to the fundamental issues, we should emphasize that oxide heterostructures furthermore challenge known paradigms in condensed matter physics due to the unique combination of materials properties. Coexistence and mutual affection of intriguing bulk-like electronic phases associated with a certain oxide compound within a single oxide heterostructure as well as the seminal role of the interface in the novel systems lead to new exotic phases, unknown in present bulk compounds. Powerful perspectives for two different materials placed in the contact can be exemplified by the emergence of the triplet superconductivity in a semiconductor host with strong spin-orbit coupling where the conventional pairing between spin-up and spin-down electrons is removed making their spin-triplet pairing preferable [8].

The goal of this book is to highlight the many-body and complex character of some oxide heterostructure problems and to discuss recent theoretical advances in this field achieved by the authors of the monograph.

In the first chapter, we discuss the concept of a self-consistent field in the theory of superconductivity based on the diagram method of the time-dependent perturbation theory. It is shown that the well-known BCS equation for the superconducting order parameter is already realized in a zero approximation. The form of the interaction Hamiltonian uniquely determines a chain of interconnected Green's functions easily calculated within this approximation. The proximity effect in a normal metal-superconductor heterostructure is analysed using the proposed approach. In contrast to the traditional McMillan and de Gennes theories with self-consistent Green's functions, the self-consistency over the order parameter provides a significantly smaller gap value induced in a normal metal. The frequency dependence of the homogeneous spectral density qualitatively agrees with the experiment.

The second chapter presents a possible mechanism of the step-like metal-insulator phase transition for a half-filled band within the framework of the Hubbard model and an effective self-consistent field. Detailed analysis of the well-known Hubbard I approximation is carried out. The correlation corrections were accounted for a minimal number of self-consistency parameters. It was determined that the typical order parameters are unique for metal or dielectric states. Based on the analysis of the electron spectral density positions of the chemical potential level and critical value of the Coulomb energy of repulsion in bandwidth units at the metal-insulator phase transition have been determined. The estimations of the inner energy value for a half-filled band exhibit a stable metal state at $\tilde{U} < 2.1$ whereas a dielectric state is stable for $\tilde{U} > 2.1$ and only in the extremely small electron-doping limit. That is why the chemical potential level underlies by the lower edge of the upper Hubbard band where the spectral density equals zero. A finite electron or hole doping causes the metal state with the Fermi level inside the upper band or a doped dielectric state with the Fermi level inside the lower band, respectively. It results in a step-like rise of conductivity at the metal-insulator phase transition.

The third chapter is dealing with the effect of the electron-phonon interaction on the excitation spectrum and damping in a narrow-band electron subsystem of cuprates. Within the

framework of the *t-J* model, we have proposed a new approach for accounting of both strong electron correlations and local electron-phonon binding with a characteristic Einstein mode ω_0 in the normal state. Within the Hubbard-I approximation an exact solution for the polaron bands was found. We have found that in a low-dimensional system with a pure kinematic part of the Hamiltonian a complicated excitation spectrum determined mainly by peculiarities of the lattice Green's function is realized. In the definite area of the electron concentration and hopping integrals, a correlation gap may be arise on the Fermi level. We found that the strong electron-phonon binding enforces a degree of coherence of electron-polaron excitations near the Fermi level and spectrum along the nodal direction weakly depends on the wave-vector module. It corresponds to the ARPES data. Possible origin of the experimentally observed kink in the nodal direction of cuprates is explained by a fine structure of the polaron band formed near the mode $-\omega_0$.

In the fourth chapter, we discuss the nature of the high-temperature superconductivity in cuprates. We have supposed that the electron-phonon interaction determines a strong-correlation narrowing of the electron band. It provides conditions for the formation of a singlet electron pair coupled by the exchange interaction. For a pure *t-J* model, it is proved that these electron pairs are destroyed by a strong effective kinematic field. The detailed analysis of an effect of Holstein polaron excitations upon normal and superconducting properties of the strongly correlated electrons is presented. Calculated superconducting critical temperature and gap function are in good agreement with experimental data for cuprates.

In the fifth chapter, we present **a** framework of the scattering-matrix formalism for the nonlinear Kubo theory of the electron transport in a metal with a tunnel barrier. A general expression for the mean electrical current was obtained. It significantly simplifies the calculation of nonlinear contributions to the conductivity of various hybrid structures. Within the tunnel Hamiltonian model, all linear and nonlinear contributions to a mean electrical current are evaluated. The linear approximation agrees with results of other theories. For effective barrier transmission $\tilde{T} = 1/5$ the ballistic transport is realized with a value of the Landauer conductivity equal to $2e^2/h$.

The aim of **the sixth chapter** was to evolve an effective-field theory of magnetic and resistive properties of manganites with account of a strong Hund exchange coupling and electron-phonon interactions. In parallel with the Lang-Firsov unitary transformation of the zeroth Hamiltonian, we have realized the diagonalization of the Hund Hamiltonian neglecting the upper triplet. The diagram technique taking into account quantum spin fluctuations of lower quintet and hole state with spin S = 3/2 was developed. The magnetic structure of the ground state and an influence of the electron-phonon interaction have been analysed using the first non-vanishing approximation of perturbation theory. Since a simple self-consistent equation for the Green's function is lacking, two approximations for effective interaction line have been applied, one of which is based on the assumption of the Green's function symmetry with respect to the change of the polaron energy sign near the phase transition. The calculated resistivity-versus-temperature dependence agrees well with experimental data including those obtained in external magnetic fields.

In the seventh chapter, we report theoretical and experimental studies of the resistive bipolar switching phenomenon in oxide-based heterostructures. Its first part is devoted to such effect in c-axis oriented normal-state $YBa_2Cu_3O_{7-c}$ (YBCO) thin films at room temperature. We have assumed that the hysteretic phenomena in current-voltage characteristics of such contacts can be explained by migration of oxygen-vacancy defects and, as a result, by the formation or

dissolution of more or less conductive regions near the metal–YBCO interface. To support our interpretation of the macroscopic resistive switching phenomenon, a minimalist model that describes radical modifications of the oxygen-vacancy effective charge in terms of a charge-wind effect was proposed. It was shown theoretically that due to the momentum exchange between current carriers (holes in the YBCO compound) and activated oxygen ions, the direction in which oxygen vacancies are moving is defined by the balance between the direct electrostatic force on them and that caused by the current-carrier. Next, we discuss a novel device based on the resistive-switching phenomenon in a nanometer-thick transition-metal oxide interlayer separating two layers, a superconductor under study and a normal counter-electrode is developed. The method proposed enables to modify the transparency of the normal-superconducting interface over a wide range and thus to probe the superconducting spectra in two limiting regimes, a perfect (without any barrier) contact and a tunneling-like configuration. To calculate expected conductance-versus-voltage curves for the experimental verification, we have modified the conventional Blonder-Tinkham-Klapwijk formalism by replacing the constant gap value with a related function in order to take into account the phonon-induced structure and introducing a constant imaginary part into the electron energy. We believe that this technique can be successfully applied for studying spectra of quasi-particle excitations in novel superconducting materials with improved characteristics.

1. EFFECTIVE-FIELD CONCEPT IN THE FRAMEWORK OF DIAGRAM TECHNICS

1.1. Introduction

The study of the induced superconductivity in a normal metal adjacent to a superconductor has attracted the attention of many researchers for a long time [10–13]. It should be noted that despite the rather tremendous list of theoretical publications on this topic in most cases the main statements of the de Gennes [14] and McMillan [15] theories have been used. As a rule, in this case, for coordinate dependence of the gap, an integral relation directly connected to the well-known Gor'kov's equations is realized [16]. If we consider the self-consistent field, it is very difficult to extract it within the framework of these theories due to the fact that self-consistency is always carried out by Green's functions and not by the order parameter. For example, McMillan [15] uses the matrix form of the Green function proposed by Eliashberg [17] in the framework of the Nambu formalism for superconductors with a strong coupling and time delay effects. Here, in the framework of the Dyson equation the self-consistency is carried out for Green's functions as well. Such approach significantly complicates the solution of the equations obtained and leads to the necessity to include additional unknown parameters. In this case, the induced gap is self-consistently connected with the energy gap of the superconductor. It is not correct since the role of the superconducting order parameter consists only in inducing a gap in a normal metal. As a result, the concept of the critical temperature T_C of the superconducting transition arises for the whole hybrid structure. Although it is obvious that T_C is determined solely by the value of the electron-phonon coupling parameter for superconductor. This leads to an overestimation of the induced energy gap value in the proximity effect. It should be noted that such consideration leads to a need to take into account the spatial dependence of the energy gap function satisfying the Eilenberger differential equation [18] with corresponding boundary conditions. The problem of the proximity effect in the case of a homogeneous gap that is quite natural for the ballistic limit remains open.

This chapter proposes a new approach to solving the problem of superconductivity in both homogeneous and inhomogeneous structures. It is based on the use of the diagram method of a time-dependent perturbation theory with selected order parameters according to which subsequent rigorous self-consistency is carried out. The advantages of such theory are the presence of the minimum number of parameters used, a simpler form of the obtained equations for order parameters, as well as a clear knowledge of the realization of one or another state of the electron ensemble in a metal. Also, starting from the indicated approximation a subsequent account for the influence of fluctuations using the loop diagrams is possible.

The structure of the chapter is as follows: the second subsection presents basic tenets of the self-consistent theory for a normal metal; in the third subsection, the BCS equation for the gap was first obtained by presented diagrammatic method. The derivation of this equation is based only on the graphical representation of the effective self-consistent field. In the fourth subsection, the proximity effect in the normal metal-superconductor hybrid structure within the framework of a tunnel Hamiltonian is considered. The general expression for the order parameter is obtained and the temperature dependences of the induced superconducting energy gap in a normal metal are calculated. In the fifth subsection, we study the spectral density of states of a normal metal with an induced energy gap function. In the sixth subsection, the main conclusions of the presented theory are given.

1.2. Self-consistent field in a metal. Diagrammatic method

The Hamiltonian of a normal metal in a site representation can be written as

$$\hat{H} = \sum_{i,j,\sigma} t_{ij} c^+_{\sigma i} c_{\sigma j} - \mu \sum_{i\sigma} c^+_{\sigma i} c_{\sigma i} , \qquad (1.1)$$

where the hopping integral t_{ij} determines the band energy $\varepsilon_{\mathbf{q}} = \sum_{ij} t_{ij} e^{-i\mathbf{q}(\mathbf{r}_i - \mathbf{r}_j)}$, μ and σ are the

chemical potential and the electron spin, respectively. Creation $c^+_{i\sigma} = \dfrac{1}{\sqrt{N}} \sum_k e^{-ikR_i} c^+_{k\sigma}$ and

annihilation $c_{i\sigma} = \dfrac{1}{\sqrt{N}} \sum_k e^{ikR_i} c_{k\sigma}$ operators are presented as the Fourier transforms in a wave

space. It is convenient to take a part of Hamiltonian (1.1) associated with the chemical potential energy as an unperturbed Hamiltonian. The question immediately arises about the validity of such choice. Strictly speaking, the remaining part in (1.1) is not a perturbation for the metal. However, this choice is fully justified since the chemical potential in the ground state always limits the electron energy. Therefore, an infinite series of perturbation theory with

$$\hat{H}_0 = -\mu \sum_{i\sigma} c^+_{\sigma i} c_{\sigma i} \qquad (1.2)$$

and perturbation Hamiltonian

$$V = \sum_{i,j,\sigma} t_{ij} c^+_{\sigma i} c_{\sigma j} \qquad (1.3)$$

will be converging. Indeed, we associate the bold line with the total causal Green's function $Y^{-+}_{k\sigma}(\tau) = - < T c_{k\sigma}(\tau) c^+_{k\sigma}(0) >$ presented in Fig.1.1. Here, the symbol $<...>$ denotes the statistical averaging over the full Hamiltonian (1.1), and T_τ is the time operator of chronological ordering, τ is the imaginary time in the Matsubara formalism.

A thin line corresponds to the unperturbed Green's function

$$G^{-+}_{p\sigma}(i\omega_n) = - < T_\tau c_{p\sigma}(\tau) c^+_{p\sigma}(0) >_{0,i\omega_n} = \frac{1}{\beta(i\omega_n + \mu)}, \qquad (1.4)$$

where a symbol $<...>_{0,i\omega_n}$ means the averaging with Hamiltonian $\hat{H}_0$. An imaginary index $i\omega_n$ $=i\pi(2n+1)/\beta$ is the standard notation for the Fourier transform of the Matsubara Green's function and $1/\beta = T$ is the temperature. The diagram in Fig. 1 represents an infinite series of convergent geometric series with a denominator $q = \left| \beta \varepsilon_p G^{-+}_{p\sigma}(i\omega_n) \right| < 1$.
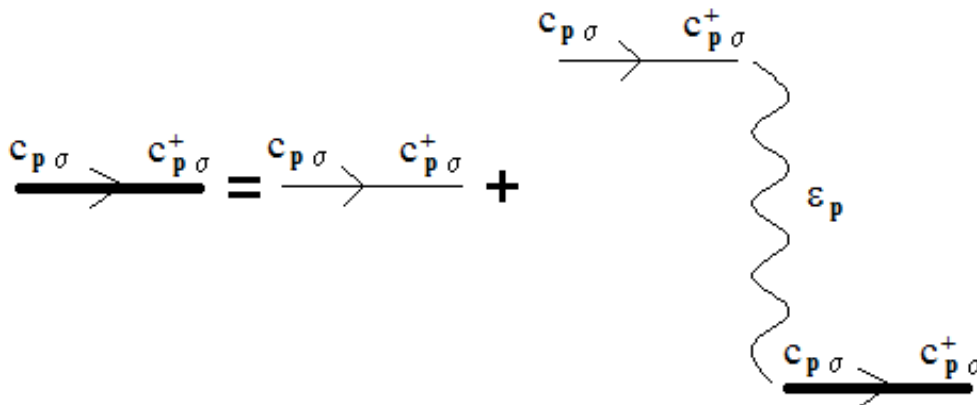

Fig.1.1. Complete diagram series for the Fourier transform of the causal Green's function $Y^{-+}_{p\sigma}(i\omega_n)$ in the zero approximation of the self-consistent field

In the Fourier space, we have the following algebraic equation for unknown $Y_{k\sigma}^{-+}(i\omega_n)$:

$$Y_{p\sigma}^{-+}(i\omega_n) = G_{p\sigma}^{-+}(i\omega_n) + \beta\varepsilon_p Y_{p\sigma}^{-+}(i\omega_n)G_{p\sigma}^{-+}(i\omega_n), \tag{1.5}$$

whose solution is trivial. In view of Eq. (1.4) it gives the traditional causal Green's function of the electron gas in a metal [10]:

$$Y_{p\sigma}^{-+}(i\omega_n) = \frac{1}{\beta(i\omega_n - \varepsilon_p + \mu)}. \tag{1.6}$$

Despite the triviality of deriving Eq. (1.6) for a zero-approximation of the self-consistent field this consideration has a deep physical meaning since it allows us to consider successively the contributions of correlation corrections related to the interaction of electrons and ions. As an example, in the next section we will consider the phenomenon of electron Cooper pairing in a system with electron-phonon coupling.

1.3. Self-consistent field in a superconducting metal

As is known, the basis for describing the phenomenon of superconductivity in a metal is the Bardeen-Cooper-Schrieffer Hamiltonian approach [11]:

$$V = \sum_{i,j,\sigma} t_{ij}a_{\sigma i}^+ a_{\sigma j} - \sum_{i,j,\sigma}\left\{\Delta_{ij\sigma}a_{\sigma i}^+ a_{\sigma j}^+ + \Delta_{ij\sigma}^* a_{-\sigma i}a_{\sigma j}\right\}, \tag{1.7}$$

where for convenience the symbols of the creation and annihilation operators in the superconductor are denoted by the letter a^+ and a, respectively. In this case, in the framework of the suggested diagram method, the Hamiltonian (1.7) is a perturbation. The unperturbed part of a total Hamiltonian, over which all averaging of the perturbation theory series is performed, has the form

$$\hat{H}_0 = -\mu\sum_{i\sigma}a_{\sigma i}^+ a_{\sigma i} \tag{1.8}$$

Fourier components $\Delta_{q\sigma}$ of the order parameters $\Delta_{ij\sigma}$ satisfy the self-consistency equation

$$\Delta_{k\sigma} = \sum_q \frac{|M_{k\text{-}q}|^2}{\omega_{k\text{-}q}} < a_{-q-\sigma}a_{q\sigma} >, \tag{1.9}$$

where $M_{k\text{-}q}$ and $\omega_{k\text{-}q}$ are a matrix element of the electron-phonon interaction [19] and a phonon frequency, respectively. Thus, to calculate the order parameter it is necessary to know the expression for the correlator $< a_{-q-\sigma}a_{q\sigma} >$. The classical expression for $\Delta_{k\sigma}$ known as the BCS equation was obtained [20] using the Bogolyubov's unitary transformation in a wave space. An elegant derivation of the BCS equation based on the equations of motion for Green's function was done by Gorkov in [16].

We will show that a zero-approximation of the self-consistent field also eventually leads to the BCS equation for the order parameter. In full analogy with the previous subsection it is necessary to present graphic images of interactions of the perturbation Hamiltonian (1.7). In a wave representation, the types of interaction lines are shown in Fig.2. Now two total Green's functions $Z_{q\sigma}^{--}(i\omega_n) = - < Ta_{-q-\sigma}(\tau)a_{q\sigma}(0) >_{i\omega_n}$ and $Z_{q\sigma}^{+-}(i\omega_n) = - < Ta_{q\sigma}^+(\tau)a_{q\sigma}(0) >_{i\omega_n}$ are connected and it is necessary to take into account two unperturbed Green functions:

$$G_{q\sigma}^{-+}(i\omega_n) \equiv G_{-q-\sigma}^{-+}(i\omega_n) = - <Ta_{q\sigma}(\tau)a_{q\sigma}^+(0)>_{0,i\omega_n} = G_1(i\omega_n) = \frac{1}{\beta(i\omega_n + \mu)}$$

$$G_{q\sigma}^{+-}(i\omega_n) \equiv G_{-q-\sigma}^{+-}(i\omega_n) = - <Ta_{q\sigma}^+(\tau)a_{q\sigma}(0)>_{0,i\omega_n} = G_2(i\omega_n) = -G_1(-i\omega_n)$$

(1.10)
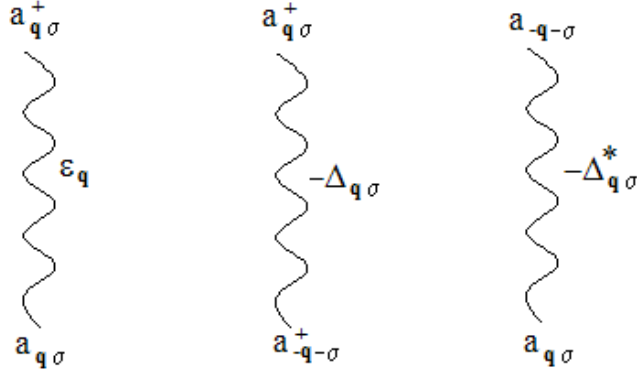
Fig. 1.2. All possible types of interaction lines for the Hamiltonian (1.7)

It directly follows from the graphic equation in Fig. 1.3 since a symbol of the end of the Green's line must always coincide with a corresponding symbol at the origin of interaction line and vice versa (see Fig. 1.3). Also, the interaction line overturn changes a sign of the corresponding parameter to the opposite one.
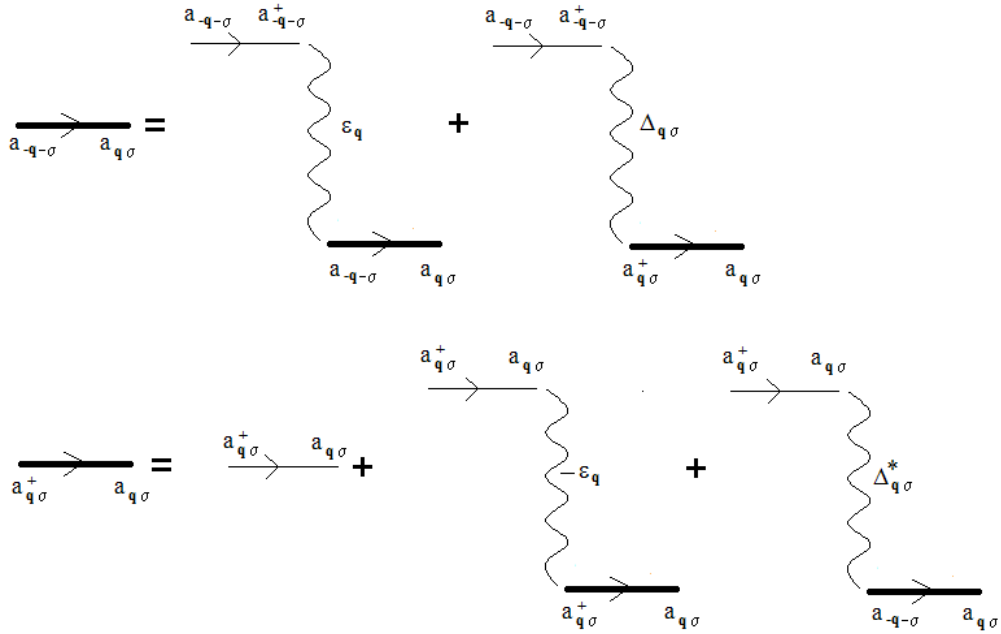
Fig. 1.3. The graphic system of equations for unknown total causal Green functions $Z_{q\sigma}^{--}(i\omega_n)$ and $Z_{q\sigma}^{+-}(i\omega_n)$

The following system of algebraic equations corresponds to the graphical system of equations in Fig. 1.3 for unknown terms:

$$Z_{-q-\sigma}^{--}(i\omega_n) = G_1(i\omega_n)\beta\Delta_{q\sigma}Z_{q\sigma}^{+-}(i\omega_n) + G_1(i\omega_n)\beta\varepsilon_{-q}Z_{-q-\sigma}^{--}(i\omega_n)$$

$$Z_{q\sigma}^{+-}(i\omega_n) = G_2(i\omega_n) - G_2(i\omega_n)\beta\varepsilon_q Z_{q\sigma}^{+-}(i\omega_n) + G_2(i\omega_n)\beta\Delta_{q\sigma}^* Z_{-q-\sigma}^{--}(i\omega_n)$$

(1.11)

17

It is not difficult to find a solution of this system with obvious condition $\varepsilon_q = \varepsilon_{-q}$. It can be written in the form:

$$Z_{q\sigma}^{+-}(i\omega_n) = \frac{G_2(i\omega_n)(1 - \beta\varepsilon_q G_1(i\omega_n))((i\omega_n)^2 - \mu^2)}{(i\omega_n - E_{q\sigma})(i\omega_n + E_{q\sigma})},$$ (1.12)

$$Z_{q\sigma}^{--}(i\omega_n) = \frac{\Delta_{q\sigma}}{2\beta E_{q\sigma}}\left\{\frac{1}{i\omega_n - E_{q\sigma}} - \frac{1}{i\omega_n - E_{q\sigma}}\right\},$$ (1.13)

where $E_{q\sigma} = \sqrt{(\varepsilon_q - \mu)^2 + |\Delta_{q\sigma}|^2}$ is the electron excitation energy with Cooper pairing. The solution (1.12) determines a spectral density of excitations and infinitesimal corrections to the chemical potential. Therefore, below we will consider the solution (1.13) that gives an expression for the correlator $< a_{-q-\sigma}a_{q\sigma} >$. It determines the self-consistent equation for the unknown gap function $\Delta_{q\sigma}$ according to Eq. (1.9). Indeed, for the times $\tau \to +0$ we have

$$< a_{-q-\sigma}a_{q\sigma} > = -Z_{-q-\sigma}^{--}(\tau \to +0) = < Ta_{-q-\sigma}(\tau \to +0)a_{q\sigma}(0) > = -\lim_{\tau \to +0}\sum_{n=-\infty}^{\infty}e^{-i\omega_n\tau}Z_{-q-\sigma}^{--}(i\omega_n)$$ (1.14)

Summation over an infinite number of frequencies is carried out on the basis of the method proposed by Luttinger and Ward in [21] for calculating the residues of the Green's function $Z_{-q-\sigma}^{--}(\omega)$ with a factor $\beta(f(\omega) - 1)$, where $f(\omega) = \dfrac{1}{e^{\beta\omega} + 1}$ is the Fermi distribution function. Thus, one can write

$$< a_{-q-\sigma}a_{q\sigma} > = -\beta\sum_i \text{Res}\left[Z_{-q-\sigma}^{--}(\omega)(f(\omega) - 1)\right]\Big|_i$$ (1.15)

From Eq. (1.13) it follows that the poles of $Z_{-q-\sigma}^{--}(\omega)$ are roots $\omega_i = \pm E_{q\sigma}$ that allows to immediately write for the correlator (1.15)

$$< a_{-q-\sigma}a_{q\sigma} > = -\frac{\Delta_{q\sigma}}{2E_{q\sigma}}\left\{f(E_{q\sigma}) - f(-E_{q\sigma})\right\}$$ (1.16)

Substituting Eq. (1.16) into Eq. (1.9), we obtain the well-known BCS equation for the superconducting energy gap:

$$\Delta_{k\sigma} = \sum_q \frac{|M_{k-q}|^2}{\omega_{k-q}}\frac{\Delta_{q\sigma}}{2E_{q\sigma}}\tanh\left(\frac{E_{q\sigma}}{2T}\right),$$ (1.17)

where $\dfrac{|M_{k-q}|^2}{\omega_{k-q}}$ is a matrix element of the electron-electron attraction.

In this subsection, it is obtained that a zero approximation of the self-consistent field is in fact an approximation of the molecular field in the theory of superconductivity. An influence of fluctuations can be taken into account by considering the contributions of loop diagrams in expressions for Green's functions. The presented theory allows us to consider the hybrid structure with a normal metal and a superconductor in which the induced superconductivity is realized as a phenomenon of the proximity effect.

1.4. Induced superconductivity in a normal metal

Let us consider a hybrid structure with a normal metal and a superconductor on the two sides of the junction. We assume that the connection between the metal and superconductor is carried out through a tunnel junction. Without applied voltage, the two subsystems are in equilibrium with a chemical potential μ. It turns out to be the simplest approximation of the self-consistent field and allows us to describe a proximity effect in the hybrid structure. It is supposed that the electronic subsystem of a normal metal can be in an ordered magnetic state. Then the unperturbed Hamiltonians of normal "left" and superconducting "right" metals in the site representation have the following form, respectively:

$$\hat{H}_{0L} = -\sum_{i\sigma} \mu_\sigma c_{\sigma i}^+ c_{\sigma i} \tag{1.18}$$

$$\hat{H}_{0R} = -\mu \sum_{i\sigma} a_{\sigma i}^+ a_{\sigma i} \, , \tag{1.19}$$

where $\mu_\sigma = \mu + \sigma J_0$, J_0 is the exchange parameter and $J_0 > 0$ for a ferromagnetic metal. Here, $\sigma = \pm 1$ in the case of a saturated state and $\sigma = \pm 2 < \sigma_z >$ for a magnet with a mean spin $< \sigma_z >$.

The total perturbation Hamiltonian for a whole system is

$$V = \sum_{i,j,\sigma} t_{1ij} c_{\sigma i}^+ c_{\sigma j} + \sum_{i,j,\sigma} t_{2ij} a_{\sigma i}^+ a_{\sigma j} - \sum_{i,j,\sigma} \left\{ \Delta_{ij\sigma} a_{\sigma i}^+ a_{\sigma j}^+ + \Delta_{ij\sigma}^* a_{-\sigma i} a_{\sigma j} \right\} + \hat{H}_T \, , \tag{1.20}$$

where the tunnel Hamiltonian is presented by the next manner

$$\hat{H}_T = \sum_{il\sigma} \left\{ T_{il} c_{i\sigma}^+ a_{l\sigma} + T_{il}^* a_{l\sigma}^+ c_{i\sigma} \right\} \tag{1.21}$$

In a full analogy with a diagram technique described in the previous subsections let us draw graphically possible types of interaction lines in a wave space in Fig. 1.4. In this case, one can assume that the wave vectors p and q with energies ε_p and ε_q belong to the "left" normal and "right" superconducting metals, respectively.
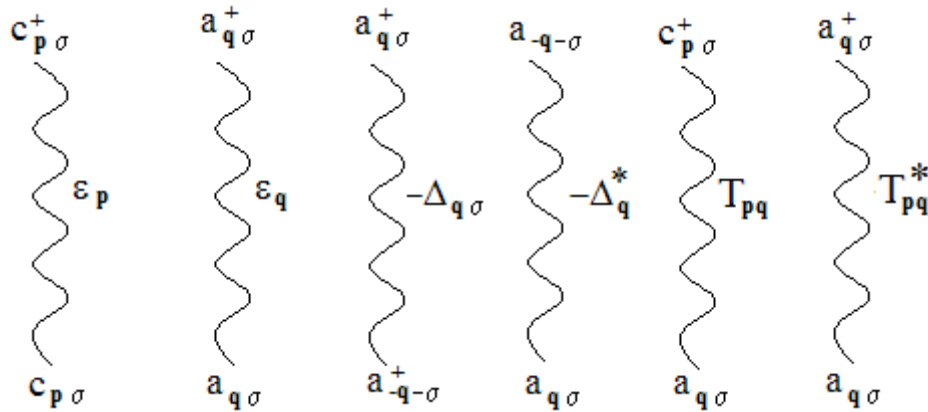
Fig. 1.4. All possible types of interaction lines for the Hamiltonian (1.20)

Here T_{pq} and T_{pq}^* are a matrix element and its complex conjugate value in a wave space, respectively. It is also necessary to consider that they depend on two wave vectors. Therefore, in the equations for Green's functions, which depend only on a single wave vector, the remaining one "internal" should be summed. Then one can write the graphical equations which determine the number of mutual connected Green's functions. In the presence of previously defined two unperturbed Green's functions $G_1(i\omega_n)$ and $G_2(i\omega_n)$ for the superconducting "right" metal there are new functions

$$\tilde{G}_{p\sigma}^{-+}(i\omega_n) \equiv \tilde{G}_{-p\sigma}^{-+}(i\omega_n) = - <Tc_{p\sigma}(\tau)c_{p\sigma}^+(0)>_{0,i\omega_n} = \tilde{G}_{1\sigma}(i\omega_n) = \frac{1}{\beta(i\omega_n + \mu_\sigma)}$$ (1.22)

$$\tilde{G}_{p\sigma}^{+-}(i\omega_n) \equiv \tilde{G}_{-p\sigma}^{+-}(i\omega_n) = - <Tc_{p\sigma}^+(\tau)c_{p\sigma}(0)>_{0,i\omega_n} = \tilde{G}_{2\sigma}(i\omega_n) = -G_{1\sigma}(-i\omega_n)$$

for a part of the hybrid structure with a normal metal. Then the correlator $<c_{-p-\sigma}c_{p\sigma}>$ for the "left" normal metal is connected with four complete Green's functions, i.e.,

$$Y_{p\sigma}^{--}(\tau) = - <Tc_{-p-\sigma}(\tau)c_{p\sigma}(0)>, \quad Z_{qp\sigma}^{--}(\tau) = - <Ta_{-q-\sigma}(\tau)c_{p\sigma}(0)>, \quad Z_{qp\sigma}^{+-}(\tau) = - <Ta_{q\sigma}^+(\tau)c_{p\sigma}(0)>$$

and $Y_{p\sigma}^{+-}(\tau) = - <Tc_{p\sigma}^+(\tau)c_{p\sigma}(0)>.$

Fig. 1.5 presents the graphical equations which are determined by the Hamiltonian (1.20) with all possible lines of the interaction in Fig. 1.4. The equations connect the Fourier components of the indicated total Green's functions. Bold points in the diagrams denote summation over the inner wave vector.

Fig. 1.5. Graphic system of equations for unknown total causal Green's functions

$$Y_{p\sigma}^{--}(i\omega_n), \ Z_{qp\sigma}^{--}(i\omega_n), \ Z_{qp\sigma}^{+-}(i\omega_n) \ \text{и} \ Y_{p\sigma}^{+-}(i\omega_n)$$

One can write this graphical system of equations in the algebraic form:

$$Y_{p\sigma}^{--}(i\omega_n) = \tilde{G}_{1-\sigma}\beta\varepsilon_p(i\omega_n)Y_{p\sigma}^{--}(i\omega_n) + \tilde{G}_{1-\sigma}\sum_q T_{-p-q}Z_{qp\sigma}^{--}(i\omega_n)$$

$$Z_{qp\sigma}^{--}(i\omega_n) = G_1(i\omega_n)\beta\Delta_{q\sigma}Z_{qp\sigma}^{+-}(i\omega_n) + G_1(i\omega_n)\beta\varepsilon_q Z_{qp\sigma}^{--}(i\omega_n) + G_1(i\omega_n)\beta T_{-p-q}^* Y_{p\sigma}^{--}(i\omega_n)$$
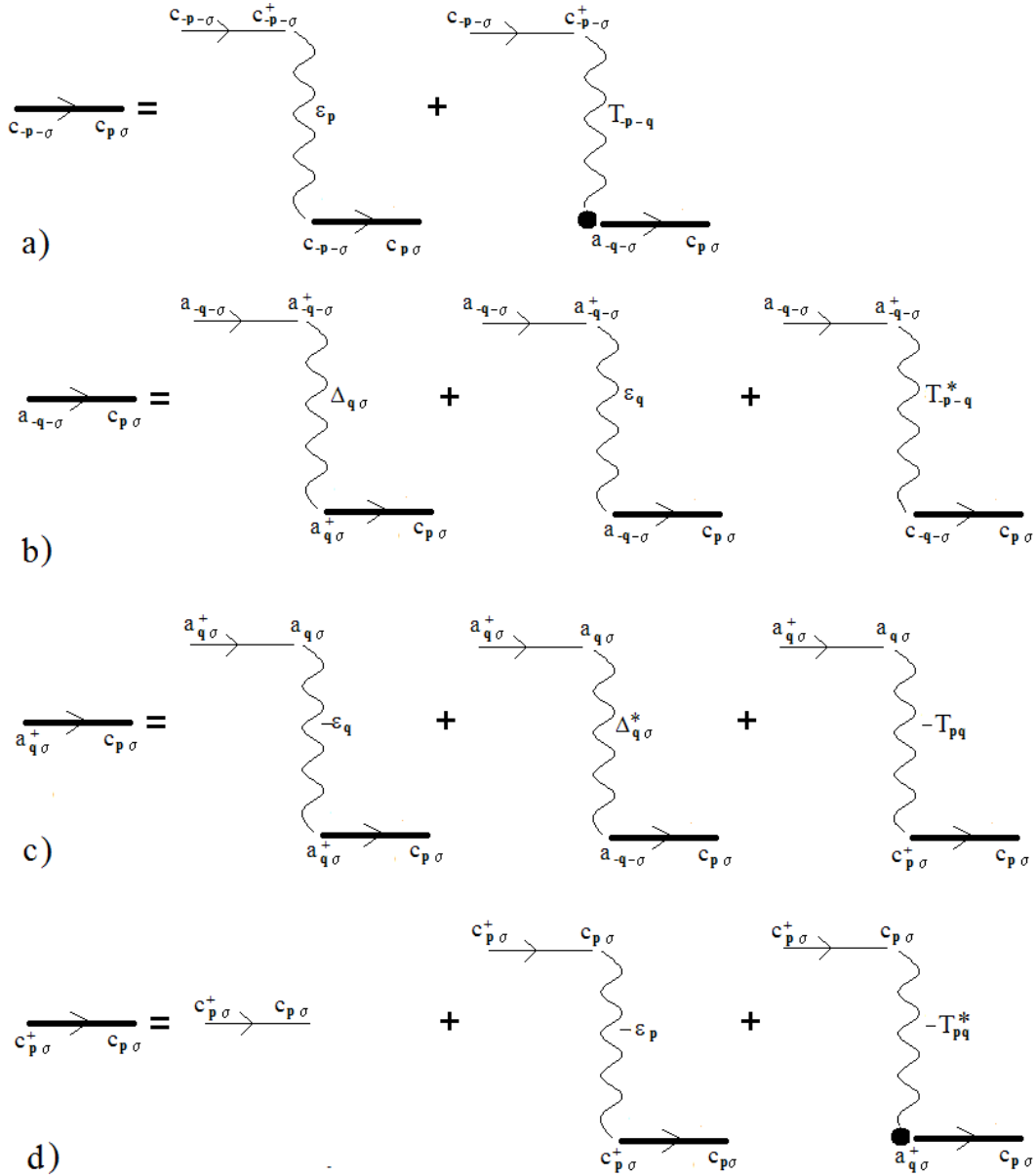
$$Z_{qp\sigma}^{+-}(i\omega_n) = -G_2(i\omega_n)\beta\varepsilon_q Z_{qp\sigma}^{+-}(i\omega_n) + G_2(i\omega_n)\beta\Delta_{q\sigma}^* Z_{qp\sigma}^{--}(i\omega_n) - G_2(i\omega_n)\beta T_{pq}Y_{p\sigma}^{+-}(i\omega_n) \qquad (1.23)$$

$$Y_{p\sigma}^{+-}(i\omega_n) = \tilde{G}_{2\sigma}(i\omega_n) - \tilde{G}_{2\sigma}(i\omega_n)Y_{p\sigma}^{+-}(i\omega_n) - \tilde{G}_{2\sigma}(i\omega_n)\sum_q \beta T_{pq}^* Z_{qp\sigma}^{+-}(i\omega_n)$$

In spite of the fact that this system of equations is integral it is easy to find its solution. Indeed, the 2-nd and 3-rd equations are linear with respect to the Green's functions depending simultaneously on the p and q wave vectors. Thus, expressing the off-diagonal $Z_{qp\sigma}^{--}(i\omega_n)$ and $Z_{qp\sigma}^{+-}(i\omega_n)$ in terms of diagonal we have

$$Z_{qp\sigma}^{--}(i\omega_n) = \frac{\beta G_1(i\omega_n)}{d_{q\sigma}(i\omega_n)}\left\{T_{-p-q}^*(1+\beta\varepsilon_q G_2(i\omega_n))Y_{p\sigma}^{--}(i\omega_n) - T_{pq}\beta\Delta_{q\sigma}G_2(i\omega_n)Y_{p\sigma}^{+-}(i\omega_n)\right\}$$

$$Z_{qp\sigma}^{+-}(i\omega_n) = \frac{\beta G_2(i\omega_n)}{d_{q\sigma}(i\omega_n)}\left\{-T_{pq}(1-\beta\varepsilon_q G_1(i\omega_n))Y_{p\sigma}^{+-}(i\omega_n) + T_{-p-q}^*\beta\Delta_{q\sigma}^* G_1(i\omega_n)Y_{p\sigma}^{--}(i\omega_n)\right\} \qquad (1.24)$$

where

$$d_{q\sigma}(i\omega_n) = (1-\beta\varepsilon_q G_1(i\omega_n))(1+\beta\varepsilon_q G_2(i\omega_n)) - \beta^2\left|\Delta_{q\sigma}\right|^2 G_1(i\omega_n)G_2(i\omega_n) \qquad (1.25)$$

Substituting the solutions (1.24) into the 1-st and 4-th equations of system (1.23) we obtain a system of two linear equations for the unknowns $Y_{p\sigma}^{--}(i\omega_n)$ and $Y_{p\sigma}^{+-}(i\omega_n)$ which do not depend on the summation over the wave vector q. For convenience, we put the following notation

$$\alpha_{p\sigma}(i\omega_n) = \beta^2\tilde{G}_{1-\sigma}(i\omega_n)G_1(i\omega_n)\sum_q \frac{1}{d_{q\sigma}(i\omega_n)}\left|T_{pq}\right|^2(1+\beta\varepsilon_q G_2(i\omega_n))$$

$$\beta_{p\sigma}(i\omega_n) = \beta^3\tilde{G}_{1-\sigma}(i\omega_n)G_1(i\omega_n)G_2(i\omega_n)\sum_q \frac{1}{d_{q\sigma}(i\omega_n)}\left|T_{pq}\right|^2\Delta_{q\sigma}$$

$$\gamma_{p\sigma}(i\omega_n) = \beta^2\tilde{G}_{2\sigma}(i\omega_n)G_2(i\omega_n)\sum_q \frac{1}{d_{q\sigma}(i\omega_n)}\left|T_{pq}\right|^2(1-\beta\varepsilon_q G_1(i\omega_n)) \qquad (1.26)$$

$$\theta_{p\sigma}(i\omega_n) = \beta^3\tilde{G}_{2\sigma}(i\omega_n)G_1(i\omega_n)G_2(i\omega_n)\sum_q \frac{1}{d_{q\sigma}(i\omega_n)}\left|T_{pq}\right|^2\Delta_{q\sigma}^*$$

Here, the identity $T_{pq}^* = T_{-p-q}$ for the tunnel matrix element is used. Then the above system of linear equations takes the form:

$$Y_{p\sigma}^{--}(i\omega_n) = \left(\tilde{G}_{1-\sigma}(i\omega_n)\beta\varepsilon_p + \alpha_{p\sigma}(i\omega_n)\right)Y_{p\sigma}^{--}(i\omega_n) - \beta_{p\sigma}(i\omega_n)Y_{p\sigma}^{+-}(i\omega_n)$$

$$Y_{p\sigma}^{+-}(i\omega_n) = \tilde{G}_{2\sigma}(i\omega_n) - \theta_{p\sigma}(i\omega_n)Y_{p\sigma}^{--}(i\omega_n) + (\gamma_{p\sigma}(i\omega_n) - \beta\varepsilon_p\tilde{G}_{2\sigma}(i\omega_n))Y_{p\sigma}^{+-}(i\omega_n) \qquad (1.27)$$

The solution of this system of equations is written as follows:

$$Y_{p\sigma}^{+-}(i\omega_n) = -\frac{1-\beta\varepsilon_p\tilde{G}_{1-\sigma}(i\omega_n) - \alpha_{p\sigma}(i\omega_n)}{\beta_{p\sigma}(i\omega_n)}Y_{p\sigma}^{--}(i\omega_n)$$

$$Y_{p\sigma}^{--}(i\omega_n) = \frac{\tilde{G}_{2\sigma}(i\omega_n)\beta_{p\sigma}(i\omega_n)}{\theta_{p\sigma}(i\omega_n)\beta_{p\sigma}(i\omega_n) - \left[1+\beta\varepsilon_p\tilde{G}_{2\sigma}(i\omega_n) - \gamma_{p\sigma}(i\omega_n)\right]\left[1-\beta\varepsilon_p\tilde{G}_{1-\sigma}(i\omega_n) - \alpha_{p\sigma}(i\omega_n)\right]} \qquad (1.28)$$

We are interested in the Green's function $Y_{p\sigma}^{--}(i\omega_n)$ since it defines the energy gap in a normal metal. In accordance with Eq. (1.15), real frequencies are used to calculate the correlators. Then in all functions we make a replacement $i\omega_n \to \omega$. Substituting the unperturbed Green's functions $G_1(\omega)$ and $G_2(\omega)$ in Eq. (1.25) it is easy to find

$$d_{q\sigma}(\omega) = \frac{\omega^2 - \mu^2}{(\omega - E_{q\sigma})(\omega + E_{q\sigma})}, \tag{1.29}$$

where $E_{q\sigma}$ is the electron excitation energy from Eq.(1.13) for a superconductor. Similarly, for real frequencies we have

$$\alpha_{p\sigma}(\omega) = \frac{\tilde{\alpha}_{p\sigma}}{\omega + \mu_{-\sigma}}, \quad \beta_{p\sigma}(\omega) = \frac{\tilde{\beta}_{p\sigma}}{\omega + \mu_{-\sigma}}, \quad \gamma_{p\sigma}(\omega) = \frac{\tilde{\gamma}_{p\sigma}}{\omega - \mu_{\sigma}}, \quad \theta_{p\sigma}(\omega) = \frac{\tilde{\theta}_{p\sigma}}{\omega - \mu_{\sigma}}, \tag{1.30}$$

where $\xi_q = \varepsilon_q - \mu$ and

$$\tilde{\alpha}_{p\sigma}(\omega) = \sum_q \left| T_{pq} \right|^2 \frac{\omega + \xi_q}{(\omega - E_{q\sigma})(\omega + E_{q\sigma})}$$

$$\tilde{\beta}_{p\sigma}(\omega) = \sum_q \left| T_{pq} \right|^2 \Delta_{q\sigma} \frac{1}{(\omega - E_{q\sigma})(\omega + E_{q\sigma})}$$

$$\tilde{\gamma}_{p\sigma}(\omega) = \sum_q \left| T_{pq} \right|^2 \frac{\omega - \xi_q}{(\omega - E_{q\sigma})(\omega + E_{q\sigma})} \tag{1.31}$$

$$\tilde{\theta}_{p\sigma}(\omega) = \tilde{\beta}_{p\sigma}^*(\omega)$$

The Green's function $Y_{p\sigma}^{--}(i\omega_n)$ is determined as

$$Y_{p\sigma}^{--}(\omega) = -\frac{1}{\beta} \frac{\tilde{\beta}_{p\sigma}(\omega)}{(\omega + \xi_p - J_0\sigma - \tilde{\gamma}_{p\sigma}(\omega))(\omega - \xi_p - J_0\sigma - \tilde{\alpha}_{p\sigma}(\omega)) - \left| \tilde{\beta}_{p\sigma}(\omega) \right|^2} \tag{1.32}$$

It follows from Eq. (1.32) that in order to find the $Y_{p\sigma}^{--}(\omega)$ poles it is necessary to solve complicated integral equations with a frequency ω. The problem is significantly simplified if we assume that the absolute value of the tunnel matrix element squared $\left| T_{pq} \right|^2$ is much less than electron excitation energies $\omega_{01} = \xi_p + J_0\sigma$ and $\omega_{02} = -\xi_p + J_0\sigma$ in a normal metal without tunneling. Then in sums of Eq. (1.31) the frequencies ω can be replaced by corresponding ω_{0i} and Green's function poles (1.32) are written in the form:

$$\omega_1 = \omega_{01} + \tilde{\alpha}_{p\sigma}(\omega_{01})$$
$$\omega_2 = \omega_{02} + \tilde{\gamma}_{p\sigma}(\omega_{02}) \tag{1.33}$$

where $\left| \tilde{\beta}_{p\sigma}(\omega) \right|^2 \sim \left| T_{p\sigma} \right|^4$ is taken into account. In Eq. (1.32), this contribution to $Y_{p\sigma}^{--}(\omega)$ poles is neglected. It should be noted that in another extreme case $\left| T_{pq} \right| \gg \omega_{0i}$ with obvious condition $\mu \gg \left| T_{pq} \right|$ we have $\tilde{\beta}_{p\sigma}(\omega) \sim \left| T_{p\sigma} \right|^2 \Delta \rho(\mu)/\mu^{3/2} \sim 0$ where $\rho(\mu)$ is the free electron density of states at the Fermi level (see 1.7 Appendix, formula (1.59)). Thus, with a high barrier transparency, the Cooper pairs of a superconductor are destroyed in a normal metal and the proximity effect is not observed.

Now one can write the final expression for $Y_{p\sigma}^{--}(\omega)$

$$Y_{p\sigma}^{--}(\omega) = \frac{1}{\beta}\left\{\frac{\tilde{\beta}_{p\sigma}(\omega_{02})}{(2\xi_p + \tilde{\alpha}_{p\sigma}(\omega_{02}) - \tilde{\gamma}_{p\sigma}(\omega_{02}))(\omega - \omega_2)} - \frac{\tilde{\beta}_{p\sigma}(\omega_{01})}{(2\xi_p + \tilde{\alpha}_{p\sigma}(\omega_{01}) - \tilde{\gamma}_{p\sigma}(\omega_{01}))(\omega - \omega_1)}\right\} \quad (1.34)$$

Further we consider the ballistic limit when $|T_{p\sigma}| = B$. Also, we put $\Delta_{q\sigma} = \Delta$, i.e., the superconducting energy gap is real and nondispersive. Then we have

$$\tilde{\alpha}_{p\sigma}(\omega_{0i}) - \tilde{\gamma}_{p\sigma}(\omega_{0i}) = 2B^2\chi(\omega_{0i})$$
$$\tilde{\beta}_{p\sigma}(\omega_{0i}) = B^2\Delta\varphi(\omega_{0i}) \quad (1.35)$$

where

$$\varphi(\omega) = \sum_q \frac{1}{(\omega^2 - \xi_q^2 - \Delta^2)}$$
$$\chi(\omega) = \sum_q \frac{\xi_q}{(\omega^2 - \xi_q^2 - \Delta^2)} \quad (1.36)$$

It is obvious that the correlator $<c_{-p-\sigma}c_{p\sigma}>$ of the electron singlet pairing in a normal metal is expressed in terms of functions $\varphi(\omega_{0i})$ and $\chi(\omega_{0i})$ using the formula

$$<c_{-p-\sigma}c_{p\sigma}> = -\beta\sum_i \text{Res}\left[Y_{p\sigma}^{--}(\omega)(f(\omega)-1)\right]\Big|_i, \quad (1.37)$$

as in the previous section. The result is

$$<c_{-p-\sigma}c_{p\sigma}> = -\frac{1}{2}B^2\Delta\left\{\frac{\varphi(\omega_{02})[f(\omega_2)-1]}{\xi_p + B^2\chi(\omega_{02})} - \frac{\varphi(\omega_{01})[f(\omega_1)-1]}{\xi_p + B^2\chi(\omega_{01})}\right\} \quad (1.38)$$

This correlator produces an energy gap function of the induced superconductivity which is determined by the matrix element $\tilde{V}_{kp}$ of the electron-electron attraction in a normal metal by means of the standard equation

$$\tilde{\Delta}_{k\sigma} = \sum_p \tilde{V}_{kp}<c_{-p-\sigma}c_{p\sigma}> \quad (1.39)$$

Since the "left" metal is in the normal state, Eq. (1.39) is not self-consistent with respect to the order parameter $\tilde{\Delta}_{k\sigma}$. This parameter is induced exclusively by a gap function Δ of the "right" superconducting metal.

As can be seen from Eq. (1.38), for finding $<c_{-p-\sigma}c_{p\sigma}>$ it is necessary to calculate the integrals (1.36) that is not difficult. We will neglect the exchange interaction of electrons, i.e. $J_0 = 0$. For a metal the obvious relation $\mu >> \Delta$ is satisfied. The results of the calculations of integrals (1.36) are given in the Appendix to this subsection. In particular, it is obtained that at $|\Delta| < |\xi_p|$ the function $\varphi(\pm\xi_p) = 0$, i.e., in a normal metal, electrons with an energy ξ_p exceeding the superconducting energy gap do not pair. In this case, the proximity effect in a hybrid structure is not realized. At $|\Delta| > |\xi_p|$, the expressions for $\varphi(\xi_p)$ and $\chi(\xi_p)$ take the form (see (1.65) and (1.66) below):

$$\varphi(\xi_p) = -\frac{\pi\rho(\mu)}{2\sqrt{\Delta^2 - \xi_p^2}}$$

$$\chi(\xi_p) = -\rho(\mu)\left\{ 2 + \ln\frac{\sqrt{\Delta^2 - \xi_p^2}}{4\mu} \right\}$$

(1.40)

Substituting functions (1.40) into Eq. (1.38) and using Eq. (1.39) we obtain the equation for an induced gap in a normal metal:

$$\tilde{\Delta} = \frac{1}{8}\pi\tilde{\lambda}r\Delta\int\limits_{-\Delta}^{\Delta} d\xi \frac{\tanh\left(\dfrac{\xi}{2T}\right)}{\sqrt{\Delta^2 - \xi^2}\left\{\xi + c\right\}},$$

(1.41)

where $c = -r\left[2 + \ln\dfrac{\sqrt{\Delta^2 - \xi^2}}{4\mu}\right]$, $r = 2B^2\rho(\mu)$ and $\tilde{\lambda} = \tilde{V}_{kp}\tilde{\rho}(\mu)$ is the effective electron attraction constant in a normal metal with the density of state $\tilde{\rho}(\mu)$ on the Fermi level. In the McMillan notation [15] for a superconductor unit volume the quantity $r = 2\Gamma_N$ is determined by the relaxation time in a normal state. We suppose that the homogeneity condition $\tilde{\Delta}_{k\sigma} = \tilde{\Delta}$ is satisfied for an induced gap in the ballistic limit.

The integral in Eq. (1.41) contains a pole singularity at $\xi = -c < 0$. It indicates the need to take into account for the adiabatic inclusion of the interaction associated with the tunnel Hamiltonian. Therefore, the integrand in Eq. (1.41) is analytically continued to the upper complex plain that makes it possible to write integral (1.41) in the form

$$\int\limits_{-\Delta}^{\Delta}....d\xi = V.p.\int\limits_{-\Delta}^{\Delta}....d\xi - i\pi\int\limits_{-\Delta}^{\Delta}....\delta(\xi + c)d\xi$$

(1.42)

in accordance with the Landau bypass rule [10]. Here, $V.p.$ denotes a principal real value of the integral and $\delta(x)$ is the Dirac delta-function which determines its imaginary part. It is also necessary to take into account that at $T = 0$ we get $\tanh\left(\dfrac{\xi}{2T}\right) = \text{sign}(\xi)$. It is supposed that $B <<$ Δ and then

$$c \approx \tilde{c}(r, \Delta) = -r\left[2 + \ln\frac{\Delta}{4\mu}\right],$$

(1.43)

since the corrections will be of a higher order of smallness over the parameter B. Also, $c > 0$ due to the ratio $4\mu >> \Delta$. It should be noted that in the most cases $\ln\dfrac{\Delta}{4\mu} \sim -10$ that results in $c \sim 8r$. Therefore, at least the inequality $\Delta > 8r$ is satisfied. Numerically integrating (1.41) as the main value we obtain the dependence of the real part of the induced gap $\tilde{\Delta}$ on both temperature T and Δ for different values of parameters. The imaginary part of this integral determines the phase ψ of the induced order parameter. At temperature $T = 0$ it is easy to find analytical expressions for both $\text{Re}\left(\tilde{\Delta}\right)$ and ψ which can be written as

$$\text{Re}\left(\tilde{\Delta}\right) = \frac{1}{8}\pi\tilde{\lambda}r\frac{\Delta}{\sqrt{\Delta^2 - \tilde{c}(r,\Delta)^2}}P\left(\Delta, r\right)$$

$$\psi = \arctan\frac{\pi}{P\left(\Delta, r\right)}$$

(1.44)

where $P\left(\Delta, r\right) = \ln\dfrac{\Delta + \sqrt{\Delta^2 - \tilde{c}(r,\Delta)^2}}{\Delta - \sqrt{\Delta^2 - \tilde{c}(r,\Delta)^2}}$. The absolute value of the induced gap has the form

$$\left|\tilde{\Delta}\right| = \frac{1}{8}\pi\tilde{\lambda}r\frac{\Delta}{\sqrt{\Delta^2 - \tilde{c}(r,\Delta)^2}}\sqrt{P^2\left(\Delta, r\right) + \pi^2}$$

(1.45)

It can be seen from Eq. (1.44) that with $r \to 0$ both gap $\tilde{\Delta}$ and phase ψ also tend to zero despite the divergence of the natural logarithm. In Fig. 1.6a and 1.6b dependences of the relative gap $\left|\tilde{\Delta}/\Delta\right|$ and induced $\tilde{\Delta}$ on the value r and superconducting gap Δ at zero temperature for $\mu = 5$ eV and $\tilde{\lambda} = 0.14$ are demonstrated, respectively. The figure shows that the induced gap value can be amount to 5-6% percent of the original although in the area $\Delta \sim 6r$ the observed strong growth is associated with an error of the chosen approximation when $\Delta \sim \tilde{c}(r,\Delta)$. With an increase the tunnelling probability the proximity effect is strengthen as well as with an increase of the superconducting gap value a relative value of the induced $\tilde{\Delta}$ decreases.
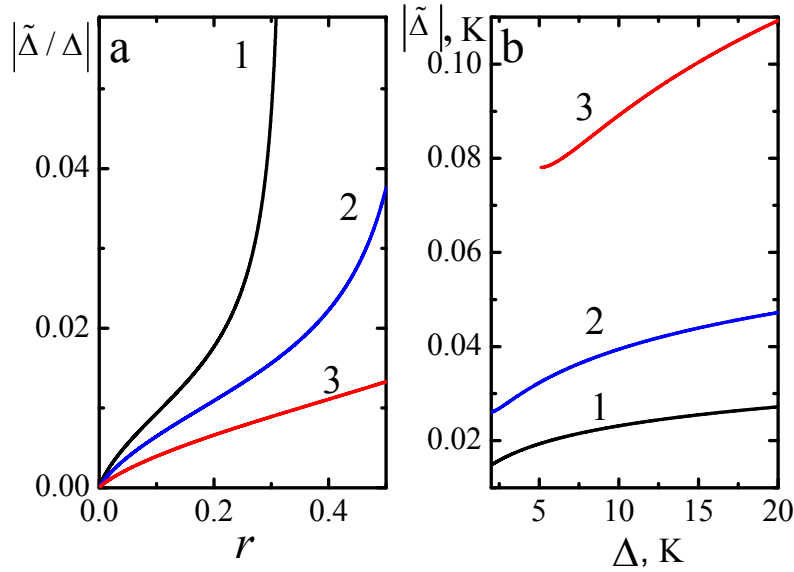
Fig. 1.6. Dependencies of (a) the absolute value of relative gap $\left|\tilde{\Delta}/\Delta\right|$ on the doubled barrier transparency $r = 2\Gamma_N$ at $\Delta = 3$, 5 and 10 K and (b) the induced gap $\tilde{\Delta}$ on the superconducting gap Δ at $r = 0.05$, 0.1 and 0.3 K (curves 1-3, respectively), temperature $T = 0$. The values $\mu = 5$ eV and $\tilde{\lambda} = 0.14$ were used

The phase of the induced order parameter depends on both r and Δ. Fig. 1.7 presents the dependences of induced order parameter phase on the doubled transparency r (*a*) and the superconducting energy gap function Δ (*b*). From the figure it can be seen that for a fixed Δ the phase of $\tilde{\Delta}$ increases from zero to 90° with increasing the barrier transparency. For a given

barrier transparency an increase in Δ leads to a decrease in the phase which for a large Δ slowly approaches to zero in accordance with the limit $\Delta \rightarrow \infty$ in Eq. (1.44) for ψ.
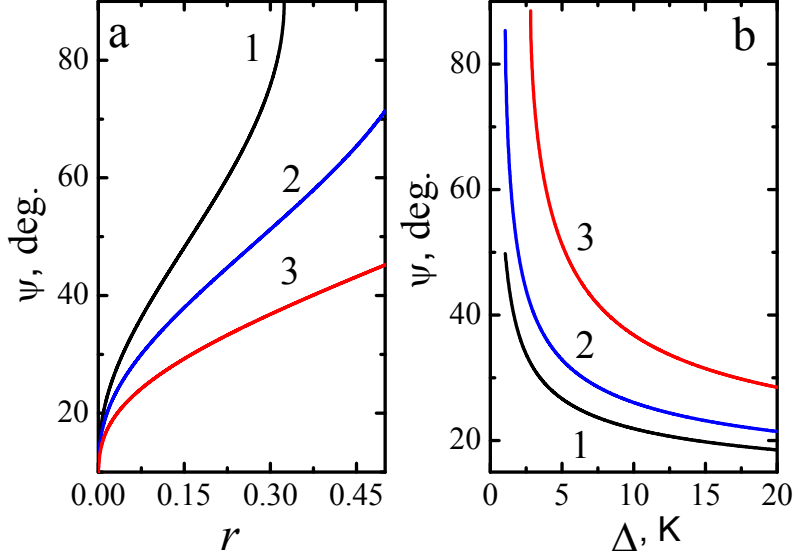
Fig. 1.7. Dependences of the order parameter phase ψ at temperature $T = 0$ (a) on the doubled barrier transparency $r = 2\Gamma_N$ at $\Delta = 3, 5$ and 10 K and (b) on the superconducting energy gap function Δ at $r = 0.05, 0.1$ and 0.3 K (curves 1- 3, respectively) with a chemical potential $\mu = 5$ eV, temperature $T = 0$

In conclusion, we will consider the temperature dependences of the absolute value of the induced superconducting energy gap and its phase in the hybrid structure Ti-barrier-Sn. The critical temperatures of phase transitions in the superconducting state for Ti and Sn are 0.4 and 3.75 K, respectively. The electron effective-attraction constant in normal metals Ti and Sn are 0.141 and 0.245 [22], respectively. Fig. 1.8 presents the temperature dependence of the energy gap function Δ for Sn used to calculate $\tilde{\Delta}$ as a function of T using Eq. (1.41). To calculate $\Delta(T)$, the relation $\omega_D(\lambda) = 0.5\Delta_0 \exp(1/\lambda)$ for the Debye frequency is taken into account, where $\Delta_0 = 6.6$ K is the superconducting energy gap for Sn at $T = 0$. In this case the root of equation $\xi = c$ is determined numerically but not by the approximate formula (1.43). Then from Eq. (1.41) it is easy to find that

$$\left|\tilde{\Delta}\right| = \sqrt{\left[\operatorname{Re}\left(\tilde{\Delta}\right)\right]^2 + \left[\operatorname{Im}\left(\tilde{\Delta}\right)\right]^2} , \qquad (1.46)$$

where $\operatorname{Im}\left(\tilde{\Delta}\right) = \dfrac{\pi^2 \tilde{\lambda} r \Delta \tanh\left(\dfrac{c}{2T}\right)}{8\sqrt{\Delta^2 - c^2}}$. Obviously, the phase ψ of the induced energy gap has the form

$$\psi = \arctan\left(\dfrac{\operatorname{Im}\left(\tilde{\Delta}\right)}{\operatorname{Re}\left(\tilde{\Delta}\right)}\right) \qquad (1.47)$$
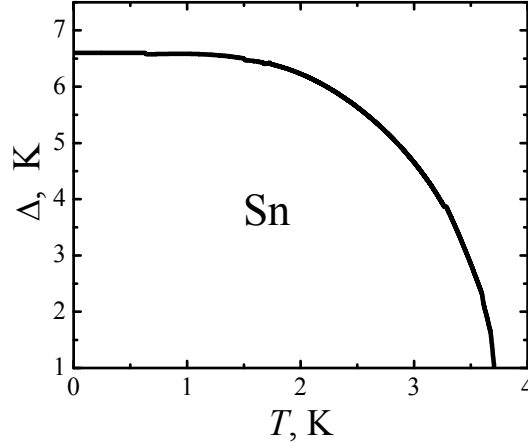
Fig. 1.8. Temperature dependence of the superconducting energy gap Δ for Sn

In Fig. 1.9 temperature dependences of both $\left|\tilde{\Delta}\right|$ and ψ for the energy gap induced in Ti are presented. From Fig.1.9 it follows that for $r = 0.3$ K the maximum proximity effect is only a few percent of the original gap. In the area of the Δ strong decay, the calculation becomes difficult due to the violation of the basic requirement $\Delta > 8r$. Note that with increasing the temperature the order parameter phase is non-monotonic and oscillates around its value at zero temperature.
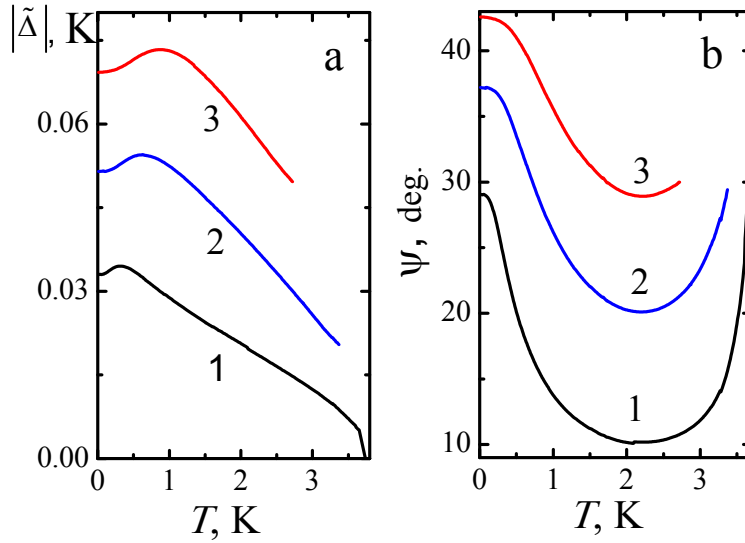
Fig. 1.9. Temperature dependences of (a) an absolute value of the induced superconducting energy gap and (b) the phase ψ of $\tilde{\Delta}$ in the hybrid structure Ti-barrier-Sn for double transparency values $r = 0.1$, 0.2 and 0.3 K (curves 1-3, respectively). The chemical potential is assumed to be 5 eV

Thus, in the framework of a weak-barrier transparency approximation it was obtained that the proximity effect is only a few percent of the initial superconducting energy gap. In the case of the strong-barrier transparency the tunneling destroys Cooper pairs in a normal metal that leads to the disappearance of the proximity effect.

1.5. Spectral density of states in a normal metal – superconductor structure

It is interesting to find the spectral density of states determined experimentally by the differential conductivity [19]. As is known [19], the Green's functions to be obtained in the previous sections (see Eqs.(1.12) and (1.28)) have imaginary parts determined by means of the analytic continuation $\omega \to \omega + i\delta$. In this case, the general property $G_{q\sigma}^{-+}(i\omega_n) = -G_{q\sigma}^{+-}(-i\omega_n)$ is used. Then for a superconductor one can write the spectral density

$$A_{q\sigma}(\omega) = -2\beta \operatorname{Im} Z_{q\sigma}^{-+}(\omega + i\delta), \tag{1.48}$$

and for a normal metal in the considered hybrid structure

$$A_{p\sigma}(\omega) = -2\beta \operatorname{Im} Y_{q\sigma}^{-+}(\omega + i\delta) \tag{1.49}$$

Further, we are interested in homogeneous spectral densities $R_\sigma^S(\omega) = \sum_q A_{q\sigma}(\omega)$ and $R_\sigma^N(\omega) = \sum_p A_{p\sigma}(\omega)$ for both the superconductor and the metal, respectively. From Eq. (1.12) at $\mu \gg \omega$ it is easy to find the traditional spectral density of a superconductor at $\omega > \Delta$:

$$R_\sigma^S(\omega) = \frac{\pi \rho(\mu) \omega}{\sqrt{\omega^2 - \Delta^2}} \tag{1.50}$$

For a normal metal from Eq. (1.28) in the linear approximation with Γ_N it follows that

$$Y_{p\sigma}^{-+}(\omega) = \frac{G_1(\omega)}{1 - \beta \varepsilon_p G_1(\omega) - \gamma_{p\sigma}(-\omega)}$$

Taking into account Eqs. (1.31) we get for a retarded Green's function which determines the spectral density of states

$$Y_{p\sigma}^{-+}(\omega + i\delta) = \frac{1}{\beta} \frac{1}{\omega + i\delta - \xi_p - \tilde{\alpha}_{p\sigma}(\omega + i\delta)}, \tag{1.51}$$

where $\tilde{\alpha}_{p\sigma}(\omega) = B^2(\omega\varphi(\omega) + \chi(\omega))$ and functions $\varphi(\omega)$ and $\chi(\omega)$ are defined by Eqs. (1.36). From Eqs. (1.36) it follows that the analytic continuation of functions $\varphi(\omega)$ and $\chi(\omega)$ gives the imaginary parts only for $\omega > \Delta$ because of the delta-functions presence. Thus, for excitation energies $\omega < \Delta$, i.e., in the area of the proximity effect realization, the spectrum of electronic excitations is coherent. From (1.63) and (1.64) at $\sqrt{\Delta^2 - \omega^2} \ll \mu$ it follows that

$$\begin{aligned} \varphi(\omega) &\approx -\frac{\rho(\mu)}{\sqrt{\Delta^2 - \omega^2}} \arctan\left(\frac{2\mu}{\sqrt{\Delta^2 - \omega^2}}\right) \\ \chi(\omega) &\approx -\rho(\mu)\left\{2 + \ln\left(\frac{\sqrt{\Delta^2 - \omega^2}}{4\mu}\right)\right\} \end{aligned} \tag{1.52}$$

Obviously, $\tilde{\alpha}_{p\sigma}(\omega)$ is a mass operator for the Green's function $Y_{p\sigma}^{-+}(\omega)$ [19]. Therefore, one can write the spectral density of coherent excitations in a normal metal as

$$A_{p\sigma}(\omega) = 2\pi Z(\omega)\delta(\omega - \xi_p), \tag{1.53}$$

where the intensity of a quasiparticle peak is

$$Z_{p\sigma}(\omega) = \frac{1}{\left| 1 - \frac{\partial}{\partial \omega} \tilde{\alpha}_{p\sigma}(\omega) \right|_{\omega = \xi_p}} \tag{1.54}$$

and

$$\frac{\partial}{\partial \omega} \tilde{\alpha}_{p\sigma}(\omega) = B^2 (\varphi(\omega) + \omega \varphi'(\omega) + \chi'(\omega)) \tag{1.55}$$

Using Eqs. (1.52) we calculate the derivatives $\varphi'(\omega)$ and $\chi'(\omega)$ and substitute in Eq. (1.55) and further in Eqs. (1.54) - (1.53). The sum of the functions $A_{p\sigma}(\omega)$ over vectors gives the final expression for the frequency dependence of the uniform spectral density

$$R_\sigma^N(\omega) = \frac{2\pi \rho(\mu)}{\left| 1 - \Gamma_N \left\{ \frac{\omega}{\Delta^2 - \omega^2} - \frac{\pi \Delta^2}{2\sqrt{(\Delta^2 - \omega^2)^3}} \right\} \right|} \tag{1.56}$$

When $\Gamma_N = 0$ we obtain the spectral density of normal metal. From Eq. (1.56) it can be seen that with decreasing Γ_N the spectral density increases approaching a constant value $2\pi \rho(\mu)$ for a normal metal. Thus, the proximity effect weakens. If Γ_N increases the contribution of the unit in the denominator Eq. (1.56) decreases and $R_\sigma^N(\omega) \sim 1/\Gamma_N$, i.e., the spectral density decreases to zero. In this case, the normal metal approaches the superconducting state. Note that in the area $\omega < \Delta$ of coherent excitations the spectral density has a maximum which position is determined only by the superconducting energy gap Δ. Indeed, the extremum point $\omega = \omega_{ext}$ of the denominator from Eq. (1.56) is found to be from the algebraic equation

$$(\Delta^4 - \omega^4)(\Delta^2 + \omega^2) = \frac{9\pi^2}{4} \omega^2 \Delta^4 \ . \tag{1.57}$$

Its approximate solution can be written in the form

$$\omega_{ext} \approx \frac{2\Delta}{\sqrt{9\pi^2 - 4}} \approx 0.217\Delta, \tag{1.58}$$

Thus, measuring the position of the maximum in the spectral density it is possible to determine the value of the superconducting energy gap. In Fig. 1.10 the frequency dependences of the uniform spectral density of states $R_\sigma^N(\omega)$ from Eq. (1.56) in a normal metal with an induced gap for the superconducting energy gap value $\Delta = 2.12 \cdot 10^{-4}$ eV and $\mu = 8.16$ eV with different barrier transparency coefficients Γ_N are presented. From this figure it can be seen that with increasing Γ_N the spectral density $R_\sigma^N(\omega)$ approaches zero that reflects the strengthening proximity effect, when a normal metal acquires the properties of a superconducting one (see curve 5 in Fig. 1.10). On the other hand, with decreasing barrier transparency the spectral density of states approaches closer to a purely metallic state (see the straight line 1 in Fig. 1.10). The $R_\sigma^N(\omega)$ behavior is consistent with the experiment [23]. The differences obtained are due to only the fact that in this model the spatial dependence of both gap functions $\tilde{\Delta}$ and Δ is not taking into account.
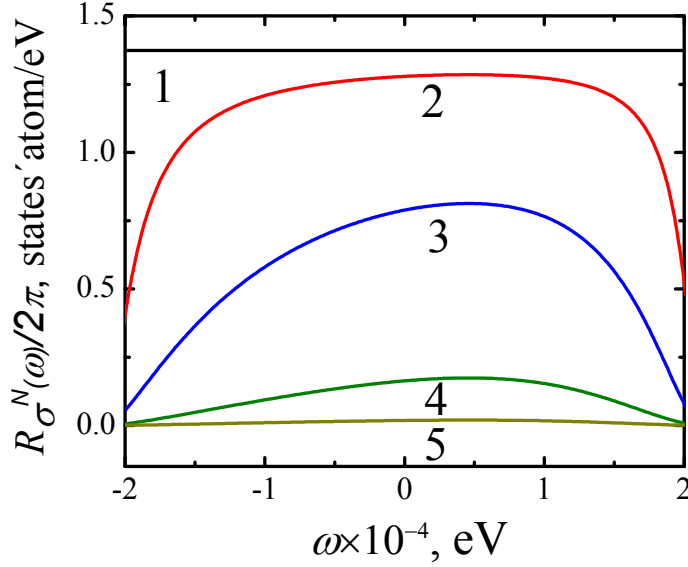
Fig. 1.10. Frequency dependences of the homogeneous spectral density of states $\dfrac{R_\sigma^N(\omega)}{2\pi}$ from

Eq. (1.56) in a normal metal with the induced gap $\tilde{\Delta}$ for the superconducting energy gap value $\Delta = 2.12 \cdot 10^{-4}$ eV, the chemical potential $\mu = 8.16$ eV and the barrier transparency coefficients $\Gamma_N = 0.,\ 10^{-5},\ 10^{-4},\ 10^{-3}$ and 10^{-2} states$\cdot$ atom$\cdot$eV (curves 1-5, respectively). The density of states at the Fermi level $\rho(\mu) = 1.37$, states $\cdot$atom / eV is taken for Ti atom (4 electrons per atom)

1.6. Conclusions

Summing up, it can be stated that the presented diagram method of a time-perturbation theory in a zero approximation of the self-consistent field gives results that coincide with the approximation of the molecular field for a metal in the normal and superconducting states. Also, for the first time, in the framework of this method the appearance of a proximity effect in the form of a complex energy gap induced by a superconductor in a normal metal is predicted. In the low-barrier transparency limit an absolute value of the induced energy gap was found to be only a few percent of the superconducting one. The temperature and parametric dependences of the energy gap $\left|\tilde{\Delta}\right|$ as well as the phase ψ of the induced order parameter are obtained. It is consistent with the increase of the barrier transparency and decrease of the energy gap of a superconductor with approaching the critical temperature. Sufficiently large value of the tunnel matrix element leads to the destruction of the Cooper pairs and the absence of the proximity effect in the considered hybrid structure.

With increasing the barrier transparency the spectral density decreases that reflects the proximity effect strengthening when a normal metal acquires superconducting properties. However, for a high transparency (*8r* > Δ) Cooper pairs in a normal metal are destroyed. When the barrier transparency decreases the density of states approaches a purely metallic one. The behaviour is consistent with the experiment although the existing quantitative differences are connected with the presence of the spatial dependence of the gap functions $\tilde{\Delta}$ and Δ that is not taken into account in the considered approximation. Also, this theory essentially simplifies a subsequent account for corrections due to the influence of fluctuations.

1.7. Appendix

Let us calculate integrals $\varphi(\omega)$ and $\chi(\omega)$ from Eq. (1.36). Consider a simpler case when $\mu \gg |\omega| > \Delta$. Then for the density of states we get $\rho(\varepsilon) = C\sqrt{\varepsilon}$ and $d(\omega) = \sqrt{\omega^2 - \Delta^2}$, where $C = \dfrac{V}{2\pi^2\hbar^3}(2m)^{3/2}$ is the constant for an electron with mass m in a crystal of the volume V.

$$\varphi(\omega) = -\int_0^\mu d\varepsilon \frac{C\sqrt{\varepsilon}}{(\varepsilon-\mu)^2 - d(\omega)^2} = -\frac{C}{2d(\omega)}\{L(\mu, d(\omega)) - L(\mu, -d(\omega))\} \approx \frac{\rho(\mu)}{4\mu^{3/2}}\ln\left(\frac{d(\omega)}{4\mu}\right) \sim 0 \quad (1.59)$$

$$\chi(\omega) = -\int_0^\mu d\varepsilon \frac{C\sqrt{\varepsilon}(\varepsilon-\mu)}{(\varepsilon-\mu)^2 - d(\omega)^2} = -2C\sqrt{\mu} - \frac{C}{2}\{L(\mu, d(\omega)) + L(\mu, -d(\omega))\} \approx -\rho(\mu)\left\{2 + \ln\left(\frac{d(\omega)}{4\mu}\right)\right\}, \quad (1.60)$$

where $L(\mu, d) = \sqrt{\mu+d}\,\ln\left|\dfrac{\sqrt{\mu+d}-\sqrt{\mu}}{\sqrt{\mu+d}+\sqrt{\mu}}\right|$. It is somewhat more difficult to calculate the indicated integrals with $|\omega| < \Delta$ when the function $b(\omega) = \sqrt{\Delta^2 - \omega^2}$ is real. But this case is the most important since the appearance of the proximity effect is connected with it. As a result, one can write

$$\varphi(\omega) = -\int_0^\mu d\varepsilon \frac{C\sqrt{\varepsilon}}{(\varepsilon-\mu)^2 + b(\omega)^2} = -\int_0^{\sqrt{\mu}} dt \frac{C}{p(\omega)}\left\{\frac{t}{t^2 - pt + q} - \frac{t}{t^2 + pt + q}\right\}, \quad (1.61)$$

where

$$\begin{aligned} p^2(\omega) &= 2(\mu + q) \\ q(\omega) &= \sqrt{\mu^2 + b^2(\omega)} \end{aligned} \quad (1.62)$$

Then it is easy to find that

$$\varphi(\omega) = -\frac{C}{2}\left\{\frac{1}{p(\omega)}\ln\left|\frac{\mu - p(\omega)\sqrt{\mu} + q(\omega)}{\mu + p(\omega)\sqrt{\mu} + q(\omega)}\right| + \frac{1}{a(\omega)}\arctan\left(\frac{\sqrt{\mu}}{a(\omega)}\right)\right\}, \quad (1.63)$$

where $2a^2(\omega) = q(\omega) - \mu$. Since $b(\omega) \ll \mu$ we have an approximate equality

$$\varphi(\omega) \approx -\frac{1}{2}\rho(\mu)\left\{\frac{1}{\mu}\ln\frac{\sqrt{\Delta^2 - \omega^2}}{4\mu} + \frac{\pi}{2\sqrt{\Delta^2 - \omega^2}} - \frac{1}{\mu}\right\} \approx -\frac{\pi\rho(\mu)}{2\sqrt{\Delta^2 - \omega^2}} \quad (1.64)$$

Similarly, one can show that

$$\chi(\omega) \approx -\rho(\mu)\left\{2 + \ln\left(\frac{b(\omega)}{4\mu}\right)\right\} \quad (1.65)$$

2. EFFECTIVE FIELD AND METAL-INSULATOR PHASE TRANSITION IN THE HUBBARD MODEL. ROLE OF THE ELECTRON COULOMB REPULSION

2.1. Introduction

The study of the Hubbard model has a semi-centennial history starting from the moment when J. Hubbard first considered the Hamiltonian with an account for a band energy and an electron single-site Coulomb repulsion. Such simplification of the solid-state complex Hamiltonian has allowed to describe a number of phenomena not fitting into a simple band picture without electronic correlations and to present a possible mechanism of the metal-dielectric Mott phase transition as well [24, 25]. The main idea was that with decreasing the Coulomb repulsion energy U of electrons with respect to their band energy of the width W a dielectric gap between the valence and conduction bands decreased and at $W/U = 1.15$ these zones merged into one. It testified a phase transition metal-insulator. The importance of the Hubbard Hamiltonian increased especially after the discovery of high-temperature superconductivity when it became clear that a strong single-site Coulomb repulsion plays an important role in the mechanism of electron pairing. In spite of the results obtained during this time and reflected in some details in the review by Izyumov [26] our attention is centred on the general features of the methods. Besides it, we point out new specifics of our work which reflects a more consistent solution of the problem of Mott-Hubbard phase transitions. It should be noted that a rather complicated picture of the electron dynamics in the case $U \sim W$ is observed. For an infinite lattice dimension with a number of nearest neighbours $z = \infty$ the problem is reduced to exact equations in an single-impurity Anderson model or an alloy theory of the coherent potential method [26]. In the framework of these theories a smooth metal-to-dielectric transition with increasing U is predicted by a spectral density behaviour at $T = 0$. Unfortunately, the observed jump-like change in the number of carriers at the phase transition has not been explained. Although it should be noted that at small finite temperatures the energy hysteresis effects were observed [27]. In [28] Mott concluded that the Hubbard model with a lack of long-range forces did not predict an abrupt change in the number of carriers. Thus, problem of carriers jump is still unsolved and is of great interest. A number of references to theories in the book [28] based on the exciton mechanism [28] and associated with overlapping zones confirmed only sufficient complexity of the issue and ambiguity of the solutions presented.

The structure of this section reflects the main ideas of the self-consistent effective field theory. Starting with zero-th approximation and well-defined order parameters we will consider the correlation effects using the diagrammatic method of the time perturbation theory. We exclude applying the additional self-consistent parameters in the form of unknown Green's functions or other correlators by the alloy analogy and which are traditionally used in the most theories [30, 31]. The main self-consistency parameters are the probabilities of electron-hole and electron-electron site filling. These parameters are formed immediately in this zero-th approximation of the self-consistent field named as Hubbard I approximation. In the framework of this theory, one can describe the mechanism of the retrace charge motions. An inclusion of open electron hopping paths is carried out by taking into account the single-loop diagram contributions of scattering matrix in combined site populations and self-energy operator. Summation of an infinite series of connected single-loop diagrams allows to get a self-consistent equation for added

unknown parameters. The Green's function, spectral density and other characteristics of the electronic dynamics have been calculated on the basis of the presented theory.

It should be also noted the emergence of new order parameters characteristic for the dielectric or metallic state. From a comparison of the energies of these states, the critical value of U is determined at which the metal-insulator phase transition occurs. The discontinuity of this transition is reflected in the concentration dependences of the conductivity.

2.2. Effective self-consistent field in the Hubbard I approximation

The Hubbard Hamiltonian is usually written as

$$\hat{H} = \sum_{<ij>} t_{ij} c_{i\sigma}^+ c_{j\sigma} + U \sum_i n_{i\uparrow} n_{i\downarrow} \quad , \qquad (2.1)$$

where the creation and annihilation operators with spin σ for i and j sites are denoted as $c_{i\sigma}^+$ and $c_{j\sigma}$, respectively. Occupation number operator with spin σ is $n_{i\sigma} = c_{i\sigma}^+ c_{i\sigma}$. The single site Coulomb repulsion of electrons on the energy level of transition or rare-earth ion is denoted by U, the hopping integral $t_{ij} = t$ is nonzero for z nearest neighbours and corresponds to the bandwidth $W = 2zt$. In what follows we consider a simple cubic lattice. Obviously, Hamiltonian (2.1) corresponds to a single band model and it is not difficult to generalize (2.1) for a multiband metal or dielectric. Despite a simple form, the Hamiltonian (2.1) is extremely difficult for theoretical research. The limiting cases $U << t$ and $U >> t$ describe metallic and dielectric states, respectively, and to which a great number of publications are devoted [26]. In the framework of the time perturbation theory we will present a consistent solution of the problem in the most difficult case when $U \sim t$. From the expression (2.1) we present the Coulomb term and the chemical potential μ energy operator as unperturbed Hamiltonian $\hat{H}_0$. Thus, one can write

$$\hat{H}_0 = -\mu \sum_{i\sigma} n_{i\sigma} + U \sum_i n_{i\uparrow} n_{i\downarrow} . \qquad (2.2)$$

The standard procedure for building a self-consistent theory presupposes the existence of an effective field with appropriate order parameters as usually done, for example, in the theory of magnetism. In our case such parameters should be the mean combined one- and two-electron site occupancies $<F^{\sigma 0}> = 1 - n/2$ and $<F^{2\sigma}> = n/2$, respectively, where n is the site electron concentration. Moreover, for simplicity, one can consider only the nonmagnetic state. Such assumption will be obvious after considering the Hubbard-I approximation in which it is easy to extract an indicated field based on the formalism of the scattering matrix. Taking into account the subsequent diagram contributions proportional to $1 / z$ it is possible to refine the picture of the electronic dynamics and to predict the phase transition from a metallic to dielectric state. Note that the inclusion of additional self-consistency parameters in the form of Green's functions or other correlators as done in the works of some authors [30, 31] and, in particular, in Hubbard's work [25], where the Hubbard III approximation was proposed for describing the Mott-Hubbard transition, has several significant drawbacks. One of which is connected with the conclusion about the continuity of phase transition as a function of the carriers number that is in contradiction with the experiment.

To study thermodynamic properties of systems described by the Hamiltonian (2.1) it is convenient to present the Hubbard operators $X^{mn} = |m\rangle\langle n|$ in the basis of eigenvectors of the

unperturbed Hamiltonian where the basis $\{|m\rangle\}$ includes two wave functions $|\sigma\rangle$ for an electron with a spin $\sigma = +1$ or -1 and for hole $|0\rangle$ and double filled $|2\rangle$ states, respectively. Using the well-known formulas

$$
\begin{aligned}
c_\sigma^+ &= X^{\sigma 0} + \sigma X^{2-\sigma} \\
c_\sigma &= X^{0\sigma} + \sigma X^{-\sigma 2}
\end{aligned}
\tag{2.3}
$$

the Hamiltonian of the zero approximation is presented as

$$
\hat{H}_0 = UX^{22} - \mu\left(X^{++} + X^{--} + 2X^{22}\right)
\tag{2.4}
$$

with energy levels $\varepsilon_\sigma = -\mu$, $\varepsilon_0 = 0$ and $\varepsilon_2 = U - 2\mu$. Similarly, we write the perturbation Hamiltonian:

$$
\hat{V} = -\sum_{lm\sigma} t_{lm}\left\{X_l^{\sigma 0}X_m^{0\sigma} + \sigma\left(X_l^{\sigma 0}X_m^{-\sigma 2} + X_l^{2-\sigma}X_m^{0\sigma}\right) + X_l^{2-\sigma}X_m^{-\sigma 2}\right\}
\tag{2.5}
$$

Using the scattering matrix formalism one can obtain that an effective self-consistent field in the zero approximation gives the same Green's function as in the Hubbard I approximation obtained on the basis of the equations of motion without taking into account the correlation terms. Indeed, for the components $G_{\alpha\beta,\gamma\delta}(\boldsymbol{r}_i - \boldsymbol{r}_j, \tau) = -<T_\tau X_i^{\alpha\beta}(\tau)X_j^{\gamma\delta}(0)>$ of the Green's function $G_\sigma(\boldsymbol{r}_i - \boldsymbol{r}_j, \tau) = -<T_\tau c_{i\sigma}(\tau)c_{j\sigma}^+(0)>$ Fourier transform one can write the Dyson operator equation

$$
\begin{aligned}
\hat{G}_\sigma^{corr.}(i\omega_n, \boldsymbol{k}) &= \begin{pmatrix} G_{0\sigma,\sigma 0} & G_{0\sigma,2-\sigma} \\ G_{-\sigma 2,\sigma 0} & G_{-\sigma 2,2-\sigma} \end{pmatrix} = \begin{pmatrix} G_{0\sigma}^0(i\omega_n) & 0 \\ 0 & G_{-\sigma 2}^0(i\omega_n) \end{pmatrix} \\
&+ \beta t(\boldsymbol{k})\begin{pmatrix} \Sigma_{\sigma 0,0\sigma}(i\omega_n) & \sigma\Sigma_{\sigma 0,-\sigma 2}(i\omega_n) \\ \sigma\Sigma_{2-\sigma,0\sigma}(i\omega_n) & \Sigma_{2-\sigma,-\sigma 2}(i\omega_n) \end{pmatrix}\begin{pmatrix} G_{0\sigma,\sigma 0}(i\omega_n,\boldsymbol{k}) & G_{0\sigma,2-\sigma}(i\omega_n,\boldsymbol{k}) \\ G_{-\sigma 2,\sigma 0}(i\omega_n,\boldsymbol{k}) & G_{-\sigma 2,2-\sigma}(i\omega_n,\boldsymbol{k}) \end{pmatrix},
\end{aligned}
\tag{2.6}
$$

where the unperturbed Green's functions $G_{\alpha\beta}^0(i\omega_n) = G_{\alpha\beta,\beta\alpha}^0(i\omega_n) = \dfrac{1}{\beta(i\omega_n + \varepsilon_\alpha - \varepsilon_\beta)}$, i.e.

$$
G_{0\sigma}^0(i\omega_n) \equiv G_{0\sigma,\sigma 0}^0(i\omega_n) = \frac{1}{\beta(i\omega_n + \mu)}, \quad G_{-\sigma 2}^0(i\omega_n) \equiv G_{-\sigma 2,2-\sigma}^0(i\omega_n) = \frac{1}{\beta(i\omega_n + \mu - U)}
\tag{2.7}
$$

are obtained from averaging over the Hamiltonian $\hat{H}_0$. The Fourier transform of the hopping integral for a simple cubic (s.c.) lattice is $t(\boldsymbol{k}) = -2t(\cos(k_x a) + \cos(k_y a) + \cos(k_z a))$ with a lattice constant a. The rest of notations are standard for Matsubara representation: the symbols $<...>$ and T_τ are the operators of statistical averaging over the total Hamiltonian and chronological ordering, respectively. $c_{i\sigma}(\tau)$ etc. are annihilation operators in the interaction representation, $1/\beta = T$ is the temperature, $\omega_n = (2n+1)\pi T$.

The self-energy operator $\Sigma_{\alpha\beta,\gamma\delta}(i\omega_n)$ with a chosen method of summing the diagrams depends only on the Fermi frequency. It is easy to find that in a zero approximation of the self-consistent field the components of this operator have a simplest form:

$$
\hat{\Sigma}_\sigma^0(i\omega_n) = \begin{pmatrix} <F^{\sigma 0}>G_{0\sigma}^0(i\omega_n) & <F^{\sigma 0}>G_{0\sigma}^0(i\omega_n) \\ <F^{2-\sigma}>G_{-\sigma 2}^0(i\omega_n) & <F^{2-\sigma}>G_{-\sigma 2}^0(i\omega_n) \end{pmatrix},
\tag{2.8}
$$

where for paramagnetic phase $<F^{\sigma 0}>=<X^{\sigma\sigma}+X^{00}>=1-n/2$ and $<F^{2-\sigma}>=<X^{22}+X^{-\sigma-\sigma}>=n/2$. Substituting Eq. (2.8) into the matrix equation (2.6) we find the solutions for components of the Green's function $\hat{G}_\sigma(i\omega_n,\boldsymbol{k})$ that gives the next expression for $G_\sigma(i\omega_n,\boldsymbol{k})$ in the Hubbard I approximation:

$$G_\sigma^H(i\omega_n,\boldsymbol{k}) = \frac{<F^{\sigma 0}>G_{0\sigma}^0(i\omega_n)+<F^{2-\sigma}>G_{-\sigma 2}^0(i\omega_n)}{1-\beta t(\boldsymbol{k})\left(<F^{\sigma 0}>G_{0\sigma}^0(i\omega_n)+<F^{2-\sigma}>G_{-\sigma 2}^0(i\omega_n)\right)} \tag{2.9}$$

This expression coincides with that obtained by Hubbard in the work [24]. The poles of Eq. (2.9) determine two spectrum branches of the coherent excitations describing the upper and lower Hubbard bands. Thus, the Hubbard I approximation does not take into account the effects of inelastic electron scattering. As a result, within the framework of this approximation it is impossible to obtain a phase transition from metallic to dielectric state since the Coulomb gap separating the two zones does not disappear at any finite U value. The availability of two spectrum branches substantially complicates the numerical analysis of both spectral density and the chemical potential dependences on electron concentration. Taking into account that there is still no such analysis in the literature we present it in details.

We will use the inverse function method that substantially simplifies the solution of this problem [32]. This method is based on a simple linear dependence of the Green's function (2.9) pole on $t(\boldsymbol{k})$.

To calculate the spectral density, it is necessary to carry out an analytical continuation $i\omega_n \to \omega+i\delta$ in Eq. (2.9). Taking into account a general definition $A_\sigma(\Omega,\boldsymbol{q}) = -2\beta \operatorname{Im} G_\sigma(\Omega+i\delta,\boldsymbol{q})$ we have the following expression for the spectral density in the Hubbard I approximation:

$$A_\sigma^{Hubb}(\Omega,\boldsymbol{q}) = -2\pi\sum_{n=1}^{2}\frac{\beta\tilde{G}_\sigma(\Omega)}{t(\boldsymbol{q})\left.\dfrac{d\beta\tilde{G}_\sigma(\Omega)}{d\Omega}\right|_{\Omega=E_{nq\sigma}}}\delta(\Omega-E_{nq\sigma}), \tag{2.10}$$

where $\tilde{G}_\sigma(\Omega) =<F^{\sigma 0}>G_{0\sigma}^0(\Omega)+<F^{2-\sigma}>G_{-\sigma 2}^0(\Omega)$, $E_{nq\sigma}$ are the resonance frequencies and $\delta(x)$ is the Dirac delta function.

The sum over wave vectors gives the uniform spectral density

$$R_\sigma^{Hubb}(\Omega) = \frac{1}{N}\sum_{\boldsymbol{q}}A_\sigma^{Hubb}(\Omega,\boldsymbol{q}) = \frac{12\pi}{W}D_C\left(\frac{6}{F(\tilde{\Omega})}\right), \tag{2.11}$$

where $F(\tilde{\Omega})=\dfrac{1-n/2}{\tilde{\Omega}+\tilde{\mu}}+\dfrac{n/2}{\tilde{\Omega}+\tilde{\mu}-\tilde{U}}$ and the tilde sign further indicates the specified parameters in units of the bandwidth W. The electron density of states $D_C(x)$ is expressed in terms of the imaginary part of the lattice Green's function $G(t)$ which is analytically continued to the lower complex plane [33]. The exact expression is presented in [24] for $G(t)$:

$$G(t) = \frac{1}{t}P\left(\frac{3}{t}\right), \tag{2.12}$$

where

$$P(z) = -\frac{\sqrt{1-0.75x_1}}{1-x_1}\left(\frac{2}{\pi}\right)^2 K(k_+)K(k_-)$$

$$z = \frac{3}{t}, \quad x_1 = \frac{1}{2} + \frac{1}{6}z^2 - \frac{1}{2}\sqrt{1-z^2}\sqrt{1-\frac{1}{9}z^2}, \quad x_2 = \frac{x_1}{x_1-1}, \tag{2.13}$$

$$k_\pm^2 = \frac{1}{2} \pm \frac{1}{4}x_2\sqrt{4-x_2} - \frac{1}{4}(2-x_2)\sqrt{1-x_2}$$

Here, $K(x)$ is the complete elliptic integrals of the first kind. To calculate $K(x)$ with a complex module an algorithm for the arithmetic-geometric mean proposed in [35] was used.

It is easy to find the electron mean site occupancy with a spin σ in accordance with the main expression:

$$< n_\sigma > = < F^{2\sigma} > = \frac{1}{N}\sum_q n_{k\sigma} = \frac{1}{2\pi N}\sum_q \int_{-\infty}^{+\infty} A_\sigma^{Hubb}(\Omega,\boldsymbol{q})f(\Omega)d\Omega = \frac{1}{2\pi}\int_{-\infty}^{+\infty} R_\sigma^{Hubb}(\Omega)f(\Omega)d\Omega, \tag{2.14}$$

where $f(\Omega) = 1/\left(e^{\beta\Omega}+1\right)$ is the Fermi distribution function. The paramagnetic phase is assumed to be a ground state at $T = 0$ with $< n_\sigma > = n/2$. Then we get the next integral equation on the chemical potential

$$\int_{w_{1d}}^{\tilde{u}} D_C\left(\frac{6w(w-\tilde{U})}{w-(1-0.5n)\tilde{U}}\right)dw = \frac{n}{12} \tag{2.15}$$

Here, in the integrand the replacement $w = (\Omega+\mu)/W$ of the variable was made. In Eq. (2.15) the integral lower limit is determined by the lower boundary of the lower (the lower sign) Hubbard band. In the general case, the lower and upper boundaries of the lower (indexes 1d and 1u, respectively) and upper (indexes 2d and 2u, respectively) Hubbard bands are determined by the expressions:

$$w_{1d,1u} = \frac{1}{4}\left(2\tilde{U} \pm 1 - \sqrt{(2\tilde{U} \mp 1)^2 \mp 8\tilde{U}(1-0.5n)}\right)$$

$$w_{2d,2u} = \frac{1}{4}\left(2\tilde{U} \pm 1 + \sqrt{(2\tilde{U} \mp 1)^2 \mp 8\tilde{U}(1-0.5n)}\right) \tag{2.16}$$

Thus, Eqs. (2.11) - (2.15) allow numerical calculations of the chemical potential and the spectral density in the Hubbard I approximation.

In Fig. 2.1 the concentration dependence of the chemical potential in the Hubbard I approximation (curve 1) with $\tilde{U} = 5$ is shown. From the figure it can be seen that for a half-filled band ($n = 1$) $\tilde{\mu}$ as a function of n is discontinuous. With a Coulomb repulsion decrease, this gap decreases. Indeed, it is easy to find the values of chemical potentials $\tilde{\mu}_L$ and $\tilde{\mu}_H$ in the limits $n \to 1-\delta$, $n \to 1+\delta$ and $\delta \to 0$, respectively:

$$\tilde{\mu}_L = \frac{1}{4}\left(2\tilde{U} + 1 - \sqrt{4\tilde{U}^2 + 1}\right)$$

$$\tilde{\mu}_H = \frac{1}{4}\left(2\tilde{U} - 1 + \sqrt{4\tilde{U}^2 + 1}\right) \tag{2.17}$$

Apparently, $\tilde{\mu}_H - \tilde{\mu}_L \to 0$ with $\tilde{U} \to 0$ and $\tilde{\mu}_H - \tilde{\mu}_L \to \tilde{U}$ with $\tilde{U} \to \infty$. Also, from Eq. (2.17) it follows that for a metal with $\tilde{U} = 0$ we have $\tilde{\mu}_H = \tilde{\mu}_L = 0$, i.e., for a half filled band the chemical potential lies in the middle of the band. For a strongly correlated ($\tilde{U} \to \infty$) weakly hole-doped ($n \to 1 - \delta$) electron system the chemical potential $\tilde{\mu} \to \tilde{\mu}_L = 1/4$, i.e., electrons in the PM phase fill only a quarter of the band W.
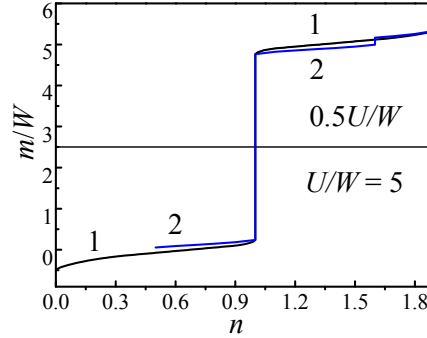

Fig. 2.1. Concentration dependences of the chemical potential in the PM phase at $T = 0$ and $\tilde{U} = 5$ in the Hubbard I approximation (curve 1) and for electron correlations accounted (curve 2)

In Fig. 2.2 the normalized spectral density

$$A_{Hubb}(w) = D_C \left(\frac{6w(w - \tilde{U})}{w - (1 - 0.5n)\tilde{U}} \right) \tag{2.18}$$

is shown for different electron concentrations at $\tilde{U} = 5$. The value $w = \tilde{\mu}$ corresponds to the chemical potential level. From the figure, it is seen that with increasing n the width of the lower band decreases and the upper bandwidth increases. At $n = 1$ the widths of the bands are equal and for $n = 2$ the lower band disappears. Thus, with the chemical potential discontinuity for a half-filled band at any finite value of the Coulomb repulsion only a dielectric phase is always realized in the Hubbard I approximation. In later papers by Hubbard [25] and other authors [25-31], the approximations for correlation effects were proposed. Within the framework of these theories, a phase transition from a dielectric to a metallic state was predicted for a certain critical value of the U/W ratio. However, their limitations are due to the fact that an additional parameter of self-consistency was introduced in the form of many particles correlators or Green's functions that did not allow to take into account more subtle correlation effects and the associated step-like transitions between thermodynamically stable states. Therefore, below we will present a subsequent account for one- loop diagrams contributions to the effective field considered above in the Hubbard approximation I.

2.3. Electron correlations

In this section, we will consider an effect of inelastic kinematic and single electron Coulomb interactions on the ground state of the Hubbard paramagnet. To solve this problem, it is necessary to have an equation for the chemical potential. At first glance, the task is to obtain an expression $R_\sigma(\Omega)$ for the spectral density as was done in the previous section and then to calculate the chemical potential by analogy with Eq. (2.15). However, this plan will not work because in this case we can sum up only a finite number of diagrams among which some

diagrams are proportional to $1/T$ that gives the singularities as $T \to 0$. That is why from the beginning we calculate directly a mean $<F^{\sigma 0}>=<X^{\sigma\sigma}+X^{00}>$ that will allow us to avoid the indicated divergences.
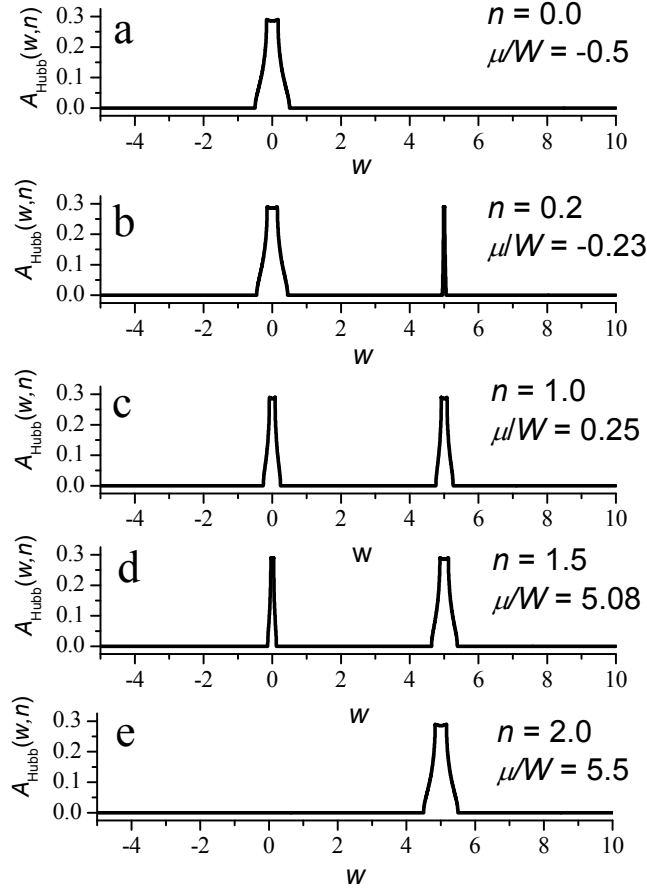
Fig. 2.2. The normalized spectral density $A_{Hubb}(w)$ at $\tilde{U}=5$ for different electron concentrations

In the first order of the reciprocal effective radius of the interaction one can write:

$$<X_p^{\sigma\sigma}+X_p^{00}>=<X_p^{\sigma\sigma}+X_p^{00}>_0 -\int_0^\beta d\tau_1\int_0^\beta d\tau_2\sum_{lm\sigma_1}<T_\tau\left(X_p^{\sigma\sigma}+X_p^{00}\right)\cdot$$

$$\cdot\left[X_l^{\sigma_1 0}(\tau_1)X_m^{0\sigma_1}(\tau_2)\frac{1}{\beta}B^{0\sigma_1,\sigma_1 0}(r_l-r_m,\tau_1-\tau_2)+X_l^{2-\sigma_1}(\tau_1)X_m^{-\sigma_1 2}(\tau_2)\frac{1}{\beta}B^{-\sigma_1 2,2-\sigma_1}(r_l-r_m,\tau_1-\tau_2)>_0\right],\ (2.19)$$

where $B^{\alpha\beta,\beta\alpha}(r_l-r_m,\tau_l-\tau_m)$ is the effective kinematic interaction line in the approximation Hubbard I and the symbol $<...>_0$ denotes statistical averaging over the unperturbed Hamiltonian. Thus,

$$<F^{\sigma 0}>_0=\frac{e^{\beta\tilde{\mu}}+1}{1+2e^{\beta\tilde{\mu}}+e^{\beta(2\tilde{\mu}-\tilde{U})}}$$

$$<F^{2\sigma}>_0=\frac{e^{\beta\tilde{\mu}}+e^{\beta(2\tilde{\mu}-\tilde{U})}}{1+2e^{\beta\tilde{\mu}}+e^{\beta(2\tilde{\mu}-\tilde{U})}}$$

$$(2.20)$$

Using the Wick's theorem for Hubbard operators it is not difficult to calculate all correlators included in (2.19). It turns out that there are only four different contributions corresponding to diagrams in Eqs. (2.21).

As can be seen from (2.21), the first two diagrams generate singularities $1/T$ as $T \to 0$. This divergence is removed by summing up an infinite set of such type diagrams. Taking into account that these diagrams contributions form a Taylor series it is easy to find their sum. In Fig. 2.3, all diagram contributions are presented. In the figure the light points indicate $<F^{\sigma 0}>_0$ or $<F^{2\sigma}>_0$ in accordance with a type of the diagram. The filled points designate index convolutions for linked diagrams that indicate derivatives of the indicated averages with respect to the Hamiltonian $\hat{H}_0$ parameters.

$$\beta \delta \mu_\sigma = \frac{1}{N} \sum_{q\omega_n} \beta B^{0\sigma,\sigma 0}(q, i\omega_n) G_{0\sigma}(i\omega_\delta)$$

$$\beta \delta \mu_{2\sigma} = \frac{1}{N} \sum_{q\omega_n} \beta B^{\sigma 2,2\sigma}(q, i\omega_n) G_{\sigma 2}(i\omega_\delta)$$

$$\nu_{0-\sigma} = \frac{1}{N} \sum_{q\omega_n} \beta B^{0-\sigma,-\sigma 0}(q, i\omega_n)\left(G_{0-\sigma}(i\omega_n)\right)^2$$

$$\nu_{2\sigma} = \frac{1}{N} \sum_{q\omega_n} \beta B^{\sigma 2,2\sigma}(q, i\omega_n)\left(G_{\sigma 2}(i\omega_n)\right)^2 \quad (2.21)$$

Here,

$$B^{0\sigma,\sigma 0}(q, i\omega_n) = \frac{t(q)}{1 - \beta t(q)\left[G_{0\sigma}(i\omega_n) < F^{\sigma 0} > + G_{-\sigma 2}(i\omega_n) < F^{-\sigma 2} >\right]} = B^{-\sigma 2, 2-\sigma}(q, i\omega_n) \quad (2.22)$$

Fig. 2.3. The diagram contributions in the combined site electron occupancy $<F^{\sigma 0}>$.

The series in Fig. 2.3 in an analytical form looks as follows

$$< F_p^{\sigma 0} > = < F^{\sigma 0} >_0 - \beta \delta \mu_\sigma < F_p^{\sigma 0} F_l^{\sigma 0} >_0 - \beta \delta \mu_{-\sigma} < F_p^{\sigma 0} F_l^{-\sigma 0} >_0 - \beta \delta \mu_{2\sigma} < F_p^{\sigma 0} F_l^{2\sigma} >_0$$

$$- \beta \delta \mu_{2-\sigma} < F_p^{\sigma 0} F_l^{2-\sigma} >_0 + \frac{1}{2!}(\beta \delta \mu_\sigma)^2 < F_p^{\sigma 0} F_l^{\sigma 0} F_m^{\sigma 0} >_0 \quad (2.23)$$

$$+ \frac{1}{2!}(\beta \delta \mu_{-\sigma})^2 < F_p^{\sigma 0} F_l^{-\sigma 0} F_m^{-\sigma 0} >_0 - \ldots - \nu_{0-\sigma} < F^{-\sigma 0} >_0 - \nu_{2\sigma} < F^{2\sigma} >_0$$

To perform the summation of an infinite series (2.23), let us introduce the generating functionals:

$$< F^{\sigma 0}(\varepsilon_\sigma, \varepsilon_{-\sigma}, \varepsilon_{2\sigma}, \varepsilon_{-2\sigma}, \lambda_0, \lambda_+, \lambda_-) >_0 = \partial_\sigma \ln Sp(e^{-\beta \tilde{H}_0(\lambda_0, \lambda_+, \lambda_-)})$$

$$< F^{2\sigma}(\varepsilon_\sigma, \varepsilon_{-\sigma}, \varepsilon_{2\sigma}, \varepsilon_{-2\sigma}, \lambda_0, \lambda_+, \lambda_-) >_0 = \partial_{2\sigma} \ln Sp(e^{-\beta \tilde{H}_0(\lambda_0, \lambda_+, \lambda_-)})$$

where the notations $\partial_\sigma = \dfrac{\partial}{\partial(-\beta\varepsilon_\sigma)}$ and $\partial_{2\sigma} = \dfrac{\partial}{\partial(-\beta\varepsilon_{2\sigma})}$, as well as $\hat{H}_0$ from Eq. (2.4) is presented in a parametric form:

$$\hat{H}_0(\lambda_0, \lambda_+, \lambda_-) = (\lambda_0 + \varepsilon_+ + \varepsilon_-)X^{00} + \sum_\sigma (\lambda_\sigma + \varepsilon_\sigma + \varepsilon_{2\sigma})X^{\sigma\sigma} + \sum_\sigma \varepsilon_{2\sigma}X^{22} \qquad (2.24)$$

Obviously, when $\lambda_\sigma = -\varepsilon_{2\sigma}$ and $\lambda_0 = -\varepsilon_\sigma - \varepsilon_{-\sigma}$, where $\varepsilon_\sigma = -\mu$ and $\varepsilon_{2\sigma} = \dfrac{U}{2} - \mu$ we get the original Hamiltonian $\hat{H}_0$. Then the series (2.23) is analytically expressed as follows:

$$< F_p^{\sigma 0} > = < F^{\sigma 0} >_0 - \beta\delta\mu_\sigma\partial_\sigma < F_p^{\sigma 0} >_0 - \beta\delta\mu_{-\sigma}\partial_{-\sigma} < F_p^{\sigma 0} >_0 - \beta\delta\mu_{2\sigma}\partial_{2\sigma} < F_p^{\sigma 0} >_0$$

$$- \beta\delta\mu_{2-\sigma}\partial_{2-\sigma} < F_p^{\sigma 0} >_0 + \frac{1}{2!}(\beta\delta\mu_\sigma)^2\partial_\sigma^2 < F_p^{\sigma 0} >_0 + \frac{1}{2!}(\beta\delta\mu_{-\sigma})^2\partial_{-\sigma}^2 < F_p^{\sigma 0} >_0 \qquad (2.25)$$

$$- ... - \nu_{0-\sigma} < F^{-\sigma 0} >_0 - \nu_{2\sigma} < F^{2\sigma} >_0$$

It can be seen from Eq. (2.25) that with the exception of the last two terms we have a series the sum of which is $< F^{\sigma 0} >_1 = < F^{\sigma 0}(\varepsilon_\sigma + \delta\mu_\sigma, \varepsilon_{-\sigma} + \delta\mu_{-\sigma}, \varepsilon_{2\sigma} + \delta\mu_{2\sigma}, \varepsilon_{-2\sigma} + \delta\mu_{2-\sigma}, \lambda_0, \lambda_+, \lambda_-) >_0$. Finally, one can get a final expression determining the equation for chemical potential

$$< F^{\sigma 0} > = 1 - 0.5n = < F^{\sigma 0} >_1 - \nu_\sigma, \qquad (2.26)$$

where taking into account the summation over the frequencies in Eq. (2.21) and the use of the inverse function method indicated in the previous section the following formulas is introduced

$$< F^{\sigma 0} >_1 = \frac{e^{\beta(\tilde{\mu}+\delta\tilde{\mu})} + 1}{1 + 2e^{\beta(\tilde{\mu}+\delta\tilde{\mu})} + e^{\beta(2(\tilde{\mu}+\delta\tilde{\mu})-\tilde{U})}}$$

$$\delta\tilde{\mu} = \delta\tilde{\mu}_{-\sigma} - \delta\tilde{\mu}_{2-\sigma} = -6\tilde{U}^2 \int_{w_{1d}/\tilde{U}}^{\tilde{\mu}/\tilde{U}} d\omega D_C \left(\frac{6\omega(\omega-1)\tilde{U}}{\omega-1+0.5n} \right) \frac{\omega(\omega-1)}{(\omega-1+0.5n)^2}$$

$$\nu_\sigma = \nu_{0-\sigma} < F^{-\sigma 0} >_0 + \nu_{2\sigma} < F^{2\sigma} >_0 \qquad (2.27)$$

$$= 6\tilde{U} \int_{w_{1d}}^{\tilde{\mu}/\tilde{U}} d\omega D_C \left(\frac{6\omega(\omega-1)\tilde{U}}{\omega-1+0.5n} \right) \frac{< F^{-\sigma 0} >_0 (\omega-1)^2 + < F^{2\sigma} >_0 \omega^2}{(\omega-1+0.5n)^2}$$

$$- \frac{< F^{-\sigma 0} >_0 f(-\tilde{\mu})}{1-0.5n} - \frac{2 < F^{2\sigma} >_0 f(\tilde{U}-\tilde{\mu})}{n}$$

As can be seen from the obtained Eqs. (2.26) – (2.27), in the limit $T \to 0$, the previously existing singularities disappeared. Thus, for the chemical potential Eq. (2.26) is obtained in which the correlation corrections are taken into account within the chosen approximation. Let consider a ground state, i.e., we set $T = 0$. It is clear that the means $< F^{\sigma 0} >_0, < F^{2\sigma} >_0, < F^{2\sigma} >_0$ and $< F^{\sigma 0} >_1$ are order parameters determining one or another type of thermodynamic state of the electronic subsystem. The analysis shows that two ground states are possible with a positive

chemical potential, according to the ratio between $\tilde{\mu}$ and $\tilde{U}$. We do not consider the area $\tilde{\mu} < 0$ because it is the case of a low-density electron gas.

For $\tilde{\mu} > 0, \tilde{\mu} < \tilde{U}$ we have $0 < \tilde{\mu} + \delta\tilde{\mu} < \tilde{U}$ and $< F^{\sigma 0} >_0 = < F^{2\sigma} >_0 = < F^{\sigma 0} >_1 = 1/2$. These order parameters indicate that in the electron dynamics a single filling of the holes prevails that is a characteristic of the dielectric. Then the equation for the chemical potential in the case of a dielectric takes the form:

$$1 - \frac{n}{2} = \frac{1}{2} - 6\tilde{U} \int_{w_{1d}/\tilde{U}}^{\tilde{\mu}/\tilde{U}} d\omega D_C \left(\frac{6\omega(\omega-1)\tilde{U}}{\omega-1+0.5n} \right) \frac{1}{2} \frac{(\omega-1)^2 + \omega^2}{(\omega-1+0.5n)^2} + \frac{1}{2-n} . \qquad (2.28)$$

The integral in Eq. (2.28) is simplified for $n = 1$ if we carry out the replacement $\dfrac{6\omega(\omega-1)\tilde{U}}{\omega-1+0.5n} = \varepsilon$. Instead of Eq. (2.28), it follows the equation

$$I\left(\frac{6\tilde{\mu}(\tilde{\mu}-\tilde{U})}{\tilde{\mu}-0.5\tilde{U}} \right) = 1 , \qquad (2.29)$$

where $I(x) = \int_{-3}^{x} D_C(\varepsilon) d\varepsilon$ if $n \to 1 - \delta$ and $\delta \to 0$ or

$$1 + I\left(\frac{6\tilde{\mu}(\tilde{\mu}-\tilde{U})}{\tilde{\mu}-0.5\tilde{U}} \right) = 1 , \qquad (2.30)$$

if $n \to 1 + \delta$ and $\delta \to 0$. Obviously, for Eq. (2.29) we have $\dfrac{6\tilde{\mu}(\tilde{\mu}-\tilde{U})}{\tilde{\mu}-0.5\tilde{U}} = 3$, whereas from Eq.

(2.30) it follows $\dfrac{6\tilde{\mu}(\tilde{\mu}-\tilde{U})}{\tilde{\mu}-0.5\tilde{U}} = -3$. The solutions of these equations for $\tilde{\mu}$ taking into account its

sign and relations with $\tilde{U}$ coincide with the chemical potentials (2.17) for the lower and upper bands in the Hubbard I approximation, respectively. Thus, with $n = 1$ the chemical potentials in the Hubbard I approximation and with account for electron correlations coincide.

For $\tilde{\mu} > \tilde{U} > 0$, $\tilde{\mu} + \delta\tilde{\mu} > \tilde{U}$ we have $< F^{\sigma 0} >_0 = < F^{\sigma 0} >_1 = 0$ and $< F^{2\sigma} >_0 = 1$. Thus, for a metal the sites are mainly filled with two electrons. From Eqs. (2.25) - (2.26) it follows that the equation for $\tilde{\mu}$ is

$$1 - \frac{n}{2} = \frac{2}{n} - 6\tilde{U} \int_{w_{1d}/\tilde{U}}^{\tilde{\mu}/\tilde{U}} d\omega D_C \left(\frac{6\omega(\omega-1)\tilde{U}}{\omega-1+0.5n} \right) \frac{\omega^2}{(\omega-1+0.5n)^2} \qquad (2.31)$$

Unfortunately, the integrals in Eq. (2.28) and (2.31) cannot be simplified. Therefore, it is necessary to carry out further numerical calculations. It will be shown below that the metal phase exists only for n ≥ 1. Assuming $n = 2$ it is easy to find that $\tilde{\mu} = \tilde{U} + 1/2$.

In Fig. 2.4, the dependences of $\tilde{\mu}$ as a function of the electron concentration n for various values of the Coulomb repulsion U/W are presented. From the figure it can be seen that in all cases there is a discontinuity in the given curves for a dielectric with a half-filled band. Also, at n ~ 1.6 the jumps from a dielectric to a metal state are observed. Unfortunately, from these

calculations it is impossible to conclude for which $\tilde{U}$ it will be a transition from a metal to a dielectric state. To answer this question, it is necessary to compare inner energies of these states.
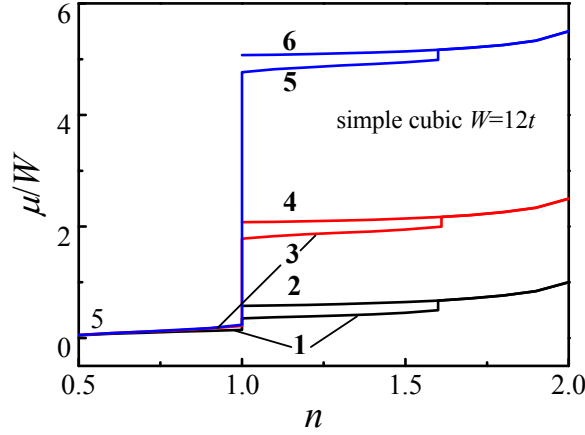
Fig. 2.4. Concentration dependences of the chemical potential $\tilde{\mu}$ for a dielectric (curves 1, 3, and 5) and for a metal (curves 2, 4, and 6) at $U/W = 0.5$, 2.0, and 5.0, respectively

2.4. Green's function in the Hubbard model

From the previous subsection, it follows that the spectral density is expressed in terms of the imaginary part of the Green's function. Therefore, it is necessary to calculate the contributions of all single-loop diagrams to this correlator. In general, the task is similar to that solved in the previous subsection for calculations of the combined occupancies. Corresponding matrix Green's function with unknown components has the form

$$\hat{G}_\sigma^{corr.}(i\omega_n, \boldsymbol{k}) = \begin{pmatrix} G_{0\sigma,\sigma 0} & G_{0\sigma,2-\sigma} \\ G_{-\sigma 2,\sigma 0} & G_{-\sigma 2,2-\sigma} \end{pmatrix} \quad (2.32)$$

A self-energy operator $\Sigma_{\alpha\beta,\gamma\delta}(i\omega_n)$ is determined by the perturbation $\hat{V}$ from Eq. (2.5)

$$\hat{\Sigma}_\sigma(i\omega_n) = \begin{pmatrix} \Sigma_{\sigma 0,0\sigma}(i\omega_n) & \sigma\Sigma_{\sigma 0,-\sigma 2}(i\omega_n) \\ \sigma\Sigma_{2-\sigma,0\sigma}(i\omega_n) & \Sigma_{2-\sigma,-\sigma 2}(i\omega_n) \end{pmatrix} \quad (2.33)$$

Then one can sum diagrams in terms of irreducible parts using the matrix Dyson's equation

$$\hat{G}_\sigma^{corr.}(i\omega_n, \boldsymbol{k}) = \hat{\Sigma}_\sigma(i\omega_n) + \beta t(\boldsymbol{k})\hat{\Sigma}_\sigma(i\omega_n)\hat{G}_\sigma^{corr.}(i\omega_n, \boldsymbol{k}), \quad (2.34)$$

The components $\Sigma_{\alpha\beta,\gamma\delta}(i\omega_n)$ are determined by grouping the inner Hubbard's operators of the perturbation Hamiltonian $\hat{V}$ from (2.5) in the scattering matrix to obtain the Dyson's equation (2.34). The indexes $\alpha\beta$ and $\gamma\delta$ coincide with corresponding indexes of product Habbard's operators $X_l^{\alpha\beta} X_m^{\gamma\delta}$ in $\hat{V}$ because they determine the ends of the self-energy operator. Evidently, these ends should correspond to the index of the initial point of the adjacent external Green's line. Then we have four correlator groups:

1) $< T_\tau X_i^{0\sigma}(\tau_i) X_j^{\sigma 0}(\tau_j) \big[B^{0\sigma,\sigma 0}(\boldsymbol{r}_l - \boldsymbol{r}_m, \tau_l - \tau_m) \big(X_l^{0\sigma}(\tau_l) X_m^{\sigma 0}(\tau_m) + X_l^{0-\sigma}(\tau_l) X_m^{-\sigma 0}(\tau_m) \big) +$

$\qquad B^{\sigma 2,2\sigma}(\boldsymbol{r}_l - \boldsymbol{r}_m, \tau_l - \tau_m) \big(X_l^{2\sigma}(\tau_l) X_m^{\sigma 2}(\tau_m) + X_l^{2-\sigma}(\tau_l) X_m^{-\sigma 2}(\tau_m) \big) \big] >_0$

2) $\sigma B^{0\sigma,2-\sigma}(\boldsymbol{r}_l - \boldsymbol{r}_m, \tau_l - \tau_m) < T_\tau X_i^{-\sigma 2}(\tau_i) X_j^{\sigma 0}(\tau_j) \big(X_l^{0\sigma}(\tau_l) X_m^{2-\sigma}(\tau_m) - X_l^{0-\sigma}(\tau_l) X_m^{2\sigma}(\tau_m) \big) >_0$ $\qquad$ (2.35)

3) $\sigma B^{-\sigma 2,\sigma 0}(\boldsymbol{r}_l - \boldsymbol{r}_m, \tau_l - \tau_m) < T_\tau X_i^{0\sigma}(\tau_i) X_j^{2-\sigma}(\tau_j) \big(X_l^{-\sigma 2}(\tau_l) X_m^{\sigma 0}(\tau_m) - X_l^{\sigma 2}(\tau_l) X_m^{-\sigma 0}(\tau_m) \big) >_0$

4) $< T_\tau X_i^{-\sigma 2}(\tau_i) X_j^{2-\sigma}(\tau_j) \big[B^{-\sigma 2,2-\sigma}(\boldsymbol{r}_l - \boldsymbol{r}_m, \tau_l - \tau_m) \big(X_l^{2-\sigma}(\tau_l) X_m^{\sigma-2}(\tau_m) + X_l^{2\sigma}(\tau_l) X_m^{\sigma 2}(\tau_m) \big) +$

$\qquad B^{0\sigma,\sigma 0}(\boldsymbol{r}_l - \boldsymbol{r}_m, \tau_l - \tau_m) \big(X_l^{0\sigma}(\tau_l) X_m^{\sigma 0}(\tau_m) + X_l^{0-\sigma}(\tau_l) X_m^{-\sigma 0}(\tau_m) \big) \big] >_0$

Here, $B^{\alpha\beta,\gamma\delta}(\boldsymbol{r}_l - \boldsymbol{r}_m, \tau_l - \tau_m)$ are effective field lines in the Hubbard I approximation, the Fourier transform of which are determined by Eq. (2.22) with relations

$$B^{0\sigma,2-\sigma}(\boldsymbol{q}, i\omega_n) = B^{-\sigma 2,\sigma 0}(\boldsymbol{q}, i\omega_n) = \sigma B^{0\sigma,\sigma 0}(\boldsymbol{q}, i\omega_n) \qquad (2.36)$$

Above for convenience we used the Hermitian conjugate operator $\hat{V}$. Also, $\varepsilon_\sigma = \varepsilon_{-\sigma}$ for a paramagnetic state at the applied field $h = 0$. The correlator groups 1-4 determine self-energy components $\Sigma_{\sigma 0,0\sigma}(i\omega_n)$, $\Sigma_{\sigma 0,-\sigma 2}(i\omega_n)$, $\Sigma_{2-\sigma,0\sigma}(i\omega_n)$ and $\Sigma_{2-\sigma,-\sigma 2}(i\omega_n)$, respectively. In Fig. 2.5, all possible diagram contributions to the self-energy component $\Sigma_{\sigma 0,0\sigma}(i\omega_n)$ from the first correlator group are presented. Here, the lines with index $\pm\sigma$, $\sigma 2$, 02 and dotted line correspond to unperturbed Green's functions $G_{0\pm\sigma}^0(i\omega_n)$, $G_{\sigma 2}^0(i\omega_n)$, $G_{02}^0(i\omega_n)$ and $G_{\sigma-\sigma}^0(i\omega_n)$, respectively. The symbols K_{1p} under diagrams denote the corresponding cumulants. Let us denote the diagram contribution in Fig. 2.5, (p) by $\Sigma_{1p)}$.

$K_{1a} = < (X_j^{\sigma\sigma} + X_j^{00})(X_m^{\sigma\sigma} + X_m^{00}) >_0$

a)

$K_{1b} = -K_{1a}$

b)

$K_{1c} = - < (X_j^{-\sigma-\sigma} + X_j^{00}) >_0$

c)

$K_{1d} = - < (X_j^{\sigma\sigma} + X_j^{00})(X_m^{-\sigma-\sigma} + X_m^{00}) >_0$

d)

$K_{1e} = < (X_j^{-\sigma-\sigma} - X_j^{\sigma\sigma}) >_0$

e)

$K_{1f} = - < (X_j^{\sigma\sigma} + X_j^{00}) >_0$

f)

$K_{1g} = - < (X_j^{22} + X_j^{\sigma\sigma}) >_0$

g)

$K_{1h} = - < (X_j^{\sigma\sigma} + X_j^{00})(X_l^{22} + X_l^{\sigma\sigma}) >_0$

h)

$K_{1k} = < (X_j^{\sigma\sigma} + X_j^{00}) >_0$

k)

$K_l = < X^{22} + X^{\sigma\sigma} >_0$

l)

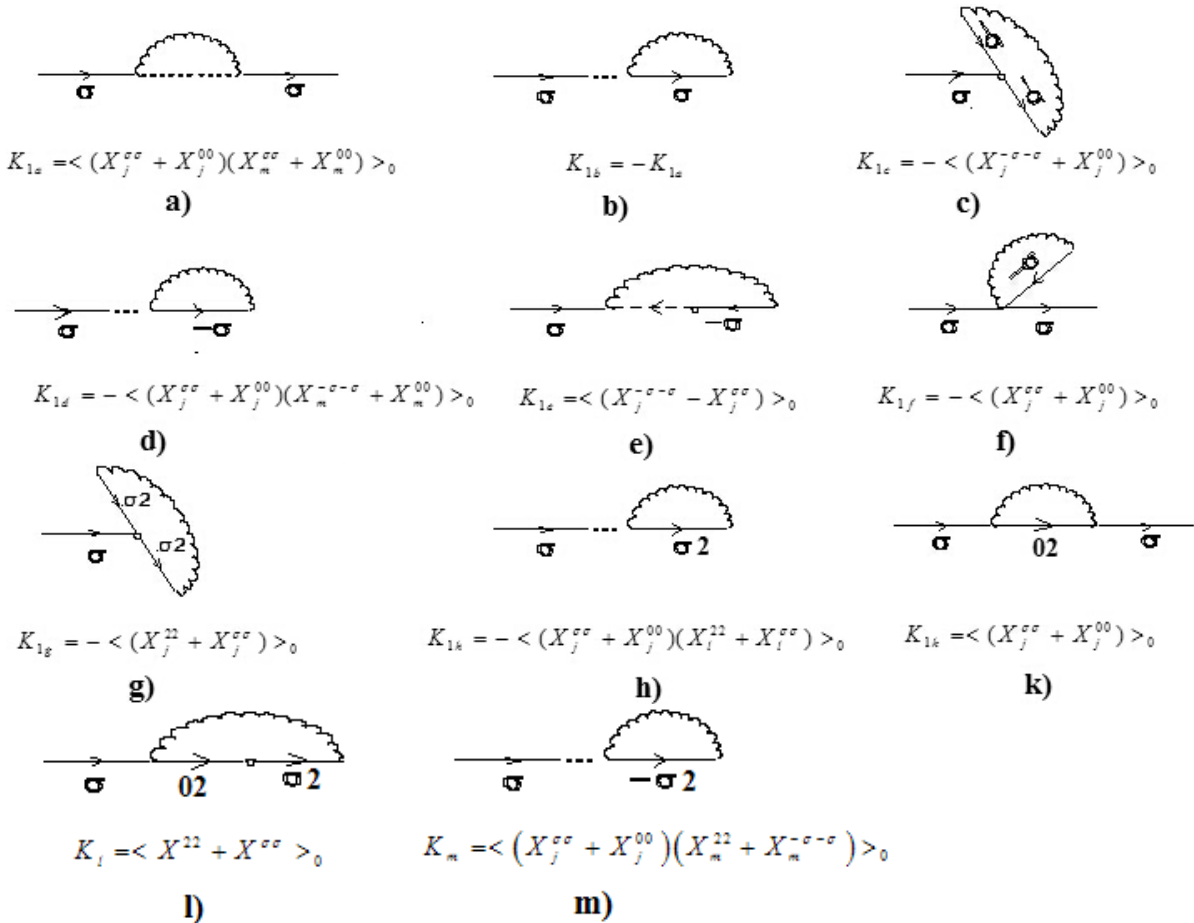$K_m = < (X_j^{\sigma\sigma} + X_j^{00})(X_m^{22} + X_m^{-\sigma-\sigma}) >_0$

m)

Fig. 2.5. All diagrams for first correlator group which determines the self-energy component $\Sigma_{\sigma 0,0\sigma}(i\omega_n)$

Next, it is easy to obtain that

$$<F^{\sigma 0}>_0 G^0_{0\sigma}(i\omega_n)+\Sigma_{1b)}+\Sigma_{1d)}+\Sigma_{1h)}+\Sigma_{1m)}+\Sigma_{1c)}+\Sigma_{1d)} =<F^{\sigma 0}> G^0_{0\sigma}(i\omega_n), \qquad (2.37)$$

where $<F^{\sigma 0}>$ is determined by Eq. (2.26), i.e., $<F^{\sigma 0}>=1-n/2$. Thus, the sum in Eq. (2.37) gives a self-energy in the Hubbard I approximation (see Eq. (2.8)). In a similar manner, one can prove that for a fourth correlator group

$$<F^{2-\sigma}>_0 G^0_{-\sigma 2}(i\omega_n)+\Sigma_{4a)}+\Sigma_{4c)}+\Sigma_{4e)}+\Sigma_{4d)}+\Sigma_{4h)}+\Sigma_{4k)} =<F^{2-\sigma}> G^0_{-\sigma 2}(i\omega_n), \quad (38)$$

as in the Hubbard I approximation for $\Sigma_{2-\sigma,-\sigma 2}(i\omega_n)$, where $<F^{2-\sigma}>=n/2$. Further we consider only zero temperatures.

Now one can write the expressions of the remaining self-energy components for all four correlator groups (2.35) with the analytic continuation $i\omega_n \to \omega+i\delta$:

1) $\beta W\Sigma_{1a)}(\omega+i\delta)=\dfrac{<F^{\sigma 0}>_0}{(\omega+\tilde{\mu})^2}(1-<F^{\sigma 0}>_0)\{\mathrm{Re}\,I_1+i\,\mathrm{Im}\,I_1\}$

$\beta W\Sigma_{1e)}(\omega+i\delta)=\dfrac{<X^{-\sigma-\sigma}>_0}{(\omega+\tilde{\mu})^2}\{\mathrm{Re}\,I_1+i\,\mathrm{Im}\,I_1\}$

$\beta W\Sigma_{1f)}(\omega)=\dfrac{-<F^{\sigma 0}>_0}{(\omega+\tilde{\mu})^2}\dfrac{\delta\mu_{-\sigma}}{W}$ $\qquad\qquad (2.39)$

$\beta W\Sigma_{1k)}(\omega+i\delta)=\dfrac{<F^{\sigma 0}>_0}{(\omega+\tilde{\mu})^2}\{\mathrm{Re}\,I_3+i\,\mathrm{Im}\,I_3-n(\tilde{U}-2\tilde{\mu})[\mathrm{Re}\,I_2+i\,\mathrm{Im}\,I_2]\}$

$\beta W\Sigma_{1l)}(\omega+i\delta)=\dfrac{<F^{2\sigma}>_0}{(\omega+\tilde{\mu})^2}n(\tilde{U}-2\tilde{\mu})[\mathrm{Re}\,I_2+i\,\mathrm{Im}\,I_2]+\dfrac{<F^{2\sigma}>_0}{\omega+\tilde{\mu}}[\mathrm{Re}\,I_4+i\,\mathrm{Im}\,I_4]$

2) $\beta W\Sigma_{2a)}(\omega+i\delta)=\dfrac{-<F^{\sigma 0}>_0<F^{2-\sigma}>_0}{(\omega+\tilde{\mu})(\omega+\tilde{\mu}-\tilde{U})}\{\mathrm{Re}\,I_1+i\,\mathrm{Im}\,I_1\}$

$\beta W\Sigma_{2b)}(\omega+i\delta)=\dfrac{<F^{2\sigma}>_0}{\omega+\tilde{\mu}-\tilde{U}}I_5$

$\beta W\Sigma_{2c)}(\omega+i\delta)=\dfrac{<X^{-\sigma-\sigma}>_0}{(\omega+\tilde{\mu})(\omega+\tilde{\mu}-\tilde{U})}\{\mathrm{Re}\,I_1+i\,\mathrm{Im}\,I_1\}$ $\qquad (2.40)$

$\beta W\Sigma_{2d)}(\omega+i\delta)=<F^{2\sigma}>_0\{\mathrm{Re}\,I_6+i\,\mathrm{Im}\,I_6\}-\dfrac{<F^{2\sigma}>_0 n(\tilde{U}-2\tilde{\mu})}{(\omega+\tilde{\mu})(\omega+\tilde{\mu}-\tilde{U})}[\mathrm{Re}\,I_2+i\,\mathrm{Im}\,I_2]$

$\beta W\Sigma_{2e)}(\omega+i\delta)=\dfrac{<F^{2\sigma}>_0}{\omega+\tilde{\mu}}[\mathrm{Re}\,I_7+i\,\mathrm{Im}\,I_7]+\dfrac{<F^{2\sigma}>_0 n(\tilde{U}-2\tilde{\mu})}{(\omega+\tilde{\mu})(\omega+\tilde{\mu}-\tilde{U})}[\mathrm{Re}\,I_2+i\,\mathrm{Im}\,I_2]$

3) $\beta W\Sigma_{3a)}(\omega+i\delta)=\dfrac{-<F^{\sigma 0}>_0<F^{2-\sigma}>_0}{(\omega+\tilde{\mu})(\omega+\tilde{\mu}-\tilde{U})}\{\mathrm{Re}\,I_1+i\,\mathrm{Im}\,I_1\}$

$\beta W\Sigma_{3b)}(\omega+i\delta)=\beta W\Sigma_{2e)}(\omega+i\delta)$

$\beta W\Sigma_{3c)}(\omega+i\delta)=\dfrac{<F^{2-\sigma}>_0}{(\omega+\tilde{\mu})(\omega+\tilde{\mu}-\tilde{U})}\{\mathrm{Re}\,I_3+i\,\mathrm{Im}\,I_3-n(\tilde{U}-2\tilde{\mu})[\mathrm{Re}\,I_2+i\,\mathrm{Im}\,I_2]\}$ $\quad (2.41)$

$\beta W\Sigma_{3d)}(\omega+i\delta)=\dfrac{-<X^{-\sigma-\sigma}>_0}{(\omega+\tilde{\mu})(\omega+\tilde{\mu}-\tilde{U})}\{\mathrm{Re}\,I_1+i\,\mathrm{Im}\,I_1\}$

$\beta W\Sigma_{3e)}(\omega+i\delta)=\dfrac{-<F^{2-\sigma}>_0}{(\omega+\tilde{\mu})(\omega+\tilde{\mu}-\tilde{U})}\dfrac{\delta\mu_{2\sigma}}{W}$

4) $\quad \beta W \Sigma_{4b)}(\omega + i\delta) = \dfrac{(1 - <F^{2-\sigma}>_0)<F^{2-\sigma}>_0}{(\omega + \tilde{\mu} - \tilde{U})^2}\{\operatorname{Re} I_1 + i \operatorname{Im} I_1\}$

$\quad \beta W \Sigma_{4d)}(\omega + i\delta) = \dfrac{<F^{2-\sigma}>_0}{(\omega + \tilde{\mu} - \tilde{U})^2}\dfrac{\delta\mu_{2\sigma}}{W}$

$\quad \beta W \Sigma_{4f)}(\omega + i\delta) = \dfrac{<X^{-\sigma-\sigma}>_0}{(\omega + \tilde{\mu} - \tilde{U})^2}\{\operatorname{Re} I_1 + i \operatorname{Im} I_1\}$ $\qquad\qquad$ (2.42)

$\quad \beta W \Sigma_{4l)}(\omega + i\delta) = -\dfrac{<F^{2\sigma}>_0}{(\omega + \tilde{\mu} - \tilde{U})^2}\{\operatorname{Re} I_3 + i \operatorname{Im} I_3 - n(\tilde{U} - 2\tilde{\mu})[\operatorname{Re} I_2 + i \operatorname{Im} I_2]\}$

$\quad \beta W \Sigma_{4m)}(\omega + i\delta) = \dfrac{<F^{2\sigma}>_0}{\omega + \tilde{\mu} - \tilde{U}}[\operatorname{Re} I_7 + i \operatorname{Im} I_7] + \dfrac{<F^{-\sigma 0}>_0\, n(\tilde{U} - 2\tilde{\mu})}{(\omega + \tilde{\mu} - \tilde{U})^2}[\operatorname{Re} I_2 + i \operatorname{Im} I_2]$

Here, $n(x) = 1/(e^x - 1)$ is the Bose distribution function and $<F^{\sigma 0}>_0$ and $<F^{2\sigma}>_0$ are determined by Eq. (2.20). The integrals I_1 and I_2 can be expressed in terms of the lattice Green's function $G(t)$ (2.12). Indeed,

$$I_1 = \sum_q \dfrac{t(q)}{1 - \beta t(q)\left[G_{0\sigma}(i\omega_n)<F^{\sigma 0}> + G_{-\sigma 2}(i\omega_n)<F^{-\sigma 2}>\right]}$$

$$I_2 = \sum_q \dfrac{t(q)}{1 + \beta t(q)\left[G_{0\sigma}(i\omega_n)<F^{\sigma 0}> + G_{-\sigma 2}(i\omega_n)<F^{-\sigma 2}>\right]}$$

$\qquad\qquad$ (2.43)

One can write after the analytic continuation $i\omega_n \to \omega + i\delta$:

$$I_1 = \dfrac{\beta W}{F^2(\tilde{\Omega})}\left(-F(\tilde{\Omega}) + 6[\operatorname{Re} G(s_1) - i \operatorname{Im} G(s_1)]\right)$$

$$I_2 = \dfrac{\beta W}{S^2(\tilde{\Omega})}\left(S(\tilde{\Omega}) + 6[\operatorname{Re} G(s_2) - i \operatorname{Im} G(s_2)]\right)$$

, $\qquad\qquad$ (2.44)

where $s_1 = 6/F(\tilde{\Omega})$, $s_2 = 6/S(\tilde{\Omega})$ and $F(\tilde{\Omega})$ is determined by Eq. (2.11) and $S(\tilde{\Omega})$ has a form

$$S(\tilde{\Omega}) = \dfrac{1 - n/2}{\tilde{\Omega} + \tilde{\mu} - \tilde{U}} + \dfrac{n/2}{\tilde{\Omega} + \tilde{\mu}} \qquad\qquad (2.45)$$

Unfortunately, the rest of the integrals is not expressed in terms of $G(t)$:

$$I_3 = \int_{-\infty}^{+\infty} dw D_C\left(\dfrac{6}{F(w)}\right)\dfrac{6f(w)}{F^2(w)(\tilde{\Omega} + i\delta + w + 2\tilde{\mu} - \tilde{U})}$$

$$I_4 = \int_{-\infty}^{+\infty} dw D_C\left(\dfrac{6}{F(w)}\right)\dfrac{6f(w)}{F^2(w)(\tilde{\Omega} + i\delta + w + 2\tilde{\mu} - \tilde{U})(w + \tilde{\mu} - \tilde{U})}$$

$$I_5 = \int_{-\infty}^{+\infty} dw D_C\left(\dfrac{6}{F(w)}\right)\dfrac{6f(w)}{F^2(w)(w + \tilde{\mu})(w + \tilde{\mu} - \tilde{U})} \qquad\qquad (2.46)$$

$$I_6 = \int_{-\infty}^{+\infty} dw D_C\left(\dfrac{6}{F(w)}\right)\dfrac{6f(w)}{F^2(w)(\tilde{\Omega} + i\delta + w + 2\tilde{\mu} - \tilde{U})(w + \tilde{\mu} - \tilde{U})(w + \tilde{\mu})}$$

$$I_7 = \int_{-\infty}^{+\infty} dw D_C\left(\dfrac{6}{F(w)}\right)\dfrac{6f(w)}{F^2(w)(\tilde{\Omega} + i\delta + w + 2\tilde{\mu} - \tilde{U})(w + \tilde{\mu})}$$

The imaginary parts of these integrals are evaluated from the Landau bypass rule

$$\frac{1}{\tilde{\Omega}+i\delta+w+2\tilde{\mu}-\tilde{U}}=V.p.\frac{1}{\tilde{\Omega}+i\delta+w+2\tilde{\mu}-\tilde{U}}-i\pi\delta(\tilde{\Omega}+w+2\tilde{\mu}-\tilde{U}) \tag{2.47}$$

and real parts are calculated numerically as the Cauchy principal value. It is easy to write for imaginary parts at $T=0$:

$$\mathrm{Im}\, I_3 = -\pi D_C\left(\frac{6}{F(\tilde{U}-2\tilde{\mu}-\tilde{\Omega})}\right)\frac{6\theta(\tilde{\Omega}+2\tilde{\mu}-\tilde{U})}{F^2(\tilde{U}-2\tilde{\mu}-\tilde{\Omega})}$$

$$\mathrm{Im}\, I_4 = -\frac{\mathrm{Im}\, I_3}{\tilde{\Omega}+\tilde{\mu}}$$

$$\mathrm{Im}\, I_5 = 0 \tag{2.48}$$

$$\mathrm{Im}\, I_6 = \frac{\mathrm{Im}\, I_3}{(\tilde{\Omega}+\tilde{\mu})(\tilde{\Omega}+\tilde{\mu}-\tilde{U})}$$

$$\mathrm{Im}\, I_7 = -\frac{\mathrm{Im}\, I_3}{\tilde{\Omega}+\tilde{\mu}-\tilde{U}}$$

To solve the matrix Dyson's equation (2.34), it is conveniently expressed by $r_{11}=\Sigma_{\sigma 0,0\sigma}$, $r_{12}=\Sigma_{\sigma 0,-\sigma 2}$, $r_{21}=\Sigma_{2-\sigma,0\sigma}$ and $r_{22}=\Sigma_{2-\sigma,-\sigma 2}$. Then the Green's function $G_\sigma(\mathbf{r}_i-\mathbf{r}_j,\tau)=-<T_\tau c_{i\sigma}(\tau)c^+_{j\sigma}(0)>$ is determined by Eq. (2.34) as

$$G_\sigma(\omega+i\delta,\mathbf{k})=\frac{r_\sigma+t(\mathbf{k})u_\sigma}{1-\beta t(\mathbf{k})\{r_{11}+r_{22}\}+\frac{1}{4}\beta^2 t^2(\mathbf{k})u_\sigma}, \tag{2.49}$$

where

$$r_\sigma = r_{11}+r_{22}+r_{12}+r_{21}$$
$$u_\sigma = -2\beta(r_{11}r_{22}-r_{12}r_{21}) \tag{2.50}$$

Next, it is not difficult to write the expression for the retarded Green's function

$$\beta G_\sigma(\omega+i\delta,\mathbf{k})=\frac{\chi_{\sigma 1}+\frac{1}{\beta}t_2\chi_{\sigma 2}}{\frac{1}{\beta}t_2-t(\mathbf{k})}-\frac{\chi_{\sigma 1}+\frac{1}{\beta}t_1\chi_{\sigma 2}}{\frac{1}{\beta}t_1-t(\mathbf{k})}, \tag{2.51}$$

where

$$t_{1,2}=\frac{r_{11}+r_{22}\pm\sqrt{(r_{11}+r_{22})^2-4(r_{11}r_{22}-r_{12}r_{21})}}{2(r_{11}r_{22}-r_{12}r_{21})}$$

$$\chi_{\sigma 1}=\frac{r_\sigma}{\sqrt{(r_{11}+r_{22})^2-4(r_{11}r_{22}-r_{12}r_{21})}} \tag{2.52}$$

$$\chi_{\sigma 2}=\frac{u_\sigma}{\sqrt{(r_{11}+r_{22})^2-4(r_{11}r_{22}-r_{12}r_{21})}}$$

Evidently, the excitation spectrum is determined from the equations

$$\mathrm{Re}(t_1)=\beta t(\mathbf{k})$$
$$\mathrm{Re}(t_2)=\beta t(\mathbf{k}) \tag{2.53}$$

2.5. Spectral density, ground state energy and transport

Let us designate

$$g_{1\sigma} = \chi_{\sigma 1} + \frac{1}{\beta} t_2 \chi_{\sigma 2} = g'_{1\sigma} + ig''_{1\sigma}$$

$$g_{2\sigma} = \chi_{\sigma 1} + \frac{1}{\beta} t_1 \chi_{\sigma 2} = g'_{2\sigma} + ig''_{2\sigma}$$

$$\quad (2.54)$$

where $g'_{i\sigma}$ and $g''_{i\sigma}$ are real and imaginary parts of function $g_{i\sigma}$. The uniform spectral density

$$R(\omega) = \frac{1}{N} \sum_k A_\sigma(\omega, k), \qquad (2.55)$$

where

$$A_\sigma(\omega, k) = -\frac{2\beta}{i} \operatorname{Im}\left[G_\sigma(\omega + i\delta, k) \right]. \qquad (2.56)$$

Taking into account Eqs. (2.54), one can write the final result for $\tilde{\Lambda}_\sigma(\omega)$:

$$R(\omega) = -\frac{12}{W} \left\{ g'_{1\sigma} \operatorname{Im}\left[G\left(\frac{6t_2}{\beta W}\right) \right] + g''_{1\sigma} \operatorname{Re}\left[G\left(\frac{6t_2}{\beta W}\right) \right] - g'_{2\sigma} \operatorname{Im}\left[G\left(\frac{6t_1}{\beta W}\right) \right] - g''_{2\sigma} \operatorname{Re}\left[G\left(\frac{6t_1}{\beta W}\right) \right] \right\}, \quad (2.57)$$

where $G(t)$ is the lattice Green's function from Eq. (2.12).

In Fig. 2.6 the total over spin electron spectral densities $R(\Omega)$ at $\tilde{U} = 0.5$ and $n = 1$ for both dielectric (a and b) and metal I are presented. From the figure, it follows that the band filling as $n = 1 - \delta$ at $\delta \to 0$ make up a gap Δ above Fermi level (hole-doped systems) and $\Delta << \tilde{U}$. In this case, the spectral density on the Fermi level is finite although it drops sharply above. As will be seen below, this contradiction is eliminated by comparison of the inner energies for a metal and a dielectric. The band filling as $n = 1 + \delta$ at $\delta \to 0$ on the Fermi level gives a small quasigap. For the metal at the Fermi energy there is no gap.
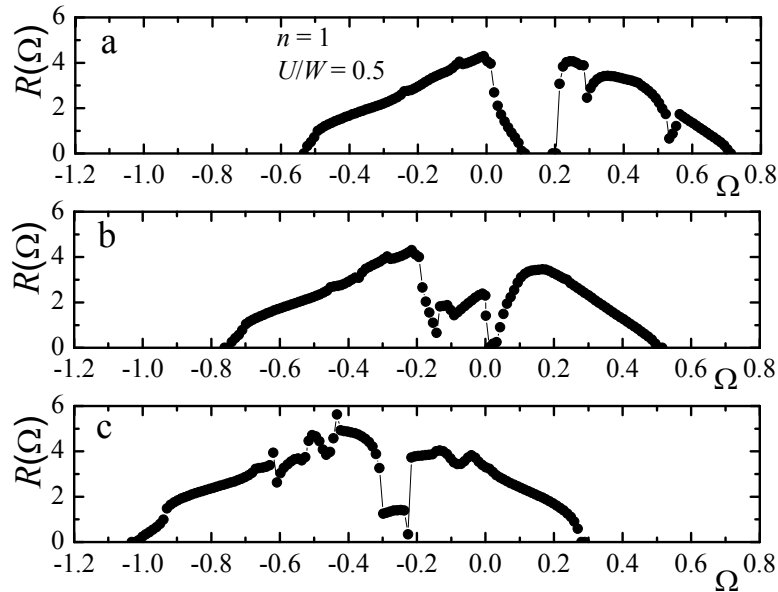

Fig. 2.6. The total over spin uniform electron spectral density $R(\Omega)$ at $\tilde{U} = 0.5$, where Ω is the frequency in the units of bandwidth, for a half-filled band in the insulator state at $n = 1 - \delta$ (a) and $n = 1 + \delta$ (b) at $\delta \to 0$ and for a metal (c). $\Omega = 0$ corresponds to a level of the chemical potential

In Fig. 2.7, the total over spin uniform electron spectral densities $R(\Omega)$ at $\tilde{U} = 2$ and $n = 1$ for both dielectric (*a* and *b*) and metal I are presented. From the figure, it can be seen that the gaps arise from such $\tilde{U}$ values above and below the Fermi level where the band filling is $n = 1 + \delta$ and $n = 1 - \delta$, respectively. Note that for an infinitely small electron doping of the half-filled band (see Fig. 2.6, *b*) in the limit $n = 1$ the spectral density at the Fermi energy is zero. Thus, in this case, the conductivity will be zero, i.e., we have a dielectric. As it takes place, the bandwidth is $\tilde{U} \sim 3/2$. For a metal state, the Fermi level lies near the middle of the upper Hubbard band that is the characteristic of a metal. For large values $\tilde{U}$, the dependencies $R(\Omega)$ are similar. It is not yet possible to say what state is realized in accordance with the previously entered order parameters. It is necessary to obtain an expression for energy of the ground state.

To determine the inner energy E we will use the basic Kalashnikov-Fradkin relation [36] which allows us to express a mean interaction energy $<\hat{V}>$ from (5) in term of the spectral density $A_\sigma(\omega, k)$:

$$\frac{1}{N}\sum_{p\sigma} <\left[\hat{H} a_{p\sigma}^+ \right] a_{p\sigma} > = \frac{1}{2\pi}\sum_{k\sigma} \int_{-\infty}^{+\infty} \frac{\omega A_\sigma(\omega, k)}{e^{\beta\omega} + 1} d\omega . \tag{2.58}$$
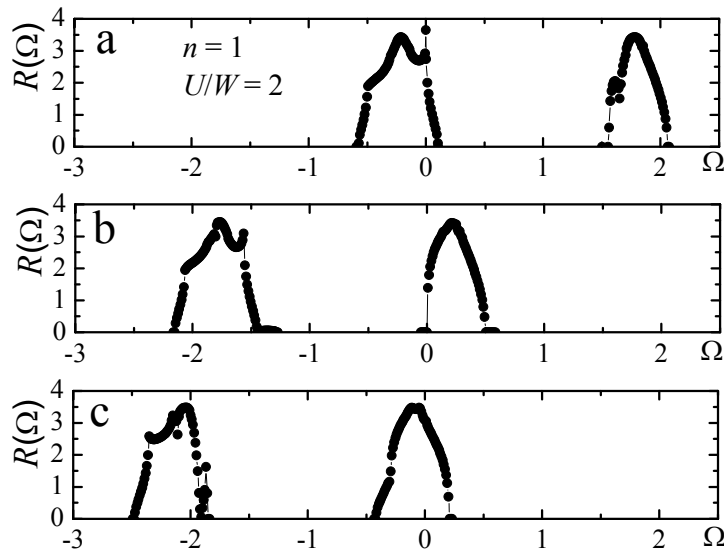
Fig. 2.7. The total over spin uniform electron spectral density $R(\Omega)$ at $\tilde{U} = 2.0$ for a half-filled band in the insulator state at $n = 1 - \delta$ (a) and $n = 1 + \delta$ (b) at $\delta \to 0$ and for a metal (c). The notations are the same as in Fig. 2.6

Extracting the unperturbed Hamiltonian $\hat{H}_0$ from $\hat{H}$ it is easy to find that

$$<\hat{V}> = \frac{1}{2\pi N}\sum_{k\sigma} \int_{-\infty}^{+\infty} \frac{\omega A_\sigma(\omega, k)}{e^{\beta\omega} + 1} d\omega - \sum_\alpha \tilde{\varepsilon}_\alpha < X^{\alpha\alpha} > , \tag{2.59}$$

where $\tilde{\varepsilon}_+ = \tilde{\varepsilon}_- = -\tilde{\mu}$, $\tilde{\varepsilon}_0 = 0$ and $\tilde{\varepsilon}_2 = 2(\tilde{U} - \tilde{\mu})$. Taking into account that $E = \mu n + <\hat{H}_0> + <\hat{V}>$ one can get the expression for the energy.

$$E = \mu n - U < X^{22} > + \frac{1}{\pi N}\sum_{k} \int_{-\infty}^{+\infty} \frac{\omega A_\sigma(\omega, k)}{e^{\beta\omega} + 1} d\omega , \tag{2.60}$$

where the site occupancy probability $< X^{22} >$ by two electrons is

$$< X^{22} >= \frac{n}{2} - < X^{\sigma\sigma} >_1 - \nu_\sigma < F^{\sigma 0} >_0 + \nu_{2\sigma} < F^{2\sigma} >_0 \qquad (2.61)$$

It should be noted that $< X^{22} > \geq 0$ is always realized. From Eq. (2.60) for chemical potential of a metal it follows that the term with an integral which we denote by I depends on n only:

$$I = \frac{2}{n} + \frac{n}{2} - 1 \qquad (2.62)$$

This term is also included in Eq. (2.61) taking into account for $< X^{\sigma\sigma} >_1 = \nu_\sigma < F^{\sigma 0} >_0 = 0$. As a result, we have the obvious relation

$$< X^{22} >= n - 1 \geq 0 \qquad (2.63)$$

Thus, the metal phase exists only for an electron-doped system. At $n < 1$, the solution for a metal phase does not exist because in this case $< X^{22} > < 0$.

Using Eq. (2.60) one can calculate energies of the ground state of a half-filled Hubbard band for both metal and dielectric states. In Fig. 2.8, we present the dependence of the ground-state energy on the value of a single-site Coulomb repulsion $\tilde{U} = U/W$ at $n = 1$ for a dielectric in the limit of an infinitely small number of holes (curve 1), for an infinitely small electron doping (curve 2) and for a metal (curve 3). From the figure, it can be seen that at $\tilde{U} = \tilde{U}_{cr.} = 2.1$ the phase transition to a metal state occurs. Note that in the Hubbard III approximation [25] the critical value $\tilde{U}_{cr.}^{Hubb} = 0.87$ is significantly less than 2.1. In the Hubbard model with an infinite lattice dimension that is reduced to the single-impurity Anderson model, a critical value $\tilde{U}_{cr.}^{\infty} = 3$ was obtained [27].
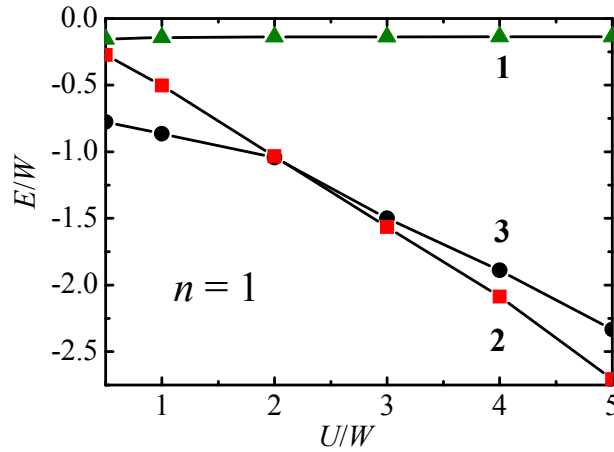
Fig. 2.8. Dependence of the ground state energy on the parameter of the single site Coulomb repulsion $\tilde{U} = U/W$ in the case of a half-filled band for an insulator in the limit of the infinitely small number of holes (curve 1), for an infinitely small electron doping (curve 2) and for a metal (curve 3)

It should be noted that at $n = 1$ and $\tilde{U} > \tilde{U}_{cr.}$ the minimum energy is realized in the system in the limit of the infinitely small electron doping (see curve 2 in Fig. 2.8). This means that the chemical potential of the half-filled band lies at the bottom of the upper Hubbard band,

i.e., we have a completely filled lower band with an energy gap (see Fig. 2.6 b) and zero spectral density at the Fermi energy level. Apparently, in this case the conductivity equals zero.

For a half-filled band at a finite small hole doping the chemical potential abruptly decreases in the magnitude according to Fig. 2.4. The energy will change from values approximately as in the curve 2 in Fig. 2.7 to values approximately those of the curve 1 of the same figure. The order parameter for a metal state is not realized since for $n < 1$ we have always $<X^{22}> < 0$. The position of the chemical potential level is such that the spectral density is finite when $\Omega = 0$ as shown in Fig. 2.7 a. As will be seen below, it leads to a step-like change in the conductivity from zero to a finite value in agreement with experiment. This fact could not be explained by previously known theories [28].

In conclusion, we consider transport properties of the Hubbard paramagnet in the ground state. It is known [37] that the diagonal component of the isotropic conductivity $\sigma(\omega, T)$ for a simple cubic lattice with a constant a is expressed in terms of the spectral density as follows

$$\sigma(\tilde{\omega}, T) = \frac{e^2}{3a\pi\hbar} \frac{W}{6} \sum_\sigma \int_{-3}^{3} d\varepsilon \varepsilon D_C(\varepsilon) \Phi_\sigma(\varepsilon, \tilde{\omega} + \tilde{\mu}), \tag{2.64}$$

where e is the electron charge and the function $\Phi(\varepsilon, \tilde{\omega} + \tilde{\mu})$ is associated with non-uniform $A_\sigma(\tilde{\omega} + \tilde{\mu}, \boldsymbol{k})$ by the differential equation

$$\frac{6}{W} \frac{d\Phi_\sigma(\varepsilon, \tilde{\omega} + \tilde{\mu})}{d\varepsilon} = \frac{1}{4} A_\sigma^2(\tilde{\omega} + \tilde{\mu}, \varepsilon). \tag{2.65}$$

We are interested in the residual conductivity $\sigma(0,0)$. As it was shown earlier, at the energy Fermi when $\tilde{\omega} = 0$ for a dielectric at $\tilde{U} > \tilde{U}_{cr.}$ the spectral density $A_\sigma(\tilde{\mu}, \varepsilon) = 0$, i.e., $\Phi_\sigma(\varepsilon, \tilde{\mu}) = \mathrm{const}$, that in accordance with Eq. (2.64) gives $\sigma(0,0) = 0$. The solution of the differential equation (2.65) for a metal is not difficult since the dependence of the Green's function on ε is very simple

$$\beta G_\sigma(\tilde{\mu}, \varepsilon) = \frac{6}{W} \left\{ \frac{g_{1\sigma}(\tilde{\mu})}{\tilde{t}_{2\sigma}(\tilde{\mu}) - \varepsilon} - \frac{g_{2\sigma}(\tilde{\mu})}{\tilde{t}_{1\sigma}(\tilde{\mu}) - \varepsilon} \right\}, \tag{2.66}$$

where the functions $g_{i\sigma}(\tilde{\mu})$ and $\tilde{t}_{i\sigma}(\tilde{\mu}) = t_{i\sigma} / W$ in the general case are complex and are determined by the Eqs. (2.52) and (2.54).

In Fig. 2.9, the dependence of the conductivity on the parameter of an electron single site Coulomb repulsion $\tilde{U}$ at the temperature $T = 0$ at $a = 5$ Å for a half-filled band (a) and conductivity as a function of the electron concentration n (b) (hole-electron doping) for $\tilde{U} = 2$ (curve 1) and $\tilde{U} = 5$ (curve 2) are presented. From Fig. 2.9a, it follows that in a metal phase there is a residual resistance due to the electron-hole inelastic scattering. In this case, the conductivity value is quite close to the metal one according to the Ioffe-Regel principle [28] when the minimum electron mean free path is of order of the lattice constant. At the phase transition an abrupt change in the resistivity occurs which is experimentally observed in metal oxides. This effect has not been explained within the framework of Hubbard theories [24, 25] as well as in the following theories [26–31] which predict the continuous evolution of the metal phase into the dielectric phase. Fig. 2.9 b shows how the hole-electron doping influences the metal conductivity (curve 1, $\tilde{U} = 2$) and the dielectric one (curve 2, $\tilde{U} = 5$). It should be noted that when $\tilde{U} = 2$ and $n < 1$ the metal state does not exist but hole doped dielectric is realized. At $n \geq 1$ the curves 1 and 2 correspond to a metal with the lowest inner energy and with a finite conductivity which tends to zero at n $\rightarrow$ 1. At $n > 1.5$ the spectral density is equal zero that may

indicate the coherence of the excitations and further electron localization due to the complete band filling. On the other hand, an increase in the Coulomb repulsion up to $\tilde{U} = 5$ influences weakly on the conductivity except for an area near the half-filling band. At $n = 1$ the conductivity abruptly drops to zero reflecting the dielectric state and then abruptly increases up to 1.53 mΩ⁻¹cm⁻¹ at $n = 1.01$ (see the curve 2 in Fig. 2.8).
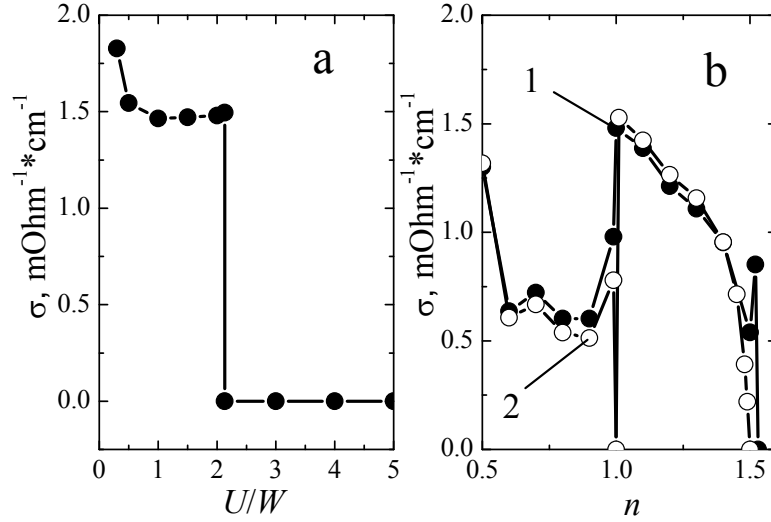
Fig. 2.9. Dependence of conductivity on the parameter of the electron single-site Coulomb repulsion $\tilde{U}$ at the temperature $T = 0$ at $a = 5$ Å for a half-filled band (a) and conductivity as a function of the electron concentration n (b) (hole-electron doping) for $\tilde{U} = 2$ (curve 1) and $\tilde{U} = 5$ (curve 2)

2.6. Conclusions

In conclusion, we formulate the main conclusions of the chapter. Within the framework of the time-perturbation theory, a method for accounting the correlation effects in the Hubbard model has been proposed. It permits to describe metal and dielectric states by corresponding order parameters that determine self-consistent probabilities of the site occupancy by electrons and holes. In this case the metallic state is realized only at $n \geq 1$ for the Coulomb-repulsion parameter $\tilde{U} < 2.1$.

It has been established that the concentration dependence of the chemical potential has a disruption near the half-band filling for the dielectric state. In this case, the lower edge of the upper Hubbard band coincides with the level of the chemical potential. Thus, the completely filled lower Hubbard band is separated from the chemical potential level by a gap which is somewhat smaller than the value $\tilde{U}$. Since the spectral density at this edge of the band equals zero, we have a zero conductivity.

A finite small hole doping of the dielectric leads to a sharp increase in the inner energy due to the chemical potential jump. Also, the position of the chemical potential level in the lower Hubbard band changes with a shift from its upper edge into a band by a finite value. This leads to an abrupt change in conductivity from zero to a finite value corresponding to experimental data for series compounds and gives an understanding of the nature of this phenomenon. Electron doping of the half-filled band shows a rather weak dependence of the conductivity on the Coulomb-repulsion value in the ground state. The observed sharp decrease σ in the area of the electron concentration $n \sim 3/2$ is the subject of our further research.

51

3. ELECTRON DYNAMICS IN THE NORMAL STATE OF CUPRATES: SPECTRAL FUNCTION, FERMI SURFACE AND ARPES DATA

3.1. Introduction

Description of the strongly correlated electron dynamics in cuprates is one of the intriguing tasks in the theory of condensed matter physics. The history of such investigations from the HTSC discovery covers considerable quantity of publications. Experimental tunnel, magnetic, resonance and ARPES data [38–40] of the mentioned objects reflect an extremely complicated character of the interplay between charge, spin and lattice degrees of freedom. In spite of a wide experimental material as well as undoubted successful description of the cuprate electron structure by ab initio methods [41, 42], some observed phenomena connected with the strong electron correlations and electron-phonon interaction are not reproduced theoretically. In our opinion, the reason is that within the framework of such approaches it is impossible to extract an effective self-consistent field by analogy with the Weiss field in magnetism or an unperturbed Hamiltonian for free electrons in metals as well as the restricted statistics and difficulties to account for hole states. In some cases, authors are using the methods of metal physics especially to build the HTSC model and to account for strong electron-phonon interactions that is not useful for electron systems with strong correlations [43–45]. One of the puzzle phenomena which is not described by existing theories is a low-energy kink experimentally observed in the nodal dispersion of various cuprate materials [46–48]. Below we present a theory explaining the origin of this anomaly and a consecutive picture of the strongly correlated electron dynamics in cuprates.

In this context, it is necessary to point out that the aim of this work is to build successive approximations for a diagrammatic method when the Hubbard-I [24] approximation is the starting point for any calculations. In this case, we have a self-consistent field with the aid of which one can account for a specific character of doped Mott insulators. Indeed, hereafter we will show the fundamental difference between metals and doped cuprates resulting in a strong correlation narrowing of the valence band for hole doping [49, 50]. Within the framework of the *t-J* model for a lower Hubbard band without exchange electron interaction it is easy to detect that in a paramagnetic phase (PM) there are two noninteracting electron liquids with spins up and down avoiding one another and being in equilibrium. Hence, it gives rise to correlation effects. Indeed, unlike metals, each electron hopping does not change a number of electrons for both sites with spins up and spins down, respectively. In a metal, each electron hopping gives a site with double occupancy changing the fixed electron quantity in the pointed subsystems. That is why we should consider the whole electron system regardless of the spin. As a result in the PM phase of doped Mott insulators in the limit of the Coulomb repulsion $U = \infty$ the excitation spectrum will be two-fold degenerate and the chemical potential μ in the limit of half-band filling is equal approximately to a half of a metal μ. It is necessary to point out that the ferromagnetically ordered strongly correlated electron system is similar to an ordinary metal since in this case the Fermi statistics is working first of all.

To take the strong electron-phonon interaction into account is one of the most complicated tasks in the condensed natter theory. To solve this problem in a given work, we

suggest to consider the Holstein model with one characteristic optical Einstein mode. The extension to the case of a few modes does not present any difficulties. We apply the method of an inverse function formulated by us in the paper [50] for building the HTSC theory. Also, in contrast to existing theories [32, 44, 51], where account of the electron-phonon interaction cannot be exact, our model based on the Lang-Firsov transformation [52] allows to solve this problem exactly. In this work, in the Hubbard-I approximation it has been shown for the first time how strong electron-phonon binding modifies the band spectrum, chemical potential and Fermi surface. To calculate the Green's function, we used a such type of the Dyson equation when the self-energy depends on frequency only and all inhomogeneity is related exceptionally to the Fourier representation of the hopping integral.

Based on the diagrammatic contributions related to inelastic electron scattering a new specific feature of the electron spectrum and spectral density is revealed when the frequency and the wave characteristic are varied abruptly through a small range. It is in a good qualitative agreement with the ARPES data. This circumstance makes the Fermi surface detection difficult and in specific cases points out the non-Fermi liquid behaviour of the electron ensemble.

The structure of the section is as follows. In the subsection 3.2, the starting fermion-boson Hamiltonian of the cuprate system is considered. It was diagonalized by unitary transformation. In the approximation Hubbard-I, detailed analysis of the dynamic electron properties is carried out by taking into account an influence of the electron-phonon interaction, next nearest neighbours and changes of the Fermi surface topology. In the subsection 3.3, low-dimensional correlations and electron-phonon interactions are included to provide the most general expression for Matsubara Green functions in the first non-vanishing approximation of the time-dependent perturbation theory with respect to the inverse effective radius of interaction $r \sim 1/z$, where z is the number of nearest neighbors in the simple square lattice. The equations for the excitation spectrum and damping were obtained. Also, the numerical analysis for a chemical potential, Fermi surface, the frequency spectrum and the spectral density of the PM phase at the value of the electron-phonon binding parameter $g = 0$ was carried out. The polaron bands, spectral densities and their modifications versus parameter g were calculated. In conclusion, we provide theoretical results with regard to the most typical experimental data.

3.2. Holstein polarons and effective self-consistent field in cuprates

3.2.1. Hamiltonian of the fermion-bosonic system

To describe the electron dynamics, it is necessary to calculate the Matsubara electron Green's function poles of which determine an excitation spectrum ω_k. Also, spectral density $A(\omega, k)$ is proportional to the square power of the imaginary part of a Green's function. In what follows, we will consider a PM phase in which the spin index σ does not play any role. The t-J model is believed to be the simplest one for the description of strong electron correlations. Apparently, in our case the exchange part of Hamiltonian is not considered. We add to the Hamiltonian of the t-J model a part used in the Holstein model of small polarons for the HTSC systems characterized by sufficiently strong electron-phonon interaction. These polarons are formed due to the interaction between electrons and lattice optical vibrations. For simplicity, we consider the Einstein model with a phonon frequency ω_0. Thus, the Hamiltonian reads as

$$\hat{H} = \hat{H}_{0f} + \hat{H}_b + V , \tag{3.1}$$

where

$$\hat{H}_0 = \hat{H}_{0f} + \hat{H}_b$$

$$\hat{V} = -\sum_{i,j,\sigma} t_{ij} c_{\sigma i}^+ c_{\sigma j} (1 - n_{i-\sigma})(1 - n_{j-\sigma})$$

$$\hat{H}_{0f} = -\mu \sum_{i\sigma} n_{i\sigma} \tag{3.2}$$

$$\hat{H}_b = -g \sum_i n_i \left(b_i^+ + b_i \right) + \omega_0 \sum_i b_i^+ b_i$$

Here, the fermionic $\hat{H}_{0f}$ and bosonic $\hat{H}_b$ terms are related to the energy of the chemical potential μ and local electron-phonon interaction in a phonon subsystem with the frequency ω_0, respectively. The sum of these terms $\hat{H}_{0f}$ and $\hat{H}_b$ is considered as an unperturbed Hamiltonian $\hat{H}_0$. For weakly doped cuprates $\hat{V}$ operator is taken as a perturbation, where both $c_{\sigma i}^+$ ($c_{\sigma i}$) and b_i^+ (b_i) create (annihilate) an electron of spin σ and phonon on the lattice site *i*, respectively, and t_{ij} is the hopping integral. $n_i = n_{i\sigma} + n_{i-\sigma}$ is the site electron concentration, where $n_{i\sigma}$ represents the concentration of electrons on the site *i* with spin σ. The exchange term of the Hamiltonian is neglected for the system in the PM state.

The Lang-Firsov unitary transform [52] allows to separate boson and fermion operators in $\hat{H}_b$. Then the transformed $\hat{H}_b$ takes the form $\hat{\tilde{H}}_b$:

$$\hat{\tilde{H}}_b = \omega_0 \sum_i b_i^+ b_i - \xi \sum_i n_i , \tag{3.3}$$

where $\xi = g^2/\omega_0$ is the polaron binding energy. Also, perturbation Hamiltonian $\hat{V}$ is transformed to $\hat{\tilde{V}}$:

$$\hat{\tilde{V}} = -\sum_{<ij>,\sigma} t_{ij} \tilde{c}_{i\sigma}^+ \tilde{c}_{j\sigma} (1 - n_{i-\sigma})(1 - n_{j-\sigma}) , \tag{3.4}$$

Here, the unitary transformated Fermi operators

$$\tilde{c}_{i\sigma} = Y_i c_{i\sigma} \tag{3.7}$$

are products of Bose $Y_i = e^{\lambda(b_i^+ - b_i)}$ and corresponding Fermi destruction operators where λ=g/ω₀. Another terms in Hamiltonian (3.1) are not transformed.

Therefore we have unperturbed Hamiltonian with a perturbation $\hat{V}$ that allows to build the approach based on the scattering matrix formalism.

3.2.2. Approximation Hubbard-I

In the work [24] J. Hubbard developed a simplest approach to decoupling of correlators in the equation of motion for a Green's function. It describes the dielectric state of the strongly correlated electron system. Although this approach denoted as the approximation Hubbard-I does not describe the correlation-induced metal-insulator transition it is quite similar to the Weiss mean field theory of magnetism with an effective field and therefore has fundamental importance

in understanding the physics of strong electron correlations. Thus in what follows we will consider this approach in details within the framework of a modern diagrammatic method taking into account that such systematic description is absent in literature. It is necessary to point out that this method is a quite equivalent to an approach to be used by Hubbard.

Below we will consider the lower Hubbard band doped by holes. In this case one can use one hole and two electron site wave functions: $|\psi_0\rangle = |0\rangle, |\psi_\sigma\rangle = |\sigma\rangle$, where σ=+ (or 1) and σ = - (or -1) for electrons with spins up and down, respectively. Let us introduce Hubbard's operators $X^{ik} = |\psi_i\rangle\langle\psi_k|$ in a given basis. Apparently, in the projective space for the destruction and creation operators $c_{\sigma j}(1-n_{j-\sigma}) = X_j^{0\sigma}$ and $c_{\sigma j}^+(1-n_{j-\sigma}) = X_j^{\sigma 0}$, respectively. With account of Eqs. (3.3)-(3.5), the Hamiltonian of the subsystem reads as

$$\hat{H}_{el.} = \hat{\tilde{H}}_0 + \tilde{V} , \qquad (3.6)$$

where the unperturbed Hamiltonian takes the form:

$$\hat{\tilde{H}}_0 = -\tilde{\mu}\sum_i n_i ,$$

and perturbation appears as

$$\tilde{V} = -\sum_{<ij>,\sigma} t_{ij} \tilde{X}_i^{\sigma 0} \tilde{X}_j^{0\sigma} , \qquad (3.7)$$

where $\tilde{\mu} = \mu + \xi$ is an effective chemical potential with the account of the electron-phonon interaction, $\tilde{X}_i^{\sigma 0} = Y_i^+ X_i^{\sigma 0}$ and $\tilde{X}_j^{0\sigma} = Y_j X_j^{0\sigma}$ are unitary transformed Hubbard's operators. In spite of the simple form, the Hamiltonian (3.6) contains practically all complicated electron dynamics with lattice coupling. It will be seen below from the given calculations.

In the context of the time-dependent perturbation theory, it is easy to show that an equation for the Fourier transform $\Lambda_{0\sigma}(i\omega_p, \boldsymbol{q})$ of the Matsubara Green's function $\Lambda_{0\sigma}(l\tau_1, m\tau_m) = - < T_\tau \tilde{X}_l^{0\sigma}(\tau_l)\tilde{X}_m^{\sigma 0}(\tau_m) >$ in the approximation Hubbard-I is presented graphically in a form as in Fig. 3.1, where the symbol $<...>$ denotes statistical averaging over the total Hamiltonian $\hat{H}_{el.}$ $\tilde{X}_l^{\alpha\beta}(\tau_l)$ and T_τ are Hubbard's operators in the interaction representation and time-ordering operator, respectively. Here, bold and thin lines correspond to $\beta\Lambda_{0\sigma}(i\omega_p, \boldsymbol{q})$ and $\beta\tilde{G}_{0\sigma}(i\omega_p) < F^{\sigma 0} >$, respectively, where $1/\beta = T$ is temperature, $\omega_p = (2p+1)\pi/\beta$, $< F^{\sigma 0} >= 1 - n/2$ is the mean electron-hole probability of site occupancy for the electron concentration n. The unperturbed Green's function [50, 53]

$$\tilde{G}_{0\sigma}(i\omega_p) = \frac{e^{-\lambda^2}}{\beta} \sum_{m=0}^{\infty} \frac{\lambda^{2m}}{m!} \left\{ \frac{f(-\tilde{\mu})}{i\omega_p + \tilde{\mu} + m\omega_0} + \frac{1 - f(-\tilde{\mu})}{i\omega_p + \tilde{\mu} - m\omega_0} \right\} \qquad (3.8)$$

Here, $f(x) = 1/(e^{\beta x} + 1)$ is the Fermi distribution. We suppose that $\omega_0/T >> 1$. A wave line in Fig. 3.1 denotes the Fourier transform

$$t(\boldsymbol{q}) = \sum_{ij} t_{ij} e^{-i\boldsymbol{q}(\boldsymbol{r}_i - \boldsymbol{r}_j)} = -2t(\cos(q_x a) + \cos(q_y a) + 2\alpha \cos(q_x a)\cos(q_y a)) = 2t\varepsilon$$

of the hopping integral, where $\alpha = t_1/t$, t and t_1 are nearest and next nearest hopping integrals, respectively, for a square lattice with the parameter a. We have electron excitations if the parameter $t > 0$ and a hole spectrum otherwise. The replacement $t \to -t$ and $\alpha \to -\alpha$ has no influence on the Fermi level position.

In the approximation Hubbard-I a mean $< F^{\sigma 0} >$ is the self-consistent parameter. Hence, we make the replacement $< F^{\sigma 0} >_0 \to < F^{\sigma 0} >$, where

$$< F^{\sigma 0} >_0 = < X^{\sigma\sigma} + X^{00} >_0 = \frac{Sp(\exp(-\beta \hat{\tilde{H}}_0(X^{\sigma\sigma} + X^{00})))}{Sp(\exp(-\beta \hat{\tilde{H}}_0))} = \frac{e^{\beta\tilde{\mu}} + 1}{1 + 2e^{\beta\tilde{\mu}}} \tag{3.9}$$
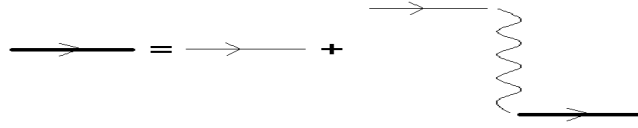
Fig. 3.1. Graphic equation for the Green's function $\Lambda_{0\sigma}(i\omega_n, \boldsymbol{q})$ in the approximation Hubbard-I

The solution of the graphic equation in Fig. 3.1 is

$$\beta \Lambda_{0\sigma}(i\omega_p, \boldsymbol{q}) = \frac{\beta \tilde{G}_{0\sigma}(i\omega_p) < F^{\sigma 0} >}{1 - \beta t(\boldsymbol{q}) \tilde{G}_{0\sigma}(i\omega_p) < F^{\sigma 0} >} \tag{3.10}$$

The retarded Green's functions are obtained by the analytic continuation $i\omega_n \to \Omega + i\delta$ in (3.10) that gives a full information about electron dynamics within the framework of the approximation Hubbard-I. For simplicity, we assume that $T = 0$. By introducing the symbol $w = (\Omega + \tilde{\mu})/\omega_0$ we have for the unperturbed Green's function (3.8)

$$\beta \tilde{G}_{0\sigma}(w\omega_0 - \tilde{\mu}) = \frac{1}{w\omega_0}\left\{ M(1, 1+w, -\lambda^2)\theta(\tilde{\mu}) + M(1, 1-w, -\lambda^2)\theta(-\tilde{\mu})) \right\}, \tag{3.11}$$

where $M(a,b,z)$ and $\theta(x)$ are the confluent hypergeometric function of Kummer [54] and Heaviside step function, respectively.

It is easy to find pole singularities based on Eq. (3.10) that gives the spectrum of electron-hole excitations in the approximation Hubbard-I:

$$-\varepsilon_{cr.m} = -4\left(\frac{t(\boldsymbol{k})}{W}\right)_{cr.m} =$$

$$= -\frac{4(\Omega_{km} + \tilde{\mu})}{< F^{\sigma 0} > M\left(1, 1+\frac{\Omega_{km} + \tilde{\mu}}{\omega_0}, -\lambda^2\right)} = \cos(k_x a) + \cos(k_y a) + 2\alpha \cos(k_x a)\cos(k_y a), \tag{3.12}$$

where bandwidth $W = 8t > 0$. Index m enumerates modes which are solutions of Eq. (3.12). Let $W = 1$, i.e., the frequencies, the chemical potential and all energy parameters are measured in the bandwidth units.

In Fig. 3.2 the k dependence of the resonance frequency Ω_k is presented. The curves were calculated along a nodal direction $k_x = k_y = k/\sqrt{2}$ at $a = 3.814$ Å for different electron

concentrations and the electron-phonon coupling for a bismuth 2212 cuprate with the phonon frequency $\omega_0 = 0.01875$. From the figure it is easy to see that the inclusion of the electron-phonon coupling ($g \neq 0$) results in the appearance of polaron bands, the bandwidth of which is increasing with increasing g. It follows from Eq. (3.12) that kinks on the curve Ω_k versus k are determined by zeros of the function $M\left(1, 1 + \dfrac{\Omega_{km} + \tilde{\mu}}{\omega_0}, -\lambda^2\right)$. Computing real zeros of hypergeometric functions is a complicated mathematical problem which can be solved only numerically [55]. However, one can state that the center of a train of polaron bands and their total bandwidth are determined approximately by parameter λ^2 which counts the number of phonon quanta in the phonon cloud around the localized electron [38], i.e. at $\dfrac{\Omega_{km} + \tilde{\mu}}{\omega_0} \sim -\lambda^2$. For high electron energies, the polaron band is localized and its energy is equal to the energy of phonon quanta in this frequency domain.
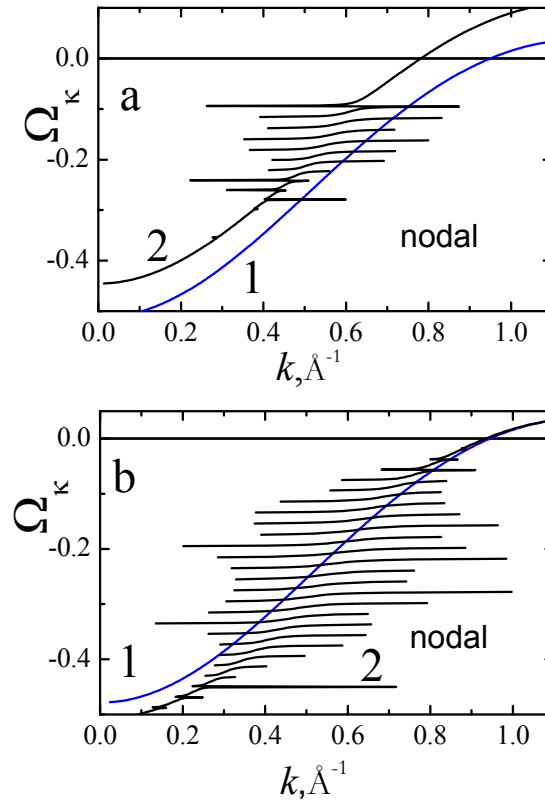
Fig. 3.2. Electron excitation frequency-momentum dispersion along the nodal direction $k_x = k_y = k / \sqrt{2}$ at $a = 3.814$ Å for the bismuth 2212 cuprate with the phonon frequency $\omega_0 = 0.01875$ and (a) $n = 0.9$, $\alpha = 0.1$, $g = 0$, $\tilde{\mu} = 0.136$ and $g = 0.03$, $\tilde{\mu} = 0.092$ (curves 1 and 2, respectively); (b) $n = 0.97$, $\alpha = 0.1$, $g = 0$, $\tilde{\mu} = 0.195358$ and $g = 0.06$, $\tilde{\mu} = 0.018765$ (curves 1 and 2, respectively)

Let us consider the case when polarons are absent, i.e., $\lambda = 0$. Then $M\left(1, 1 + \dfrac{\Omega_{km} + \tilde{\mu}}{\omega_0}, -\lambda^2\right)$ and the electron excitation spectrum consists of a single mode and has the form:

$$\Omega_k + \tilde{\mu} = \frac{-1}{4} < F^{\sigma 0} > \left(\cos(k_x a) + \cos(k_x a) + 2\alpha \cos(k_x a)\cos(k_x a)\right) \qquad (3.13)$$

The spectrum (3.13) has a characteristic feature that radically differentiates the metal state from the state of doped Mott's dielectrics. Indeed, the site probability $<F^{\sigma 0}>$ of the electron-hole state enters in Eq. (3.13). In general case of ordered spins $<F^{\sigma 0}>=1-n/2+\sigma<S^z>$. In a ferromagnetic phase, a mean spin $<S^z>=n/2$ that gives $<F^{+0}>=1$ and $<F^{-0}>=1-n$. Thus, in the limit of a half-filled band at $n\to 1$ we have practically one band in accordance with Eq. (3.13). It is typical for a metal state. On the other hand, in the PM state $<S^z>=0$, $<F^{+0}>=<F^{-0}>=1-n/2$, i.e., the mode (3.13) is two-fold degenerated. This is because in this case two electron liquids with spins up and down coexist in cuprates. These liquids do not interact because their Hamiltonians (3.7) commute. Apparently, the Fermi level should be shifted essentially since the electron liquids are in thermodynamic equilibrium. This factor should be taken into account especially when the metal-theory methods are applied to hole-doped Hubbard's systems. Let us dwell on this problem in detail by the example of calculation of chemical potential value.

To solve the problem, it is necessary to find the electron density of states that is determined by an imaginary part of the lattice Green's function analytically continued to the lower half-plane [56]:

$$G(\mathrm{s},\alpha)=\frac{1}{N}\sum_q \frac{1}{s-i\delta-\cos(k_x a)-(1+2\alpha\cos(k_x a))\cos(k_y a)} \qquad (3.14)$$

The given sum is calculated exactly. Taking into account that $2|\alpha|<1$ one can write the real part of $G(\mathrm{s},\alpha)$ for $s>0$:

$$\mathrm{Re}\,G(s,\alpha)=\begin{cases} \dfrac{2}{|s+2\alpha|}\dfrac{1}{\pi}K\left(\dfrac{2\sqrt{2\alpha s+1}}{|s+2\alpha|}\right), & 2\alpha s+1>0, s>0, s>2(\alpha+1) \\[3mm] \dfrac{1}{\sqrt{2\alpha s+1}}\dfrac{1}{\pi}K\left(\dfrac{|s+2\alpha|}{2\sqrt{2\alpha s+1}}\right), & 2\alpha s+1>0, s>0, 2(\alpha-1)\le s\le 2(\alpha+1) \\[3mm] \dfrac{2}{\sqrt{(2\alpha-s)^2-4}}\dfrac{1}{\pi}K\left(2\sqrt{\dfrac{-2\alpha s-1}{(2\alpha-s)^2-4}}\right), & 2\alpha s+1\le 0, s>0, s>2(\alpha+1) \end{cases} \qquad (3.15)$$

and for the imaginary part:

$$\mathrm{Im}\,G(s,\alpha)=\begin{cases} \dfrac{1}{\sqrt{2\alpha s+1}}\dfrac{1}{\pi}K\left(\dfrac{1}{2}\sqrt{\dfrac{4-(2\alpha-s)^2}{2\alpha s+1}}\right), & 2(\alpha-1)<s<2(\alpha+1) \\[3mm] 0, & otherwise \end{cases} \qquad (3.16)$$

where $K(k)$ is a complete elliptic integral of the first order. We point out that

$$G(-s+i\delta,\alpha)=-G(s-i\delta,-\alpha) \qquad (3.17)$$

Using Eq. (3.17) we write the next symmetric property for a real part of the lattice Green's function:

$$\mathrm{Re}\,G(s,-\alpha)=-\mathrm{Re}\,G(-s,\alpha) \qquad (3.18)$$

The pointed property allows to consider an electron spectrum type of Eq. (3.13) since the determination of the lattice Green's function corresponds to a hole spectrum for s > 0. In what follows, for calculations we use the left part of Eq. (3.18) and keep in mind that values -α and α

correspond to electrons and holes, respectively. Hence, in expressions for lattice Green's functions in the electron spectrum with the parameter α we will take $\operatorname{Re}G(s,-\alpha)$.

The imaginary part required for further calculations is only determined by the analytic continuation in a lower half-plane independently of the replacement $s \to -s$. As a result, we have the next relationship for the imaginary part of $G(\mathrm{s},\alpha)$:

$$\operatorname{Im}G(-s,\alpha) = \operatorname{Im}G(s,-\alpha) \tag{3.19}$$

Eqs. (3.18) and (3.19) allow to obtain real and imaginary parts of $G(\mathrm{s},\alpha)$ for all values of s.

In Fig. 3.3 dependences on the parameter s for real (a) and imaginary (b) parts of the lattice Green's function (3.14) at $\alpha = 0$, -0.4, and 0.4 (curves 1-3, respectively) are presented. From the figure one can see the asymmetry of curves and van Hove singularities for nonzero values of the parameter α that is typical for two-dimensional systems. For $s = 0$ $\operatorname{Re}G(s,\alpha)$ discontinues. It has to give rise to qualitative changes in the spectrum near the point $s = 0$.
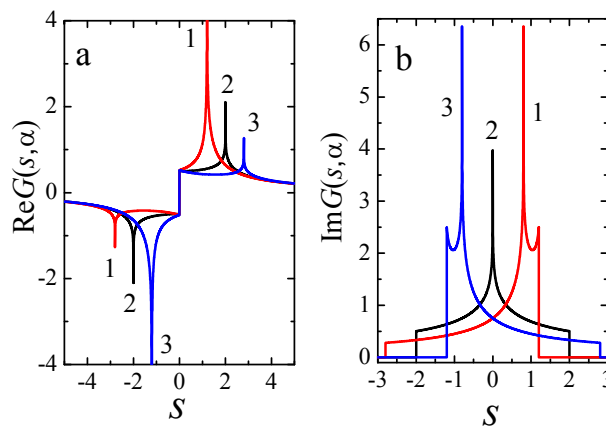
Fig. 3.3. The s-dependences of real (a) and imaginary (b) parts of the lattice Green's function (14) at $\alpha = $ -0.4, 0, and 0.4 (curves 1-3, respectively)

From Eq. (3.15) it follows that for a transition from a hole to an electron consideration the sign of a resonance frequency is changed to the opposite one. The equation for a chemical potential is determined by $\operatorname{Im}G(s,\alpha)$ which does not depend on the hole or electron formalism.

One can make the summation over all wave vectors for any function $V(\varepsilon)$ by the use of a lattice Green's function. Indeed, we have

$$S(\alpha) = \frac{1}{N}\sum_q V(\cos(k_x a) + (1 + 2\alpha\cos(k_x a))\cos(k_y a)) =$$

$$= \frac{1}{N}\sum_q \int_{-2+2\alpha}^{2+2\alpha} \delta(-\varepsilon - \cos(k_x a) - (1 + 2\alpha\cos(k_x a))\cos(k_y a))V(-\varepsilon)\,d\varepsilon = ,$$

$$= \int_{-2-2\alpha}^{2-2\alpha} D_C(\varepsilon,\alpha)V(\varepsilon)\,d\varepsilon$$

where $\delta(x)$ is the Dirac delta function. The electron density of state $D_C(\varepsilon,\alpha)$ has the form:

$$D_C(\varepsilon,\alpha) = \frac{1}{N}\sum_q \delta(\varepsilon - \cos(q_x\,a) - (1 + 2\alpha\cos(q_x\,a))\cos(q_y\,a)) = \frac{1}{\pi}\operatorname{Im}G(\varepsilon,\alpha) \tag{3.20}$$

Apparently, $D_C(\varepsilon,\alpha)$ has nonzero values for ε in the range from -2-2α to 2-2α.

From Eq. (3.10) for the Green's function $\beta\Lambda_{0\sigma}(i\omega_n,\mathbf{q})$ in the approximation Hubbard-I we find a spectral density of the fermion-bosonic system:

$$A_{Hubb.}(\Omega,\mathbf{k}) = -2\beta\operatorname{Im}\Lambda_{0\sigma}(\Omega+i\delta,\mathbf{k}) \tag{3.21}$$

Expanding the denominator of $\Lambda_{0\sigma}(\Omega+i\delta,\mathbf{k})$ in a series in the vicinity of its m-th pole $E_{nk\sigma}$ we get

$$A_{Hubb.}(\Omega,\mathbf{k}) = -2\pi\sum_m \frac{\beta\tilde{G}_{0\sigma}(E_{mk\sigma})}{t(\mathbf{k})\dfrac{d\beta\tilde{G}_{0\sigma}(\Omega)}{d\Omega}}\delta(\Omega-E_{mk\sigma}) \tag{3.22}$$

Here, the sum is over m-th modes $E_{mk\sigma}$ that are implicit solutions of the dispersion in Eq. (3.12). It is evident from Eq. (3.22) that the approximation Hubbard-I describes coherent excitations only. Having calculated spectral density it is easy to find the equation for a chemical potential. Indeed, a mean site occupancy $<X^{\sigma\sigma}>$ of electrons with spin σ is determined by $A_{Hubb.}(\Omega,\mathbf{k})$:

$$<X^{\sigma\sigma}> = \frac{1}{N}\sum_q \frac{1}{2\pi}\int_{-\infty}^{+\infty} f(\Omega)A_{Hubb.}(\Omega,\mathbf{q})d\Omega \tag{3.23}$$

In the work [50] the method of an inverse function was suggested to compute the integrals like those in Eq. (3.23) when an infinite number of modes $E_{nk\sigma}$ cannot be expressed explicitly. For that let us introduce the notation $\beta\tilde{G}_{0\sigma}(\Omega)=F(\Omega)$. The complicated delta function from Eq. (3.22) is simplified by the relationship [53]:

$$W\delta[\Omega-E_{mq\sigma}] = \frac{\delta(\varepsilon-\varepsilon_{cr.m})}{\left|(\Omega-E_{mq\sigma})'\right|_{\varepsilon_{cr.m}}}, \tag{3.24}$$

where $\varepsilon_{cr.m} = \dfrac{4}{F(\Omega)<F^{\sigma 0}>}$ and index m gives the range $m\omega_0 < \Omega < (m+1)\omega_0$ in which the inverse function $F^{-1}(\varepsilon)$ is determined. Apparently, that $E_{nq\sigma}(\varepsilon) = F^{-1}\left(\dfrac{4}{\varepsilon<F^{\sigma 0}>}\right)$ and $E_{nq\sigma}(\varepsilon_{cr.m}) = \Omega$. Taking into account the differentiation of the inverse function $F^{-1}(x)$ we have

$$\left|(\tilde{\Omega}-\tilde{E}_{mq\sigma}(\varepsilon))'\right|_{\varepsilon=\varepsilon_{cr.m}} = \frac{4}{\varepsilon^2<F^{\sigma 0}>\left|F'(\varepsilon)\right|}\Bigg|_{\varepsilon=\varepsilon_{cr.m}} \tag{3.25}$$

Substituting (3.25) in (3.24) and (3.24) in (3.23) with an account for $\left|F'(\Omega)\right|/F'(\Omega) = -1$ we obtain

$$<X^{\sigma\sigma}> = \sum_{m=0}^{\infty}\int_{m\omega_0}^{(m+1)\omega_0} d\Omega f(\Omega)\int_{-2-2\alpha}^{2-2\alpha} d\varepsilon\varepsilon D_c(\varepsilon,\alpha)\delta(\varepsilon-\varepsilon_{cr.m})F(\Omega)<F^{\sigma 0}>,$$

that gives the next expression for the mean site occupancy with the electron-phonon attraction:

$$<X^{\sigma\sigma}> = 4\int_{-\infty}^{+\infty} d\Omega f(\Omega)D_c\left(\frac{4}{F(\Omega)<F^{\sigma 0}>},\alpha\right) \tag{3.26}$$

At the temperature $T=0$ in the PM phase $<X^{\sigma\sigma}> = n/2$ and from Eq. (3.26) we obtain the equation for a chemical potential $\tilde{\mu}$:

$$\frac{n}{2} = 4\omega_0\int_{-\infty}^{\tilde{\mu}/\omega_0} dwD_c\left(\frac{4w\omega_0}{M(1,1+w,-\lambda^2)(1-0.5n)},\alpha\right) \tag{3.27}$$

From (3.27) it follows that in the absence of the electron-phonon interaction the chemical potential is expressed as [50]:

$$\tilde{\mu} = \frac{2-n}{8} I^{-1}\left(\frac{n}{2-n}, \alpha\right),\qquad(3.28)$$

where $I^{-1}(x)$ is the inverse function of $I(x,\alpha) = \int_{-2-2\alpha}^{x} D_C(\varepsilon,\alpha)d\varepsilon$. In particular, we have $I^{-1}(1,\alpha) = 2-2\alpha$ and $\tilde{\mu} = \frac{1}{4}(1-\alpha)$ for $n = 1$. Thus, in the PM phase the level of a chemical potential tends to the middle of the upper half of a nearly half-filled band but not to the band edge as is required for a normal metal. This correlation effect narrows the lower Hubbard's band by reasons of the existence of two spin-up and spin-down electron liquids avoiding one another. For the first time this phenomena was observed in [49].

In Fig. 3.4 concentration dependencies of the effective chemical potential $\tilde{\mu}$ evaluated from Eq. (3.27) at $g = 0$ for different values of α (a), at $\alpha = 0$ for different values g (b) and the phase diagram in the coordinates g - n for $\alpha = 0$ and 0.1 (curves 1 and 2, respectively) are presented. From Fig. 3.4a it is easy to see that for $n > 0.87$ the chemical potential is increased with decreased α. For $n < 0.87$ in the area of positive $\tilde{\mu}$ the inverse trend is observed. From Fig. 3.4b one sees that with increasing g the area of the PM phase narrows and for $g = 0.072$ a dielectric state is realized (see Fig. 3.4c). Thus, the effective chemical potential $\tilde{\mu}$ is decreased up to zero with increasing g, i.e., the Fermi level is shifted to the band centre.

Fig. 3.4. Concentration dependences of the effective chemical potential $\tilde{\mu}$ in the approximation Hubbard-I without and with an account for polaron excitations for $\omega_0 = 0.01875$ at (a) $g = 0$ and $\alpha = 0.4, 0.3, 0.2, 0.1, 0, -0.1, -0.2, -0.3$ and -0.4 (curves 1-9, respectively); (b) $\alpha = 0$ and $g = 0$, 0.03, 0.04, 0.05 and 0.06 (curves 1-5, respectively); (c) phase diagrams for $\alpha = 0$ and 0.1 (curves 1 and 2, respectively)

In Fig. 3.5 the critical values of $-\varepsilon_{ck}$ from Eq. (3.12) versus n on the Fermi level when $\Omega_{km} = 0$ at $g = 0.03, 0.05$ and 0.06 are shown. One sees that near the PM phase boundary when $\tilde{\mu} \sim 0$ the antibonding orbitals of second-nearest neighbors become important. That is why in this

area of the electron concentration the Fermi surface has a hole origin with the center in the Γ point (see Fig.6). As n is increased, the electron Fermi surface arises. Fig. 3.6 reflects the topology dependence of the electron Fermi surface on both electron-phonon attraction and doping. One shrinks as doping decreases. With increasing the constant of the electron-phonon interaction g this shrink decreases. Also, when the hole doping goes to zero the Fermi surface does not vanish. Hence, the transition to a dielectric state implies discontinuous disappearance of the Fermi surface.
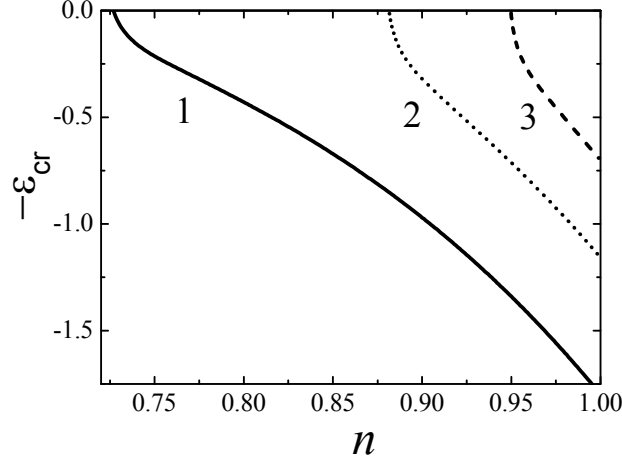
Fig. 3.5. The critical values of $-\varepsilon_{cr.}$ versus n from Eq. (3.12) on the Fermi level at $\alpha = 0.1$, $g = 0.03$, 0.05 and 0.06 (curves 1–3, respectively)
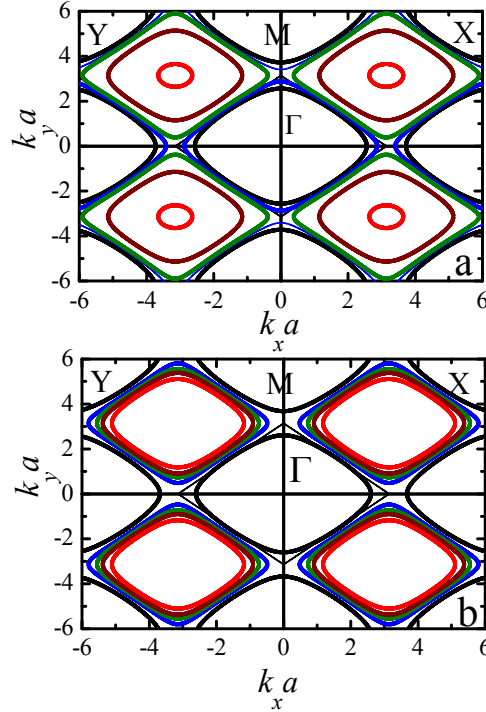
Fig. 3.6. Fermi surfaces in the approximation Hubbard-I square of which is decreased increase an electron concentration n at $\alpha = 0.1$ and (a) $g = 0.03$ and $n = 0.727$, 0.74, 0.76, 0.85 and 0.99 ($\tilde{\mu} = 0$, 0.004, 0.011, 0.057 and 0.171, respectively); (b) $g = 0.06$ and $n = 0.95$, 0.96, 0.97, 0.98 and 0.999 ($\tilde{\mu} = 0.0004$, 0.0095, 0.0188, 0.0285 and 0.0478, respectively)

3.3. Effects of *d*-electron inelastic scattering

3.3.1. Green's function and self-energy

In the previous subsection a detailed consideration of the approximation Hubbard-I was presented. Although this approach does not describe electron scattering it may be a good start to account for correlation effects.

To find the time-ordered Green's function we will consider the contributions of the one-loop diagrams only. It is the first non-vanishing approximation of the time-dependent perturbation theory with respect to the inverse effective radius of the interaction. Since the phonon and fermion subsystems are independent, we have

$$\Lambda_{0\sigma}(p\tau_1, q\tau_m) = - < T_\tau \tilde{X}_p^{0\sigma}(\tau_p) \tilde{X}_q^{\sigma 0}(\tau_q) >= -U_{ep}(\tau_p - \tau_q) < T_\tau X_p^{0\sigma}(\tau_p) X_q^{\sigma 0}(\tau_q) >,$$

where the first factor $U_{ep}(\tau_p - \tau_q) = < T_\tau Y_p(\tau_p) Y_q^+(\tau_q) >_{\hat{H}_b}$ is the unperturbed time-ordered uniform bosonic Green's function for the system of Einstein phonons. The Fourier transform of $U_{ep}(\tau_p - \tau_q)$ is

$$U_{ep}(i\omega_n) = \frac{1}{\beta} \sum_{m=-\infty}^{+\infty} \frac{\psi_m}{i\omega_n + m\omega_0}, \tag{3.29}$$

where $\psi_m = 2d_m \sinh(\beta m\omega_0 / 2)$ $\omega_n = 2n\pi / \beta$, $d_m = e^{-\lambda^2(2B+1)} I_m(2\lambda^2 \sqrt{B(B+1)})$. $I_m(x)$ are Bessel functions of a complex argument, $B = n(\omega_0)$. $n(x) = 1 / (\exp(\beta x) - 1)$ is the Bose distribution. In the second factor, external Hubbard's operators are not multiplied by bosonic operators $Y_p(\tau_p)$ but inner ones are unitary transformed. That is why at first the normalized Green's function is conveniently considered in the form

$$H_{0\sigma}(p\tau_1, q\tau_m) = \frac{\Lambda_{0\sigma}(p\tau_1, q\tau_m)}{U_{ep}(\tau_p - \tau_q)} \tag{3.30}$$

By $\Sigma_\sigma(i\omega_n)$ we denote a self-energy part of the total Green's function $\Lambda_{0\sigma}(i\omega_n, \mathbf{k})$. Then one can write the Dyson's equation for $\Lambda_{0\sigma}(i\omega_n, \mathbf{k})$ in the next form:

$$\Lambda_{0\sigma}(i\omega_n, \boldsymbol{k}) = \Sigma_\sigma(i\omega_n) + \beta t(\boldsymbol{k}) \Sigma_\sigma(i\omega_n) \Lambda_{0\sigma}(i\omega_n, \boldsymbol{k})$$

Apparently, the self-energy is expressed as

$$\Sigma_\sigma(i\omega_n) = \sum_{\omega_{n1}} U_{ep}(i\omega_n - i\omega_{n_1}) H_{0\sigma}(i\omega_{n_1}), \tag{3.31}$$

where $H_{0\sigma}(i\omega_{n_1})$ is the Fourier transform of the function $H_{0\sigma}(p\tau_1, q\tau_m)$. The poles are supposed to be known. Then it is easy to evaluate the frequency summation in Eq. (3.31) that gives

$$\Sigma_\sigma(i\omega_n) = \beta \operatorname{Res}\left[f(\omega) G_{ph.}(i\omega_n - \omega) H_{0\sigma}(\omega)\right]\Big|_{G_{ph.}} + \beta \operatorname{Res}\left[f(\omega) G_{ph.}(i\omega_n - \omega) H_{0\sigma}(\omega)\right]\Big|_{H_{0\sigma}}, \tag{3.32}$$

where the residues are taken as poles of the corresponding Green's functions.

We use the effective self-consistent field in the approximation Hubbard-I as a start. In this case, an account should be taken over all inner convolutions of adjacent unitary transformed Hubbard's operators. For a dressed line of the hopping integral $B_{\sigma 0}(\tau_j - \tau_i, \boldsymbol{R}_j - \boldsymbol{R}_i)$ with the Fourier transform $B_{\sigma 0}(i\omega_n, \boldsymbol{k})$ one can write the graphic equation in the form as in Fig. 3.7. Here, thin and bold wave lines are $t(\boldsymbol{k})$ and $B_{\sigma 0}(i\omega_n, \boldsymbol{k})$, respectively. The thin straight arrow corresponds to $\tilde{G}_{0\sigma}(i\omega_n)$ from Eq. (3.8).
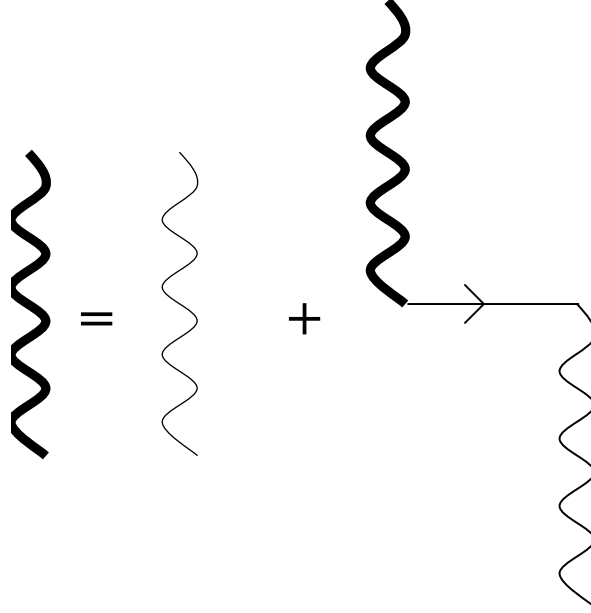
Fig. 3.7. Graphic equation for the effective hopping integral $B_{\sigma 0}(i\omega_n, \boldsymbol{k})$

The solution of this equation is trivial and has a form:

$$\beta B_{\sigma 0}(i\omega_n, \boldsymbol{k}) = \frac{\beta t(\boldsymbol{k})}{1 - \beta t(\boldsymbol{k})\tilde{G}_{0\sigma}(i\omega_n) < F^{\sigma 0} >} \tag{3.33}$$

Then in this approach two main terms have to be added to the unperturbed Green's function $G_{0+}(\tau_p - \tau_q) < F^{+0} >_0$:

$$\int_0^\beta d\tau_1 \int_0^\beta d\tau_2 \frac{1}{N} \sum_{ij\boldsymbol{q}} \frac{1}{\beta} B_{+0}(\tau_1 - \tau_2, \boldsymbol{q}) e^{i\boldsymbol{q}(\boldsymbol{R}_l - \boldsymbol{R}_m)} < T_\tau X_p^{0+}(\tau_p) X_q^{+0}(\tau_q) \mathrm{Y}_l^+(\tau_1) X_l^{+0}(\tau_1) \mathrm{Y}_m(\tau_2) X_m^{0+}(\tau_2) >_0$$

and

$$\int_0^\beta d\tau_1 \int_0^\beta d\tau_2 \frac{1}{N} \sum_{ij\boldsymbol{q}} \frac{1}{\beta} B_{-0}(\tau_1 - \tau_2, \boldsymbol{q}) e^{i\boldsymbol{q}(\boldsymbol{R}_l - \boldsymbol{R}_m)} < T_\tau X_p^{0+}(\tau_p) X_q^{+0}(\tau_q) \mathrm{Y}_l^+(\tau_1) X_l^{-0}(\tau_1) \mathrm{Y}_m(\tau_2) X_m^{0-}(\tau_2) >_0$$

Using the Vick's theorem for Hubbard's operators and taking into account independent averaging of a product of the bosonic operators $\mathrm{Y}_m(\tau_2)$ we evaluate these integrals. In Fig. 3.8 the self-energy terms in the form to linked diagrams (points in Fig. 3.8 denote index convolutions) are presented generally for $\sigma = \pm$. In the figure the dashed line with an arrow corresponds to the bosonic unperturbed Green's function $G_{+-}(i\omega_n) = 1/(\beta(i\omega_n + \varepsilon_+ - \varepsilon_-))$ where $\varepsilon_+ - \varepsilon_- = -h$ and h is the effective exchange field.
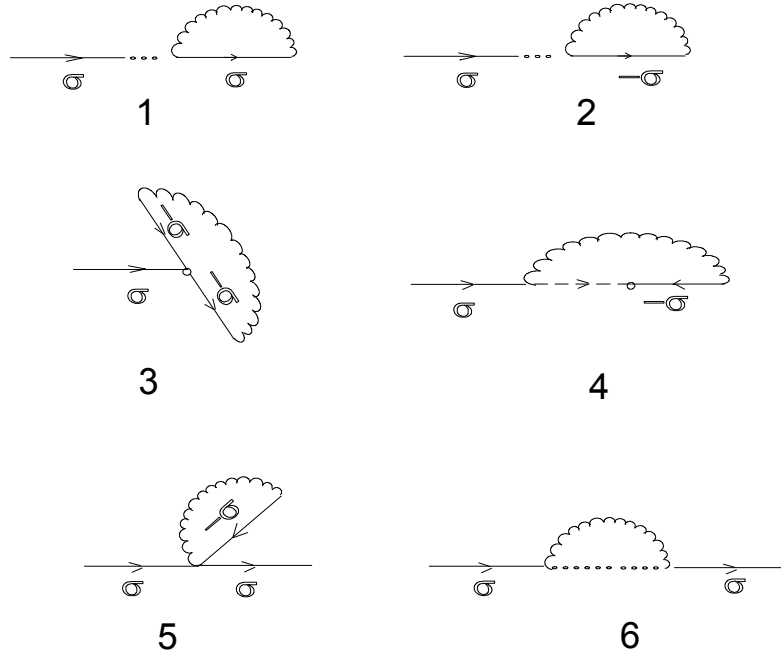
Fig. 3.8. Diagrams for the self - energy $\Sigma_\sigma(i\omega_n)$ in the first approximation of the perturbation theory [50]

Let us write the analytic expressions for diagrams 1–3:

1) $-\beta\delta\tilde{\mu}_\sigma\partial_\sigma < F^{\sigma 0} >_0 G_{0\sigma}(i\omega_n) = -\dfrac{1}{N}\sum_{\mathbf{q}n_1}\beta B_{\sigma 0}(i\omega_{n_1},\mathbf{q})\tilde{G}_{0\sigma}(i\omega_{n_1})\partial_\sigma < F^{\sigma 0} >_0 G_{0\sigma}(i\omega_n)$

2)
$$-\beta\delta\tilde{\mu}_{-\sigma}\partial_{-\sigma} < F^{\sigma 0} >_0 G_{0\sigma}(i\omega_n) =$$
$$= -\dfrac{1}{N}\sum_{\mathbf{q}n_1}\beta B_{-\sigma 0}(i\omega_{n_1},\mathbf{q})\tilde{G}_{0-\sigma}(i\omega_{n_1})\partial_{-\sigma} < F^{\sigma 0} >_0 G_{0\sigma}(i\omega_n)$$

3)
$$\tilde{\nu}_{-\sigma} < F^{-\sigma 0} >_0 G_{0\sigma}(i\omega_n) =$$
$$= \dfrac{1}{N}\sum_{\mathbf{q}n_1 m_1}\beta B_{-\sigma 0}(i\omega_{n_1},\mathbf{q})U_{ep}(i\omega_{n_1} - i\omega_{m_1})\left[G_{0-\sigma}(i\omega_{m_1})\right]^2 < F >_0 G_{0\sigma}(i\omega_n)$$

Here, the derivative $\partial_\sigma < F^{\sigma 0} >_0 = \partial < F^{\sigma 0} >_0 / \partial(-\beta\varepsilon_\sigma)$ and $\varepsilon_\sigma = -\tilde{\mu}$. These diagrams are proportional to the external unperturbed Green's function $G_{0\sigma}(i\omega_n) = 1/(\beta(i\omega_n + \tilde{\mu}))$. One can factor out and add $G_{0\sigma}(i\omega) < F^{+0} >_0$. Then in parentheses we obtain a series expansion for an average $< F^{\sigma 0} >= 1 - n/2$. The series was considered in the work [32]. It gives an equation for a chemical potential $\tilde{\mu}$. Therefore, the sum of diagram terms 1-3 and $G_{0\sigma}(i\omega) < F^{+0} >_0$ gives a contribution $G_{0\sigma}(i\omega_n)(1 - n/2)$ to $H_{0\sigma}(i\omega_{n_1})$.

Contribution from the diagram 5 to $H_{0\sigma}(i\omega_{n_1})$ is written as

5) $-\beta\delta\tilde{\mu}_{-\sigma} < F^{\sigma 0} >_0 G_{0\sigma}^2(i\omega_n)$.

One can prove that diagrams 4 and 6 only differ by factors $< X^{\sigma\sigma} >_0$ and $< F^{\sigma 0} >_0 (1- < F^{\sigma 0} >_0)$, respectively, i.e., one writes 4)+6)= $K_0(I_1(i\omega_n) + I_2(i\omega_n))G_{0\sigma}^2(i\omega_n)$, where $K_0 =< X^{\sigma\sigma} >_0 + < F^{\sigma 0} >_0 (1- < F^{\sigma 0} >_0) = 3/4$ at $T = 0$. Evaluating the sum over inner discrete frequencies by means of the previously considered method of an inverse function we write the final expression for $H_{0\sigma}(i\omega_n)$:

$$H_{0\sigma}(i\omega_n) = G_{0\sigma}(i\omega_n)(1-\mathrm{n}/2) + K_0(I_1(i\omega_n) + I_2(i\omega_n))G_{0\sigma}^2(i\omega_n) - \beta\delta\tilde{\mu}_{-\sigma} < F^{\sigma 0} >_0 G_{0\sigma}^2(i\omega_n), \quad (3.34)$$

where

$$I_1(i\omega_n) = \int\limits_{-\infty}^{+\infty} d\Omega \tilde{D}_C(\Omega,\alpha) \frac{4\beta f(\Omega)}{\left[F(\Omega) < F^{\sigma 0} >\right]^2} \beta U_{ep}(\Omega - i\omega_n)$$

$$I_2(i\omega_n) = \frac{1}{N} \sum\limits_{\boldsymbol{q}m_1=-\infty}^{+\infty} \frac{\beta t(\boldsymbol{q})(n(m_1\omega_0) + 1)\psi_{m_1}}{1 - t(\boldsymbol{q}) < F^{\sigma 0} > \beta\tilde{G}_{0\sigma}(i\omega_n - m_1\omega_0)} \quad (3.35)$$

where $\tilde{D}_C(\Omega,\alpha) = D_C\left(\dfrac{4}{F(\Omega) < F^{\sigma 0} >},\alpha\right)$. It follows from presented above expressions that diagrams 4 and 6 describe electron-polaron and electron-electron scatterings only. The rest of diagrams renormalizes the excitation spectrum. At $T \sim 0$ the factor $(n(m_1\omega_0) + 1)\psi_{m_1}$ in $I_2(i\omega_n)$ may be simplified. It easy to find that $\psi_m \approx \tilde{\psi}(|m|)sign(m)$, where $\tilde{\psi}(m) = e^{-\lambda^2}\dfrac{\lambda^{2m}}{m!}$, $sign(0) = 0$ and $(n(m_1\omega_0) + 1)\psi_{m_1} \approx \tilde{\psi}(|m|)\theta(m)$. After analytic continuation $i\omega_n \to \omega + i\delta$ a real part of the integral $I_1(\omega)$ is evaluated numerically as the Cauchy principal value. The imaginary part of $I_1(\omega)$ is easily calculated since $\mathrm{Im}[\beta U_{ep}(\Omega - \omega - i\delta)]$ gives the Dirac delta function.

To obtain the final expression for the self-energy $\Sigma_\sigma(i\omega_n)$ it is necessary to substitute $H_{0\sigma}(i\omega_n)$ in Eq. (3.32). As a result, in the limit $T \sim 0$ we have

$$\Sigma_\sigma(i\omega_n) = \mathrm{P}_0(i\omega_n) + \mathrm{P}_5(i\omega_n) + \mathrm{P}_{46}(i\omega_n) \quad (3.36)$$

with

$$\mathrm{P}_0(\omega) = \frac{1 - 0.5n}{\beta(\omega + \tilde{\mu})} M\left(1,1 + \frac{\omega + \tilde{\mu}}{\omega_0}, -\lambda^2\right)$$

$$\mathrm{P}_5(\omega) = - < F^{\sigma 0} >_0 \frac{1}{\beta}\delta\mu_{-\sigma} \sum\limits_{m=0}^{\infty} e^{-\lambda^2}\frac{\lambda^{2m}}{m!}\frac{1}{(\omega + m\omega_0 + \tilde{\mu})^2} = -\frac{1}{\beta}\frac{J_5(\omega)}{(\omega + \tilde{\mu})^2} \quad (3.37)$$

$$\mathrm{P}_{46}(\omega) = J_1(\omega) + J_2(\omega) + J_3(\omega)$$

Here, $w(\omega) = \dfrac{\omega + \tilde{\mu}}{\omega_0}$ and $J_5(\omega) =< F^{\sigma 0} >_0 \delta\mu_{-\sigma} e^{-\lambda^2} {}_2F_2(w, w; 1 + w, 1 + w; \lambda^2)$, where ${}_2F_2(w, w; 1 + w, 1 + w; \lambda^2)$ is the generalized hypergeometric function. For $T = 0$ we have $< F^{\sigma 0} >_0 = 1/2$ and

$$J_1(\omega) = \sum\limits_{m_1,m_2=-\infty}^{+\infty} K_0 \frac{1}{\beta^2}\frac{\psi_{m_1}\psi_{m_2}(n(m_1\omega_0) - n(m_2\omega_0))}{(\omega + i\delta + m_1\omega_0 + \tilde{\mu})^2} \int\limits_{-\infty}^{+\infty} d\Omega \frac{Z(\Omega, n, \alpha)f(\Omega)}{\Omega - \omega - i\delta + (m_2 - m_1)\omega_0}, \quad (3.38)$$

where

$$Z(\Omega, n, \alpha) = \tilde{D}_C\left(\Omega, -\alpha\right)\frac{4\beta}{\left(\beta\tilde{G}_{0\sigma}(\Omega) < F^{\sigma 0} >\right)^2}$$

$$J_2(\omega) = \sum_{m_1,m_2=-\infty}^{+\infty} K_0 \frac{1}{\beta^2} \frac{\psi_{m_1}\psi_{m_2}(n(m_1\omega_0) - n(m_2\omega_0))}{(\omega + i\delta + m_1\omega_0 + \tilde{\mu})^2} \cdot \frac{1}{N}\sum_q \frac{\beta t(q)(n([m_2 - m_1]\omega_0) + 1)}{1 - t(q) < F^{\sigma 0} > \beta\tilde{G}_{0\sigma}(\omega + i\delta - [m_2 - m_1]\omega_0)} \quad (3.39)$$

$$J_3(\omega) = \sum_{m_1,m_2=-\infty}^{+\infty} K_0 \frac{1}{\beta^2} \frac{\psi_{m_1}\psi_{m_2}(n(m_2\omega_0) + f(-\tilde{\mu}))}{(\omega + i\delta + m_1\omega_0 + \tilde{\mu})^2}\int_{-\infty}^{+\infty} d\Omega \frac{Z(\Omega, n, \alpha)f(\Omega)}{\Omega + m_2\omega_0 + \tilde{\mu}} \cdot \left[1 + \frac{\omega + m_1\omega_0 + \tilde{\mu}}{\Omega + m_2\omega_0 + \tilde{\mu}}\right] \quad (3.40)$$

$$\delta\mu_{-\sigma} = \int_{-\infty}^{+\infty}\frac{1}{\beta}Z(\Omega, n, \alpha)\beta\tilde{G}(\Omega)f(\Omega) \quad (3.41)$$

In Eq. (3.39) for $m_1 = m_2$ the uncertainty is observed. Thus for $m_1 -> m_2$ we get the function

$$J_0(\omega) = \frac{K_0 e^{-2\lambda^2}}{\beta(\omega + i\delta + \tilde{\mu})^2}\frac{1}{N}\sum_{qm_1=-\infty}^{+\infty}\frac{1}{1 - t(q) < F^{\sigma 0} > \beta\tilde{G}_{0\sigma}(\omega + i\delta)}, \quad (3.42)$$

that is determined by the lattice Green's function $G(s, \alpha)$. And so, for the sum (3.39) the term with $m_1 = m_2$ is excluded. It is necessary to add the expression (3.42) to Eq. (3.39) instead of this abnormal term.

One writes for the imaginary part $J_1(\omega)$ at $T = 0$

$$\mathrm{Im}\, J_1(\omega) = \frac{4\pi K_0}{\beta(1 - 0.5n)^2}\sum_{m=-\infty}^{\infty} R(\omega, \tilde{\mu}, m)\omega_0^2\varphi\left(\frac{\omega + \tilde{\mu}}{\omega_0}, n\right)\theta(m\omega_0 - \omega), \quad (3.43)$$

where

$$\varphi(\mathrm{w}, n) = D_C\left(\frac{4\,\mathrm{w}\,\omega_0}{M(1, 1 + \mathrm{w}, -\lambda^2)(1 - 0.5n)}, -\alpha\right)\frac{\mathrm{w}^2}{M^2(1, 1 + \mathrm{w}, -\lambda^2)} \quad (3.44)$$

$$R(\omega, \tilde{\mu}, m) = \sum_{m_1=-\infty}^{+\infty}\frac{\{\tilde{\psi}(|m + m_1|)\tilde{\psi}(|m_1|)sign(m + m_1)\theta(m_1) - \tilde{\psi}(|m_1|)\tilde{\psi}(m + |m_1|)sign(m_1)\theta(m + m_1)\}}{(\omega + \tilde{\mu} + m_1\omega_0)^2}$$

Notice that $R(\omega, \tilde{\mu}, m) = 0$ at $m = 0$. The real part of $J_1(\omega)$ and the complex function $J_2(\omega + i\delta)$ are expressed as

$$\mathrm{Re}\, J_1(\omega) = \frac{1}{\beta}K_0\sum_{m=0}^{\infty} R(\omega, \tilde{\mu}, m)I_{11}(\omega, n, m) \quad (3.45)$$

$$J_2(\omega) = \frac{K_0}{\beta}\sum_{m=-\infty}^{+\infty} R(\omega, n, m)S_2(\omega, n, \alpha, m). \quad (3.46)$$

Here,

$$I_{11}(\omega, n, m) = \frac{4\omega_0^2}{(1 - 0.5n)^2}\left\{\sum_{k=-\infty}^{-1} V.p.\int_k^{k+1} d\,\mathrm{w}\frac{\varphi(\mathrm{w})}{\mathrm{w} - \left(\frac{\omega + \tilde{\mu}}{\omega_0} + m\right)} + V.p.\int_0^{\tilde{\mu}/\omega_0} d\,\mathrm{w}\frac{\varphi(\mathrm{w})}{\mathrm{w} - \left(\frac{\omega + \tilde{\mu}}{\omega_0} + m\right)}\right\} \quad (3.47)$$

$$S_2(\omega, n, \alpha, m) = \frac{\omega + \tilde{\mu} - m\omega_0}{(1 - 0.5n)M\left(1, 1 + \frac{\omega + \tilde{\mu}}{\omega_0} - m, -\lambda^2\right)}\{-1 + (\omega + \tilde{\mu} - m\omega_0)S_3(\omega, n, \alpha, m)\}, \quad (3.48)$$

$$S_3(\omega,n,\alpha,m) = \frac{4}{(1-0.5n)M\left(1,1+\dfrac{\omega+\tilde{\mu}}{\omega_0}-m,-\lambda^2\right)}\,G^*\left(\frac{4\omega_0\left[\dfrac{\omega+\tilde{\mu}}{\omega_0}-m\right]}{(1-0.5n)M\left(1,1+\dfrac{\omega+\tilde{\mu}}{\omega_0}-m,-\lambda^2\right)},\alpha\right),\quad (3.49)$$

where the integrals are evaluated numerically as a Cauchy principal value and theintegrand $\varphi(w,n)$ is determined by (3.44). $G^*(s,\alpha)$ is the conjugate lattice Green's function.

Thus Eqs. (3.36)-(3.49) contain the total information about spectral properties of the cuprate d-electron subsystem with an electron-phonon interaction. Hereafter a numerical solution of the previously obtained equations is given in order to analyze both the excitation spectrum and the dissipation caused by electron-electron and electron-polaron interactions. Finally, let us write the contribution $P_{46}(\omega)$ in the form:

$$P_{46}(\omega) = J_0(\omega) + J_1(\omega) + J_2(\omega) + J_3(\omega),$$

where $R(\omega,\tilde{\mu},m) = 0$ for $m = 0$.

3.3.2. Electron spectrum in the absence of the electron-phonon interaction

In this subsection, we will discuss dynamical properties of electrons for the temperature $T = 0$ in the absence of electron phonon interaction, i.e., at $g = 0$. Before we proceed further, we evaluate numerically the chemical potential $\tilde{\mu}$. In the works [32, 57] an approach to calculate the chemical potential versus the band filling was presented. In particular, in the reference [32] we obtained Eq. (3.51) for $\tilde{\mu}$ versus n in the PM-2 state with the nearest hopping energy. One can generalize this equation when the influence of next-nearest neighbors is taken into account, i.e., for $\alpha \neq 0$:

$$\tilde{\mu} = \frac{2-n}{8}I^{-1}\left(1-\frac{1}{2}(1-n)(2-n),\alpha\right), \quad (3.50)$$

where $I^{-1}(x,\alpha)$ is the inverse function (see Eq. (3.28)). Similarly, the term $\delta\mu_\sigma$ of the diagram 5 in Fig. 3.7 is

$$\delta\mu_\sigma = E\left(I^{-1}\left(1-\frac{1}{2}(1-n)(2-n),\alpha\right)\right), \quad (3.51)$$

where

$$E(x,\alpha) = \int_{-2-2\alpha}^{x} x D_C(x,\alpha)dx \quad (3.52)$$

In Fig. 3.9a concentration dependencies of the chemical potential at α = -0.4, -0.3, -0.2, -0.1, 0, 0.1, 0.2, 0.3 and 0.4 (curves 1-9, respectively) are presented. In Fig. 3.9b an area of the PM-2 phase existence in coordinates α-n is demonstrated. From Eq. (3.50) it follows that the chemical potential $\tilde{\mu}$ of the filled band coincides with the solution (3.28) within the approximation Hubbard-I.

The spectral density function is expressed as

$$A(\boldsymbol{k},\omega) = -\frac{1}{\pi}\frac{(\omega+\tilde{\mu})^4\beta\,\mathrm{Im}\Sigma(\omega)}{\left[(\omega+\tilde{\mu})^2-t(\boldsymbol{k})(\omega+\tilde{\mu})^2\beta\,\mathrm{Re}\Sigma(\omega)\right]^2+(\omega+\tilde{\mu})^2t^2(\boldsymbol{k})\left[(\omega+\tilde{\mu})^2\beta\,\mathrm{Im}\Sigma(\omega)\right]^2} \quad (3.53)$$

In view of (3.32) at $T = 0$ and $K_0 = 3/4$ we have

$$(\omega + \tilde{\mu})^2 \beta \operatorname{Re}\Sigma(\omega) = (\omega + \tilde{\mu})\left[1 - 0.5n - \frac{3}{4(1 - 0.5n)}\right] + \frac{3(\omega + \tilde{\mu})^2}{(1 - 0.5n)^2} \operatorname{Re}G\left(\frac{4(\omega + \tilde{\mu})}{1 - 0.5n}, -\alpha\right) - 0.5\delta\mu_\sigma$$

(3.54)

$$(\omega + \tilde{\mu})^2 \beta \operatorname{Im}\Sigma(\omega) = -\frac{3(\omega + \tilde{\mu})^2}{(1 - 0.5n)^2} \pi D_C\left(\frac{4(\omega + \tilde{\mu})}{1 - 0.5n}, -\alpha\right)$$

Taking into account Eq. (3.54) it is easy to write the dispersion equation

$$-\varepsilon_{cr.}(\Omega_k) = \cos(k_x a) + \cos(k_x a) + 2\alpha\cos(k_x a)\cos(k_x a) = -\frac{4(\Omega_k + \tilde{\mu})^2}{(\Omega_k + \tilde{\mu})^2 \beta \operatorname{Re}\Sigma(\Omega_k)}$$

(3.55)
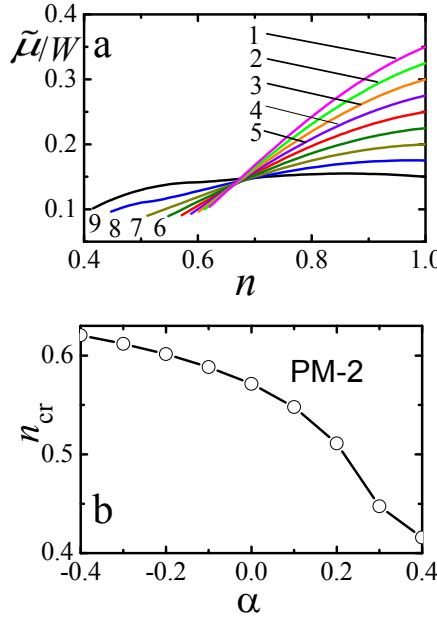
Fig. 3.9. (a) Concentration dependencies of the chemical potential in the PM-2 phase with $g = 0$ and α = -0.4, -0.3, -0.2, -0.1, 0, 0.1, 0.2, 0.3 and 0.4 (curves 1-9, respectively); (b) the phase diagram in the α-n plane at $T = 0$

From Eq. (3.55) it follows that now the excitation spectrum depends on the real part $\operatorname{Re}G(s, -\alpha)$ of the lattice Green's function (3.15) that has both two singularities at the edges of an unperturbed electron band, i.e., at $s = s_L = -2(1+\alpha)$ and $s = s_R = 2(1-\alpha)$. Also, there is one breakdown at $s = 0$ (see Fig. 3.3a that corresponds to the frequency $\Omega_k = -\tilde{\mu}$). These circumstances cause radical changes to the spectrum of the electron excitations in comparison with the approximation Hubbard-I.

In Fig. 3.10 resonance frequencies Ω_k along the nodal direction for bismuth 2212 cuprates at different electron band filling are shown. In Fig. 3.10 the values of n correspond to the most typical points of function $-\varepsilon_{cr.}(n)$ from (3.55) at $\Omega_k = 0$ (the Fermi level) to be shown in the inset to the figure. So, at $\alpha = 0$ (curve 1 in the inset) the curve $-\varepsilon_{cr.}(n)$ tends to own lower edge -2 at $n = 0.7$. For this value of n, a small gap arises on the Fermi level. It has a correlation origin that is reflected in Fig. 3.10a (curve 2). Such gap (see Fig. 3.10, curves 1 and 3) is absent at other values of n. The function $-\varepsilon_{cr.}(n)$ does not approach the edge value -2-2α with the increased influence of the next-nearest neighbours where a paramagnetic phase is realized. In this case, a gap does not appear at the Fermi level for all possible values of n (see Fig. 3.10b).

The kinks in the dispersion Ω_k at $\Omega_k = \omega_L = -0.531$ and $\Omega_k = \omega_R = 0.019$ for n = 0.9 (curve 3) are determined by the equation

$$\frac{4(\omega + \tilde{\mu})}{1 - 0.5n} - s = 0 \qquad (3.56)$$

at $s = s_L$ and s_R, respectively. From this equation, we obtain the lower $\omega_L = -\tilde{\mu} - 0.5(1+\alpha)(1-0.5n)$ and the upper $\omega_L = -\tilde{\mu} + 0.5(1-\alpha)(1-0.5n)$ edges of the incoherent spectrum the bandwidth $\Delta\omega_{LR} = 1 - 0.5n$ of which is determined only by the electron concentration.
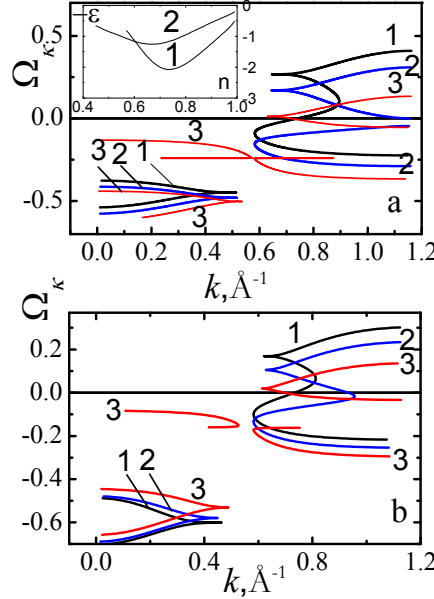
Fig. 3.10. Electron excitation frequency-momentum dispersions for bismuth 2212 cuprates (the lattice constant a = 3.814 Å) along the nodal direction without electron-phonon interaction: (a) α = 0, n = 0.571 ($\tilde{\mu}$ = 0.090), n = 0.7 ($\tilde{\mu}$ = 0.155) and n = 0.97 ($\tilde{\mu}$ = 0.245); (b) α = 0.3, n = 0.46 ($\tilde{\mu}$ = 0.101), n = 0.63 ($\tilde{\mu}$ = 0.134) and n = 0.90 ($\tilde{\mu}$ = 0.173) (curves 1-3, respectively). In the inset: - $\varepsilon_{cr.}$ versus n on the Fermi level ($\Omega_k = 0$) from the dispersion, Eq. (3.55) for α = 0 and α = 0.3 (curves 1 and 2, respectively)

Thus, the imaginary part of the lattice Green's function equals zero out of the indicated area and the electron excitations are coherent. Also, two peculiarities are determined by equation (3.56) at $s = 0$ and $s = 2\alpha$. In this case, real and imaginary parts of $G(s,\alpha)$ have discontinuity and van Hove singularity, respectively. In the excitation spectrum near the indicated points there is sufficiently complicated dispersion with the appearance of pseudogaps.

Therefore, the inclusion of the electron-electron scattering in cuprate planes causes an essential rebuilding of the excitation spectrum in comparison with the approximation Hubbard-I where this scattering is absent. The correlation gap appears in the area of electron concentrations when at the Fermi level $\varepsilon_{c.}(0) \leq -2 + 2\alpha$ that leads to the disappearance of the Fermi surface.

In Fig. 3.11 the Fermi surfaces are presented with an account for electron-electron scattering in the accordance to the formula (3.56) at $\Omega_k = 0$. The non-monotone change in the Fermi-surface square in Fig. 3.11a and 3.11b takes place due to the dependences $-\varepsilon_{cr.}(n)$ (see

curves 1 and 2 in the inset in Fig. 3.9a). In Fig. 3.11b electron Fermi surfaces at $n = 0.46$ and 0.63 are shown. At $n = 0.9$ we get the hole Fermi surface.
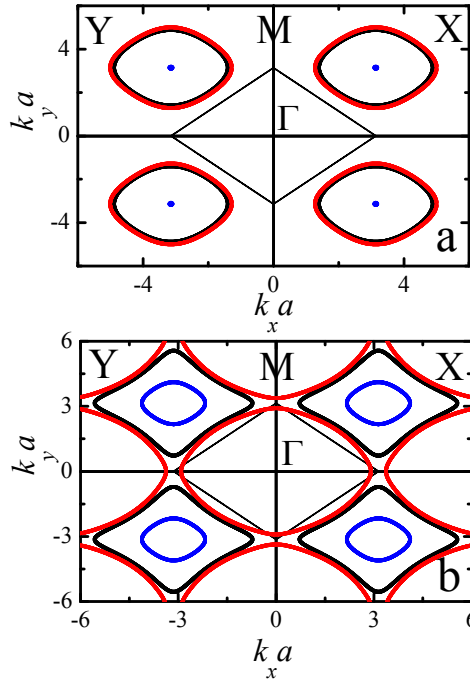
Fig. 3.11. Electron and hole Fermi surfaces in the absence of the electron-phonon coupling. The values of the parameters are those as in Fig. 3.10. In Fig. 3.11a the inner surfaces as point and big oval are obtained for $n = 0.7$ and 0.571, respectively. The outside surface corresponds to $n = 0.97$. In Fig. 3.11b electron Fermi surfaces as a deformed square and an inner oval centered out of Γ point are shown for $n = 0.46$ and 0.63, respectively. The hole Fermi surface has a shape of a big oval centered at the point Γ at $n = 0.9$, where Γ is the center of the Brillouin band

It is interesting to study corresponding spectral densities using Eq. (3.54). In the accordance with the ARPES terminology [38] let the EDC denotes the frequency dependence $A(\mathbf{k}, \omega)$ along nodal direction ($k_x = k_y$) of $\mathbf{k}$ at a fixed value of its module. MDC spectral density is evaluated from $A(\mathbf{k}, \omega)$ at a fixed frequency along the nodal direction for different values of k.

In Fig. 3.12a the EDC spectral densities at $\alpha = 0$ and $g = 0$ for Fermi momentum $k = k_F$ and different electron concentration (a) and near the k_F at $n = 0.97$ (b) are shown. The EDC curves have an asymmetrical character that in accordance with experimental results [46, 47]. From this figure it is easy to see that the maxima of $A(\mathbf{k}, \omega)$ correspond to resonance frequencies in Fig. 3.10a. At the same time, the maximum at $k = k_F$ is at the Fermi level. Notice that the degree of an excitation coherence near the Fermi level is abruptly increased for a peculiar area of the electron spectrum where there is a frequency change from an electron character ($\frac{\partial \Omega_k}{\partial k} > 0$) to a hole ($\frac{\partial \Omega_k}{\partial k} < 0$) one. Indeed, near the Fermi level the curve 1 in Fig. 3.12 a is strongly washed out unlike the curve 3 which corresponds to the curve 3 in Fig. 3.10 a with a kink at $\Omega_k \sim 0$. On the other hand, the curve 2 in Fig. 3.12a reflects an incoherent character of the electron excitations that is in agreement with a nearly point Fermi surface in Fig. 3.11a.
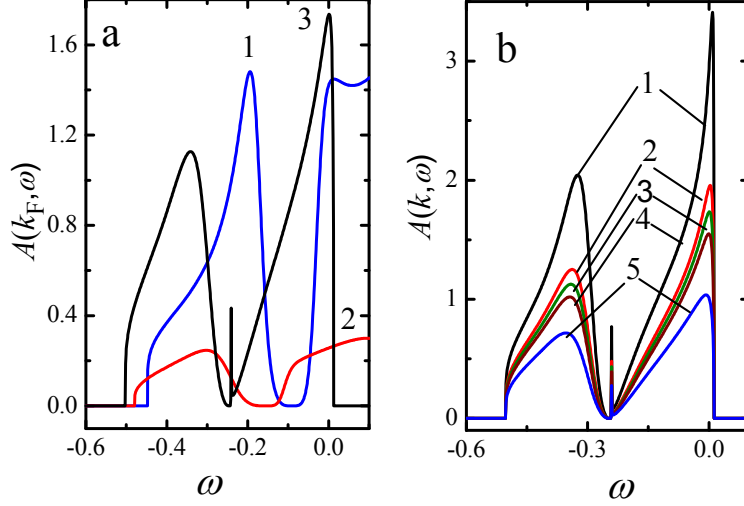
Fig. 3.12. EDC spectral density $A(\boldsymbol{k}, \omega)$ from Eq. (3.53) as a function of the frequency at $a = 3.814$ Å, $\alpha = 0$ and $g = 0$ along a nodal direction of the wave vector $\boldsymbol{k}$ with a module (a) $k=k_F$ at $n = 0.571$, 0.7 and 0.97 (curves 1-3, respectively); (b) $k = k_F$-0.05, k_F-0.01, k_F, k_F+0.01 and k_F+0.05, where $k_F = 0.717$ at $n = 0.97$ (curves 1-5, respectively)

In Fig. 3.13 the MDC spectral density $A(\boldsymbol{k}, \omega)$ versus $|\boldsymbol{k}|$ along a nodal direction at $n = 0.97$ for different frequencies (a) and frequency dependence maxima of $A(\boldsymbol{k}, \omega)$ (b) are shown. The curve $A(\boldsymbol{k}, \omega)$ has a Lorentz-line shape that agree with the ARPES data. Also, we observe a nontrivial character of the frequency dependence maxima of $A(\boldsymbol{k}, \omega)$. The maximum of $A(\boldsymbol{k}, \omega)$ appears at $k_{max} = 0.647$ at the Fermi level when the Fermi momentum is equal to 0.717. Thus, the maxima of the MDC spectral density do not correspond to resonance frequencies of the electron excitation spectrum.

Fig. 3.13. MDC spectral density $A(\boldsymbol{k}, \omega)$ from Eq. (3.53) as a function of a wave vector module at $a = 3.814$ Å, $n = 0.97$, $\alpha = 0$ and $g = 0$ along nodal direction of $\boldsymbol{k}$: (a) $\omega = 0$, -0.01, -0.025 and -0.05 (curves 1-4, respectively); (b) frequency dependence of the $A(\boldsymbol{k}, \omega)$ maxima
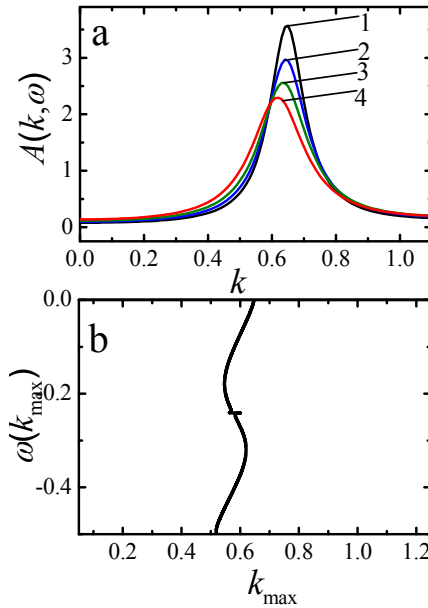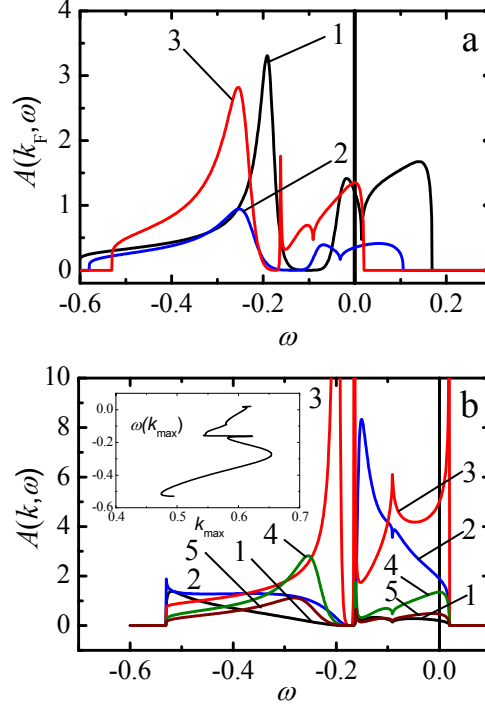
Fig. 3.14. EDC spectral density $A(\boldsymbol{k}, \omega)$ from Eq. (3.53) as a function of frequency along a nodal direction of the vector k at $a = 3.814$ Å, $g = 0$, $\alpha = 0.3$ and (a) $k = k_F$, $n = 0.46$, 0.63 and 0.9 (curves 1-3 for $k_F = 0.734$, 0.933 and 0.698, respectively); (b) $n = 0.9$ and $k = 0.4$, 0.55, 0.6, 0.698 and 0.8 (curves 1-5, respectively). In the inset in Fig. 3.13b we demonstrate the frequency dependence of $A(\boldsymbol{k}, \omega)$ maxima at $n = 0.9$

In Fig. 3.14 similar dependencies of $A(\boldsymbol{k}, \omega)$ are shown with an account for the next-nearest neighbors effect. We have considered only the electron concentration $n = 0.46$ when a correlation gap on the Fermi level is not developed. All conclusions to be formulated earlier relating Figs. 3.12 and 3.13 remain valid. Strong coherent modes appear near $k \sim 0.6$. It is a result of the abrupt change of derivation $\partial\Omega_k / \partial k$ (see Fig. 3.10b) for $\Omega_k = -\tilde{\mu}$. The edges of the area of abruptly changing $A(\boldsymbol{k}, \omega)$ are determined by Eq. (3.56) at $s = s_L$ and s_R. It is noted that van Hove anomaly (see Fig. 3.14b at $\omega \sim -0.1$) is determined by the expression $\omega = \Omega_{k0} = -\tilde{\mu} + 0.5\alpha(1 - 0.5n)$. It reflects a low-dimensional character of the electron behavior.

3.3.3. Influence of the electron-phonon interaction on the electron dynamics in cuprates

Now let us study dynamics of a d-electron subsystem with the electron-phonon coupling. First of all, it is necessary to evaluate numerically the chemical potential. It was noted earlier that diagrams 1-3 in Fig. 3.8 give an equation for chemical potential. The solution of this equation was presented in the work [32]. That is why we write this equation for temperature $T = 0$ as

$$\tilde{\mu} = \frac{(2-n)}{8} M\left(1, 1 + \frac{\tilde{\mu}}{\omega_0}, -\lambda^2\right) I^{-1}\left(1 - \frac{1}{2}(1-n)(2-n), \alpha\right). \qquad (3.57)$$

This expression differs from a similar Eq. (3.50) in that it has factor $M\left(1,1+\dfrac{\tilde{\mu}}{\omega_0},-\lambda^2\right)$ to be equal unity in the limit case $g = 0$.

In Fig. 3.15 the chemical potential $\tilde{\mu}$ versus constant g at $n = 0.9$ and $\alpha = 0$, 0.1 and 0.3 and $\tilde{\mu}$ versus n at $\alpha = 0$ and $g = 0.01$, 0.03 and 0.06 ((curves 1-3, respectively) are presented. In Fig. 3.15a the curves have kinks at $n = n_{cr.}$. For $n < n_{cr.}$ and $n > n_{cr.}$ the chemical potential $\tilde{\mu}$ is determined by Eq. (3.57) and equation $\tilde{\mu} = -\delta\mu_{-\sigma}$, respectively. From figure it is seen that $\tilde{\mu}$ is decreased with increasing both α and g.

Knowing the chemical potential and using Eqs. (3.36) - (3.49), it is fairly easy to calculate the excitation spectrum and spectral density of the electron cuprate system. Therefore let us write the expression for $\varepsilon_{cr.}$ similar to Eq. (3.55) that determines the dispersion equation

$$-\varepsilon_{cr.}(\Omega_k) = -\frac{4(\Omega_k + \tilde{\mu})^2}{L(\Omega_k)} \ , \tag{3.58}$$

$$L(\omega) = (\omega + \tilde{\mu})(1 - 0.5n)M\left(1,1+\frac{\omega+\tilde{\mu}}{\omega_0}\right) + J_5(\omega) + (\omega + \tilde{\mu})^2 \operatorname{Re} P_{46}(\omega) \tag{3.59}$$
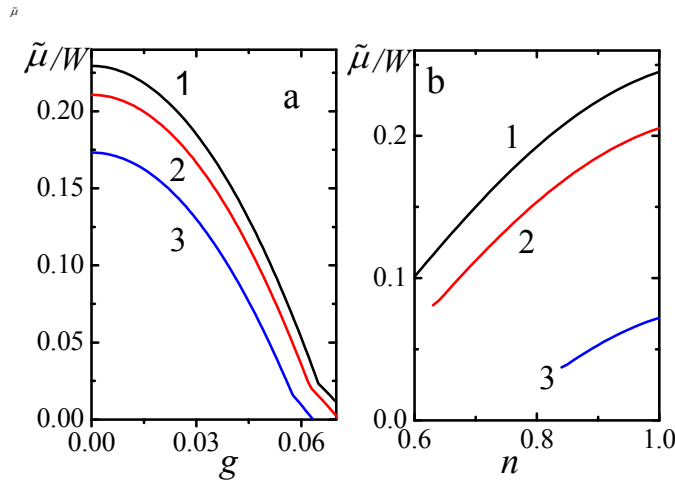
Fig. 3.15. (a) The chemical potential versus a constant of the electron-phonon interaction g with the phonon frequency $\omega_0 = 0.01875$ at the electron concentration $n = 9$ and $\alpha = 0$, 0.1 and 0.3 (curves 1-3, respectively); (b) concentration dependencies of the chemical potential at $\alpha = 0$ and $g = 0.01$, 0.03 and 0.06 (curves 1-3, respectively)

In particular, along the nodal direction the module of k-momentum as a function of the resonance frequency is written in the form

$$k(\Omega_k) = \arccos\left(\frac{-1+\sqrt{1-2\alpha\varepsilon_{cr.}(\Omega_k)}}{2\alpha}\right) \tag{3.60}$$

Apparently, the momentum k_F on the Fermi surface is determined from the condition $k_F = k(0)$. If $-\varepsilon_{cr.}(0) = -\varepsilon_F < 0$ then we get an electron Fermi surface and the hole one otherwise. A given statement may be disrupted for $\alpha \neq 0$.

74
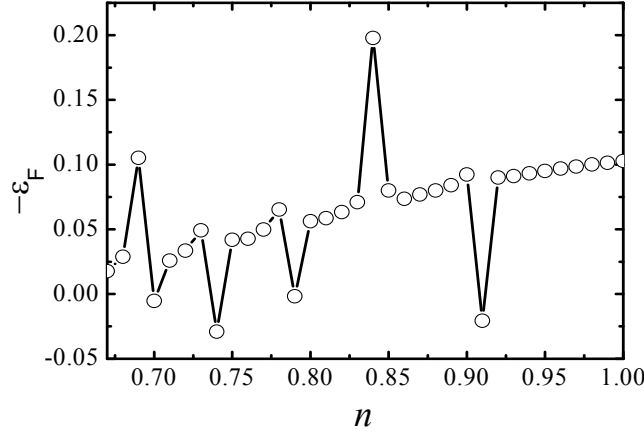
Fig. 3.16. Dependence of the critical parameter $-\varepsilon_F$ on the electron concentration

at $g = 0.03$ and $\alpha=0$

In Fig. 3.16 the dependence $-\varepsilon_F$ versus n at $g = 0.03$ and $\alpha = 0$ is shown. It is evident from Fig. 3.16 that the hole Fermi surface is changed to the electron one in a certain area of the electron concentrations.

In Fig. 3.17 electron excitation frequency-momentum dispersion curves in a wide area of a spectrum (a) and near the Fermi level (b) along the nodal direction at $n = 0.9$, $\alpha = 0$ for different values of g are depicted. One can see from Fig. 3.17 that the radical rebuilding of the excitation spectrum occurs with increasing the electron-phonon coupling energy. It is a result of the appearance of polaron bands grouped near the frequencies to be multiple the phonon frequency ω_0. It should be noted that there is a weak dependence of the resonance frequency on k at $g = 0.06$ (see Fig. 3.17a, curve 4) that is in agreement with ARPES experimental data [48].
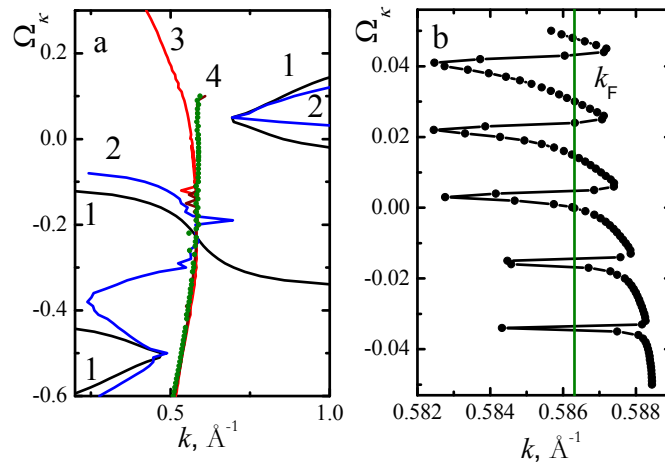
Fig. 3.17. (a) Excitation frequency-momentum dispersion along the nodal direction at $n = 0.9$, $\alpha = 0$ for values of $g = 0$, 0.01, 0.03 and 0.06 (curves 1-4, respectively). The points in Fig. correspond to $\alpha = 0.1$ and $g = 0.06$; (b) a fine structure of excitation spectrum (a) at $g = 0.06$. The vertical line corresponds to the wave vector $k = k_F$ on the Fermi surface

A fine spectrum structure near the Fermi level shows an enough drastic frequency change with a small change of k. In particular, below the Fermi level the first kink is observed at $\Omega_k \sim -\omega_0$, i.e., at the frequency of the typical optic phonon mode. It is in agreement with

75

experimental data $\Omega_k \sim$ 50-70 meV [47, 58] for the bandwidth $W \sim 4$ eV. A somewhat different kink direction from right to left may be changed by sign replacement of the hopping integral, i.e., t to $-t$. Also, when the kink is observed the value of the momentum $k_{th} \sim 0.586$ Å^{-1}. It is in accordance with the experimental value $k_{exp.} \sim 0.41$ Å^{-1} [38, 46, 47] if to put $k_{th.}/\sqrt{2}$. Seemingly, the maximal value of the hopping integral t is realized along a diagonal of the square lattice. Although, the other factors determining the kink position are not excluded.

A high degree of the coherence of excitations near the Fermi level is the distinctive feature of the obtained spectrum with polaron bands. Indeed, for a square lattice the excitation spectrum is very diverse at $g = 0$. But strong low-dimensional fluctuations responsible for a low degree of coherence of excitations excluding some edge points determined by $\operatorname{Im} G(s, \alpha)$. To verify this, we write the expression for a spectral density generally

$$A(\boldsymbol{k},\,\omega) = \frac{1}{\pi} \frac{(\omega + \tilde{\mu})^4 \beta \operatorname{Im} P_{46}(\omega)}{\left[(\omega + \tilde{\mu})^2 - t(\boldsymbol{k})L(\omega)\right]^2 + (\omega + \tilde{\mu})^2 t^2(\boldsymbol{k})\left[(\omega + \tilde{\mu})^2 \beta \operatorname{Im} P_{46}(\omega)\right]^2},\qquad(3.61)$$

where $P_{46}(\omega)$ and $L(\omega)$ are determined in the subsection 3.3 and by Eq. (3.59), respectively.

In Fig. 3.18 the EDC dependencies of the spectral density at $n = 0.9$, $\alpha = 0$ and $g = 0.06$ ($\tilde{\mu} = 0.053$) are presented for different momentums along the nodal direction near the Fermi wave vector $k_F = 0.586$ Å^{-1}. From Fig. 3.18 it can be seen that sharp peaks are observed on the curve $A(\boldsymbol{k},\,\omega)$ for a Fermi momentum $k = k_F$ (see curve 2). Satellite peaks with smaller amplitudes are seen for other energies of excitations as well. These peaks correspond to points of the intersection of polaron bands by a straight line $k = k_F$ depicted in Fig. 3.17a.
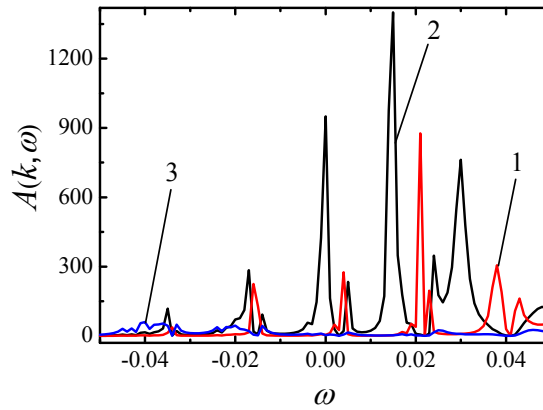
Fig. 3.18. Frequency dependencies of the spectral density at $n = 0.9$, $\alpha = 0$, $g = 0.06$ and $k = k_F$-0.003, k_F and k_F +0.003 (curves 1-3, respectively) for momentums along the nodal direction where $k_F = 0.586$ Å and the square lattice parameter $a = 3.814$ Å

It should be noted that a small change of k from k_F results in a sharp decrease of the spectral density (see curves 1 and 3 in Fig. 3.18). The coherence of excitations is reduced as the electron-phonon coupling is weakened. A correlation gap arises on the Fermi level for sufficiently small values of g as well (see Fig. 3.17a).

Thus, for cuprates in the strong-coupling polaron limit the hole or electron Fermi surface is realized, depending on the electron concentration and the value of g. The spectral density reflects a high degree of the excitation coherence near the Fermi level. The availability of the narrow polaron bands, which are grouped near the frequencies to be multiples of the phonon frequency ω_0, results in a sharp resonance frequency along the nodal direction of the momentum. It explains the origin of a kink observed at energy $\omega \sim -\omega_0$ in ARPES data for bismuth cuprates.

3.4. Conclusions

For strongly correlated electron subsystem with Holstein's polarons within the framework of the diagrammatic method of perturbation theory a generalization for Hubbard-I approximation had been done. Strong electron correlations narrow a valence band in a doped Mott insulator that results in a radically difference one from metal. The Lang-Firsov unitary transform was made to separate fermionic and bosonic subsystems. It allows to evaluate all polaron bands each of which is formed near the Einstein mode.

In the first nonvanishing approximation of the time-dependent perturbation theory with respect to the inverse effective radius of the interaction, we account for the influence of inelastic electron-electron scattering on a chemical potential and the time-ordered Green's function. Taking into account a low-dimensional character of system it was obtained that all peculiarities of excitation spectrum and damping are determined by the lattice Green function for which there is a closed analytic expression. An influence of the electron concentration and the next-nearest-neighbour hopping integral on the chemical potential, the spectrum structure and the spectral density has been determined. In particular, with well-defined electron concentrations the correlation gap in the spectrum arises at the Fermi level. In the absence of the gap, the Fermi surface can be of a hole or electron character depending on the electron concentration and the effect of the next-nearest-neighbour hopping integral. In spite of the complicated picture of the spectrum, the spectral density shows relatively low degree of the coherence. It is connected to a low space dimension of the system where the role of quantum fluctuations is important.

In addition to the previously considered approach, the inclusion of the electron-phonon interaction has allowed to reveal the main peculiarities of the spectrum. They are in good correspondence with experimental ARPES data. Indeed, in a wide area of frequencies a weak momentum dependence of spectrum along the nodal direction was found in agreement with the experiment [48]. The spectral density turned out to be typical for strongly coherent excitations near the Fermi level when the electron-phonon coupling is strong. It simplifies the experimental measure of the Fermi surface. Thus, the electron-phonon interaction partially suppresses low-dimensional quantum fluctuations and strengthen the coherence of excitations. From the above analysis of a fine structure in the polaron spectrum one can conclude that the observed kink [46, 47] appears at the characteristic optical phonon frequency in the vicinity of the polaron band.

4. HIGH-TEMPERATURE SUPERCONDUCTIVITY AND A NORMAL STATE IN THE HOLSTEIN-*T-J* MODEL

4.1. Introduction

In the 21st century the phenomenon of the high-temperature superconductivity (HTSC) in cuprates continues to attract attention of many researches [59]. There is a tremendous number of proposed mechanisms for this phenomenon. In any case, up to now there is no theory able to describe all properties of this complicated state. In this work, we have concentrated on the main peculiarity that in our opinion might help to illuminate the origin of high–T_{SC} in cuprates. The electron-phonon coupling is supposed to be not essential in the Cooper electron pairings. But this interaction forms polaron excitations which play an important role in the correlation narrowing of the electron band. In that case, it is necessary to differentiate collectivized electrons in metals and those in doped cuprates. Indeed, in metals there is wave electron states with a possibility of the site double occupancy. But their hole states are virtual. And that is why we have the partition function $\exp(\varepsilon_{k\sigma}/T) + \exp(\varepsilon_{k-\sigma}/T)$ for electron excitations $\varepsilon_{k\pm\sigma}$. In cuprates, a coordinate representation is realized for electron wave functions and we have the partition function $1 + \exp(\varepsilon_{\sigma}/T) + \exp(\varepsilon_{-\sigma}/T)$ with electron levels $\varepsilon_{\pm\sigma}$ and hole states.

The cuprates belong to a class of a strongly correlated electron system. In the work [60] an effective Hamiltonian of the *t-J* model was suggested based on the use of a Gutzwiller projection operator. It allowed to exclude the upper Hubbard band with a double site occupancy by electrons and essentially to simplify a study of strongly correlated electron systems. In the work [61], a mean field approximation of the *t-J* model was developed to study the high-temperature superconductivity. In this work, a fundamental idea about spin pairing via the electron exchange interaction was formulated. Unfortunately, the authors did not take into account the essential difference between metal and strongly correlated electrons. Using the Bogolyubov's *u-v* transform of the Hamiltonian, they obtained the equation for the gap function similar to that in the BCS theory.

In this work, we propose to divide the mean field BCS type Hamiltonian into uniform and nonuniform parts. The perturbation theory was built with uniform unperturbed Hamiltonian. The nonuniform part is ignored since it has a weak influence on the hopping integral. A hopping term of the total *t-J* Hamiltonian is considered as a perturbation in the limit of a weak doping with *u-v* transformed creation and destruction operators. The mean values to be proportional the superconductive gap function were calculated. It has been obtained the condition on the values of the chemical potential and an exchange parameter. With account of the correlation band narrowing, we arrive to the conclusion about impossibility of the HTSC in the pure *t-J* model.

In what follows, we include into consideration the electron-phonon interaction. The evidences for a presence of one and its important role in strongly correlated systems were emphasized in the works [51, 62, 63]. In view of the fact that Hamiltonian of an electron-phonon coupling is nonuniform, many authors simplify the kinematic part by a simple renormalization of the hopping integral [63] or using the theory by Eliashberg for collectivized metal electrons [51]. In the former case, it gives rise to drastic suppression of the electron band and is responsible for the absence of the HTSC in a system without interaction of polarons. The simplest form of the Holstein Hamiltonian for polarons needs to be considered with a uniform electron-phonon interaction and the Einstein phonon mode. One can provide an exact unitary transform to

separate fermion and boson degrees of freedom. It allows to build a subsequent perturbation theory of the strongly correlated electron system with Holstein's polarons.

The structure of the section is as follows. In the subsection 4.2, we consider a Hamiltonian of a pure *t-J* model in the superconducting state. It was separated into a uniform mean field part with corresponding coefficients of the *u-v* transform. It enables us in the subsection 4.3 to build a perturbation theory for strongly correlated electrons in the superconducting state. In particular, transformed Hubbard operators in the coordinate representation using the Bogolyubov's *u-v* transform will be obtained. As a result, the equation for the gap function and superconducting state conditions are presented. In the subsection 4.4 the properties of a normal state without electron-phonon coupling are considered. In the framework of the developed diagrammatic method, the absence of superconductivity in a pure *t-J* model is demonstrated. In the subsection 4.5, a normal state of the cuprate d-electrons with polaron excitations is investigated to find the critical temperature of superconducting state. In this part the problem of the frequency summation with an infinity number of poles as implicit functions is solved. The suggested method of an inverse function allowed to calculate the diagrammatic contributions for all polaron bands. In the subsection 4.5, the obtained equations are solved numerically that allowed to find the critical temperature T_{SC} and the gap function Δ versus temperature concentration dependences. Theoretical values of T_{SC} and Δ are in good agreement with an experiment that supports the model to put forward by us.

4.2. Hamiltonian of the system

The Hamiltonian of the Holstein model with strongly correlated electrons takes the form:

$$\hat{H} = \hat{H}_f + \hat{H}_b, \tag{4.1}$$

where the Fermi part, $\hat{H}_f$, is expressed as follows :

$$\hat{H}_f = \sum_{i,j} J_{ij} \left(\mathbf{S}_i \mathbf{S}_j - \frac{1}{4} n_i n_j \right) - \mu \sum_{i\sigma} n_{i\sigma} + V \tag{4.2}$$

Here, J_{ij} is the indirect exchange of the collectivized *d*-electrons with spins S_i and S_j, $n_i = n_{i\sigma} + n_{i-\sigma}$ is the electron concentration on *i*-site, μ is the chemical potential. The perturbation *V* is written as

$$\hat{V} = \sum_{i,j,\sigma} t_{ij} c_{\sigma i}^+ c_{\sigma j} (1 - n_{i-\sigma})(1 - n_{j-\sigma}), \tag{4.3}$$

where $c_{\sigma i}^+$ ($c_{\sigma i}$) creates (annihilates) an electron of spin σ on the lattice site *i* and t_{ij} is the hopping integral to be equal to *t*. The Hamiltonian (4.2) of the *t-J* model reflects strong electron correlations. At a weak doping level, we will consider the part (4.3) as a perturbation.

The boson part of the Hamiltonian (4.1) has a form similar to that used in the Holstein model of small polarons:

$$\hat{H}_b = -g \sum_i n_i \left(b_i^+ + b_i \right) + \omega_0 \sum_i b_i^+ b_i, \tag{4.4}$$

where *g* is the electron-phonon coupling strength, b_i^+ and b_i are phonon creation and destruction operators. We will use the Einstein model where the phonon frequency ω_0 is assumed to be dispersion-free.

The Lang-Firsov unitary transform [52] $\tilde{U} = \exp(\tilde{S})$ of the Hamiltonian allows to separate boson and fermion operators in Eq. (4.4), where $\tilde{S} = -\dfrac{g}{\omega_0} \sum_i n_i (b_i^+ - b_i)$. As a result,

$$\hat{\tilde{H}}_b = \tilde{U}^{-1} \hat{H}_b \tilde{U} = \omega_0 \sum_i b_i^+ b_i - \xi \sum_i n_i , \qquad (4.5)$$

where $\xi = g^2 / \omega_0$ is the polaron binding energy. The unitary transformed perturbation V reads as

$$V = \sum_{<ij>,\sigma} t_{ij} \tilde{c}_{i\sigma}^+ \tilde{c}_{j\sigma} (1 - n_{i-\sigma})(1 - n_{j-\sigma}) \qquad (4.6)$$

Here, unitary transformed Fermi operators

$$\tilde{c}_{i\sigma} = Y_i c_{i\sigma} \qquad (4.7)$$

are products of Bose $Y_i = e^{\lambda(b_i^+ - b_i)}$ and corresponding Fermi destruction operators with $\lambda = g/\omega_0$. It is necessary to point out that first and second terms of the Hamiltonian (4.2) are not changed under the transformation $\tilde{U}$.

By a standard approach, one can separate a mean field connected to abnormal averages in a Heisenberg part of the Hamiltonian (4.2) [61]. Then an unperturbed Hamiltonian takes the form

$$\hat{H}_{0f} = \sum_{<ij>\sigma} \left\{ \Delta_{ij\sigma} c_{i\sigma}^+ c_{j-\sigma}^+ + \Delta_{ij\sigma}^* c_{i-\sigma} c_{j\sigma} \right\} - \sum_{i\sigma} \tilde{\mu}_\sigma n_{i\sigma} , \qquad (4.8)$$

where $\tilde{\mu}_\sigma = \tilde{\mu} - \sigma J(0) < S^z >$, $\tilde{\mu} = \mu + \xi$, $< S^z >$ is a mean electron spin and $\sigma = \pm 1$. The gap functions are expressed via exchange parameters:

$$\begin{aligned} \Delta_{ij\sigma} &= -J_{ij} < c_{i-\sigma} c_{j\sigma} > \\ \Delta_{ij\sigma}^* &= -J_{ij} < c_{i\sigma}^+ c_{j-\sigma}^+ > \end{aligned} \qquad (4.9)$$

In a wave space the Hamiltonian (4.8) takes the form

$$\hat{H}_{0f} = \sum_{k\sigma} \left\{ \Delta_{k\sigma} c_{k\sigma}^+ c_{-k-\sigma}^+ + \Delta_{k\sigma}^* c_{-k-\sigma} c_{k\sigma} \right\} - \sum_{k\sigma} \tilde{\mu}_\sigma n_{k\sigma} , \qquad (4.10)$$

where the gap functions $\Delta_{k\sigma}$ can be presented as

$$\Delta_{k\sigma} = -\frac{1}{N} \sum_q J(q+k) < c_{-q-\sigma} c_{q\sigma} > \qquad (4.11)$$

and $\Delta_{k\sigma}^*$ is conjugate function $\Delta_{k\sigma}$. One can point out that in Eqs. (4.9) and (4.11) creation and destruction operators are not transformed by the operator Y_i from (4.7). The *u-v* transform

$$\begin{aligned} c_{k\sigma} &= u_{k\sigma}^* \alpha_{k\sigma} + v_{k\sigma} \alpha_{-k-\sigma}^+ \\ c_{k\sigma}^+ &= u_{k\sigma} \alpha_{k\sigma}^+ + v_{k\sigma}^* \alpha_{-k-\sigma} \end{aligned} \qquad (4.12)$$

to new operators $\alpha_{k\sigma}$ and $\alpha_{-k-\sigma}^+$ allows to diagonalize $\hat{H}_{0f}$ with the next conditions

$$u_{k\sigma} = u_{-k-\sigma}, \quad v_{k\sigma} = -v_{-k-\sigma}, \quad |u_{k\sigma}|^2 + |v_{k\sigma}|^2 = 1 \qquad (4.13)$$

Then we have

$$\hat{H}_{0f} = \sum_{k\sigma} \tilde{E}_{k\sigma} \alpha^{+}_{k\sigma} \alpha_{k\sigma},$$ (4.14)

where

$$\tilde{E}_k = -\tilde{\mu}\sqrt{1 + \left(\frac{\Delta_k}{\tilde{\mu}}\right)^2}$$ (4.15)

In what follows we will consider a paramagnetic state when $<S^z> = 0$. Then one can put

$$\tilde{\mu}_\sigma = \tilde{\mu}, \quad |\Delta_{k\sigma}| = |\Delta_{-k-\sigma}| = \Delta_k$$ (4.16)

So far it has been obtained that the BCS Hamiltonian (4.14) coincides with a similar Hamiltonian by Baskaran-Zou-Anderson [61]. Unfortunately, the authors of the work [61] do not separate the perturbation V from (4.1). Instead of this, they narrow the band multiplying the hopping integral t by factor x equal to a hole concentration. It does not allow to find the rigorous statement relatively an appearance of the superconductivity since the band energy at $x \sim 0$ has a finite quantity. That is why we will expand Eq. (4.15) in terms of the small parameter $(\Delta_k / \tilde{\mu})^2$ up to the third order:

$$\tilde{E}_k = -\tilde{\mu}\left\{1 + \frac{1}{2}\frac{\Delta_k^2}{\tilde{\mu}^2} - \frac{1}{8}\frac{\Delta_k^4}{\tilde{\mu}^4} + \frac{3}{48}\frac{\Delta_k^6}{\tilde{\mu}^6} - ...\right\}$$ (4.17)

Apparently, the corrections to chemical potential in Eq. (4.17) will produce an additional nonuniform part ΔH to the perturbation $\hat{V}$ from (4.3) in the coordinate space:

$$\Delta H = \sum_{ij} \delta t_{ij} \alpha^{+}_{i\sigma} \alpha_{j\sigma},$$ (4.18)

where

$$\delta t_{ij} = \frac{1}{N}\sum_k \left\{-\frac{1}{2}\frac{\Delta_k^2}{\tilde{\mu}^2} + \frac{1}{8}\frac{\Delta_k^4}{\tilde{\mu}^4} - \frac{3}{48}\frac{\Delta_k^6}{\tilde{\mu}^6} + ...\right\} e^{ik(R_i - R_j)}$$ (4.19)

In what follows our consideration is limited by the square lattice and s- or d- symmetry of order parameter $\Delta_k = \Delta(\cos k_x a \pm \cos k_y a)$. In (4.18) we will extract one site part of ΔH_1:

$$\Delta H_1 = \sum_{ij} \delta t_{ii} \alpha^{+}_{i\sigma} \alpha_{i\sigma}$$ (4.20)

The rest ΔH_2 of (4.18) may be presented as

$$\Delta H_2 = \sum_{i \neq j} \delta t_{ij} <\alpha^{+}_{i\sigma} \alpha_{j\sigma}> + \sum_{i \neq j} \delta t_{ij} \alpha^{+}_{i\sigma} \alpha_{j\sigma} - \sum_{i \neq j} \delta t_{ij} <\alpha^{+}_{i\sigma} \alpha_{j\sigma}>$$ (4.21)

The first term of (4.21) is a nonoperator part and last two contributions are connected to correlation corrections to the superconducting state. In our mean field theory, these corrections are not considered.

Therefore, we have

$$\Delta H = \Delta H_1 \ , \tag{4.22}$$

where

$$\frac{1}{N}\sum_k \Delta_k^{2p} = \frac{\Delta^{2p}}{\pi^2}\int_0^\pi dx \int_0^\pi dy (\cos x \pm \cos y)^{2p}$$

and

$$\delta t_{ii} = -\frac{\Delta^2}{2\tilde{\mu}} + \frac{9\Delta^4}{32\tilde{\mu}^3} - \frac{75\Delta^6}{192\tilde{\mu}^5} + ... \tag{4.23}$$

Finally, an unperturbed BCS Hamiltonian in the coordinate space takes a simple form

$$\hat{H}_{0f} = -\sum_i \mu_g \alpha_{i\sigma}^+ \alpha_{j\sigma} \ , \tag{4.24}$$

where the renormalized chemical potential μ_g reads as

$$\mu_g = \tilde{\mu} - \delta t_{ii} \tag{4.25}$$

In the view of the unitary transformed Hamiltonian (4.24) one can build the perturbation theory with the operator V from (4.6) in which $\tilde{c}_{i\sigma}^+$ and $\tilde{c}_{j\sigma}$ are replaced by $\tilde{\tilde{c}}_{i\sigma}^+$ and $\tilde{\tilde{c}}_{j\sigma}$, respectively, where

$$\tilde{\tilde{c}}_{i\sigma} = \frac{1}{N}\sum_{kp} e^{ik(R_i - R_p)}\left\{u_k^* \alpha_{p\sigma} + v_k \alpha_{p-\sigma}^+\right\}$$

$$\tilde{\tilde{c}}_{i\sigma}^+ = \frac{1}{N}\sum_{kp} e^{-ik(R_i - R_p)}\left\{u_k \alpha_{p\sigma}^+ + v_k^* \alpha_{p-\sigma}\right\} \tag{4.26}$$

Here the coefficients of the u-v transform are

$$u_k = \frac{\tilde{\mu} - \tilde{E}_k}{\sqrt{2\tilde{E}_k(\tilde{E}_k - \tilde{\mu})}}, \quad v_k = \frac{\Delta_k}{\sqrt{2\tilde{E}_k(\tilde{E}_k - \tilde{\mu})}} \tag{4.27}$$

4.3. Perturbation theory for an electron system in a superconducting state

Scattering matrix formalism for a system with strongly correlated electrons differs from that in the band theory of metals. Indeed, in our case we must exclude the upper Hubbard's band by the Gutzwiller's projection operator. As a result, one may not use the wave representation at the disentanglement of correlators arising from series of the perturbation theory. Unfortunately, the BCS Hamiltonian is diagonalized if and only if we work in the k-space. That is why the coordinate representation (4.26) is introduced to connect coordinate and k-spaces of the transformed Hamiltonian $\hat{H}$. There is a powerful method of Hubbard operators to account for excluding double-electron site occupancy. In the works [64, 50], the general diagram method for the Hubbard operator was presented. Let us dwell on the main statements related to our model.

Let us introduce Hubbard's operators $X^{ik} = |\psi_i\rangle\langle\psi_k|$, where we have three electron wave functions $|\psi_0\rangle = |0\rangle, |\psi_\sigma\rangle = |\sigma\rangle$, corresponding to hole, spin up ($\sigma = +$) and spin down ($\sigma = -$) electron states, respectively. Apparently, in a normal state $\alpha_{p\sigma} = X_p^{0\sigma}, \alpha_{p\sigma}^+ = X_p^{\sigma 0}$ and anticommutator $\{\alpha_{p\sigma}\alpha_{p\sigma}^+\} = F_p^{\sigma 0} = X_p^{\sigma\sigma} + X_p^{00}$, which differs from the unit as for destruction and creation operators. It is the result of neglecting the upper Hubbard's band. The main task is to find the average of operators $A = F_p^{\sigma 0}$ and $A = c_{i-\sigma}c_{j\sigma}$. In the first case, we obtain a self-consistent equation for the chemical potential of the paramagnetic state. Apparently, from the condition $\Delta/\mu << 1$ one can neglect the influence of the order parameter Δ on μ. In the second case, we will have the equation for a gap function. Since the fermion and boson subsystems are divided in accordance with the Hamiltonian (4.5) now we will consider creation and destruction operators with one tilda corresponding to the *u-v* transform. The second tilda will reflect a unitary transform (4.7). The average of the operator *A* is determined by a standard way:

$$< A > = \frac{1}{< \sigma(\beta) >_0} < A\sigma(\beta) >_0, \tag{4.28}$$

where the symbol $<...>_0 = \mathrm{Sp}(\exp(-\beta\hat{H}_0...))/\mathrm{Sp}(\exp(-\beta\hat{H}_0))$ denotes statistical averaging over the unperturbed Hamiltonian with the temperature $1/\beta = T$, Sp is a trace of the operator. The S matrix $\sigma(\beta)$ is written as [19]

$$\sigma(\beta) = \sum_{n=0}^{\infty} \frac{(-1)^n}{n!} \int_0^\beta ... \int_0^\beta d\tau_1 ... d\tau_n T_\tau \{V(\tau_1)...V(\tau_n)\} \tag{4.29}$$

In the expression for $\sigma(\beta)$ the symbols $V(\tau_i) = e^{\hat{H}_0\tau_i}\hat{V}e^{-\hat{H}_0\tau_i}$ and T_τ are an operator in the interaction representation and a time-ordering operator, respectively. Now the task is to calculate all possible averages of the product of *A* operators for different sites. These correlators can be reduced to a product of semi-invariants of the diagonal operators and unperturbed Fermi Green's functions $G_{\alpha\beta}(\tau) = -<T_\tau X^{\alpha\beta}(\tau)X^{\beta\alpha}(0)>_0/<F^{\sigma 0}>_0$ using the Vick's theorem for Hubbard's operators [64]. The Fourier transform of these functions has the form

$$G_{\alpha\beta}(i\omega_n) = \frac{1}{2\beta}\int_{-\beta}^\beta e^{-i\omega_n\tau}G_{\alpha\beta}(\tau)d\tau = \frac{1}{\beta}\frac{1}{i\omega_n + \varepsilon_\alpha - \varepsilon_\beta}, \tag{4.30}$$

where $\omega_n = (2n+1)\pi/\beta$ and ε_α is the energy level of the unperturbed Hamiltonian $\hat{H}_{0f}$. In the case when the electron-phonon interaction is accounted, the unperturbed Fermi-Bose Green's function reads as $\tilde{G}_{\alpha\beta}^{-+}(\tau) = \tilde{G}_{\alpha\beta}(\tau) = - <T_\tau X^{\alpha\beta}(\tau)Y(\tau)X^{\beta\alpha}(0)Y^+(0)>_0/<F^{\sigma 0}>_0$. The Fourier component $\tilde{G}_{\alpha\beta}(i\omega_n)$ of $\tilde{G}_{\alpha\beta}(\tau)$ is expressed as follows [50]:

$$\tilde{G}_{\alpha\beta}(i\omega_n) = \frac{1}{\beta}f(\varepsilon_{\alpha\beta})\sum_{m=-\infty}^{+\infty}d_m\frac{e^{\beta\varepsilon_{\alpha\beta}+\frac{1}{2}\beta m\omega_0} + e^{-\frac{1}{2}\beta m\omega_0}}{i\omega_n + m\omega_0 + \varepsilon_{\alpha\beta}}, \tag{4.31}$$

where $f(x) = 1/(e^{\beta x} + 1)$ and $B = 1/(e^{\beta \omega_0} - 1)$ are Fermi and Bose distributions, respectively, $d_m = e^{-\lambda^2(2B+1)} I_m \left(2\lambda^2 \sqrt{B(B+1)} \right)$, $I_m(x)$ are Bessel functions of the complex argument and ω_n is the same quantity as in (4.30).

Unfortunately, the Vick's theorem cannot be used for the transformed Hubbard's operators in accordance with (4.7). That is why for averaging we have to separate the boson subsystem from the fermion one. In the case of isolated pairings, such separation is not needed. As it will be seen later, similar situation is realized for the effective kinematic interaction and diagrams to be formed by one effective line of interactions and one unperturbed Green's function. Further, we denote by $U_{ep}(\tau_i - \tau_j) = < T_\tau Y_i(\tau_i) Y_i^+(\tau_j) >_0$.

Let us write possible pairings between creation and destruction operators. The normal operator pairing has the form

$$T_\tau \underrightarrow{\tilde{c}_{i\sigma}(\tau) \tilde{c}_{j\sigma}^+(0)} = \frac{1}{N^2} \sum_{k_1, k_2, p} e^{ik_1 R_i - ik_2 R_j} e^{i(k_1 - k_2) R_p} \left\{ -u_{k_1}^* u_{k_2} \tilde{G}_{0\sigma}(\tau) F_p^{\sigma 0} - v_{k_2}^* v_{k_1} \tilde{G}_{-\sigma 0}(\tau) F_p^{-\sigma 0} \right\} \quad (4.32)$$

and an average over the Hamiltonian $\hat{H}_{0f}$ gives the next unperturbed Green's functions:

$$\tilde{\tilde{G}}_{0\sigma}(\tau) = -< T_\tau \tilde{c}_{i\sigma}(\tau) \tilde{c}_{j\sigma}^+(0) >_0 = \frac{1}{N} \sum_k e^{ik(R_i - R_j)} \left\{ |u_k|^2 \tilde{G}_{0\sigma}(\tau) < F_p^{\sigma 0} >_0 + |v_k|^2 \tilde{G}_{-\sigma 0}(\tau) < F_p^{-\sigma 0} >_0 \right\}, \quad (4.33)$$

where $\tilde{G}_{0\sigma}(i\omega_n)$ is the unperturbed Green's function from (4.31). The abnormal operator pairing is presented as

$$T_\tau \underrightarrow{\tilde{c}_{m\sigma}(\tau) \tilde{c}_{l-\sigma}(0)} = \frac{1}{N^2} \sum_{k_1, k_2, p} e^{ik_1 R_m + ik_2 R_l} e^{-i(k_1 + k_2) R_p} \left\{ -u_{k_1}^* v_{k_2} G_{0\sigma}(\tau) F_p^{\sigma 0} - v_{k_1} u_{k_2}^* G_{-\sigma 0}(\tau) F_p^{-\sigma 0} \right\} (4.34)$$

Here the arrows are directed from an "active" operator to the "passive" one with the use of the Vick's theorem. In particular, the average of (4.34) at $\tau \to -0$ gives unperturbed gap functions:

$$< \tilde{c}_{l-\sigma} \tilde{c}_{m\sigma} >_0 = -\frac{1}{N} \sum_k e^{ik(R_l - R_m)} u_{-k}^* v_k < F^{\sigma 0} >_0 = \frac{1}{N} \sum_k e^{ik(R_l - R_m)} \varphi_{k\sigma}^{11(0)}(0) \quad (4.35)$$

The pairing with the diagonal operator takes the form:

$$T_\tau \underrightarrow{\tilde{c}_{i\sigma}(\tau) F_m^{\sigma 0}} = -\frac{1}{N} \sum_k e^{ik(R_i - R_m)} v_k \tilde{G}_{-\sigma 0}(\tau) \alpha_{m-\sigma}^+$$

Similar expressions can be done for other pairings. One can point out that anticommutator

$$\{ \tilde{c}_{i\sigma} \tilde{c}_{i\sigma}^+ \} = \tilde{F}_i^{\sigma 0} = \frac{1}{N^2} \sum_{k_1 k_2 p} e^{i(k_1 - k_2)(R_i - R_p)} \left[u_{k_1}^* u_{k_2} F_p^{\sigma 0} + v_{k_1} v_{k_2}^* F_p^{-\sigma 0} \right].$$

We shall calculate the average value $< \tilde{c}_{l-\sigma} \tilde{c}_{m\sigma} >$. This average is conveniently calculated by the replacement

$$< \tilde{c}_{l-\sigma} \tilde{c}_{m\sigma} > = \lim_{\tau \to +0} < T_\tau \tilde{c}_{l-\sigma}(\tau) \tilde{c}_{m\sigma}(0) >$$

Let $B_{0\sigma}(\tau_j - \tau_i, \mathbf{k})$ is the Fourier components of the effective kinematic interaction caused by the perturbation V from Eq. (4.3). Then it is necessary to find an average of the next pairings in the first approximation of the perturbation theory:

$$-\int_0^\beta d\tau_j \int_0^\beta d\tau_i \frac{1}{N}\sum_{ijk}\frac{1}{\beta}B_{0\sigma}(\tau_j-\tau_i,\boldsymbol{k})e^{ik(R_j-R_i)}<T_\tau \overline{\tilde{c}_{l-\sigma}(\tau)\tilde{c}_{m\sigma}(0)\,\overrightarrow{\tilde{c}^+_{j\sigma}(\tau_j)\tilde{c}_{i\sigma}(\tau_i)}}>_0 =$$

$$=-\frac{1}{N}\sum_k e^{ik(R_l-R_m)}\left\{ u_k^* v_{-k} G_{0-\sigma}(\tau)\beta\,\delta\tilde{\mu}_{-\sigma} + u_{-k}^* v_k G_{\sigma 0}(\tau)\beta\,\delta\tilde{\mu}_\sigma \right\} \tag{4.36}$$

where function $\beta\,\delta\tilde{\mu}_\sigma$ is determined as

$$\beta\delta\tilde{\mu}_\sigma = \frac{1}{N}\sum_{q\omega_n} \beta B_{0\sigma}(\boldsymbol{q},i\omega_n)\tilde{G}_{0\sigma}(i\omega_n) \tag{4.37}$$

High orders of the perturbation theory with pairings of the type (4.36) renormalize the combined occupancy $<F^{\sigma 0}>_0$ to $<F^{\sigma 0}>_1$ in accordance with the expanding function

$$<F^{\sigma 0}(\varepsilon_\sigma,\varepsilon_{-\sigma},\lambda)>_0 = \frac{e^{-\beta\varepsilon_\sigma}+e^{-\beta(\lambda+\varepsilon_\sigma+\varepsilon_{-\sigma})}}{e^{-\beta\varepsilon_\sigma}+e^{-\beta(\lambda+\varepsilon_\sigma+\varepsilon_{-\sigma})}+1}$$

to be equal to $<F^{\sigma 0}>_0$ at $\lambda=-\varepsilon_- -\varepsilon_+$ into a Taylor's series [50]

$$<F^{\sigma 0}>_1 = <F^{\sigma 0}>_0 - \beta\delta\tilde{\mu}_\sigma\partial_\sigma <F^{\sigma 0}>_0 - \beta\delta\tilde{\mu}_{-\sigma}\partial_{-\sigma} <F^{\sigma 0}>_0 +$$

$$+\frac{1}{2!}(\beta\delta\tilde{\mu}_\sigma)^2\partial_\sigma^2 <F^{\sigma 0}>_0 +\frac{1}{2!}(\beta\delta\tilde{\mu}_{-\sigma})^2\partial_{-\sigma}^2 <F^{\sigma 0}>_0 -... = \tag{4.38}$$

$$=<F^{\sigma 0}(\varepsilon_\sigma+\delta\tilde{\mu}_\sigma,\varepsilon_{-\sigma}+\delta\tilde{\mu}_{-\sigma},-\varepsilon_\sigma-\varepsilon_{-\sigma})>_0$$

Thus, summing (4.35), (4.36) and so on, we obtain

$$\varphi_{k\sigma}^{11}(\tau\to+0) = u_k^* v_{-k} G_{0-\sigma}(\tau)<F^{-\sigma 0}>_1 + u_{-k}^* v_k G_{\sigma 0}(\tau)<F^{\sigma 0}>_1 \tag{4.39}$$

The next more complicated pairings appear as

$$-\int_0^\beta d\tau_j \int_0^\beta d\tau_i \frac{1}{N}\sum_{ijk}B_{0\sigma}(\tau_j-\tau_i,\boldsymbol{k})e^{ik(R_j-R_i)}<T_\tau \overleftarrow{\tilde{c}_{l-\sigma}(\tau)\tilde{c}_{m\sigma}(0)\overleftarrow{\tilde{c}^+_{j\sigma}(\tau_j)\tilde{c}_{i\sigma}(\tau_i)}}>_0 =$$

$$-\int_0^\beta d\tau_j \int_0^\beta d\tau_i \frac{1}{N}\sum_{ijk}B_{0\sigma}(\tau_j-\tau_i,\boldsymbol{k})e^{ik(R_j-R_i)}<T_\tau \underleftarrow{\tilde{c}_{l-\sigma}(\tau)\tilde{c}_{i\sigma}(\tau_i)\tilde{c}_{m\sigma}(0)\tilde{c}^+_{j\sigma}(\tau_j)}>_0 U_{ep}(\tau_j-\tau_i) = ,$$

$$=\frac{1}{N}\sum_k e^{ik(R_l-R_m)}\varphi_{k\sigma}^{12}(\tau)$$

where

$$\varphi_{k\sigma}^{12}(\tau\to+0) = \int_0^\beta d\tau_j \int_0^\beta d\tau_i \frac{1}{N}\sum_{k'}\frac{1}{\beta}B_{0\sigma}(\tau_j-\tau_i,\boldsymbol{k}')\cdot$$

$$\cdot\left\{ \begin{array}{l} u_k^* v_{k'}^* v_k^2 G_{0\sigma}(\tau_i-\tau)G_{0-\sigma}(\tau_j-\tau)G_{-\sigma 0}(-\tau)<F^{-\sigma 0}>_0 - \\ v_k u_{k'}(u_k^*)^2 G_{-\sigma 0}(\tau_i-\tau)G_{\sigma 0}(\tau_j-\tau)G_{0\sigma}(-\tau)<F^{\sigma 0}>_0 \end{array}\right\}\cdot U_{ep}(\tau_i-\tau_j)-$$

$$-\int_0^\beta d\tau_j \int_0^\beta d\tau_i \frac{1}{N}\sum_{k'}\frac{1}{\beta}B_{0\sigma}(\tau_j-\tau_i,\boldsymbol{k}')U_{ep}(\tau_i-\tau_j)\cdot\left\{ \begin{array}{l} |u_{k'}|^2 v_k u_{-k}^* G_{0\sigma}(\tau_i-\tau)G_{\sigma 0}(\tau_j)\partial_\sigma <F^{\sigma 0}>_0 + \\ +u_k^* v_{k'}^* v_k v_{-k} G_{0\sigma}(\tau_i-\tau)G_{0-\sigma}(\tau_j)\partial_{-\sigma} <F^{\sigma 0}>_0 + \\ +v_k u_k u_k^* u_{-k}^* G_{-\sigma 0}(\tau_i-\tau)G_{\sigma 0}(\tau_j)\partial_{-\sigma} <F^{\sigma 0}>_0 + \\ +|v_{k'}|^2 u_k^* v_{-k} G_{-\sigma 0}(\tau_i-\tau)G_{0-\sigma}(\tau_j)\partial_{-\sigma} <F^{\sigma 0}>_0 \end{array}\right\}$$

85

Here, the cumulants $<F_p^{\sigma 0} F_{p'}^{\sigma 0}>_0$ and $<F_p^{-\sigma 0} F_{p'}^{\sigma 0}>_0$ correspond to linked diagrams and expressed in the terms of derivatives $\partial_\sigma <F^{\sigma 0}>_0$ and $\partial_{-\sigma} <F^{\sigma 0}>_0$, respectively, where $\partial_\sigma = \partial/\partial(-\beta\varepsilon_\sigma)$.

Also, we have to evaluate the mean value $K_2 = <T_\tau \tilde{c}_{l-\sigma}(\tau)\tilde{c}_{m\sigma}(0)\tilde{c}_{j-\sigma}^+(\tau_j)\tilde{c}_{i-\sigma}(\tau_i)>_0$ at $\tau \to +0$. In the previous correlator $K_1 = <T_\tau \tilde{c}_{l-\sigma}(\tau)\tilde{c}_{m\sigma}(0)\tilde{c}_{j\sigma}^+(\tau_j)\tilde{c}_{i\sigma}(\tau_i)>_0$ after the replacements $\sigma \to -\sigma$ and $m \leftrightarrow l$, we obtain $-K_2$ in the limit for $\tau \to -0$. Thus from K_1 it follows

$$\varphi_{k\sigma}^{21}(0) = -\varphi_{-k-\sigma}^{12}(\tau \to -0).$$

One can point out that the Fourier transform of $<\tilde{c}_{l-\sigma}\tilde{c}_{m\sigma}>$ is $\varphi_{k\sigma}$, i.e.,

$$<\tilde{c}_{l-\sigma}\tilde{c}_{m\sigma}> = \frac{1}{N}\sum_k e^{ik(R_l - R_m)}\varphi_{k\sigma}$$

It follows that $<\tilde{c}_{-k-\sigma}\tilde{c}_{k\sigma}> = \varphi_{-k\sigma}$. Using the relations $G_{0\sigma}(\tau \to +0) = G_{\sigma 0}(\tau \to -0) = 0$ and $G_{\sigma 0}(\tau \to +0) = -G_{0\sigma}(\tau \to -0) = -1$ at $\varepsilon_\sigma < 0$ as well as that in the paramagnetic phase the indices σ and -σ denote the same state we obtain

$$\varphi_{k\sigma}^{12}(0) + \varphi_{k\sigma}^{21}(0) = \int_0^\beta d\tau_j \int_0^\beta d\tau_i \frac{1}{N}\sum_{k'}\frac{1}{\beta} B_{0\sigma}(\tau_j - \tau_i, k') \cdot U_{ep}(\tau_i - \tau_j) <F^{\sigma 0}>_0 \cdot$$
$$\cdot \{v_{k'}u_{k'}(u_k^*)^2 G_{-\sigma 0}(\tau_i)G_{\sigma 0}(\tau_j) + u_{k'}^* v_{k'}^* v_{-k}^2 G_{0-\sigma}(\tau_i)G_{0\sigma}(\tau_j)\} \qquad (4.40)$$

Apparently, those integrals

$$\int_0^\beta d\tau_j \int_0^\beta d\tau_i \frac{1}{N}\sum_{k'}\frac{1}{\beta} B_{0\sigma}(\tau_j - \tau_i, k') \cdot U_{ep}(\tau_i - \tau_j)G_{-\sigma 0}(\tau_i)G_{\sigma 0}(\tau_j) =$$

$$= \int_0^\beta d\tau_j \int_0^\beta d\tau_i \frac{1}{N}\sum_{k'}\frac{1}{\beta} B_{0\sigma}(\tau_j - \tau_i, k') \cdot U_{ep}(\tau_i - \tau_j)G_{0-\sigma}(\tau_i)G_{0\sigma}(\tau_j) =$$

$$= \frac{1}{N}\sum_{k'n_1n_2}\frac{1}{\beta} B_{0\sigma}(i\omega_{n_1}, k')U_{ep}(i\omega_{n_1} - i\omega_{n_2})G_{-\sigma 0}(i\omega_{n_2})G_{\sigma 0}(-i\omega_{n_2})$$

Here we used the next property of the unperturbed Green's function $G_{0\sigma}(i\omega_n) = -G_{\sigma 0}(-i\omega_n)$.

Thus, the left hand of Eq. (4.40) does not depend on the wave vector **k** because of Eq. (4.27) and this contribution in the gap function (4.11) equals zero. Then for the gap function

$$<\tilde{c}_{-k-\sigma}\tilde{c}_{k\sigma}> = -u_{-k}^* v_k <F^{\sigma 0}>_1$$

Using Eqs. (4.27) we obtain the equation for the gap

$$\Delta_k = \frac{1}{N}\sum_q J(q+k)\frac{\Delta_q}{2|\tilde{E}_q|}<F^{\sigma 0}>_1 \qquad (4.41)$$

In the limit $T \to 0$, Eq. (4.41) practically coincides with a similar one obtained in [61]. There is one essential difference. In [61] the temperature factor depends on the wave vector and tends to unity at $T \to 0$. In our case, the electron-hole presence is accounted for it. As a result, we have **k**–independent factor $<F^{\sigma 0}>_1$ equal to 1/2 at $T \to 0$. This factor is determined by Eq. (4.38). When finding the critical temperature of the superconducting state we can put $\delta\tilde{\tilde{\mu}}_\sigma = \delta\tilde{\mu}_\sigma$

Then one can write

$$< F^{\sigma 0} >_1 = \frac{e^{\beta E_\sigma} + 1}{1 + e^{\beta E_\sigma} + e^{\beta E_{-\sigma}}}, \tag{4.42}$$

where $E_\sigma = -\varepsilon_\sigma + \delta\tilde{\mu}_{-\sigma}$ and

$$\beta\delta\tilde{\mu}_\sigma = \frac{1}{N}\sum_{q\omega_n} \beta B_{0\sigma}(q, i\omega_n)\tilde{G}_{0\sigma}(i\omega_n) \tag{4.43}$$

with $\tilde{G}_{0\sigma}(i\omega_n)$ from Eq. (4.31). The solution of Eq. (4.41) at the temperature $T = T_{SC}$ when $\Delta = 0$ gives the self-consistent equation for the superconducting transition temperature

$$T_{SC} = \frac{\tilde{\mu} + \delta\tilde{\mu}_\sigma}{\ln\dfrac{J - 2\tilde{\mu}}{4\tilde{\mu} - J}} . \tag{4.44}$$

From Eq. (4.44) the next requirement on the chemical potential is following:

$$J/4 \le \tilde{\mu} \le J/3 . \tag{4.45}$$

This condition is rigorous and that is why the preceding spin-fluctuation theories failed in the explanation of the high-temperature superconductivity. As will be seen from a next section, the chemical potential of the paramagnetic state of strongly correlated electrons substantially exceeds an exchange parameter J, i.e., strong charge-spin fluctuations destroy Cooper pairs.

4.4. Normal state of electrons in the absence of the electron-phonon interaction

Theory of the effective self-consistent field and the phase transition in a system of strongly correlated d-electrons in cuprates was developed in our works [65, 66]. In particular, an equation for the chemical potential in a paramagnetic state reads as

$$< F^{\sigma 0} > = 1 - \frac{n}{2} = < F^{\sigma 0} >_1 - \tilde{v}_{-\sigma} < F^{-\sigma 0} >_1, \tag{4.46}$$

where $< F^{\sigma 0} >_1$ is determined by Eq. (4.42) and at $g = 0$

$$\delta\tilde{\mu}_\sigma = \delta\mu_\sigma = \frac{1}{N}\sum_q t(q)f(E_{q\sigma}) \tag{4.47}$$

$$\tilde{v}_\sigma = v_\sigma = \frac{1}{< F^{\sigma 0} >}\left\{\frac{1}{N}\sum_q f(E_{q\sigma}) - f(\varepsilon_\sigma)\right\} \tag{4.48}$$

Here, the band energy $E_{q\sigma} = \varepsilon_\sigma + t(q) < F^{\sigma 0} >$ and Fourier components of the hoping integral $t(\mathbf{q}) = \sum_{ij} t_{ij} e^{-i\mathbf{q}(\mathbf{r}_i - \mathbf{r}_j)} = 2t(\cos(q_x a) + \cos(q_y a))$ for a rectangular lattice with constant a.

Let the functions $I(x)$ and $E(x)$ be given by

$$I(x) = \int_{-2}^x D_C(x)dx \qquad E(x) = \int_{-2}^x x D_C(x)dx , \tag{4.49}$$

where the electron density of state $D_C(x)$ has the following form for a rectangular lattice

$$D_C(x) = \frac{1}{\pi^2} K\left(\sqrt{1 - (x/2)^2}\right) \tag{4.50}$$

and $K(x)$ is a complete elliptic integral of the first order. At $T = 0$ and $\tilde{\mu} + \delta\mu_\sigma > 0$ it is easy to write the solution of Eq. (4.46) for a chemical potential of the paramagnetic (PM-2) phase:

$$\tilde{\mu}/W = \frac{2-n}{8} I^{-1}\left(1 - \frac{1}{2}(1-n)(2-n)\right), \qquad (4.51)$$

where $I^{-1}(x)$ is an inverse function of $I(x)$. It corresponds to the gas limit in a hole concentration $1-n$, when $< F^{\sigma 0} >_1 = 1/2$. Indeed, $< F^{\sigma 0} > = 1 - n/2$, i.e., at $n \sim 1$ we have $< F^{\sigma 0} > \sim 1/2$. At $T = 0$ and $\tilde{\mu} + \delta\mu_\sigma < 0$ we obtain for the paramagnetic (PM-1) phase:

$$\tilde{\mu}_{PM1}/W = \frac{2-n}{8} I^{-1}\left(\frac{n}{2}\left(1 - \frac{n}{2}\right)\right)$$

that corresponds to the gas limit in the electron concentration n: $< F^{\sigma 0} >_1 = 1$ and $< F^{\sigma 0} > \sim 1$. In Fig. 4.1 the concentration dependence of the chemical potential in units of the bandwidth W in PM-1 and PM-2 phases is shown. One can see the disrupt of $\tilde{\mu}$ at $n = n_{cr.} = 0.5714$. From Fig. 4.1 it is easy to see the correlation narrowing of the band W in the PM-2 phase. Indeed, at $n = 1$ we have $\tilde{\mu}/W = 0.25$ that it less then $\tilde{\mu}/W = 0.5$ for the ferromagnetic state when such narrowing is absent [57]. In the work [49] similar narrowing of PM is also observed. Unfortunately, this narrowing is insufficient to fulfill the condition (4.45) even at $n = n_{cr.}$ when $\tilde{\mu}(n_{cr.})/W \approx 0.09$. With an increase in temperature, the chemical potential is also increased.
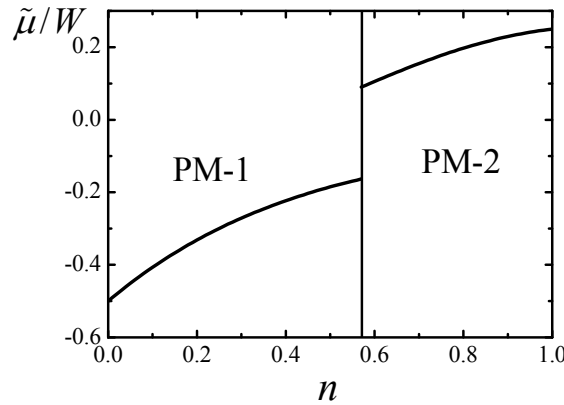

Fig. 4.1. Concentration dependence of the chemical potential in PM-1 and PM-2 phases in units of the bandwidth W. At $n = 0.5714$ there is a disrupt of $\tilde{\mu}$
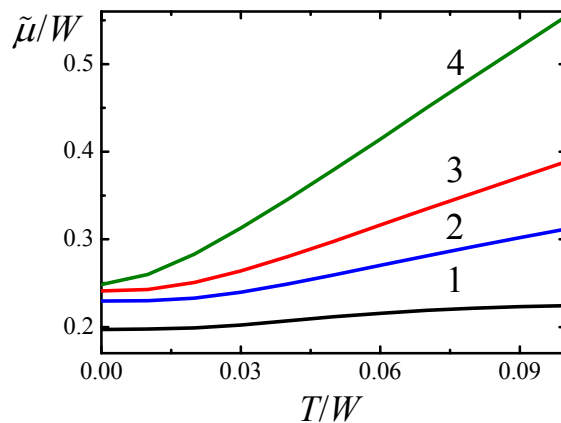

Fig. 4.2. Temperature dependencies of the chemical potential at the electron concentration $n = 0.8, 0.9, 0.95$ and 0.99 (curves 1–4, respectively)

In Fig. 4.2 temperature dependencies of the chemical potential at the electron concentration n = 0.8, 0.9, 0.95 and 0.99 (curves 1–4, respectively) are demonstrated. These curves were obtained by the numerical solution of Eq. (4.46). It turns out that the inclusion of the electron-phonon interaction may enforce essentially the correlated band narrowing at which conditions (4.45) can be fulfilled.

4.5. Normal state of the cuprate d-electrons with polaron excitations

The problem of the polaron excitations in a system of d-electrons has been considered by many authors [51, 62, 63, 67]. We will not analyze these works in detail but rather point out on the main their limitations. Unfortunately, the authors simplify the Hamiltonian V renormalizing a hopping integral t by a factor $e^{-\lambda^2}$. As a result, we obtain a drastic decrease in temperature of the superconducting state [63] and the authors have to use effects of interactions of a higher order of smallness. In fact, the situation is more complicated. It is connected with properties of the unperturbed Green's functions $\tilde{G}_{\alpha\beta}(i\omega_n)$. In the series expansion of Eq. (4.31) for m-th order we have product $e^{-\lambda^2}$ and $\lambda^{2m}/m!$. As was proved by Mahan G.D. in his book [19], there is a Gaussian $\dfrac{1}{\sqrt{2\pi m}}\exp\left[-(\lambda^2-m)/(2m)\right]$ instead of $e^{-\lambda^2}$. Thus, with increasing λ a number m of the polaron band, where the spectral function has a maximum, is increased.

Let us consider this question more thoroughly. In zeroth order of the effective field for a total Green's function $\Lambda_{0\sigma}(i\omega_n,\boldsymbol{q})$ the graphic equation is presented in Fig. 4.3, where the bold, thin straight and wave lines correspond to $\beta\Lambda_{0\sigma}(i\omega_n,\boldsymbol{q})$, $\beta\tilde{G}_{0\sigma}(i\omega_n)$ and $t(\mathbf{q})$, respectively The solution of this equation is written as

$$\beta\Lambda_{0\sigma}(i\omega_n,\mathbf{q}) = \frac{\beta\tilde{G}_{0\sigma}(i\omega_n)<F^{\sigma 0}>}{1-\beta t(\mathbf{q})\tilde{G}_{0\sigma}(i\omega_n)<F^{\sigma 0}>} \tag{4.52}$$

In this equation, we replace $<F^{\sigma 0}>_0$ on the total average $<F^{\sigma 0}>$ to obtain a self-consistent parameter for the effective kinematic field. The main problem in Eq. (4.52) is related to the determination of poles defined by the following equation

$$1-\beta t(\mathbf{q})\tilde{G}_{0\sigma}(i\omega_n)<F^{\sigma 0}> = 0 \tag{4.53}$$
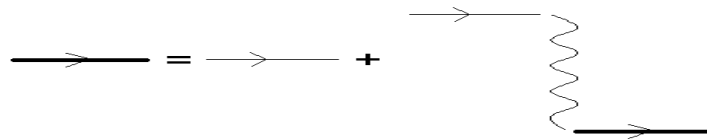

Fig. 4.3. Graphic equation for the Green's function $\Lambda_{0\sigma}(i\omega_n,\boldsymbol{q})$

Indeed, in the diagram methods one should often evaluate frequency summations. Traditional methods solve this problem if the poles of Matsubara Green's functions are known

[19]. Unfortunately, Eq. (4.53) for $i\omega_n$ gives the algebraic equation of an infinity order and the task becomes unsolved. It turn out that one can overcome this difficulty by the method of an inverse function. To understand the essence of the problem we will simplify the Green's function $\tilde{G}_{0\sigma}(i\omega_n)$. It is supposed that in the system studied the condition $\omega_0/T \gg 1$ should be fulfilled. Then the Bose factor B in Eq. (4.31) is replaced by $\exp(-\beta\omega_0)$ that allows to write $\tilde{G}_{0\sigma}(\Omega)$ in a more simple form:

$$\tilde{G}_{0\sigma}(\Omega) = \frac{e^{-\lambda^2}}{\beta} \sum_{m=0}^{\infty} \frac{\lambda^{2m}}{m!} \left\{ \frac{f(\varepsilon_\sigma)}{\Omega - \varepsilon_\sigma + m\omega_0} + \frac{1 - f(\varepsilon_\sigma)}{\Omega - \varepsilon_\sigma - m\omega_0} \right\} \tag{4.54}$$

Let $(\Omega - \varepsilon_\sigma)/\omega_0 = w$. Then we have

$$\beta\tilde{G}_{0\sigma}(w) = \frac{1}{w\omega_0} \left\{ M(1, 1+w, -\lambda^2) f(\varepsilon_\sigma) + M(1, 1-w, -\lambda^2)(1 - f(\varepsilon_\sigma)) \right\}, \tag{4.55}$$

where $M(a,b,z)$ is the confluent hypergeometric function of Kummer [54]. In Fig. 4.4 $\beta\tilde{G}_{0\sigma}(w)$ as a function of w is presented at $T = 0$ for $\varepsilon_\sigma = -\tilde{\mu} < 0$, $g/W = 0.07$ and phonon frequency $\omega_0/W = 0.01875$. As illustrated in Fig. 4.4, it has monotonous behavior between poles m and $m+1$. It allows to determine an inverse function $[\beta\tilde{G}_{0\sigma}(\Omega)]^{-1}$ in this area. Let us denote by $E_{nq\sigma}$ the n-th root of Eq. (4.53). In the vicinity of $E_{nq\sigma}$ one can expand $\beta\tilde{G}_{0\sigma}(\Omega)$ in powers of $\Omega - E_{nq\sigma}$ and we have

$$\beta\Lambda_{0\sigma}(\Omega, \boldsymbol{q}) \approx \sum_n \frac{\beta\tilde{G}_{0\sigma}(E_{nq\sigma}) <F^{\sigma 0}>}{-t(\boldsymbol{q}) <F^{\sigma 0}> \left. \dfrac{d\beta\tilde{G}_{0\sigma}(\Omega)}{d\Omega} \right|_{\Omega = E_{nq\sigma}}} (\Omega - E_{nq\sigma})$$

After the analytic continuation $\Omega \to \Omega + i\delta$ we obtain the imaginary part of $\beta\Lambda_{0\sigma}(\Omega, \boldsymbol{q})$:

$$\mathrm{Im}(\beta\Lambda_{0\sigma}(\Omega, \boldsymbol{q})) = \pi \sum_n \frac{\beta\tilde{G}_{0\sigma}(E_{nq\sigma})}{t(\boldsymbol{q}) \dfrac{d\beta\tilde{G}_{0\sigma}(\Omega)}{d\Omega}} \delta(\Omega - E_{nq\sigma}),$$

where $\delta(x)$ is the Dirac delta function. The uniform spectral density $R_\sigma(\Omega, 0)$ is determined as

$$R_\sigma(\Omega, 0) = -\frac{2}{N} \sum_q \mathrm{Im}(\beta\Lambda_{0\sigma}(\Omega, \boldsymbol{q})) \tag{4.56}$$
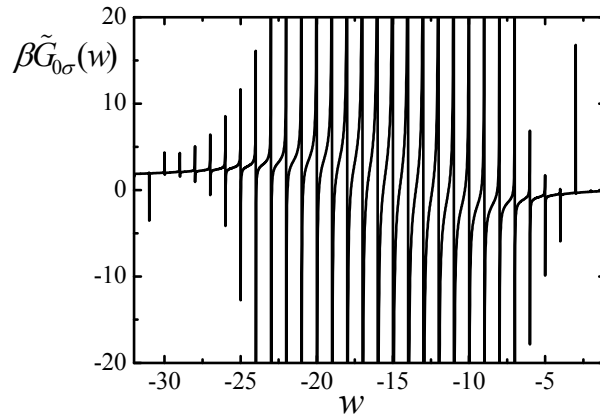

Fig. 4.4. The frequency dependence of the unperturbed fermion-boson Green's function $\beta w \omega_0 \tilde{G}_{0\sigma}(w)$ at $T = 0$, $g/W = 0.07$, $\omega_0/W = 0.01875$ and $\tilde{\mu} > 0$

To sum over q we will consider the dimensionless functions $\beta W \tilde{G}_{0\sigma}(\Omega) = F(\tilde{\Omega})$, $\tilde{E}_{nq\sigma} = E_{nq\sigma}/W$, $\tilde{\Omega} = \Omega/W$ and $t(q)/W = \varepsilon/4$, where the variable $\varepsilon \in [-2, 2]$. Then the two-dimensional integral (4.56) is replaced by the one-dimensional one with the density of states $D_C(\varepsilon)$ from (4.50). The complicated delta function can be simplified by the relation [19]:

$$W\delta[\Omega - E_{nq\sigma}] = \frac{\delta(\varepsilon - \varepsilon_{0n})}{\left|(\tilde{\Omega} - \tilde{E}_{nq\sigma})'\right|_{\varepsilon = \varepsilon_{0n}}},$$

where $\varepsilon_{0n} = \dfrac{4}{F(\tilde{\Omega}) < F^{\sigma 0} >}$ is the function of the external frequency $\tilde{\Omega}$. To find the derivative of $\tilde{E}_{nq\sigma}$ as a function of variable ε, we use the equation for the n-th pole

$$1 - \frac{1}{4}\varepsilon < F^{\sigma 0} > F(\tilde{E}_{nq\sigma}) = 0$$

that gives $\tilde{E}_{nq\sigma}(\varepsilon) = F^{-1}\left(\dfrac{4}{\varepsilon < F^{\sigma 0} >}\right)$ and $\tilde{E}_{nq\sigma}(\varepsilon_{0n}) = \tilde{\Omega}$. After the differentiation of the inverse function $F^{-1}(x)$ we get

$$\left|(\tilde{\Omega} - \tilde{E}_{nq\sigma}(\varepsilon))'\right|_{\varepsilon = \varepsilon_{0n}} = \frac{4}{\varepsilon^2 < F^{\sigma 0} > \left|F'(\varepsilon)\right|}\Bigg|_{\varepsilon = \varepsilon_{0n}} \tag{4.57}$$

Using (4.56) and (4.57) one can write the electron spectral density for the n-th band

$$R_{\sigma n}(\Omega, 0) = -\int_{-2}^{2} d\varepsilon \frac{2\pi}{W} D_C(\varepsilon) \delta(\varepsilon - \varepsilon_{0n}) \frac{F(\tilde{\Omega})\left|F'(\tilde{\Omega})\right|}{F'(\tilde{\Omega})} \varepsilon < F^{\sigma 0} >,$$

where $n\omega_0 < \Omega < (n+1)\omega_0$ and $\left|F'(\tilde{\Omega})\right|/F'(\tilde{\Omega}) = -1$ (see Eq. (4.54)). We have to combine all n bands into one that gives a uniform electron spectral density throughout the whole frequencies interval:

$$R_{\sigma}(\Omega, 0) = \frac{8\pi}{W} D_C(\psi(\Omega)), \tag{4.58}$$

where $\psi(\Omega) = 4/\left\{\beta W \tilde{G}_{0\sigma}(\Omega) < F^{\sigma 0} >\right\}$.

In Fig. 4.5 the frequency dependences of the electron spectral density $R_{\sigma}(w, 0)$ at the temperature $T = 0$ in units of W are presented. In the absence of the electron-phonon interaction, a typical two-dimensional spectral density with a van Hove singularity is observed. With increasing electron-phonon interaction constant g, the polaron bands are formed, each of which has a pointed singularity. Also, a whole band is shifted to the left edge and its bandwidth depends on g weakly.

Now we will calculate functions $\tilde{\nu}_{\sigma}$ and $\delta\tilde{\mu}_{\sigma}$ in Eq. (4.46) for $\tilde{\mu}$ with account of the electron-phonon interactions. These functions correspond to diagrams a and b in Fig. 4.6, where the straight and wave lines denote $\tilde{G}_{0\sigma}(i\omega_n)$ from (4.31) and the effective kinematic interaction $B_{0\sigma}(i\omega_n, q,)$, respectively,

$$\beta B_{0\sigma}(i\omega_n, \mathbf{q}) = \frac{\beta t(\mathbf{q})}{1 - \beta t(\mathbf{q})\tilde{G}_{0\sigma}(i\omega_n) < F^{\sigma 0} >}$$
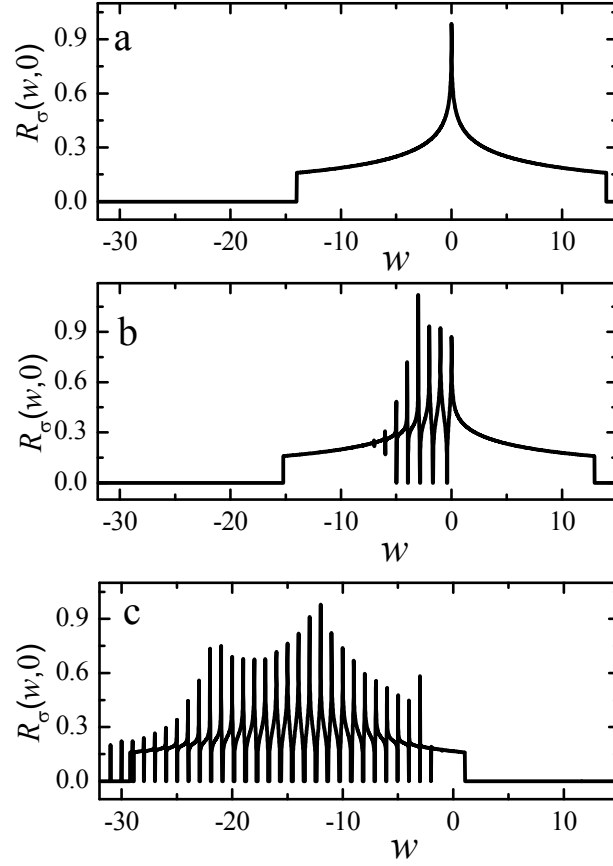
Fig. 4.5. Frequency dependences of the electron spectral density $R_\sigma(w,0)$ at the temperature $T = 0$ in units of W, $g/W = 0$ (a), 0.02 (b) and 0.07(c), $w = (\Omega - \varepsilon_\sigma)/\omega_0$

Fig. 4.6. Diagrams for functions $\beta\delta\tilde{\mu}_\sigma$ (a) and $\tilde{\nu}_\sigma < F^{\sigma 0} >_1$ (b) from Eq. (4.46)

Then one can write

$$\beta\delta\tilde{\mu}_\sigma = \frac{1}{N}\sum_{qn}\beta B_{0\sigma}(i\omega_n,\mathbf{q})\tilde{G}_{0\sigma}(i\omega_n)$$

$$\tilde{\nu}_\sigma < F^{\sigma 0} >_1 = \frac{1}{N}\sum_{qnm}\beta B_{0\sigma}(i\omega_n,\mathbf{q})U_{ep}(i\omega_n - i\omega_m)\left[G_{0\sigma}(i\omega_m)\right]^2 < F >_1 \qquad , \quad (4.59)$$

where the Fourier component $U_{ep}(i\omega_n)$ of the boson unperturbed Green's function $U_{ep}(\tau_i - \tau_j)$ has the following form

$$U_{ep}(i\omega_n) = \frac{1}{\beta}\sum_{m=-\infty}^{+\infty} d_m \frac{2\sinh(\beta m\omega_0/2)}{i\omega_n + m\omega_0}$$

92

and $\omega_n = 4\pi n T$. Also, $\tilde{\nu}_\sigma$ in (4.59) depends on the unperturbed pure electron Green's function (4.30), whereas $\delta\tilde{\mu}_\sigma$ is determined by $\tilde{G}_{0\sigma}(i\omega_n)$ from (4.31). The method of an inverse function can be used to Eq. (4.59) to perform the frequency summation. Indeed, in accordance with a formula from [19] one can evaluate the summation by integration over a contour C to be a circle of the radius R $\to \infty$. Then we have

$$\delta\tilde{\mu}_\sigma = \frac{-1}{N}\sum_q \frac{1}{2\pi i}\oint_C \frac{\beta B_{0\sigma}(\omega,\mathbf{q})\tilde{G}_{0\sigma}(\omega)}{e^{\beta\omega}+1}d\omega = \frac{1}{N}\sum_q \frac{1}{2\pi i}\sum_k \mathrm{Re}\,s\left[\beta B_{0\sigma}(\omega,\mathbf{q})\tilde{G}_{0\sigma}(\omega)\right]_{\omega_k} f(\omega_k),$$

where $\mathrm{Re}\,s\left[\varphi(x)\right]_{\omega_k}$ is the residue of $\varphi(x)$ in the pole ω_k. On then applying the similar procedure as for $R_\sigma(\Omega,0)$ above, we obtain

$$\delta\tilde{\mu}_\sigma = \int_{-\infty}^{+\infty} d\Omega f(\Omega)\frac{4D_C\left(\psi(\Omega)\right)}{W < F^{\sigma 0} >^2 \beta\tilde{G}_{0\sigma}(\Omega)} \tag{4.60}$$

The expression for $\tilde{\nu}_\sigma$ is more complicated:

$$\tilde{\nu}_\sigma = \tilde{\nu}_{\sigma 1} + \tilde{\nu}_{\sigma 2} + r_\sigma, \tag{4.61}$$

where $\tilde{\nu}_{\sigma i}$ and r_σ are equal

$$\tilde{\nu}_{\sigma i} = \int_{-\infty}^{+\infty} d\Omega f(\Omega)\frac{4\varphi_{0\sigma}^i(\Omega)D_C\left(\psi(\Omega)\right)}{W < F^{\sigma 0} >^2 \left[\tilde{G}_{0\sigma}(\Omega)\right]^2} \tag{4.62}$$

$$r_\sigma = -\frac{1}{< F^{\sigma 0} >}\sum_{m=-\infty}^{+\infty} f(\varepsilon_\sigma - m\omega_0)$$

Here,

$$\varphi_{0\sigma}^1(\Omega) = -\frac{1}{\beta}\sum_{m=-\infty}^{+\infty} \frac{2d_m f(\varepsilon_\sigma)(1-f(\varepsilon_\sigma))\sinh\left(\beta m\omega_0/2\right)}{\Omega + m\omega_0} \approx$$

$$\approx -\frac{1}{\beta\Omega} f(\varepsilon_\sigma)(1-f(\varepsilon_\sigma))\left\{M(1,1+\Omega/\omega_0,-\lambda^2) - M(1,1-\Omega/\omega_0,-\lambda^2)\right\}$$

$$\varphi_{0\sigma}^2(\Omega) = -\frac{1}{\beta^2}\frac{\partial(\beta\tilde{U}_{0\sigma}(\Omega))}{\partial\Omega} = -\frac{1}{\beta^2\omega_0}\frac{\partial(\beta\tilde{U}_{0\sigma}(w))}{\partial w}$$

The function (4.61) seems to be divergent since we have in Eq. (4.62) a sum of Fermi functions. However, the detailed analysis shows that the pointed divergence is absent. To prove this statement we divide the integration area in sections from one singularity m to other $m+1$ and then the sum over all intervals reads as

$$\tilde{\nu}_{\sigma 2} + r_\sigma = \frac{1}{< F^{\sigma 0} >}\sum_{m=-\infty}^{+\infty}\left\{R_m - f(\varepsilon_\sigma - m\omega_0)\right\}, \tag{4.63}$$

where the integral on the m-th segment has the form

$$R_m = \int_m^{m+1} dw f(w\omega_0 + \varepsilon_\sigma)\frac{\partial}{\partial w}\left(\psi(w)\right)D_C\left(\psi(w)\right) \tag{4.64}$$

Let w_{lm} and w_{rm} be left and right edges of the segment with the m singularity, respectively. They are determined by equations:

$$\frac{4}{W\beta\tilde{G}_{0\sigma}(w_{im}) < F^{\sigma 0} >} = \pm 2,$$

where upper and lower signs correspond to w_{lm} and w_{rm}, respectively. On now carrying out the partial integration in Eq. (4.64) it is easy to obtain for R_m:

$$R_m = \frac{1}{2}\left[f(w_{lm}\omega_0 + \varepsilon_\sigma) + f(w_{rm}\omega_0 + \varepsilon_\sigma)\right] - \int\limits_{m}^{w_{lm}} dw \frac{df(w\omega_0 + \varepsilon_\sigma)}{dw} S\left(\psi(w)\right) -$$
$$- \int\limits_{w_{lm}}^{m+1} dw \frac{df(w\omega_0 + \varepsilon_\sigma)}{dw} S\left(\psi(w)\right) \tag{4.65}$$

Here, $S(x) = I(x) - 0.5$ (see Eq. (4.49)). Apparently, when $m \to \pm\infty$ the frequency $w_{lm} \to w_{rm}$ and the Fermi functions from Eq. (4.65) will compensate ones from Eq. (4.63). It reflects the existence of only localized phonon modes at high frequencies. One can point out that the number of polaron bands does not exceed 35 - 40 (see Fig. 4.5c) for the considered temperature region and $g/W < 0.085$. Finally, Eqs. (4.60), (4.61) and (4.65) allow to find the numerical solution of a set of equations (4.44) and (4.46) without any difficulties.

4.6. Results of numerical calculations

To calculate the temperature of the superconducting state (4.44), we take the value of the hopping integral $t \sim 0.5$ eV and that of the exchange parameter $J \sim 0.023$ eV [51, 68]. It corresponds to the cuprate YBa$_2$Cu$_3$O$_6$ with the Neel temperature $T_N = 420$ K. The parameter J is determined with the account of ~30% contribution of the spin fluctuations. Then we have the bandwidth $W = 4$ eV. Also, we take the frequency $\omega = 75$ meV to be typical for cuprates in the Einstein model for phonons [19]. Finally, we have $\omega/W = 0.01875$ and $J/W = 0.058$.

Let us consider solutions of Eq. (4.46) at the temperature $T = 0$. At $T \sim 0$ one can rewrite Eq. (4.46) as

$$\tilde{\mu} + \delta\tilde{\mu}_\sigma = T\ln\frac{n/2 - \tilde{v}_\sigma}{1/2 - n/2 + \tilde{v}_\sigma/2} \tag{4.66}$$

It follows from Eq. (4.66) that at $T = 0$ for the PM-2 phase, when $\tilde{\mu} + \delta\tilde{\mu}_\sigma > 0$, the chemical potential obeys the equation $1/2 - n/2 + \tilde{v}_\sigma/2 = 0$. Surprisingly, but there is a situation, when $\tilde{\mu} + \delta\tilde{\mu}_\sigma = 0$ and $1/2 - n/2 + \tilde{v}_\sigma/2 \neq 0$, $n/2 - \tilde{v}_\sigma \neq 0$.

In Fig. 4.7 the curves of $\tilde{\mu}$ as a function of g are presented for different electron concentrations. On curves 2 - 4 at $g = g_{cr.}$ one can see kinks. When $g > g_{cr.}$ the chemical potential obeys the equation $\tilde{\mu} + \delta\tilde{\mu}_\sigma = 0$ and at $g < g_{cr.}$ for $\tilde{\mu}$ we have $1/2 - n/2 + \tilde{v}_\sigma/2 = 0$. At a critical concentration $n = n_{cr.}$ of the transition in the PM-1 phase we have $g_{cr.} = 0$. In the inset the temperature effect is shown.
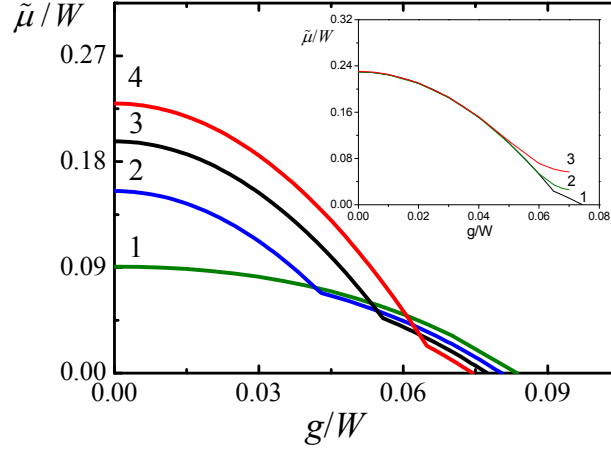
Fig. 4.7. Chemical potential versus constant of the electron-phonon interaction g for electron concentrations $n = 0.571, 0.7, 0.8$ and 0.9 (curves 1-4, respectively) and temperature $T = 0$. In the inset: $\tilde{\mu}$ as a function of g at $n = 0.9$ and temperatures $T/W = 0, 0.005$ and 0.0136 (curves 1–3, respectively)

In Fig. 4.8 the phase diagram in coordinates g-n at $T = 0$ is shown. The upper and lower parts of the superconducting state (SC) boundary is determined by $g_{cr.}$ as a function of n and the value of g at which $\tilde{\mu} = 0$ (see Fig. 4.7). In the SC phase the contribution of the polaron excitation in the narrowing of the electron band is essential. The chemical potential decreases to zero. Thus, the condition (4.45) for the emergence of the SC state can be realized. In the area of the localized state we cannot obtain the solution for $\tilde{\mu}$ corresponding to a hole-doped electron system (the PM-2 phase).

In Fig. 4.9 the concentration dependences of the chemical potential for different parameters of the electron-phonon coupling are presented at $T = 0$. Straight lines show a region of acceptability of $\tilde{\mu}$ at different values of g and n. One can see that at small values of g the bandwidth is insufficiently narrow. At large values of g the pointed region is shifted to the high hole concentration, where the effects of kinematic interactions are strong.
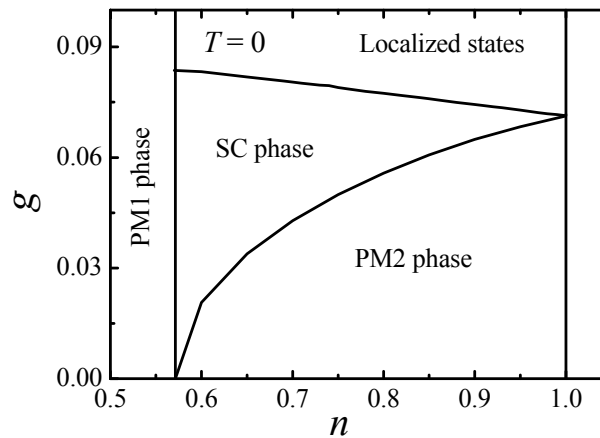
Fig. 4.8. Phase diagram of a strongly correlated electron system with the electron-phonon coupling

Now we will calculate the temperature of the superconducting state T_{SC}. In accordance with Eq. (4.44) it is necessary to find $\tilde{\mu}$ and $\delta\tilde{\mu}_\sigma$ as functions of T and the electron concentration. In Fig. 4.10 the temperature dependences of $\tilde{\mu}$ and $\delta\tilde{\mu}_\sigma$ at $g/W=0.07$ and different electron concentrations were obtained by solving Eq. (4.46). From Fig. 4.10, a it is easy to see that the chemical potential in a definite temperature and concentration regions meets the condition (4.45) and as a result one can solve Eq. (4.44) for T_{SC}. In Fig. 4.11 the concentration dependence of the superconducting state temperature is given for $g/W = 0.07$ and $W = 4eV$. We observe a high-temperature superconductivity with left and right edges of the superconducting phase on the axis n.
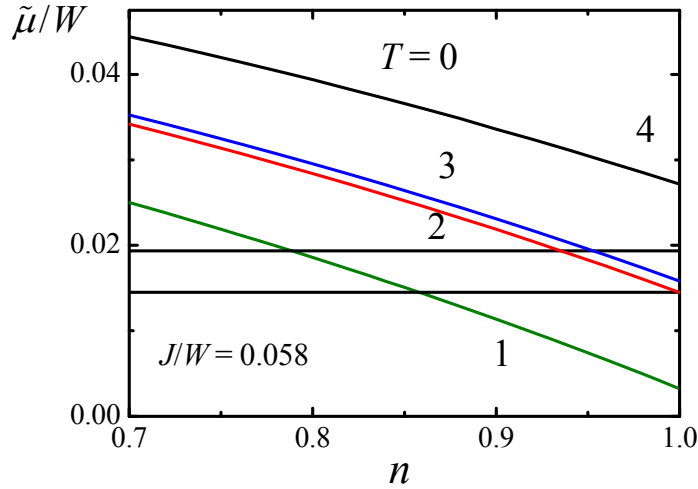
Fig. 4.9. Concentration dependences of the chemical potential at $T = 0$ and parameters of the
electron-phonon coupling $g/W = 0.07$, 0.06555, 0.065 and 0.6 (curves 1-4, respectively)

The area between straight lines determines $\tilde{\mu}$ according to the requirement (4.45) for a SC phase. Indeed, the left edge of the SC phase $n_{LSC} = 0.858$ when $T_{SC}(n_{LSC}) = 0$ is determined from the equation $J/4 + \delta\tilde{\mu}_\sigma = 0$ (see Eq. (4.60)), i.e.,

$$\frac{4(\omega_0/W)^2}{(1-n/2)^2}\int_{-\infty}^{\tilde{\mu}/\omega_0} dw \cdot w \frac{4D_C\left(\dfrac{4w\omega_0/W}{(1-n/2)M(1,1+w,-\lambda^2)}\right)}{M(1,1+w,-\lambda^2)} = -\frac{J}{4W}$$

The right edge $n = 1$ when $T_{SC} = 0$ follows from the condition $\delta\tilde{\mu}_\sigma/W \to 0$ at $n \to 1$ (see Fig. 4.10b). It reflects the weakening of the effective kinematic field at half filling of the band near T_{SC}. Since $\tilde{\mu} \to J/4$ then $\ln\dfrac{J-2\tilde{\mu}}{4\tilde{\mu}-J} \to +\infty$ and $T_{SC} \to 0$. The maximum of T_{SC} from Fig. 4.11 is in a good agreement with the experimental value $T_{SC} \sim 100$ K for $YBa_2Cu_3O_7$ cuprate [51].
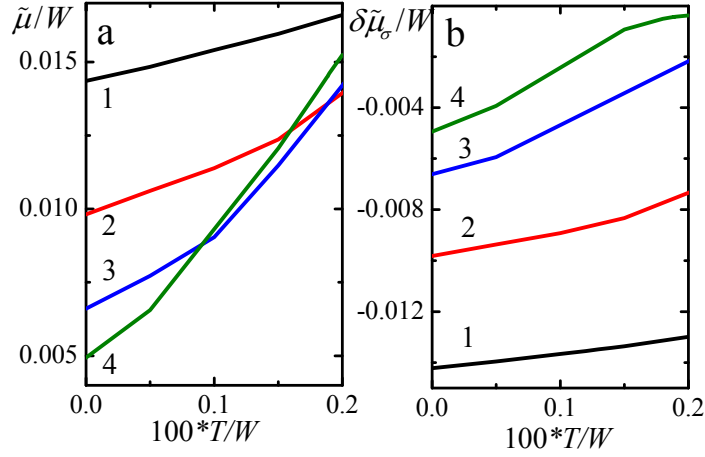
Fig. 4.10. Temperature dependences of $\tilde{\mu}$ (a) and $\delta\tilde{\mu}_\sigma$ (b) at $g/W = 0.07$ and $n = 0.86, 0.92,$ 0.96 and 0.98 (curves 1-4, respectively)
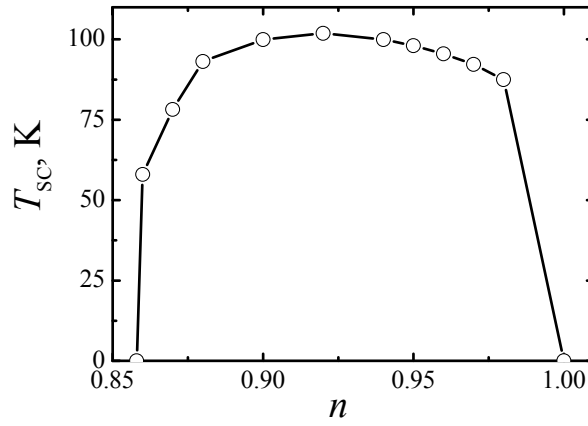
Fig. 4.11. Temperature of the superconducting state T_{SC} versus the electron concentration n with the electron-phonon coupling strength $g/W = 0.07$ and the bandwidth $W=4$ eV

It is interesting to find the gap as a functions of n at $T = 0$ and its temperature dependence for fixed n. The gap Δ is determined from Eq. (4.41) by an expansion $\left|\tilde{E}_q\right|$ into a series in $\Delta/\tilde{\mu}$. It is easy to find that

$$\Delta_k = <F^{\sigma 0}>_1 \Delta_k \frac{J}{2\tilde{\mu}}\left\{1 - \frac{9}{8}\frac{\Delta^2}{\tilde{\mu}^2} + \frac{75}{32}\frac{\Delta^4}{\tilde{\mu}^4} - \frac{18375}{3072}\frac{\Delta^6}{\tilde{\mu}^6} + ...\right\},$$

where $<F^{\sigma 0}>_1$ is determined by (4.42) with $\varepsilon_\sigma = -\mu_g$. At $T = 0$ we have $<F^{\sigma 0}>_1 = 1/2$ and it gives algebraic equations for $\Delta/\tilde{\mu}$. For example, at $n = 0.9$ and $g/W = 0.07$ from Fig. 4.7 (curve 4) we have $\tilde{\mu}/W = 0.0114$ and $\Delta/W = 0.0055$. With the account of $T_{SC}/W = 0.00215$ at $n = 0.9$ we obtain $2\Delta/T_{SC} = 5.15$. In a similar way, the gap Δ versus T dependence was calculated.

In Fig. 4.12 concentration (a) and temperature (b) dependencies of the relationship $2\Delta/T_{SC}$ are shown. An optimal doping gives the maximal value of $2\Delta/T_{SC} \sim 5$ that also corresponds to experimental results for cuprates [51].
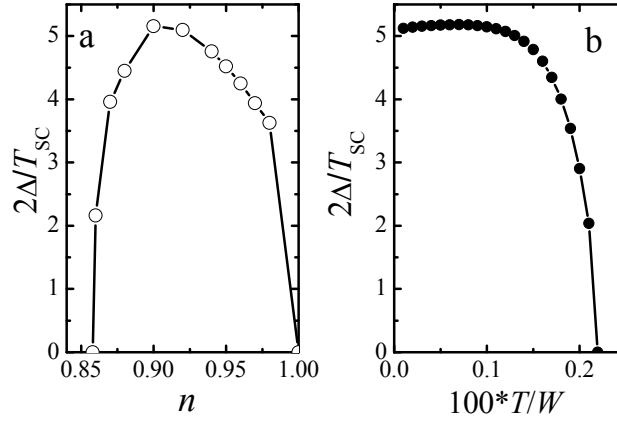
Fig. 4.12. Relationship between the gap and T_{SC} as a function of the electron concentration n at zero temperature (a). Temperature dependence of $2\Delta / T_{SC}$ for $n = 0.92$, $g/W = 0.07$, $J/W = 0.058$ and $T_{SC}/W = 0.0022$ (b)

4.7. Conclusions

In the present chapter, an effect of the electron-phonon interaction on normal and superconducting characteristics of strongly correlated electrons has been studied. It was shown that strong kinematic interactions in a doped system destroy singlet pairs of electrons formed by an indirect exchange. Inclusion of the sufficiently strong electron-phonon coupling stabilizes these pairs by virtue of correlation band narrowing manifested in a drastic decrease of the chemical potential. The phase diagram of ground states in coordinates of the electron-phonon coupling constant g and the electron concentration n was found. At optimal values of g and n for the cuprate $YBa_2Cu_3O_7$ the calculated critical temperature of superconductivity T_{SC} and $2\Delta/T_{SC}$ are very close to experimentally observed values. Thr value $g/W = 0.07$ corresponds to the energy of the Holstein's polaron $E_p = g^2/\omega_0 \sim 1.05$ eV and its radius $R_p = a(W/E_p) \sim 4a$. New method of the frequency summation with an infinite number of poles of unperturbed Green's function was proposed. Exact analytic expressions of diagrams in the first nonvanishing approximation of the perturbation theory were obtained to find the contribution of polarons to the chemical potential.

5. TRANSPORT IN HYBRID STRUCTURES WITH OXIDE BARRIERS

5.1. Introduction

At present, the method for solving a problem of the electron transport in hybrid structures is one of the key tasks from the theoretical as well as practical viewpoint. On the one hand, the derivation of the theory in the framework of modern diagrammatic methods based on the scattering matrix formalism makes it possible to understand better the nature of electronic dynamics in nonequilibrium processes and to study nonlinear effects in the condensed matter as well. On the other hand, the design of electron devices demands sufficiently detailed information concerning processes of the electron scattering in contacts, barriers and impurities caused by industrial technologies. The problem of accounting quantum properties in nanocontacts and nanowires somehow arises as well following the miniaturization of electronic devices.

It should be noted that researchers have accumulated considerable experience in solving these problems [69 - 72] for both normal metals and superconductors. Nevertheless, there are still a number of unsolved questions related to the effects of nonlinear contributions to the current-voltage characteristics of various solid-state structures.

One of the problems is related to the fact that, when a mean current is calculated, it is necessary to take into account the time-dependent evolution of a wave function and the dependence of a current operator on the real time t. Unfortunately, the developed method by Matsubara [73] for evaluating a mean value of the operators at $T \neq 0$ implies a transition to the imaginary time. Indeed, in this case the density matrix is used which satisfies the Bloch equation. As a result, a formula for calculating the S-matrix contains integrals over the imaginary time $\tau = it$. This discrepancy raises a problem of the passage to the limiting case of zero temperatures. Therefore, we will study this question in more detail, which will allow us to generalize the Kubo theory for the transport in a nonlinear limit using the S-matrix. In [74], studying the statistical mechanics of irreversible processes, R. Kubo presented a general expression for the evolution of the density matrix in the quantum-mechanical case, which was expressed in terms of commutators of the perturbation operators in the interaction representation with unperturbed density matrix. However, the obtained formula is technically very difficult to use due to the presence of complicated commutators. Therefore, in most cases [19, 75] only a linear response is considered that does not provide a complete picture of the influence of nonlinear contributions to the transport.

Taking into account the above arguments, the structure of the section is as follows. Subsection 5.2 develops the Kubo theory for chronological products of perturbation operators. This allows us to do away with complex commutators of the time-dependent operators and to obtain a simplified Kubo formula for the mean current. Subsection 5.3 discusses a specific application of the resulting formula for the mean current in a hybrid metal structure with a tunnel barrier. In the subsection 5.4 a linear approximation for the mean current in the mentioned structure is considered. The results obtained are consistent with already known data. In subsection 5.5, the theory is further generalized to the contribution to the mean current in any order of the time perturbation theory. We obtain a quantum-statistical correction to the already known Landauer formula for conductance. It is also shown that the tunneling Hamiltonian correctly describes transport properties of hybrid structures.

5.2. Nonlinear transport theory in the metal with a tunnel barrier

Scattering-matrix formalism in the nonlinear Kubo theory for the electron transport. In this subsection, we consider an effect of the barrier and the applied voltage on the electron transport in a metal at a nonzero temperature T. In the framework of the perturbation theory, the evolution of the wave function in the interaction representation is determined only by the perturbation. It simplifies the calculations considerably. Taking it into account, we start with the Liouville equation for the evolution of the density matrix in the real time ($\hbar = 1$):

$$i\frac{\partial \rho(t)}{\partial t} = [H_T(t), \rho(t)], \tag{5.1}$$

where $\rho(t) = e^{-i\hat{H}_0 t}\rho_I(t)e^{i\hat{H}_0 t}$, $\rho_I(t)$ and $H_T(t)$ are the density matrix $\rho(t)$ and perturbation Hamiltonian H_T in the interaction representation. It is easy to show that

$$\rho_I(t) = \tilde{U}(t)\rho_0\tilde{U}^+(t), \tag{5.2}$$

where the operator $\tilde{U}(t) = e^{i\hat{H}_0 t}e^{-i\hat{H}t}$. The operator $\rho_0 = \dfrac{e^{-\beta\hat{H}_0}}{Tr(e^{-\beta\hat{H}_0})}$ is a standard expression for the unperturbed density matrix at $t = -\infty$ and $1/\beta = T$ is the temperature. Here, it is supposed an infinite slow switching of the perturbation H_T to the unperturbed part $\hat{H}_0$ up to the full Hamiltonian $\hat{H}$. The Schrödinger evolution operator $U(t) = e^{-i\hat{H}_0 t}\tilde{U}(t)$ of the wave function, where $\tilde{U}(t)$ is expressed in terms of the scattering matrix $S(t,-\infty)$ by the next manner

$$\tilde{U}(t) = S(t,-\infty) = T_t \exp\left[-i\int_{-\infty}^{t} H_T(t)dt\right], \tag{5.3}$$

Here, T_t is the time-ordered operator. Apparently, the Hermitian conjugate operator is $U^+(t) = \tilde{U}^+(t)e^{i\hat{H}_0 t}$. Then the mean current is determined by the expression

$$< I >= Tr(\rho I) = \frac{1}{\sum_n \langle n|U^+(t)\rho_0 U(t)|n\rangle}\sum_n \langle n|U^+(t)IU(t)U^+(t)\rho_0 U(t)|n\rangle =$$

$$\frac{1}{Tr(\tilde{U}(t)\rho_0\tilde{U}^+(t))}Tr\left(e^{i\hat{H}_0 t}Ie^{-i\hat{H}_0 t}\tilde{U}(t)\rho_0\tilde{U}^+(t)\right) \tag{5.4}$$

where I is the current operator and the symbol $Tr = \sum_n \langle n|...|n\rangle$ denotes trace with the summation over a complete set of states. By using both the cyclic property of the trace and the definition of the current operator in the interaction representation, we write the expression for a mean current in the form:

$$< I >= \frac{1}{Tr(\rho_I(t))}Tr(I(t)\rho_I(t)) \tag{5.5}$$

It is easy to present the expression (5.2) for $\rho_I(t)$ as a series using the Baker-Campbell-Hausdorff formula [76]:

$$e^A Be^{-A} = \sum_{j=0}^{\infty}\frac{1}{j!}[A,B]_{(j)}, \tag{5.6}$$

where the symbol $\left[A,B\right]_{(j)}$ denotes the *k*-order commutator determined in accordance with the recurrence relation

$$\left[A,B\right]_{(j+1)} = \left[A,\left[A,B\right]_{(j)}\right] \tag{5.7}$$

Here $\left[A,B\right]_{(0)} = B$ and $\left[A,B\right]_{(1)} = \left[A,B\right] = AB - BA$ is the ordinary commutator. Assuming that the perturbation H_T is a Hermitian operator, we write the final expression for $\rho_I(t)$ in any order of the perturbation theory:

$$\rho_I(t) = \sum_{j=0}^{\infty} \frac{(-i)^j}{j!} \int_{-\infty}^{t} dt_j dt_{j-1}...dt_1 T_t \left\{ \left[H_T(t_j), \left[H_T(t_{j-1}), \left[...\left[H_T(t_2), \left[H_T(t_1), \rho_0 \right] \right]...\right] \right\} \tag{5.8}$$

From Eq. (5.8), in the first order in $H_T(t_1)$, it is easy to obtain the linear response in the framework of the Kubo theory for the charge transport. A generalization to higher orders of the perturbation theory causes certain difficulties due to the presence of a large number of commutators under the signs of integrals. It considerably complicates their calculation. Therefore, for convenience, we transform the integrand (5.8). It is obvious that for any t_j the identity holds

$$\left[H_T(t_j), \rho_0 \right] = H_T(t_j)\rho_0 - \rho_0 H_T(t_j)\rho_0^{-1}\rho_0 = A(t_j)\rho_0, \tag{5.9}$$

where

$$A(t_k) = H_T(t_k) - \rho_0 H_T(t_k)\rho_0^{-1} \tag{5.10}$$

Let us consider the commutator in the second order of the expansion (5.8):

$$\left[H_T(t_2)\left[H_T(t_1), \rho_0 \right] \right] = A(t_1)\left[H_T(t_2), \rho_0 \right] + \left[H_T(t_2), A(t_1) \right]\rho_0 = A(t_1)A(t_2)\rho_0 + \left[H_T(t_2), A(t_1) \right]\rho_0 \tag{5.11}$$

The last term in Eq. (5.11) under the signs of the integrals and T_t equals identically zero, since the operator $H_T(t_2)$ is of the Bose-type. Thus, the sign of the commutator term with a minus sign after time ordering is not changed. Obviously, the commutators of higher orders are simplified in a similar way. Then Eq. (5.8) reads as

$$\rho_I(t) = \sum_{j=0}^{\infty} \frac{(-i)^j}{j!} \int_{-\infty}^{t} dt_j dt_{j-1}...dt_1 T_t \left\{ A(t_1)A(t_2)...A(t_j)\rho_0 \right\} \tag{5.12}$$

Substituting Eq. (5.12) into Eq. (5.5) we obtain the formula for the mean current

$$<I> = \frac{1}{Tr(\rho_I(t))} \sum_{j=0}^{\infty} \frac{(-i)^j}{j!} \int_{-\infty}^{t} dt_j dt_{j-1}...dt_1 Tr(T_t \left\{ I(t)A(t_1)A(t_2)...A(t_j)\rho_0 \right\}) \tag{5.13}$$

This expression is essentially simplified by using the linked-diagram theorem [10], which excludes from consideration the diagrams containing unlinked blocks. This theorem is typical in quantum-field methods of statistical physics. Let us introduce the notation

$$\frac{1}{Tr(\rho_I(t))} Tr(T_t \left\{ I(t)A(t_1)A(t_2)...A(t_j)\rho_0 \right\}) = <T_t \left\{ I(t)A(t_1)A(t_2)...A(t_j)\rho_0 \right\} >_{0\,con.},$$

for contributions from the linked diagrams. Then Eq. (5.13) takes the simplest form

$$<I> = \sum_{j=0}^{\infty} (-i)^j \int_{-\infty}^{t} dt_j dt_{j-1}...dt_1 <T_t \left\{ I(t)A(t_1)A(t_2)...A(t_j)\rho_0 \right\} >_{0\,con.} \tag{5.14}$$

Expression (5.14) is the main one when we consider an influence of the nonlinear contributions of the perturbation theory on the transport in electronic systems.

Tunnel barrier in the hybrid structure: normal metal-barrier-normal metal. Let us consider a simple problem of the electron transport in a system formed by two layers of a normal metal which are separated by an oxide film playing the role of a tunnel barrier. In Fig. 5.1 the energy structure of the given model is shown and can be written in the form of the Hamiltonian

$$\hat{H} = \hat{H}_0 + H_T, \qquad (5.15)$$

where $\hat{H}_0 = \hat{H}_L + \hat{H}_R$. The unperturbed parts are $\hat{H}_L = \sum_k (\varepsilon_k - \mu_L)n_k = \sum_p \xi_k n_k$ and $\hat{H}_R = \sum_p (\varepsilon_p - \mu_R)n_p = \sum_p \xi_p n_p$ with ε_k and ε_p, electron energies. The number operators $n_k = a_k^+ a_k$ and $n_p = a_p^+ a_p$ for electron states k and p and chemical potentials μ_L and μ_R are designated for left- and right-hand sides of the hybrid structure, respectively.

The applied electrical voltage bias V shifts the chemical potentials relatively one another in such manner that the relation $\mu_L - \mu_R = eV$ is fulfilled, where e is the electron charge modulus. The perturbation Hamiltonian H_T describing electron tunneling from left- to right-hand side of the hybrid structure reads as

$$H_T = \sum_{kp}\left(T_{kp}a_k^+ a_p + T_{kp}^* a_p^+ a_k\right) \qquad (5.16)$$
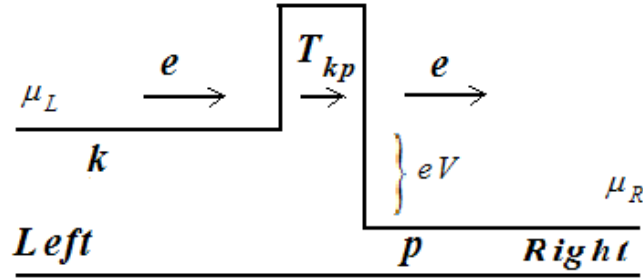
Fig. 5.1. The energy structure of a normal metal-barrier-normal metal model structure

To evaluate the mean electrical current it is necessary to find an expression for operators $A(t_j)$ entering in Eq. (5.14). From the whole set of states with wave vectors k we will fix a single k value. Then one can consider a subspace of two wave functions $|1_k\rangle$ and $|0_k\rangle$ with and without electron in the k state, respectively. It is obvious that the space of all states of the wave vectors is the direct product of these subspaces for each vector k. For example, the operator exponent for the left-hand side of the metal, which determines the unperturbed density matrix, can be represented as a direct product:

$$e^{-\beta\hat{H}_L} = e^{-\beta\sum_k \xi_k n_k} = \prod_k \left\{E_k + \left(e^{-\beta\varepsilon_k} - 1\right)n_k\right\}, \qquad (5.17)$$

where $E_k = \begin{pmatrix} 1 & 0 \\ 0 & 1 \end{pmatrix}$ is the unit matrix and $n_k = \begin{pmatrix} 1 & 0 \\ 0 & 0 \end{pmatrix}$. Obviously, that

$$Tr\left(e^{-\beta\hat{H}_L}\right) = \prod_k \left\{1 + e^{-\beta\varepsilon_k}\right\} \qquad (5.18)$$

One can simplify the expression (5.10) using Eq. (5.6), i.e., the task is reduced to the calculation of commutators of $\hat{H}_0$ and H_T. Indeed, it is not difficult to find a commutator in the first order of the expansion (5.6), which is expressed as follows:

$$\left[\hat{H}_0, H_T\right] = \sum_{kp} (\xi_k - \xi_p)\left\{T_{kp} a_k^+ a_p - T_{kp}^* a_p^+ a_k\right\}$$

It can be shown that the commutator of the next order looks as

$$\left[\hat{H}_0\left[\hat{H}_0, H_T\right]\right] = \sum_{kp} (\xi_k - \xi_p)^2 \left\{T_{kp} a_k^+ a_p + T_{kp}^* a_p^+ a_k\right\}$$

The structure of higher-order commutators is evident. Therefore, we immediately write the operator $A(t_j)$ from (5.10) in the form:

$$A(t_j) = \sum_{kp} \left\{\left(1 - e^{\beta(\xi_p - \xi_k)}\right) T_{kp} a_k^+(t_j) a_p(t_j) + \left(1 - e^{-\beta(\xi_p - \xi_k)}\right) T_{kp}^* a_p^+(t_j) a_k(t_j)\right\} \tag{5.19}$$

This operator cannot be substituted in Eq. (5.14) for the calculation of $<I>$, because in the correlators it is necessary to carry out convolutions with respect to the indices $\boldsymbol{k}$ and $\boldsymbol{p}$. On the other hand, the same indices are also included in ρ_0 of the expression (5.14). Therefore, we select the factors with these indices from ρ_0 and substitute them in (5.19) that leads to the replacement $A(t_j)$ in Eq. (5.14) by $\tilde{A}(t_j)$. This is easy to do if we take into account that the factors in ρ_0 with indices $\boldsymbol{k}$ and $\boldsymbol{p}$ have the form

$$\frac{\left(E_k + \left(e^{-\beta\xi_k} - 1\right)n_k\right)\left(E_p + \left(e^{-\beta\xi_p} - 1\right)n_p\right)}{Tr\left\{\left(E_k + \left(e^{-\beta\xi_k} - 1\right)n_k\right)\left(E_p + \left(e^{-\beta\xi_p} - 1\right)n_p\right)\right\}} = \frac{\left(E_k + \left(e^{-\beta\xi_k} - 1\right)n_k\right)\left(E_p + \left(e^{-\beta\xi_p} - 1\right)n_p\right)}{\left(1 + e^{-\beta\xi_k}\right)\left(1 + e^{-\beta\xi_p}\right)}$$

As a result of this substitution we obtain the expression for $\tilde{A}(t_j)$:

$$\tilde{A}(t_j) = \sum_{kp} \left[f(\xi_p) - f(\xi_k)\right]\left\{T_{kp} a_k^+(t_j) a_p(t_j) - T_{kp}^* a_p^+(t_j) a_k(t_j)\right\}, \tag{5.20}$$

which is substituted in Eq. (5.14) instead of $A(t_j)$. Now in the density matrix ρ_0 the factors with indices $\boldsymbol{k}$ and $\boldsymbol{p}$ are absent, i.e., ρ_0 is replaced by $\tilde{\rho}_0$.

It should be noted that the theory presented in the subsection 5.3 described the evolution of the density matrix for a system with a fixed number of particles. In the reality, there are two subsystems with chemical potentials μ_L and μ_R. Due to the current, the number of particles at the time t in the left- and right-hand sides is not fixed. Therefore, evolution in a system with current should be described by the complete Hamiltonian [19]

$$\hat{H}' = \hat{H}_0' + H_T, \tag{5.21}$$

where

$$\hat{H}_0' = \sum_k \varepsilon_k n_k + \sum_p \varepsilon_p n_p = \sum_k \xi_k n_k + \sum_p \xi_p n_p + \mu_L N_L + \mu_R N_R$$

$N_L = \sum_k n_k$ and $N_R = \sum_p n_p$ is the total number of electrons in the left- and right-hand side of the discussed hybrid structure, respectively. Taking it into account, creation and annihilation operators in the expressions for $H_T(t_j)$ and $\tilde{A}(t_j)$ take the form

$$\tilde{a}_k(t_j) = e^{-it_j\mu_L} a_k(t_j)$$

$$\tilde{a}_k^+(t_j) = e^{it_j\mu_L} a_k^+(t_j)$$

(5.22)

and likewise for the right-hand side of the metal. Thus, we have

$$H_T(t_j) = \sum_{kp} \left\{ e^{ieVt_j} T_{kp} a_k^+(t_j) a_p(t_j) + e^{-ieVt_j} T_{kp}^* a_p^+(t_j) a_k(t_j) \right\}$$

(5.23)

$$\tilde{A}(t_j) = \sum_{kp} \left\{ \tilde{T}_{1kp} e^{ieVt_j} a_k^+(t_j) a_p(t_j) + \tilde{T}_{2kp} e^{-ieVt_j} a_p^+(t_j) a_k(t_j) \right\}$$

(5.24)

where

$$\tilde{T}_{1kp} = \left[f(\xi_p) - f(\xi_k) \right] T_{kp}$$

$$\tilde{T}_{2kp} = -\tilde{T}_{1kp}^*$$

(5.25)

Since $\dfrac{d(N_L + N_R)}{dt} = 0$ and $\dfrac{dN_L(t)}{dt} = i[H, N_L] = -i[N_L, H_T]$, then the current operator is determined as

$$I(t) = -e \frac{dN_L(t)}{dt}$$

and

$$I(t) = ie \sum_{kp} \left\{ e^{ieVt} T_{kp} a_k^+(t) a_p(t) - e^{-ieVt} T_{kp}^* a_p^+(t) a_k(t) \right\}$$

(5.26)

The initial density matrix ρ_0 is determined by the unperturbed Hamiltonian $\hat{H}_0$ since in each subsystem without the current the particle numbers are fixed.

Linear response in the metal with a tunnel barrier. Here, we will consider the application of Eq. (5.14) to calculate the electrical current in a linear approximation. The expression (5.14) takes the form

$$<I>_1 = -i \int_{-\infty}^{t} dt_1 < T_t \left\{ I(t) \tilde{A}(t_1) \tilde{\rho}_0 \right\} >_{0\,con.}$$

(5.27)

Substituting expressions (24) and (26) in Eq. (5.27) we obtain the linear current

$$<I>_1 = 2e \sum_{kpk_1p_1} \int_{-\infty}^{t} dt_1 < T_t \left\{ \begin{matrix} \left\{ e^{ieVt} T_{kp} a_k^+(t) a_p(t) - e^{-ieVt} T_{kp}^* a_p^+(t) a_k(t) \right\} \times \\ \left\{ \tilde{T}_{1k_1p_1} e^{ieVt_1} a_{k_1}^+(t_1) a_{p_1}(t_1) + \tilde{T}_{2k_1p_1} e^{-ieVt_1} a_{p_1}^+(t_1) a_{k_1}(t_1) \right\} \tilde{\rho}_0 \end{matrix} \right\} >_{0\,con.}$$

(5.28)

Factor 2 arises from summing up over electron spins. Keeping in Eq. (5.28) only nonzero correlators and taking into account definitions (5.25) we get

$$<I>_1 = -2e \sum_{kpk_1p_1} \left[f(\xi_{p_1}) - f(\xi_{k_1}) \right] \int_{-\infty}^{t} dt_1 \left\{ \begin{matrix} e^{i(t-t_1)eV} T_{kp} T_{k_1p_1}^* < T_t a_k^+(t) a_p(t) a_{p_1}^+(t_1) a_{k_1}(t_1) \tilde{\rho}_0 >_{0\,con.} + \\ T_{kp}^* T_{k_1p_1} e^{-i(t-t_1)eV} < T a_p^+(t) a_k(t) a_{k_1}^+(t_1) a_{p_1}(t_1) \tilde{\rho}_0 >_{0\,con.} \end{matrix} \right\}$$

(5.29)

The correlators in Eq. (5.29) are decoupled by the Wick's theorem that allows us to write down

$$<I>_1 = -2e \sum_{kp} \left[f(\xi_p) - f(\xi_k) \right] |T_{kp}|^2 \int_{-\infty}^{t} dt_1 \left\{ \begin{matrix} e^{i(t-t_1)eV} < T_t a_k^+(t) a_k(t_1) >_0 < T_t a_p(t) a_p^+(t_1) >_0 + \\ e^{-i(t-t_1)eV} < T_t a_p^+(t) a_p(t_1) >< T_t a_k(t) a_k^+(t_1) >_0 \end{matrix} \right\}$$

(5.30)

104

In Eq. (5.30) the operator $\tilde{\rho}_0$ disappears since it has not multipliers with indices $\boldsymbol{k}$ and $\boldsymbol{p}$. Also in Eq. (5.30) there are unperturbed Green's functions which one can define as

$$G_k(t-t_1) = -<T_t a_k(t) a_k^+(t_1)>_0 = -\theta(t-t_1)<a_k(t)a_k^+(t_1)>_0 + \theta(t_1-t)<a_k^+(t_1)a_k(t)>_0 =$$
$$e^{i\xi_k(t_1-t)}\left(-\theta(t-t_1)Tr(E_k-n_k)+\theta(t_1-t)Tr(n_k)\right) = e^{i\xi_k(t_1-t)}\left(-\theta(t-t_1)+\theta(t_1-t)\right)$$

(5.31)

since $Tr(E_k - n_k) = Tr(n_k) = 1$. The Fourier transform for $G_k(t-t_1)$ has a form:

$$G_k(\omega) = \int_{-\infty}^{+\infty} G_k(t-t_1)e^{i\omega t}dt = \frac{1}{i}\left(\frac{1}{\omega-\xi_k-i\delta}+\frac{1}{\omega-\xi_k+i\delta}\right),$$

(5.32)

where the infinitesimal imaginary corrections are due to adiabatic switching on and off of the perturbation. The Fourier transform of the Green's functions in Eq. (5.30) gives

$$<I>_1 = 2e\sum_{kp}\left[f(\xi_p)-f(\xi_k)\right]\left|T_{kp}\right|^2\int_{-\infty}^{+\infty}\frac{d\omega_1 d\omega_2}{(2\pi)^2}G_k(\omega_1)G_p(\omega_2)\left\{\int_{-\infty}^{t}dt_1\left(e^{i(t_1-t)(\omega_2-\omega_1-eV)}+e^{-i(t_1-t)(\omega_2-\omega_1-eV)}\right)\right\}$$

As a result of the integration over variable t_1, we obtain

$$<I>_1 = 2e\sum_{kp}\left[f(\xi_p)-f(\xi_k)\right]\left|T_{kp}\right|^2\int_{-\infty}^{+\infty}\frac{d\omega_1 d\omega_2}{(2\pi)^2}G_k(\omega_1)G_p(\omega_2)\times$$
$$\left\{\frac{1}{i(\omega_2-\omega_1-eV-i\delta)}-\frac{1}{i(\omega_2-\omega_1-eV+i\delta)}\right\}$$

(5.33)

After substituting the expressions for Fourier transforms of the Green functions in Eq. (5.33), it is easy to integrate with respect to the variables ω_1 and ω_2. The contours of the integration are closed in the upper or lower half-planes of complex variables, depending on the presence of the minimal number of poles. Thus, we have

$$<I>_1 = 2e\sum_{kp}\left[f(\xi_p)-f(\xi_k)\right]\left|T_{kp}\right|^2\left\{\frac{1}{i(\xi_p-\xi_k-eV+3i\delta)}-\frac{1}{i(\xi_p-\xi_k-eV-3i\delta)}\right\}$$

(5.34)

In order to perform the summation in Eq. (5.34) over the wave vectors let us assume $\left|T_{kp}\right|^2 = \left|T\right|^2$ and put for simplicity constant electron densities of the states D_L and D_R and denote the integration variables ξ_L and ξ_R for left- and right-hand sides of the metal, respectively. In accordance with the Landau rule for the poles bypass one can write expression (5.34) in the form:

$$<I>_1 = 4\pi e|T|^2 D_L D_R \int_{-E_F}^{+\infty} d\xi_R \int_{-E_F}^{+\infty} d\xi_L\left[f(\xi_L)-f(\xi_R)\right]\delta\left(\xi_L-\xi_R+eV\right)=$$
$$4\pi e|T|^2 D_L D_R \int_{-E_F}^{+\infty} d\xi_R\left[f(\xi_R-eV)-f(\xi_R)\right]$$

(5.35)

where $\delta(x)$ is the Dirac delta function. Let us consider the case of temperatures $T << E_F$ where E_F is the Fermi energy. Then the Fermi distribution function can be replaced by the Heaviside step function $\theta(-x)$. As a result, we get

$$<I>_1= 4\pi e |T|^2 D_L D_R \int\limits_{-E_F}^{+\infty} d\xi_R \left[\theta(-(\xi_R - eV)) - \theta(-\xi_R) \right] =$$

$$= 4\pi e |T|^2 D_L D_R \int\limits_0^{eV} d\xi_R = 4\pi e^2 |T|^2 D_L D_R V \qquad (5.36)$$

This expression reflects the Ohm's law and coincides with a similar formula obtained in [19] within the framework of the linear Kubo theory for the electron transport.

Nonlinear contribution in the electron transport. Using Eq. (5.14) it is not difficult to generalize an expression for the current to any order of the perturbation theory. Obviously, the next nonzero contribution appears only in the third order since the second order of the series expansion (5.14) includes an odd number of creation and annihilation operators for each metal subsystems. One can write the contribution of the third order from the expression (5.14):

$$<I>_3= -i \int\limits_{-\infty}^t dt_1 dt_2 dt_3 <T_t \left\{ I(t)\tilde{A}(t_1)\tilde{A}(t_2)\tilde{A}(t_3)\tilde{\rho}_0 \right\}>_{0\,con.} \qquad (5.37)$$

Substituting in Eq. (5.37) the expression for $\tilde{A}(t_j)$ (5.19) we have

$$<I>_3= -2e \sum_{\substack{kpk_1p_1 \\ k_2p_2k_3p_3}} \int\limits_{-\infty}^t dt_1 dt_2 dt_3 \begin{Bmatrix} e^{i(t-t_1+t_2-t_3)eV} T_{kp}\tilde{T}_{2k_1p_1}\tilde{T}_{1k_2p_2}\tilde{T}_{2k_3p_3} \times \\ <T_t a_k^+(t)a_p(t)a_{p_1}^+(t_1)a_{k_1}(t_1)a_{k_2}^+(t_2)a_{p_2}(t_2)a_{p_3}^+(t_3)a_{k_3}(t_3)\tilde{\rho}_0 >_{0\,con.} - \\ e^{-i(t-t_1+t_2-t_3)eV} T_{kp}^*\tilde{T}_{1k_1p_1}\tilde{T}_{2k_2p_2}\tilde{T}_{1k_3p_3} \times \\ <T a_p^+(t)a_k(t)a_{k_1}^+(t_1)a_{p_1}(t_1)a_{p_2}^+(t_2)a_{k_2}(t_2)a_{k_3}^+(t_3)a_{p_3}(t_3)\tilde{\rho}_0 >_{0\,con.} \end{Bmatrix} \qquad (5.$$

38)

An additional factor of 2 arises from summing up over spin indices. Carrying out the decoupling of the correlators entering in Eq. (5.38), we obtain

$$<I>_3= 2e \sum_{kpk_1p_1} \varphi_{kpk_1p_1} \int\limits_{-\infty}^t dt_1 dt_2 dt_3 \begin{Bmatrix} e^{i(t-t_1+t_2-t_3)eV} G_k(t_3-t)G_p(t-t_1)G_{k_1}(t_1-t_2)G_{p_1}(t_2-t_3)+ \\ e^{-i(t-t_1+t_2-t_3)eV} G_k(t-t_3)G_p(t_1-t)G_{k_1}(t_2-t_1)G_{p_1}(t_3-t_2) \end{Bmatrix}, (5.39)$$

where $\varphi_{kpk_1p_1} = |T|^4 \left[f(\xi_p) - f(\xi_{k_1}) \right] \left[f(\xi_{p_1}) - f(\xi_{k_1}) \right] \left[f(\xi_{p_1}) - f(\xi_k) \right]$. The Fourier transform of the Green functions and the following integration over t_1, t_2 and t_3 allows to write

$$<I>_3= 2e \sum_{kpk_1p_1} \varphi_{kpk_1p_1} \times \int\limits_{-\infty}^{+\infty} d\omega_1 d\omega_2 d\omega_3 d\omega_4 \begin{Bmatrix} G_k(\omega_1)G_p(\omega_2)G_{k_1}(\omega_3)G_{p_1}(\omega_4) \times \\ \times \{\Psi(\omega_1,\omega_2,\omega_3,\omega_4,\delta) - \Psi(\omega_1,\omega_2,\omega_3,\omega_4,-\delta)\} \end{Bmatrix}, (5.40)$$

where

$$\Psi(\omega_1,\omega_2,\omega_3,\omega_4,\delta) = \frac{1}{i(\omega_2-\omega_3-eV-i\delta)} \frac{1}{i(\omega_3-\omega_4+eV-i\delta)} \frac{1}{i(\omega_4-\omega_1-eV-i\delta)}$$

From Eq. (5.40) it follows that $<I>_3$ as $<I>_1$ are determined by the difference of the complex conjugate values, i.e. $<I>_3$ is real and equal to a double imagine part of one of the integrals. Obviously, this is due to the structure of the current operator, which describes the electron hopping through the barrier in certain as well as the opposite directions, independently

on the order of the perturbation theory. The integrals in Eq. (5.40) are calculated using the theory of residues. Denoting the fourfold integral in Eq. (5.40) as $J_{kpk_1p_1}(\delta)$, we can write its expression in the form:

$$J_{kpk_1p_1}(\delta) = \sum_{i=1}^{4} (J_{kpk_1p_1}^{i}(\delta) - J_{kpk_1p_1}^{i}(-\delta)),$$ (5.41)

where

$$J_{kpk_1p_1}^{1}(\delta) = -\frac{1}{i(\xi_p - \xi_{k_1} - eV - 3i\delta)} \frac{1}{i(\xi_p - \xi_{p_1} - 4i\delta)} \frac{1}{i(\xi_p - \xi_k - eV - 5i\delta)}$$

$$J_{kpk_1p_1}^{2}(\delta) = -\frac{1}{i(\xi_p - \xi_{k_1} - eV - 3i\delta)} \frac{1}{i(\xi_k - \xi_{p_1} + eV + 3i\delta)} \frac{1}{i(\xi_p - \xi_k - eV - 5i\delta)}$$

$$J_{kpk_1p_1}^{3}(\delta) = \frac{1}{i(\xi_{p_1} - \xi_{k_1} - eV + 3i\delta)} \frac{1}{i(\xi_{p_1} - \xi_p + 4i\delta)} \frac{1}{i(\xi_{p_1} - \xi_k - eV - i\delta)}$$

$$J_{kpk_1p_1}^{4}(\delta) = \frac{2}{i(\xi_k - \xi_{k_1} + 4i\delta)} \frac{1}{i(\xi_k - \xi_{p_1} + eV + i\delta)} \frac{1}{i(\xi_k - \xi_p + eV + 5i\delta)}$$

(5.42)

The factor 2 in the last term of Eq. (5.42) appears due to the fact that in Eq. (5.41) there should be 5 terms, but 2 of them are the same. It is seen from Eq. (5.42) that the poles are located both in the upper and lower complex planes. For calculations of the current in a limit $\delta \to 0$ the numerical factors in the front of δ do not play any role. Also, in Eq. (5.41) only the differences of complex conjugate quantities enter. Thus, in the expression for $< I >_3$ the integrals in the sense of a principal value are absent. By analogy with this evaluation, taking into account the Landau rule for bypassing poles we get

$$< I >_3 = 4\pi^3 e \sum_{kpk_1p_1} |T|^4 \left[f(\xi_p) - f(\xi_{k_1}) \right] \left[f(\xi_{p_1}) - f(\xi_{k_1}) \right] \left[f(\xi_{p_1}) - f(\xi_k) \right] \times$$

$$\left\{ \begin{array}{c} -\delta(\xi_{p_1} - \xi_p)\delta(\xi_{k_1} - \xi_p + eV)\delta(\xi_p - \xi_k - eV) + \delta(\xi_{k_1} - \xi_p + eV)\delta(\xi_{p_1} - \xi_k - eV)\delta(\xi_p - \xi_k - eV) + \\ \delta(\xi_{p_1} - \xi_p)\delta(\xi_k - \xi_{p_1} + eV)\delta(\xi_{p_1} - \xi_{k_1} - eV) - 2\delta(\xi_{k_1} - \xi_k)\delta(\xi_{p_1} - \xi_k - eV)\delta(\xi_p - \xi_k - eV) \end{array} \right\}$$

Assuming that the electronic densities of states are constant, we replace the sums over wave vectors by integrals with the same integration variables. It is easy to find that

$$< I >_3 = 4\pi^3 e |T|^4 D_L^2 D_R^2 \int_{-E_F}^{+\infty} d\xi_R \left[f(\xi_R - eV) - f(\xi_R) \right]^3 =$$

$$= 4\pi^3 e^2 |T|^4 D_L^2 D_R^2 \int_{0}^{eV} d\xi_R = 4\pi^3 e^2 |T|^4 D_L^2 D_R^2 V$$

(5.43)

Apparently, in the fifth order of the perturbation theory we have the contribution to a mean electrical current

$$< I >_5 = 4\pi^5 e |T|^6 D_L^3 D_R^3 \int_{-E_F}^{+\infty} d\xi_R \left[f(\xi_R - eV) - f(\xi_R) \right]^5$$

and so on. Summing up the contributions for all orders we obtain geometric series assuming that $\pi^2 |T|^2 D_L D_R \left[f(\xi_L) - f(\xi_R) \right]^2 < 1$. Thus, the common factor of all contributions to the current is

twice the geometric ratio. Then the general expression for the current $<I>$ at finite temperatures takes the form:

$$< I >= 4\pi e |T|^2 D_L D_R \int\limits_{-E_F}^{+\infty} d\xi_R \frac{f(\xi_R - eV) - f(\xi_R)}{1 - \pi^2 |T|^2 D_L D_R \left[f(\xi_R - eV) - f(\xi_R) \right]^2} \qquad (5.44)$$

In particular, at zero temperature a mean electrical current is presented in the form of the renormalized Landauer [77] formula with $\hbar \neq 1$:

$$< I >= \frac{4\pi e^2}{\hbar} \frac{|T|^2 D_L D_R}{1 - \pi^2 |T|^2 D_L D_R} V = \frac{2e^2}{h} \frac{4\tilde{T}}{1 - \tilde{T}} V \ , \qquad (5.45)$$

from which it follows that the barrier transmission should be determined as $\tilde{T} = \pi^2 |T|^2 D_L D_R$. It relates to the probability of the barrier tunneling and depends on electron densities of the left- and right-hand metal sides.

From Eq. (5.45) it follows that for the barrier transmission $\tilde{T} = 1$ the current becomes infinity since the scattering centers are absent. In a single electron approximation, the presence of the finite Landauer resistance $R_k = \frac{h}{2e^2}$ at full barrier transparency gives rise to a contradiction that is explained by many- channel processes in the leads [73]. However, from the general Eq. (5.45) it follows that with the nonlinear contributions the pointed contradiction is removed. The barrier transmission is determined by repeated electron penetrations and reflections. The electron statistic does not allow a separation of penetration and reflection electron processes. Thus, one can say about an effective barrier transmission in hybrid structures. Only at $\tilde{T} = 1/5$ we obtain a ballistic transport with the Landauer conductivity $G = \frac{2e^2}{h}$. Also, the account for electron quantum statistics leads to the fact that the effective coefficient of the electron reflection $\tilde{R}$ from the barrier cannot be represented in a form $\tilde{R} = 1 - \tilde{T}$ as for the one-electron approximation.

It can be seen from Eq. (5.45) that the value $|T|$ of the tunnel matrix element that determines the probability of the electron penetration through the barrier cannot exceed the value of $\frac{1}{2\pi\sqrt{D_L D_R}}$. For this maximum value, the transport of electrons is equivalent to the transport in systems without barriers and scattering. The form of Eq. (5.44), apparently, removes the contradiction of applying the tunnel Hamiltonian [19], where it was indicated that the exponential growth $|T|^2$ as a function ξ_k can exceed the power-law drop of the spectral density. Then the main contribution to the transport is determined by the barrier top. It is an unphysical result. As seen from Eq. (5.44), $|T|^2$ enters both in the numerator and the denominator. It significantly complicates the relationship between the spectral density and the barrier height.

5.3. Asymmetry of the current-voltage characteristic in a hybrid normal meal- superconductor structure with a tunnel barrier

Within the framework of the scattering matrix formalism [78], the nonlinear Kubo theory for the electron transport in the hybrid structure normal metal - superconductor with a tunnel

barrier has been considered. A general expression for the mean electrical current was obtained. In the model of the tunnel Hamiltonian, all linear and nonlinear contributions to a mean electrical current are evaluated. It was obtained that the asymmetry of the current-voltage characteristic is caused by the geometry of the heterostructure. The asymmetry degree asymmetry is determined approximately by the ratio of currents for voltage biases $\pm|eV|>\Delta$ and is equal to $\dfrac{1}{1-\tilde{T}}$ where $\tilde{T} = \pi^2 |T|^2 \rho^2(\mu_R)$ is the effective barrier transmission and Δ is the gap function. T is the bare tunnel matrix element, ρ is the density of states and μ_R is the chemical potential of the normal metal. Also, we observed the appearance an extra current $<I>_{S1}$ proportional to the Debye frequency ω_D with a flow direction from a normal to a superconductive part of the heterostructure.
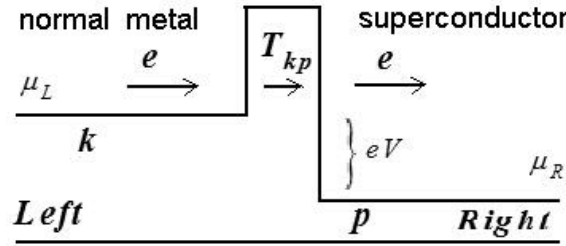
Fig. 5.2. The energy structure of the normal metal-barrier-superconductor model

The expression for a mean current $<I>$ reads as ($\hbar = 1$) [78]

$$<I> = \sum_{j=0}^{\infty} (-i)^k \int_{-\infty}^{t} dt_j dt_{j-1}...dt_1 < T_t \left\{ I(t)\tilde{A}(t_1)\tilde{A}(t_2)...\tilde{A}(t_j)\tilde{\rho}_0 \right\} >_{0\,con.}, \qquad (5.46)$$

where the operators $\tilde{A}(t_i)$ in the interaction representation

$$\tilde{A}(t_j) = \sum_{kp} \left[f(\xi_p) - f(\xi_k) \right] \left\{ T_{kp} a_k^+(t_j) a_p(t_j) - T_{kp}^* a_p^+(t_j) a_k(t_j) \right\}$$

are determined by the tunnel Hamiltonian with matrix element T_{kp} and Fermi distribution function $f(\xi_m)$ for the electron energy ξ_m relatively Fermi level $\mu_{R,L}$. $\tilde{\rho}_0$ is the density matrix and symbol $< T_t \left\{...\right\} >_{0\,con.}$ is the statistical averaging.

The unperturbed Green's functions are

$$G_k(\omega) = \frac{1}{i}\left(\frac{1}{\omega - \xi_k - i\delta} + \frac{1}{\omega - \xi_k + i\delta} \right) \qquad (5.47)$$

$$G_p(\omega) = \frac{u_p^2}{i}\left(\frac{1}{\omega - E_p - i\delta} + \frac{1}{\omega - E_p + i\delta} \right) + \frac{v_p^2}{i}\left(\frac{1}{\omega + E_p - i\delta} + \frac{1}{\omega + E_p + i\delta} \right), \qquad (5.48)$$

for normal and superconductive parts of the heterostructure, respectively. Here, $E_p = \sqrt{\xi_p^2 + \Delta_p^2}$ is the energy of the Cooper pairs and Bogoliubov coefficients

$$u_p^2 = \frac{1}{2}\left(1 + \frac{\xi_p}{E_p}\right)$$
$$v_p^2 = \frac{1}{2}\left(1 - \frac{\xi_p}{E_p}\right)$$

(5.49)

It is easy to find the mean current in the linear approximation

$$<I>_1 = 4\pi e \sum_{kp} \left[f(\xi_k) - f(E_p) \right] |T_{kp}|^2 \left\{ u_p^2 \delta(\xi_k - E_p + eV) + v_p^2 \delta(\xi_k + E_p + eV) \right\} \quad (5.50)$$

For the next nonvanishing approximation we have

$$<I>_3 = -4e\pi^3 |T|^4 \rho^2(\mu_R) \sum_{kp} \left[f(E_p) - f(\xi_k) \right]^3 u_p^2 \delta(\xi_k - E_p + eV) \quad (5.51)$$

For arbitrary voltage polarity at zeroth temperature one can write it in the linear approximation

$$<I>_1 = 4\pi e |T|^2 \rho^2(\mu_R) \Big(\theta(eV - \Delta)\sqrt{(eV)^2 - \Delta^2} + \theta(eV)\omega_D +$$
$$\Big[\theta(-eV)\theta(\Delta + eV)\omega_D - \theta(-\Delta - eV)\sqrt{(eV)^2 - \Delta^2} \Big] \Big), \quad (5.52)$$

where $\theta(x)$ is the Heaviside step function. We get the current as a square root function of the voltage at $\pm|eV| > \Delta$ observed experimentally. It is surprisingly that there is a positive extra current $<I>_{S1} = \frac{2e^2}{h} 4\tilde{T}\frac{\omega_D}{e}$ for an infinitely weak voltage. For example, for Pb at $\tilde{T} = 1$ and the Debye energy $\omega_D = 8.3$ meV with a quantum conductance $G_0 = \frac{2e^2}{h} = 7.75 \cdot 10^{-5} \frac{1}{\text{Ohm}}$ we have $<I>_{S1} \sim 2.6\,\mu\text{A}$.

Similarly, in the third order of the perturbation theory

$$<I>_3 = 4e\pi^3 |T|^4 \rho^3(\mu_R) \sum_p f^3(E_p + eV)u_p^2 = 4e\pi^3 |T|^4 \theta(eV - \Delta)\rho^4(\mu_R)\sqrt{(eV)^2 - \Delta^2} \quad (5.53)$$

Such form of the Eq. (5.53) allows to sum up high orders of the series expansion and to write a general expression for the current as

a) $eV > 0$

$$<I> = \frac{2e^2}{h}\left(\theta(eV - \Delta) \cdot \frac{4\tilde{T}}{1 - \tilde{T}}\sqrt{V^2 - \left(\frac{\Delta}{e}\right)^2} + \theta(eV)4\tilde{T}\left(\frac{E_D}{e}\right)\right) \quad (5.54)$$

b) $eV < 0$

$$<I> = \frac{2e^2}{h}\left(-\theta(|eV| - \Delta) \cdot 4\tilde{T}\sqrt{V^2 - \left(\frac{\Delta}{e}\right)^2} + \theta(\Delta - |eV|)4\tilde{T}\left(\frac{E_D}{e}\right)\right) \quad (5.55)$$

From Eqs. (5.54) - (5.55) we find the current asymmetry determining the barrier transmission $\tilde{T}$. Also, there is an extra current for arbitrary $eV > 0$ and for $|eV| < \Delta$ at $eV < 0$. It is supposed that the origin of this extra current is connected with Andreev reflections of the electrons.

5.4. Conclusions

This part of the book presents a modified nonlinear Kubo theory for the electron transport in hybrid structures of normal metals with a tunnel barrier. Our results can be generalized to the case of superconducting layers and Josephson junctions. The general expression for a mean current is obtained with account of all contributions of the time-dependent perturbation theory. It is found that the nonlinearity of the theory causes a substantial renormalization of the Landauer formula for conductivity in the ground state. It turns out that the Landauer formula is working only in the framework of the one-electron approximation. The ballistic transport conductivity $G = \dfrac{2e^2}{h}$ is realized for the barrier transmission $\tilde{T} = 1/5$. The validity of the tunneling Hamiltonian for transport phenomena in hybrid structures is also justified.

Resuming, (i) a nonlinear theory of the current states in normal metal-barrier-superconductor junctions has been proposed; (ii) the current-voltage asymmetry has been revealed; (iii) in the hybrid structures there is an extra current connected to the Andreev reflections of the electrons.

6. MAGNETIC AND RESISTIVE PROPERTIES
OF MANGANITES

6.1. Introduction

At present, thermodynamics investigation of the double-exchange (DE) model is an actual problem because the theory taking into account consistently the quantum nature of electron and ion spins is still lacking. In manganites with dominant DE and strong electron correlations, strong Hund`s rule coupling of collective e_g electron with the Mn^{4+} ion spin should be taken into account. This essentially extends the wave function basis used and creates some difficulties in the construction of diagram techniques. Anderson and Hasegawa [79] have calculated exactly the spectrum of electron excitations in a system of two multivalent ions Mn^{3+} and Mn^{4+}. De Gennes [80] studied the thermodynamics of a system of classical spins neglecting strong electron correlations. Kubo and Ohata [81] proposed an exact projective transformation of a Hamiltonian with Hund's rule coupling. Unfortunately, because of complicated dependence of this transformation on charge and spin degrees of freedom, the description of thermodynamics was possible only in the low-temperature approximation. In dynamic mean field approximation (DMF), the spins, as a rule, are classical [82]. Moreover, the account of a kinematic electron contribution presupposes both an infinite space dimension and the Dyson's method of the diagram summation. In a coherent potential approximation (CPA) [37, 83], the nonzero value of the imaginary part of the Green's function on the Fermi level was obtained, and the sum rule for a spectral density did not hold. One can suppose that evidently the contribution of charge and spin fluctuations was overestimated. Moreover, this model does not show that the paramagnetic phase is unstable.

In this chapter, the Hamiltonian investigated includes the strong Hund's rule coupling of localized t_{2g} electrons of Mn^{3+} ion with e_g electrons, superexchange of localized spins, electron-phonon interactions as well as the contributions from phonon subsystem and interaction with applied magnetic field, h. In the diagram method used, the effective self-consistent field is extracted.

The thermodynamics of the DE model with an account of Hund's rule coupling in a mean field approximation was previously considered in papers [57, 84, 85]. All contributions to total Green's functions in the first nonvanishing approximation with respect to inverse effective radius of interaction $r \sim 1/z$, where z is the number of nearest neighbours in the simple cubic (s.c.) lattice, were determined.

Let us emphasize that up to now quantum fluctuations in an effective field theory as applied to manganites were not taken into account. We have calculated all quantum states corresponding to the lower quintet of a zeroth Hund's Hamiltonian neglecting the influence of the upper triplet. It is valid in the limit of infinite Hund's rule coupling J_H.

As a basis for the zeroth Hamiltonian, Hund's exchange and its additive part involved with a chemical potential were applied. In this theory, the Hamiltonian describing the kinetic electron energy is a perturbation. We suppose that in the system studied there are strong electron correlations, and then one may neglect the states with twofold site filling. In a weakly doped electron subsystem with electron concentration $n \sim 1$, the Fermi level lies near the top of the valence band. Then the chemical potential μ is proportional to the bandwidth W. In this case, a zeroth Hamiltonian, H_0, meets the necessary criteria of perturbation theory, $H_0 \gg V$.

6.2. Hamiltonian of the system

In the DE model with electron-phonon interactions the Hamiltonian of the system reads as:

$$\hat{H} = \hat{H}_f + \hat{H}_b \ , \tag{6.1}$$

where the Fermi part, $\hat{H}_f$, is expressed as follows :

$$\hat{H}_f = -\sum_i J_H \mathbf{S}_i \boldsymbol{\sigma}_i - \sum_{i,j} J_{ij} (\mathbf{S}_i + \boldsymbol{\sigma}_i)(\mathbf{S}_j + \boldsymbol{\sigma}_j) - h\sum_i \left(\mathbf{S}_i^z + \boldsymbol{\sigma}_i^z\right) - \mu \sum_i n_i + V \tag{6.2}$$

The Bohr magneton, μ_B, and $\tilde{g}$-factor were taken in unit system with $\mu_B \tilde{g} = 1$. The perturbation Hamiltonian may be written as

$$\hat{V} = \sum_{i,j,\sigma} t_{ij} c_{\sigma i}^+ c_{\sigma j} \ , \tag{6.3}$$

where $c_{\sigma i}^+$ ($c_{\sigma i}$) creates (annihilates) an electron of spin σ on a lattice site i. The boson part of the Hamiltonian (6.1) has a form similar to that used in the theory of small polaron:

$$\hat{H}_b = -g\sum_i n_i \left(b_i^+ + b_i\right) + \omega_0 \sum_i b_i^+ b_i \ , \tag{6.4}$$

where g is the electron-phonon coupling strength. In the Einstein model the phonon frequency ω_0 is assumed to be dispersion-free. b_i^+ и b_i are phonon creation and annihilation operators.

In the theory proposed, the following interrelation of parameters : $J_H \gg t_{ij} \sim g \gg |J_{ij}| \sim h$ was used. At first glance, the operator V is not the perturbation. However, as will be seen in the further consideration the hopping integral t_{ij} enters into the expression for a chemical potential μ which is proportional to bandwidth $W = 2zt$, where t is the nearest-neighbour hopping integral. The zeroth Hamiltonian contains only the part of V, which does not depend on the free-carrier concentration. The perturbation near the band half filling is proportional to the hole concentration, since the electron jumps at $n = 1$ are forbidden for this strongly correlated system. This provides the basis for the construction of perturbation theory at $n \sim 1$, which results are correct with an accuracy of $1/z$.

The electron-phonon interactions in manganites were first taken into account in the paper [86] assuming the phonon to be localized classical oscillator. The main conclusion obtained is that in La$_{1-x}$Sr$_x$MnO$_3$ the pure DE model is usable, while in La$_{1-x}$Ca$_x$MnO$_3$ the strong electron-phonon interaction plays an essential role.

In the following, a part of the Hamiltonian (6.2) related to the superexchange interaction is considered in a mean field approximation. We will carry out the unitary transformation S of the Hamiltonian (6.1) as a result of which the fermion and boson operators are separated from one another. The expression for S given by Lang and Firsov [52] has the following form:

$$S = -\frac{gn}{\omega_0} \sum_i (b_i^+ - b_i) \tag{6.5}$$

The Bose shift

$$\tilde{b} = b + \frac{gn}{\omega_0} \tag{6.6}$$

and multiplying Fermi operators

$$\tilde{c}_\sigma = Y c_\sigma \ , \tag{6.7}$$

where $Y = e^{\lambda(b^+ - b)}$ connected exceptionally with phonon degrees of freedom results from the transformation of S, $\lambda = g / \omega_0$. The Hermitian conjugate of Eq. (6.7) is an expression for the creation operator. Substituting transformed operators in Eq. (6.1) we obtain the following zeroth Hamiltonian for the fermion subsystem:

$$\hat{\tilde{H}}_{0f} = \sum_i J_H \mathbf{S}_i \boldsymbol{\sigma}_i - 2J(0) \sum_{ij} (\mathbf{S}_i + \boldsymbol{\sigma}_i)(<S_i^z> + <\sigma_i^z>) - \mu \sum_i n_i - h \sum_i (S_i^z + \sigma_i^z) - \xi \sum_i n_i^2 , \quad (6.8)$$

where $J(0) = zJ$ in the nearest-neighbour approximation, $\xi = g^2 / \omega_0$ is the polaron binding energy, n_i is the number of e_g electrons on the i-th site. The boson part reads as

$$\hat{H}_{0b} = \omega_0 \sum_i b_i^+ b_i \quad (6.9)$$

The Hamiltonian of the interaction V as a function of c_σ and c_σ^+ is expressed in terms of operators $\tilde{c}_\sigma$ and $\tilde{c}_\sigma^+$, respectively.

We will consider the transformed Hamiltonian (6.1) where the tilde sign was omitted. Preliminary we should carry out a diagonalization of the Hamiltonian (6.8) for the Fermi subsystem. The main difficulty is associated with the first term describing Hund's rule coupling between the ion core and a mobile electron. The total basis of the zeroth Fermi Hamiltonian (6.8) includes 12 spin wave functions supposing that Mn^{4+} ion spin S = 3/2 and e_g electron spin σ = 1/2. At h = 0, in the Hund's part of Eq. (6.8), eight spin functions correspond to five- and three-fold degenerated levels of $E_H^0 = -\frac{1}{2} S J_H$ and $E_H^2 = \frac{1}{2}(S+1) J_H$ with S$_2$ = 2 and S$_1$ = 1 spins, respectively. Spin S = 3/2 corresponds to the hole state (Mn^{4+} ion) with four-fold degenerated energy level of $E_H^1 = 0$. The wave functions for the above multiplets are [76]

$$\left|(3/2, 1/2) S' m\right\rangle = \left|\varphi_{S'm}\right\rangle = \sum_{m_1 m_2} C_{m_1 m_2 m}^{3/2 \, 1/2 \, S'} \left|2m_1, 2m_2\right\rangle, \quad (6.10)$$

where $\left|2m_1, 2m_2\right\rangle = \left|3/2, m_1\right\rangle \otimes \left|1/2, m_2\right\rangle$, $C_{m_1 m_2 m}^{3/2 \, 1/2 \, S'}$ are the Clebsch-Gordan coefficients. In Eq. (6.10), at first, m_2 and then m_1 are changing from maximum to minimum values. Setting such numeration order the vectors $\left|2m_1, 2m_2\right\rangle$ can convert to $\left|\psi_i\right\rangle$, where index i = 1, 2…12. First five vectors correspond to the quintet E_H^0, the next three vectors belong to the triplet E_H^2 with an electron spin being antiparallel to the ion spin and the last four vectors describe the hole state E_H^1 with spin S = 3/2.

Let us introduce Hubbard's operators $X^{ik} = \left|\psi_i\right\rangle\left\langle\psi_k\right|$. Then the matrix $\hat{\mathbf{C}}$ of Clebsch-Gordan coefficients in Eq. (6.10) may be written as

$$\hat{\mathbf{C}} = X^{1,1} + X^{5,8} + X^{9,9} + X^{10,10} + X^{11,11} + X^{12,12} + \frac{1}{2}(X^{2,2} + X^{4,7} - X^{6,3} + X^{8,6})$$

$$+ \frac{\sqrt{3}}{2}(X^{2,3} + X^{4,6} + X^{6,2} - X^{8,7}) + \frac{1}{\sqrt{2}}(X^{3,4} + X^{3,5} + X^{7,4} - X^{7,5}) \quad (6.11)$$

The vector system can be written as $\left|\psi_i\right\rangle$: $\left|3,1\right\rangle, \left|3,-1\right\rangle, \left|1,1\right\rangle, \left|1,-1\right\rangle, \left|-1,1\right\rangle, \left|-1,-1\right\rangle, \left|-3,1\right\rangle, \left|-3,-1\right\rangle$, where i = 1,2…8, for electron states, and $\left|\psi_i\right\rangle$: $\left|3,0\right\rangle, \left|1,0\right\rangle, \left|-1,0\right\rangle, \left|-3,0\right\rangle$, where i = 9, 10, 11, 12 for hole states. Vectors $\left|\psi_i\right\rangle$

are connected with eigenfunctions $|\varphi_i\rangle$ of the Hund's part in the Hamiltonian (6.8) by linear relation

$$|\varphi_k\rangle = \sum_i C_{ki} |\psi_i\rangle ,\tag{6.12}$$

where coefficient C_{ki} forms a matrix $\hat{\mathbf{C}}$ in Eq. (6.11).

Using the function $|\varphi_k\rangle$ the Hamiltonians (6.2) and (6.3) will be transformed. In Eq. (6.2), superexchange interaction includes z-projection of total spin operator. Then in the $|\varphi_k\rangle$ basis the latter will be presented as a direct sum of diagonal operators $S^z \oplus S_1^z \oplus S_2^z$ for spins S = 3/2, $S_1 = 1$ and $S_2 = 2$ [12], respectively. Having constructed system of Hubbard's operators $L^{ik} = |\varphi_i\rangle\langle\varphi_k|$, one can write the unitary transformed zeroth Hamiltonian in a diagonal form

$$\hat{\tilde{H}}_0 = -\sum_{i=1}^N \left\{ \sum_{l=1}^5 \varepsilon_l L_i^{ll} + \sum_{l=9}^{12} \varepsilon_l L_i^{ll} \right\},\tag{6.13}$$

where $\tilde{H} = h + 2J(0)(<S^z> + <\sigma^z>)$ is the sum of applied magnetic and effective Weiss fields, $\varepsilon_l = \frac{1}{2}SJ_H + \mu + \xi + \left(S + \frac{3}{2} - l\right)\tilde{H}$ for the state with a spin $S_2 = 2$ ($l \le 5$) and $\varepsilon_l = \left[(S + 9 - l)\tilde{H}\right]$ for the hole state with S = 3/2 ($l \ge 9$). At the same time, we have taken into account the following inequalities $J_H \gg t \gg J$. Therefore the triplet level with $S_1 = 1$ lies considerably above the state with $S_2 = 2$ and can be neglected. We also ignore a contribution of the chemical potential $-\mu(L^{6,6} + L^{7,7} + L^{8,8})$. The above statements more strictly can be proved if to introduce a projective operator

$$P = \sum_{\alpha=1}^5 L^{\alpha\alpha} + \sum_{\alpha=9}^{12} L^{\alpha\alpha}\tag{6.14}$$

Acting by the P operator on both the Hamiltonian (6.1) and wave functions with an accuracy of t/J_H we eliminate all states with numbers $\alpha = 6, 7$ and 8.

The operator **A** in the matrix form can be written as

$$\mathbf{A} = \sum_{lm} \langle l|A|m\rangle X^{lm}$$

One can write the following expressions for electron creation operators:

$$\begin{aligned}c_\uparrow^+ &= X^{1,9} + X^{3,10} + X^{5,11} + X^{7,12}\\ c_\downarrow^+ &= X^{2,9} + X^{4,10} + X^{6,11} + X^{8,12}\end{aligned}\tag{6.15}$$

The corresponding formulae for electron annihilation operators can be obtained using the Hermitian conjugate of Eq. (6.15). Hubbard operators X^{ik} and L^{lm} are related to each other by the unitary transformation:

$$X^{ik} = \sum_{lm} C_{li}^* C_{mk} L^{lm} ,\tag{6.16}$$

where coefficients are determined by matrix $\hat{\mathbf{C}}$ from Eq. (6.11). Substituting (6.16) in (6.15) we find expressions for unitary transformed $\tilde{c}_\uparrow^+$ and $\tilde{c}_\uparrow$ operators as a functions of L^{lm}. An explicit form of both $c_\uparrow^+$ and $c_\uparrow$ operators and electron and ion spin operators is given in the Appendix. The operator of electron number, n, is invariant relative to the unitary transformation (6.12).

6.3. Fermion-boson free-particle Green's function and an effective kinematic interaction

In the study of electron dynamics we have used Matsubara Green's functions:

$$G_\sigma(\tau, r_l - r_m) = - < T_\tau c_{l\sigma}(\tau) c_{m\sigma}^+(0) > , \qquad (6.17)$$

where T_τ is the chronological ordering operator. The operators $c_\uparrow^+$ and $c_\uparrow$ are expressed in the Heisenberg representation. The brackets $<...>$ mean that the Gibbs thermodynamic average is obtained using the total Hamiltonian (6.1).

The problem of finding Green's functions reduces to the calculation of various correlators appearing in the scattering matrix series expansion of perturbation theory with Hamiltonian in interaction representation. Wick's theorem [87, 31] for Hubbard's operators is used for unlinking the correlators, and then the task reduces to the calculation of elementary Green's functions. Every contribution of perturbation theory has its graphical form. In accordance with Eq. (6.7) the free-particle Green's functions $U(\tau, \varepsilon_{lm})$ are determined as

$$U(\tau, \varepsilon_{lm}) = - < T_\tau X(\tau) X(0) >_{0 ph} < T_\tau L^{l,m}(\tau) L^{m,l}(0) >_0 \frac{1}{< F^{l,m} >_0} , \qquad (6.18)$$

where $< F^{l,m} >_0 = < L^{l,l} + L^{m,m} >_0$, $\varepsilon_{lm} = \varepsilon_l - \varepsilon_m$. Thermal averages of the 1-st and 2-nd correlators in Eq. (6.18) are calculated with the Hamiltonians (6.9) and (6.13), respectively. The Fermi part of Eq. (6.18) is easily derived using the Wick's theorem :

$$G_{0el.}^{lm}(\tau) = < T_\tau L^{l,m}(\tau) L^{m,l}(0) >_0 \frac{(-1)}{< F^{l,m} >_0} = e^{\varepsilon_{lm}\tau} \cdot \begin{cases} -f(\varepsilon_{lm}), & \tau > 0 \\ 1 - f(\varepsilon_{lm}), & \tau < 0 \end{cases} ,$$

where $f(x) = 1/(e^{\beta x} + 1)$ is the Fermi distribution function, $1/\beta = T$ is the temperature.

The Bose part of Eq. (6.18) may be determined using both relations for boson operators b^+ and b: $e^{\lambda(b^+ - b)} = e^{-\frac{1}{2}\lambda^2} e^{\lambda b^+} e^{-\lambda b}$ and Feynman disentangling of the operators products. A detailed calculation is given in [19].

As is seen in Eq. (6.18), the Bose part has the form $G_0^{ph.}(\tau) = < T_\tau X(\tau) X(0) >_{0 ph} = e^{\Phi(\tau)}$ with

$$\Phi(\tau) = -\lambda^2 \left\{ 2B + 1 - 2\sqrt{B(B+1)} \cosh\left[\omega\left(\tau \mp \frac{\beta}{2} \right) \right] \right\},$$

upper minus and lower plus signs correspond to $\tau > 0$ and $\tau < 0$, respectively. $B = 1/(e^{\beta\omega_0} - 1)$ is the Bose distribution function for the Einstein phonon mode. The appearance of hyperbolic cosine instead of ordinary, as in [19], arises from the Matsubara formalism where the time t is imaginary, and therefore we must make the substitution $t \to it$. It is interesting to point out that the function $G_0^{ph.}(\tau)$ describes nondiagonal transitions by Holstein definition [88], which are responsible for number of phonons changing in hopping process. In the function $G_0^{ph.}(\tau)$, the time-independent Debye-Waller factor $e^{-\lambda^2(2B+1)}$ corresponds to diagonal transitions without changing the number of virtual phonons.

The Fourier transformation of a single-particle Green's function has the form

$$U(i\omega_n, \varepsilon_{lm}) = \frac{1}{2\beta} \int_{-\beta}^{\beta} U(\tau, \varepsilon_{lm}) e^{i\omega_n \tau} d\tau.$$ It is easy to write the following relation

$$e^{x\cosh(z)} = \sum_{k=-\infty}^{\infty} I_k(x) e^{kz},$$

where $I_k(x)$ are the Bessel functions of complex argument. Note that in an initial time space we have a simple product of single particle Green functions of Fermi and Bose subsystems. In the Fourier inverse space this relation is complicated:

$$U(i\omega_n, \varepsilon_{lm}) = \frac{1}{\beta} f(\varepsilon_{lm}) e^{-\lambda^2(2B+1)} \sum_{k=-\infty}^{+\infty} I_k\left(2\lambda^2\sqrt{B(B+1)}\right) \frac{e^{\beta\varepsilon_{lm}+\frac{1}{2}\beta k\omega_0} + e^{-\frac{1}{2}\beta k\omega_0}}{i\omega_n + k\omega_0 + \varepsilon_{lm}} \quad (6.19)$$

with $\omega_n = \pi(2n+1)\beta$ and the unit system $k_B = \hbar = 1$. Since the operators $c_\sigma^{\pm}$ and $L^{l,m}$ are linearly connected (see Eqs. (6.56) in the Appendix) one can write the single particle Green's function as a linear combination of functions $U(i\omega_n, \varepsilon_{lm})$:

$$\tilde{G}_{0\sigma}(i\omega_n) = -\left\{ \begin{array}{l} (\delta_{j,0} + \frac{\delta_{j,1}}{4}) <F^{9,1+j}>_0 U(i\omega_n, \varepsilon_{9,1+j}) + \frac{3-j}{4} <F^{10,2+j}>_0 U(i\omega_n, \varepsilon_{10,2+j}) + \\ + \frac{2+j}{4} <F^{11,3+j}>_0 U(i\omega_n, \varepsilon_{11,3+j}) + \left(\frac{\delta_{j,0}}{4} + \delta_{j,1}\right) <F^{12,4+j}>_0 U(i\omega_n, \varepsilon_{12,4+j}) \end{array} \right\}, \quad (6.20)$$

where index $j = 0$ for $\sigma = +1$ (spin up) and $j = 1$ for $\sigma = -1$ (spin down), $\delta_{i,j}$ is the Kronecker symbol. The following identities $\varepsilon_{9,1} = \varepsilon_{10,2} = \varepsilon_{11,3} = \varepsilon_{12,4} = \tilde{\mu} + \frac{1}{2}\tilde{H} = \varepsilon_{0\uparrow}$ and

$\varepsilon_{9,2} = \varepsilon_{10,3} = \varepsilon_{11,4} = \varepsilon_{12,5} = \tilde{\mu} - \frac{1}{2}\tilde{H} = \varepsilon_{0\downarrow}$ are valid with $\tilde{\mu} = \mu + \xi + \frac{1}{2}SJ_H$. Here the change of the electron energy with spin σ transferring between the sites is denoted by $\varepsilon_{0\sigma}$. Then the expression (6.20) is simplified and takes the form

$$\tilde{G}_{0\sigma}(i\omega_n) = <F^{\sigma 0}>_0 G_{0\sigma}(i\omega_n) = <F^{\sigma 0}>_0 U(i\omega_n, \varepsilon_{0\sigma}), \quad (6.21)$$

where a combined occupancy of electron-hole states $<F^{\sigma 0}>_0$ in a mean-field approximation is done as

$$<F^{+0}(\varepsilon_1, \varepsilon_2, \varepsilon_3, \varepsilon_4, \varepsilon_5, \varepsilon_9, \varepsilon_{10}, \varepsilon_{11}, \varepsilon_{12})>_0 = <F^{9,1}>_0 + \frac{3}{4}<F^{10,2}>_0 + \frac{1}{2}<F^{11,3}>_0 + \frac{1}{4}<F^{12,4}>_0$$

$$<F^{-0}(\varepsilon_1, \varepsilon_2, \varepsilon_3, \varepsilon_4, \varepsilon_5, \varepsilon_9, \varepsilon_{10}, \varepsilon_{11}, \varepsilon_{12})>_0 = \frac{1}{4}<F^{9,2}>_0 + \frac{1}{2}<F^{10,3}>_0 + \frac{3}{4}<F^{11,4}>_0 + <F^{12,5}>_0 \quad (6.22)$$

For the sake of convenience we have written $<F^{\sigma 0}>_0$ as a function of all energy parameters ε_l. The equality

$$F^{\sigma 0} = n_\sigma + p_\sigma, \quad (6.23)$$

where n_σ and p_σ are the operators of the number of electrons and holes with the spin σ expressed in terms of L^{lm} (see the Appendix) will be further used. Using equalities (6.57-6.59) from the Appendix, Eq. (6.23) can be written as:

$$< F^{\sigma 0} > = \frac{1}{8}(5-n) + \sigma < \sigma^z + \frac{1}{4}S_0^z >, \tag{6.24}$$

where $S_0^z = \frac{3}{2}(L^{9,9} - L^{12,12}) + \frac{1}{2}(L^{10,10} - L^{11,11})$ is a z-projection of a spin in the basis of t_{2g} electrons as in the Mn^{4+} ion. It is easy to check itinerant e_g-electrons not only by the Hund's exchange but also by the effective kinematic interaction. This viewpoint will be confirmed in the following discussion where expectations of operators $< \sigma^z + \frac{1}{4}S_0^z >$ and $\frac{1}{4} < \sigma^z + S^z >$ are equal (see the Appendix). Therefore, a quarter of the Mn^{4+} ion spin fluctuates with electron spins. The reason is that Mn^{4+} ion spins are coupled to spins.

We will formulate some rules for finding contributions of series of the perturbation theory in both Green's functions and combined occupancies using a graphic representation. In Figs. 6.1 and 6.2, electron Green's functions $G_{0\sigma}(i\omega_n)$, $G_{+-}(i\omega_n) = U(i\omega_n, \varepsilon_{\uparrow\downarrow})$ and Fourier components of the interaction

$$t(\mathbf{q}) = \sum_{ij} t_{ij} e^{-i\mathbf{q}(\mathbf{r}_i - \mathbf{r}_j)} = 2t(\cos(q_x a) + \cos(q_y a) + \cos(q_z a)),$$

where $\varepsilon_{\uparrow\downarrow} = \varepsilon_{0\downarrow} - \varepsilon_{0\uparrow}$ and a is the constant of the s.c. lattice, are presented by solid, dashed and wave lines, respectively.

Using the Wick's theorem one can write all possible pairings realizing in the framework of this consideration. The c_σ operators and new Bose operator $B^+ = \sigma^+ + \frac{1}{2}S_0^+$ are an "active" operators where

$$S_0^+ = \frac{\sqrt{3}}{2}\left(L^{9,10} + L^{11,12}\right) + L^{10,11},$$

$$\sigma^+ = \frac{1}{2}\left(L^{1,2} + L^{4,5}\right) + \sqrt{\frac{3}{8}}\left(L^{2,3} + L^{3,4}\right).$$

The operators B^- and σ^- appear due to the Hermitian conjugate of operators B^+ and σ^+ ($B^- = (B^+)^+$, $\sigma^- = (\sigma^+)^+$), respectively. We have the following zero pairings:

$$(n_{\sigma i} + p_{\sigma i})\,c_{\sigma j} = c_{\sigma_1 i}\,c_{\sigma_2 j} = c^+_{\sigma_1 i}\,c^+_{\sigma_2 i} = B_i^\sigma\,c_{\bar\sigma j} = 0 \tag{6.25}$$

Here i and j site symbols mean the time indexes in the interaction representation. In the pairings, the arrows are directed from an "active" to "passive" operators. The remaining nonzero pairings have the form:

$$(n_{\sigma i} + p_{\sigma i})\,c_{\bar\sigma j} = \frac{1}{4}\delta_{ij}G_{0\bar\sigma}(\tau_j - \tau_i)c_{\bar\sigma i}, \quad c^+_{\sigma i}\,c_{\bar\sigma j} = \delta_{ij}G_{0\bar\sigma}(\tau_j - \tau_i)B_i^\sigma$$

$$B_i^\sigma\,c_{\sigma j} = -\frac{1}{4}\delta_{ij}G_{0\sigma}(\tau_j - \tau_i)c_{\bar\sigma i}, \quad (\sigma_i^z + \frac{1}{4}S_{0i}^z)\,c_{\sigma j} = -\frac{\sigma}{8}\delta_{ij}G_{0\sigma}(\tau_j - \tau_i)c_{\sigma i} \tag{6.26}$$

$$(n_{\sigma i} + p_{\sigma i})\,B_j^+ = \frac{\sigma}{4}\delta_{ij}G_{+-}(\tau_j - \tau_i)B_i^+, \quad B_i^-\,B_j^+ = -\frac{1}{2}\delta_{ij}G_{+-}(\tau_j - \tau_i)(\sigma_i^z + \frac{1}{4}S_{0i}^z)$$

These expressions are closed and allow to find the contribution of series of the perturbation theory using only three single particle Green's functions in spite of the existence of a large number of Hubbard operators L^{ik}. This result is important and essentially simplifies the construction of the diagram technique in the DE model with a strong Hund's rule coupling.

Let us find an analytic expression for effective kinematic interactions $\beta B^{c_\sigma^+ c_\sigma}(\mathbf{q}, i\omega_n)$ displayed by a bold line in Fig. 6.1. It looks as

$$\beta B^{c_\sigma^+ c_\sigma}(\mathbf{q}, i\omega_n) = \frac{\beta t(\mathbf{q})}{1 - \beta t(\mathbf{q}) G_{0\sigma}(i\omega_n) < F^{\sigma 0} >} \qquad (6.27)$$

In the absence of the electron-phonon interaction, the calculation of the diagrams is non-problematic [57]. In this case, Eq. (27) has the simplest form

$$\beta B^{c_\sigma^+ c_\sigma}(\mathbf{q}, i\omega_n) = \frac{\beta t(\mathbf{q})(i\omega_n + \varepsilon_{0\sigma})}{i\omega_n - E_{\sigma\mathbf{q}}}, \qquad (6.28)$$

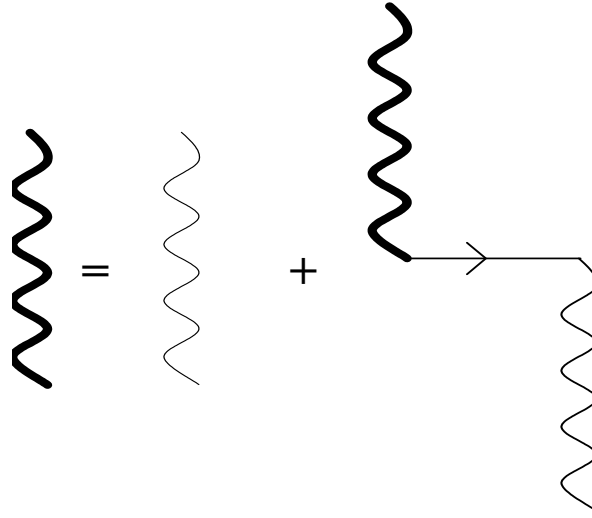where $E_{\sigma\mathbf{q}} = -\varepsilon_{0\sigma} + t(\mathbf{q}) < F^{\sigma 0} >$.

Fig. 6.1. A graphic equation for the effective kinematic interaction

If Eq. (6.28) contains one pole, the infinite quantity of poles in Eq. (6.27) are solutions of the algebraic equation of an infinite order. As a result, there is an unlimited quantum number of phonons. For practical applications, Eq. (6.27) has to be simplified.

6.4. Electron-phonon interaction

In the CPA method [83], the polaron problem is considerably simplified after an analytic continuation $i\omega_n \to \omega + i\delta$ and application of the self-consistent equation for the total Green function $G_\sigma(\omega, 0) = U(\omega - \frac{W^2}{16} G_\sigma(\omega, 0), \varepsilon_{0\sigma})$. Writing $G_\sigma(\omega, 0)$ as a sum of real and imaginary parts it is easy to solve the derived set of equations by a simple iteration method.

Let us consider two approximations in solving Eq. (6.27) for frequency poles. As will be seen later, the first approximation well works far from the phase FM-PM transition. However, in this case calculated values of resistivity contradict the experimental data. It is not only because of an approximate solution of the equation for an electron-phonon effective line. In the Kubo formula, the two-particle correlator is decoupled in a product of Green's functions $G_\sigma(-\tau, \mathbf{r}_{j_2} - \mathbf{r}_{i_1}) G_\sigma(\tau, \mathbf{r}_{j_1} - \mathbf{r}_{i_2})$ (a bubble approximation). Then the vertex corrections, which

contribution in the magnetoresistance effect may be essential, are not taken into account. This problem calls for further investigations and is not considered in this work.

a) **First approximation**. The equation of poles singularities for the effective kinematic interaction (6.27) is written in the form:

$$\prod_m (x + m\omega_0) - t(\mathbf{q}) < F^{\sigma 0} > P_\sigma \sum_m \varphi_{m\sigma} \prod_{k(\neq m)} (x + k\omega_0) = 0, \qquad (6.29)$$

where

$$x = i\omega_n + \varepsilon_{0\sigma} \quad P_\sigma = f(\varepsilon_{0\sigma})e^{-\lambda^2(2B+1)}, \quad \varphi_{m\sigma} = I_m\left(2\lambda^2\sqrt{B(B+1)}\right)\left(e^{\beta\left[\varepsilon_{0\sigma}+\frac{1}{2}m\omega_0\right]} + e^{-\frac{1}{2}\beta m\omega_0}\right).$$

The second term in Eq. (6.29) is considered as a perturbation. It is correct in the limit of a strong electron-phonon coupling, when $P_\sigma\varphi_{m\sigma} << 1$. In the case of $g = 0$, using Eq. (6.29) we obtain a solution corresponding to the DE model. In Eq. (6.29) the term with $m = 0$ corresponds to the central polaron band. Expressing n-th root of Eq. (6.29) as $x = x_n + \Delta_n$, where $x_n = -n\omega_0$ is the root in the absence of the perturbation, it is easy to calculate the correction to the n-th pole in the linear approximation relative to smallness of the $P_\sigma\varphi_{m\sigma}$ parameter

$$\Delta_n = t(\mathbf{q}) < F^{\sigma 0} > P_\sigma \varphi_{n\sigma} \qquad (6.30)$$

Then one can write the equation (6.27) with a precision of $t(q)^2$ as

$$\beta B^{c_\sigma^+ c_\sigma}(\mathbf{q}, i\omega_n) = \beta t(\mathbf{q})\prod_m \frac{i\omega_n + \varepsilon_{0\sigma} + m\omega_0}{(i\omega_n - E_{m\sigma\mathbf{q}})} \approx \beta t(\mathbf{q})\left\{1 + t(\mathbf{q}) < F^{\sigma 0} > P_\sigma \sum_{m=-\infty}^{\infty} \frac{\varphi_{m\sigma}}{i\omega_n - E_{m\sigma\mathbf{q}}}\right\}, \quad (6.31)$$

where $E_{m\sigma\mathbf{q}} = -\varepsilon_{0\sigma} - m\omega_0 + t(\mathbf{q}) < F^{\sigma 0} > P_\sigma\varphi_{m\sigma}$.

b) **Second approximation**. It is used to calculate the magnetoresistance effect near the phase transition. We suppose that constant $\lambda^2 >> 1$, i.e., the electron-phonon coupling is sufficiently strong in comparison with the phonon energy of the vibration. The $U(i\omega_n, \varepsilon_{0\sigma})$ function can be written in the form of an infinite series expansion

$$U(i\omega_n, \varepsilon_{0\sigma}) = \frac{1}{\beta}e^{-\lambda^2(2B+1)}\sum_{k=0}^{\infty}\left(\frac{-2}{\beta}\right)^k \frac{\omega_0^k}{(i\omega_n + \varepsilon_{0\sigma})^{k+1}}\frac{d^k\psi}{d\omega_0^k}\eta_k, \qquad (6.32)$$

where the derivative of zeroth-order $\dfrac{d^0\psi}{d\omega_0^0} = \psi = \exp\left\{2\lambda^2\sqrt{B(B+1)}\cosh\left(\dfrac{\beta\omega_0}{2}\right)\right\}$, and

$\eta_k = 1 - 2f(\varepsilon_{0\sigma})$ and $\eta_k = 1$ for odd and even k, respectively. Keeping the term with a maximal

power of λ in the expressions $\dfrac{d^k\psi}{d\omega_0^k}$, it is easy to obtain that

$$\frac{d^k\psi}{d\omega_0^k} \approx \psi\left[\frac{\beta}{2}\lambda^2\sqrt{B(B+1)}\sinh\left(\frac{\beta\omega_0}{2}\right)\right]^k = \psi\left(\frac{\beta\xi}{2}\right)^k \qquad (6.33)$$

It should be noted that this approximation is valid at sufficiently low temperatures, when ω/T is of the order of unity, since at high temperatures ($T >> \omega$) the Bose function has a value comparable to the maximal power of the parameter λ, and Eq. (6.33) will be wrong. Eq. (6.32) is exact if the inequality

$\lambda^4 >> 2B+1$ is fulfilled. In this case, the following relation $\dfrac{\omega}{T} >> \ln\dfrac{\lambda^4 + 1}{\lambda^4 - 1}$ is valid.

The high temperature range is studied in detail using the small polaron theory [19, 88]. For a nondiagonal transition it was shown that a hopping rate has an activation character. The

gap value is equal to one-half of the polaron binding energy. The most interesting temperature range is $T \sim \omega$ because the phase transition temperature is usually of the order of ω.

By substituting Eq. (6.33) for Eq. (6.32) and replacing ξ for $-\xi$ we obtain the terms of series with the opposite sign. Such asymmetry is quite typical for a system with electron-phonon interactions [19] when polarons are formed. We will suppose that near the transition into an ordered state the processes of both formation and destruction of polarons would be apparently interchangeable. Therefore Green's function will be invariant relatively to the sign change for the polaron energy ξ. Neglecting the terms with odd power of ξ in Eq. (6.32), we obtain the ordinary geometric series which sum is easily calculated. The following expression for a single particle Green's function with electron-phonon coupling was obtained:

$$U(i\omega_n, \varepsilon_{0\sigma}) = \frac{i\omega_n + \varepsilon_{0\sigma}}{\beta(i\omega_n + \varepsilon_{0\sigma} - \xi)(i\omega_n + \varepsilon_{0\sigma} + \xi)} \tag{6.34}$$

Eq. (6.34) has a simple physical meaning. At the emission or absorption of a phonon by ion coupled with an itinerant electron, the chemical potential changes by value ξ. In this case, the effective interaction line is determined as

$$\beta B^{c_\sigma^+ c_\sigma}(\mathbf{q}, i\omega_n) = \frac{\beta t(\mathbf{q})\left[(i\omega_n + \varepsilon_{0\sigma})^2 - \xi^2\right]}{(i\omega_n - E_{1\sigma\mathbf{q}})(i\omega_n - E_{2\sigma\mathbf{q}})}, \tag{6.35}$$

where $E_{1,2\sigma\mathbf{q}} = -\varepsilon_{0\sigma} + \frac{1}{2}\left\{t(\mathbf{q}) < F^{\sigma 0} > \pm \sqrt{t(\mathbf{q})^2 < F^{\sigma 0} >^2 + 4\xi^2}\right\}$. Using Eq. (6.35) one can calculate the spectral density characteristic for a Mott-Hubbard dielectric with the gap of the order of the polaron energy ξ.
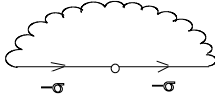
6.5. Analysis of the magnetic structure

Using first and second approximations for the effective kinematic interaction, we will write the system of equations determining the chemical potential and the mean spin of the system. The graphic image of the series expansion for combined occupancies $<F^{\sigma 0}>$ is shown in Fig. 6.2a. A small circle ∘ corresponds to $<F_i^{\sigma 0}>_0$ of the i-th site. The lower index for the $<F_i^{\sigma 0}>_0$ quantity denotes the averaging over Hamiltonian $\hat{\tilde{H}}_0$ (Eq. (6.13)) with a parametric part tending to zero :

$$\hat{H}_0(r_\uparrow, r_\downarrow) = \hat{\tilde{H}}_0 + \sum_i^N \left(r_{\uparrow i} F_i^{+0} + r_{\downarrow i} F_i^{-0}\right) \tag{6.36}$$

The dots connecting the diagram blocks (Fig. 6.2) mean the equality of their external site indexes. According to the linked cluster theorem, such diagrams characterize contributions in both combined occupancies and Green's function. The form of the zeroth Hamiltonian (6.36) is very suitable for calculations of the operator average

$$< F_i^{\sigma 0} >_0 = \frac{\partial}{\partial(-\beta r_{\sigma i})} \ln Tr(\exp(-\beta\hat{H}_0(r_\uparrow, r_\downarrow))) = \partial_\sigma \ln Z_0(r_\uparrow, r_\downarrow) \tag{6.37}$$

The blocks of ⌢ and ⌢ in Fig. 6.2 are described by the functions $\beta\delta\mu_\sigma$ and $v_{-\sigma} < F^{-\sigma 0} >$.

a) First approximation

$$\delta\mu_\sigma = \frac{1}{N}\sum_{\mathbf{q}} t(\mathbf{q})P_\sigma \sum_{m=-\infty}^{\infty} \varphi_{m\sigma} f(E_{m\sigma\mathbf{q}}) \tag{6.38}$$

$$\nu_\sigma < F^{\sigma 0} >= \frac{1}{N}\sum_{\mathbf{q}} P_\sigma \sum_{m=-\infty}^{\infty} \varphi_{m\sigma}\left(f(E_{m\sigma\mathbf{q}}) - f(-m\omega_0 - \varepsilon_{0\sigma}) \right)$$

(b)

(a)
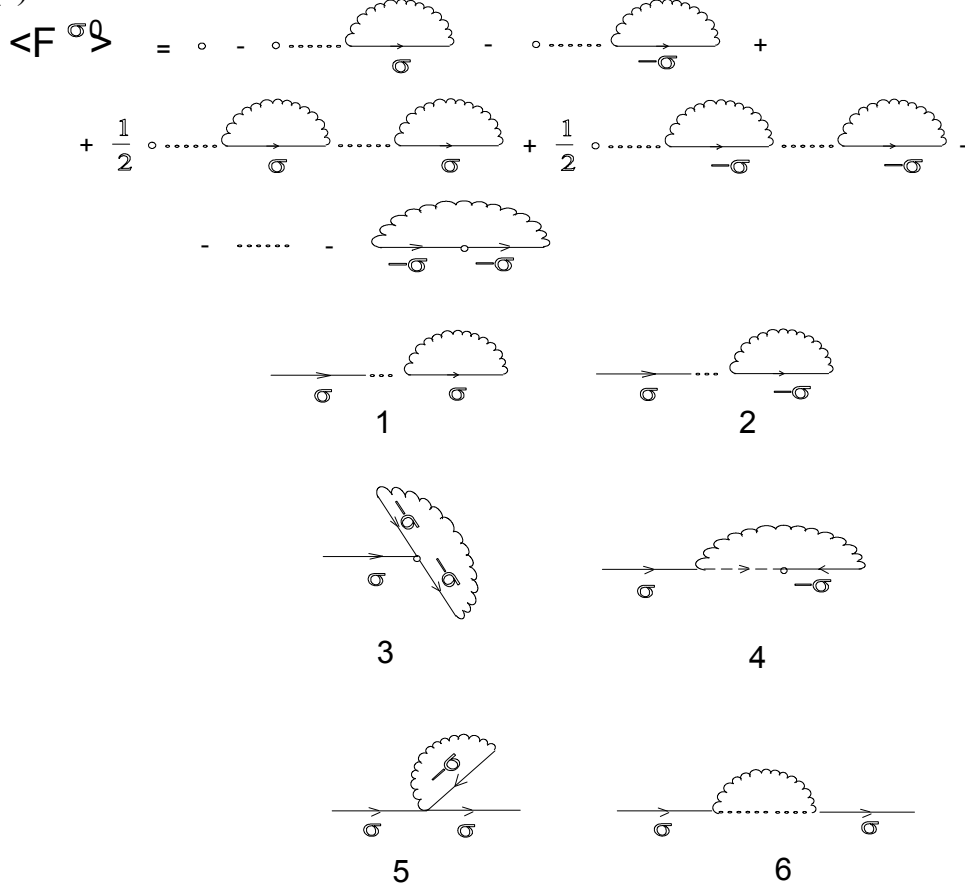
Fig. 6.2. Graphic image of the equation for a combined occupancy $< F^{\sigma 0} >$ (a) and diagrams for the Green function in the first approximation of the perturbation theory (b)

In the sums of Eq. (6.38) m_1 and m_2 indexes were taken equal to m, since corresponding series terms are proportional to the high-order power of the parameter $P_\sigma\varphi_{m\sigma}$.

b) Second approximation

$$\delta\mu_\sigma = \frac{1}{2N}\sum_{\mathbf{q}} t(\mathbf{q})\left\{ f(E_{1\sigma\mathbf{q}}) + f(E_{2\sigma\mathbf{q}}) + t(\mathbf{q}) < F^{\sigma 0} > \frac{f(E_{1\sigma\mathbf{q}}) - f(E_{2\sigma\mathbf{q}})}{E_{1\sigma\mathbf{q}} - E_{2\sigma\mathbf{q}}} \right\} \tag{6.39}$$

$$\nu_\sigma < F^{\sigma 0} >= \frac{1}{8N}\sum_{\mathbf{q}}\left[\frac{t(\mathbf{q}) < F^{\sigma 0} >}{E_{1\sigma\mathbf{q}} - E_{2\sigma\mathbf{q}}}\{ f(E_{1\sigma\mathbf{q}}) - f(E_{2\sigma\mathbf{q}})\} + f(E_{1\sigma\mathbf{q}}) + f(E_{2\sigma\mathbf{q}}) \right] -$$

$$- \frac{1}{8}\{ f(\xi - \varepsilon_{0\sigma}) + f(-\xi - \varepsilon_{0\sigma})\}$$

Here, $E_{1\sigma\mathbf{q}}$ and $E_{2\sigma\mathbf{q}}$ are determined by the formula (6.35).

In Fig. 6.2a, graphic series may be easily summed, since all terms of the sums with the exception of the last one $v_{-\sigma} < F^{-\sigma 0} >$ generate the Taylor power series

$$< F^{\sigma 0} >_0 - \partial_\sigma < F^{\sigma 0} >_0 \beta \delta \mu_\sigma - \partial_{-\sigma} < F^{-\sigma 0} >_0 \beta \delta \mu_{-\sigma} +$$

$$+ \frac{1}{2!} \partial_\sigma^2 < F^{\sigma 0} >_0 \left(\beta \delta \mu_\sigma \right)^2 + \frac{1}{2!} \partial_{-\sigma}^2 < F^{-\sigma 0} >_0 \left(\beta \delta \mu_{-\sigma} \right)^2 - ... \; ,$$

which sum is equal to $< F^{\sigma 0} >_1$:

$$< F^{\sigma 0} >_1 = < F^{\sigma 0} (\tilde{\varepsilon}_1, \tilde{\varepsilon}_2, \tilde{\varepsilon}_3, \tilde{\varepsilon}_4, \tilde{\varepsilon}_5, \tilde{\varepsilon}_9, \tilde{\varepsilon}_{10}, \tilde{\varepsilon}_{11}, \tilde{\varepsilon}_{12}) >_0 , \tag{6.40}$$

The function $< F^{\sigma 0} (\varepsilon_1, \varepsilon_2, \varepsilon_3, \varepsilon_4, \varepsilon_5, \varepsilon_9, \varepsilon_{10}, \varepsilon_{11}, \varepsilon_{12}) >_0$ is determined by Eq. (6.22) and

$$\tilde{\varepsilon}_1 = \varepsilon_1 + \delta \mu_\uparrow, \; \tilde{\varepsilon}_2 = \varepsilon_2 + \frac{3}{4} \delta \mu_\uparrow + \frac{1}{4} \delta \mu_\downarrow, \; \tilde{\varepsilon}_3 = \varepsilon_2 + \frac{1}{2} \left(\delta \mu_\uparrow + \delta \mu_\downarrow \right), \; \tilde{\varepsilon}_4 = \varepsilon_4 + \frac{1}{4} \delta \mu_\uparrow + \frac{3}{4} \delta \mu_\downarrow,$$

$$\tilde{\varepsilon}_5 = \varepsilon_5 + \delta \mu_\downarrow, \; \tilde{\varepsilon}_9 = \varepsilon_9 + \delta \mu_\uparrow + \frac{1}{4} \delta \mu_\downarrow, \; \tilde{\varepsilon}_{10} = \varepsilon_{10} + \frac{3}{4} \delta \mu_\uparrow + \frac{1}{2} \delta \mu_\downarrow, \; \tilde{\varepsilon}_{11} = \varepsilon_{11} + \frac{1}{2} \delta \mu_\uparrow + \frac{3}{4} \delta \mu_\downarrow,$$

$$\tilde{\varepsilon}_{12} = \varepsilon_{12} + \frac{1}{4} \delta \mu_\uparrow + \delta \mu_\downarrow$$

The equations for a mean spin $< \sigma^z + \frac{1}{4} S_0^z >$ as well as for the chemical potential μ can be written in the following form

$$\frac{1}{8} (5 - n) + < \sigma^z + \frac{1}{4} S_0^z > = < F^{+0} >_1 - v_\downarrow < F^{-0} >$$

$$\frac{1}{8} (5 - n) - < \sigma^z + \frac{1}{4} S_0^z > = < F^{-0} >_1 - v_\uparrow < F^{+0} > \tag{6.41}$$

We will consider different solutions of the set of equations (6.41). Supposing that $\xi = 0$ and $T = 0$ (a pure double exchange) as well as $\mu > 0$, one introduces the functions $E(x) = \frac{1}{6} \int_{-3}^{x} D_c(x) x dx$ and $I(x) = \int_{-3}^{x} D_c(x) dx$, where the electron density of states is

$$D_c(x) = \frac{1}{N} \sum_{\mathbf{q}} \delta \left(x - \frac{t(\mathbf{q})}{2t} \right) \tag{6.42}$$

From Eq. (6.42) it follows that for the s.c. lattice the variable $|x| \leq 3$. The plots of $I(x)$ and $E(x)$ functions for this lattice are displayed in Fig. 6.3. Function $E(x)$ characterizes an effective field contribution to the electron dynamics which does not exceed $1/(2z)$. This contribution roughly determines the Curie temperature, T_C, in units of the bandwidth W.

For the case of $< F^{+0} >_1 = 1, < F^{-0} >_1 = 0$, the set of equations (6.41) can be written as :

$$< F^{\sigma 0} > = < F^{\sigma 0} >_1 + \frac{1}{4} \left[1 - I \left(\frac{6\mu}{W < F^{-\sigma 0} >} \right) \right], \tag{6.43}$$

which solutions exist, if

$$\frac{6\mu}{W < F^{-0} >} \geq 3 , \tag{6.44}$$

Then the expressions for both mean spin of the saturated ferromagnet (FM) and chemical potential have the form $<\sigma^z + \frac{1}{4} S_0^z> = \frac{1}{8}(3+n)$ and $\frac{\tilde{\mu}}{W} = \frac{1}{6} I^{-1}(n)$, respectively, where $I^{-1}(x)$ is the inverse function of $I(x)$. In Fig. 6.3 it is seen that $I^{-1}(x) > 0$ at $x > 0.5$. Therefore, the self-consistent FM solution is valid for electron concentrations $n > 1/2$. In perovskite manganites. this fact was fixed experimentally in the work [89]. Using Eq. (6.44) we obtain a more precise estimate of the electron concentration, namely, $n_{FM} \approx 0.588$ above of which the FM state exists.
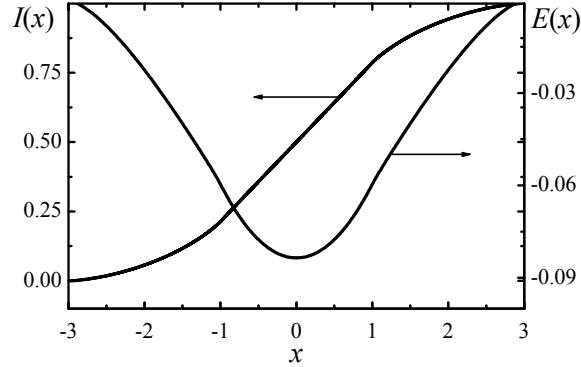

Fig. 6.3. $I(x)$ and $E(x)$ functions

The set of Eq. (6.41) has solutions $<\sigma^z + \frac{1}{4} S_0^z> = 0$, $\tilde{\mu} = \tilde{\mu}_{PM2} = \frac{W}{48}(5-n)I^{-1}\left(\frac{n+1}{2}\right)$

and $\tilde{\mu} = \tilde{\mu}_{PM1} = \frac{W}{48}(5-n)I^{-1}\left(\frac{n}{2}\right)$, corresponding to two paramagnetic phases PM-2 and PM-1.

In these phases $<F^{\sigma 0}>_1 = 1/2, \tilde{\mu} + \delta\mu_\sigma / 4 > 0$ and $<F^{\sigma 0}>_1 = 5/8, \tilde{\mu} + \delta\mu_\sigma / 4 < 0$, respectively. Existence of two paramagnetic phases was also predicted in the work [57] for HTSC systems.

To find the temperature T_C the set of equations in the linear approximation is expanded in terms of a small parameter $<\sigma^z + \frac{1}{4} S_0^z>$ at $T \sim T_C$. Neglecting superexchange and supposing that $\xi = 0$ (pure DE model), we obtain the following equations for μ and T_C:

$$1 - n = \frac{1}{1 + \frac{5}{4} e^{\beta_C (\tilde{\mu} + \frac{1}{4}\delta\mu)}} - \frac{2}{N} \sum_{\bar{q}} f(E_{0\bar{q}}) + 2f(-\tilde{\mu})$$

$$4T_C^2 = \frac{1}{N} \sum_{\bar{q}} t(\bar{q}) f(E_{0\bar{q}})\left[1 - f(E_{0\bar{q}})\right]\left\{5t(\bar{q}) \frac{e^{\beta_C (\tilde{\mu} + \frac{1}{4}\delta\mu)} + \frac{1}{2}}{5 e^{\beta_C (\tilde{\mu} + \frac{1}{4}\delta\mu)} + 4} - T_C\right\}$$

(6.45)

where $\beta_C = 1/T_C$, $\delta\mu = \frac{1}{N} \sum_{\bar{q}} t(\bar{q}) f(E_{0\bar{q}})$, $E_{0\bar{q}} = -\tilde{\mu} + \frac{1}{8}(5-n)t(\bar{q})$.

The calculated $T_C(n)$ dependencies in W units are shown in Fig. 6.4 (curve 1). The $T_C(n)$ curves obtained assuming that $\tilde{\mu} = \tilde{\mu}_{PM2}$ (see the above formula for the chemical potential defined at $T = 0$) and $\frac{df(E_{0\bar{q}})}{dE_{0\bar{q}}} = -\delta(E_{0\bar{q}})$ has the form :

$$T_C / W \approx \frac{768(\tilde{\mu}/W)^2 D_c\left(\dfrac{48\tilde{\mu}/W}{5-n}\right)}{\left[(5-n)\right]^3 + 384(5-n)D_c\left(\dfrac{48\tilde{\mu}/W}{5-n}\right)\tilde{\mu}/W} \tag{6.46}$$

and is also demonstrated in Fig. 6.4 (curve 2). The formula (6.46) somewhat differs from the result obtained in [85], when Hund's coupling was considered in a mean field approximation. The curve (3) corresponds to an approximate solution of the set of equations (6.45) with a chemical potential at $T = 0$ and a step-like Fermi function (Eq. (6.46)). Therefore, one can note that rigorous account of quantum spin fluctuation with Hund's coupling decreases the Curie temperature essentially (up to 30 %).
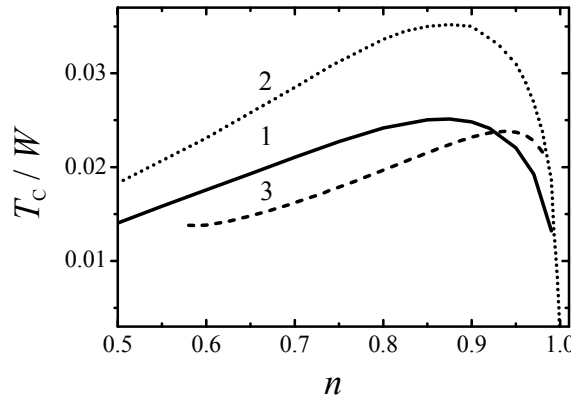
Fig. 6.4. The Curie temperature, T_C, versus electron concentration, n, with account of Hund's rule coupling in the framework of the given theory (curve 1), in a mean field approximation [57] (curve 2). The curve (3) corresponds to an approximate solution of the set of equations (6.45)

The above equations correspond to a pure DE model. There are no difficulties to derive similar formulae taking into account the electron-phonon coupling. Unfortunately, the two above considered approximations provide different results for magnetic and transport properties.
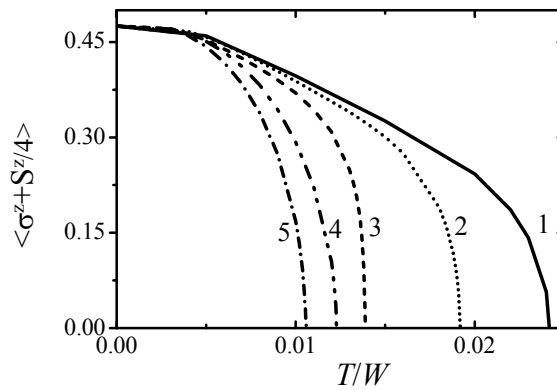
Fig. 6.5. Temperature dependences of the magnetization $< \sigma^z + \dfrac{1}{4} S_0^z >$ at $n = 0.8$

with $\xi / W = 0$, 0.003, 0.01, 0.03 and 0.04 (curves 1-5, respectively)

In the first approximation (Eq. 6.38), a strong influence of the polaron binding energy ξ on the ferromagnetic phase is found. Temperature dependences of the mean spin obtained by solution of the set of equations (6.41) at the electron concentration $n = 0.8$ for various ξ values

are illustrated in Fig. 6.5. It is seen that the Curie temperature is reduced more than by a half at $\xi/W = 0.04$ together with the chemical potential. It is an indicator of the narrowing effective band. The polaron size calculated using the Holstein expression $aW/\xi \approx 25a$ is not small. Thus the electron-phonon interaction suppresses the DE interaction as predicted in [83, 86].
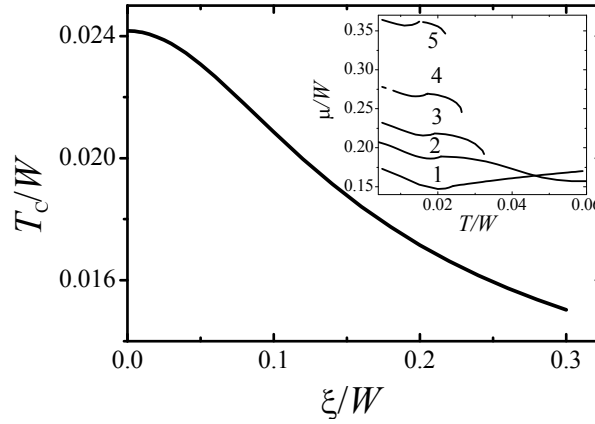
Fig. 6.6. The Curie temperature, T_C, versus the polaron energy ξ at $n = 0.8$. Inset: temperature dependences of the chemical potential μ at $\xi/W = 0, 0.1, 0.14, 0.2$ and 0.3 (curves 1–5, respectively)

In Fig. 6.6 calculated in the second approximation (6.35) dependence $T_C(\xi)$ is shown. One can see that T_C decreases by one third at $\xi \sim 0.25$ that corresponds to the small polaron theory. However, in this case the chemical potential is increased (see inset in Fig. 6.6). The increase of μ near the phase transition with increasing polarons binding energy reflects the processes of polaron destruction owing to scattering on spin fluctuations. Note that the function $T_C(g)$ obtained in [83] decreases faster with increasing g parameter at $n = 0.5$. Therefore, the contribution of electron correlations is expected to be overestimated in the CPA method.

Fig. 6.7 demonstrates the influence of both superexchange and an applied magnetic field, h, on the magnetic ordering temperature with an account of the electron-phonon coupling (6.35). The value $J(0)/W = 0.00215$ obtained in the work [90] for $LaMnO_3$ corresponds to $J(0) = 25$ K. The value $h/W = 0.0001$ will correspond to the applied magnetic field of 8.64 kOe, since the bandwidth $W = 1$ eV. From Fig. 6.7 it follows that the superexchange enhances T_C while an applied magnetic field smears the phase transition, as it should be in the 2-nd kind phase transitions theory.

Fig. 6.7. Influence of both applied magnetic field, h, and superexchange, $J(0)$, on the temperature dependences of the magnetization at $n = 0.8$ and $\xi/W = 0.2$: 1) $J(0) = 0, h = 0$; $J(0)/W = 0.00215$ for the case when 2) $h = 0$; 3) $h/W = 0.0001$ and 4) $h/W = 0.0006$

6.6. Spectral and transport properties of electron-hole excitations

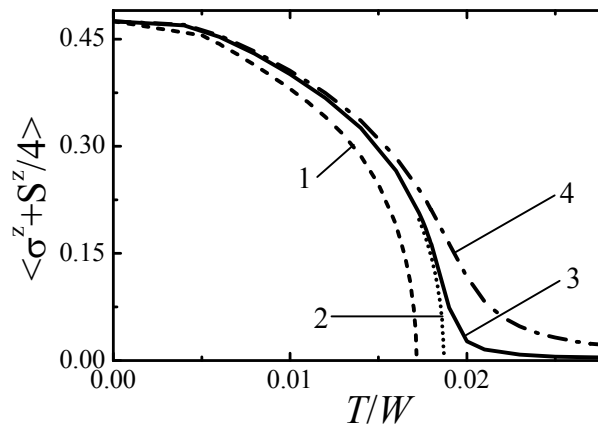In Fig. 6.2b, all diagrams in the first order relatively to the inverse effective radius of the interaction for the Green's function $G_\sigma(i\omega_n, \vec{k})$ are shown. Diagrams 1, 2, 3 and similar in higher order of the expansion form a series $<F^{\sigma 0}>$ depicted in Fig. 6.2a. Consequently, the appropriate correction to $G_\sigma(i\omega_n, \vec{k})$ is equal to $<F^{\sigma 0}> G_{0\sigma}(i\omega_n)$.

Let us write analytic expressions for diagrams 4, 5 and 6 in the first approximation (6.31) for the electron-phonon interaction:

$$\Lambda_4^\sigma(i\omega_n) = \frac{\sigma}{2N}\sum_{\vec{q}m}\frac{t(\vec{q})P_{-\sigma}\varphi_{m-\sigma}P_0\varphi_{00}}{i\omega_n - E_{m-\sigma\vec{q}} + \varepsilon_{-\sigma\sigma}}\left\{f(E_{m-\sigma\vec{q}}) + b(\varepsilon_{-\sigma\sigma})\right\} <\sigma^z + \frac{1}{4}S^z>_0$$

$$\Delta_5^\sigma = -\frac{1}{4}\beta\delta\mu_{-\sigma} <F^{\sigma 0}> \tag{6.47}$$

$$\Delta_6^\sigma(i\omega_n) = \frac{1}{N}\sum_{\vec{q}m}\frac{\beta t^2(\vec{q}) <F^{\sigma 0}> P_\sigma\varphi_{m\sigma}}{i\omega_n - E_{m\sigma\vec{q}}} <F_p^{\sigma 0} F_l^{\sigma 0}>_0$$

Here, $b(x) = 1/(\exp(\beta x)-1)$ is the Bose distribution function, $P_0\varphi_{00} = e^{-\lambda^2(2B+1)}I_0\left(2\lambda^2\sqrt{B(B+1)}\right)$,

$<\sigma^z + \frac{1}{4}S^z>_0 \approx \frac{5}{4}\beta\tilde{H}\frac{2e^{\beta\tilde{\mu}}+1}{5e^{\beta\tilde{\mu}}+4}$. Since $\beta\tilde{H} \ll 1$, the nonzero contribution to $\Lambda_4^\sigma(i\omega_n)$ is

proportional to $b(\varepsilon_{-\sigma\sigma}) <\sigma^z + \frac{1}{4}S^z>_0 \approx \frac{1}{2\sigma}$ at $\beta\tilde{\mu} \gg 1$. Also, for linked diagrams which are

proportional to δ_{pl} we have $<F_p^{\sigma 0} F_l^{\sigma 0}>_0 = m(\tilde{\mu})\delta_{pl}$, where $m(\tilde{\mu}) = \frac{5}{8}\frac{(5e^{\beta\tilde{\mu}}+2)(e^{\beta\tilde{\mu}}+1)}{(5e^{\beta\tilde{\mu}}+4)^2}$.

The formulae for diagrams 4, 5 and 6 in the second approximation (6.34)-(6.35) can be written in the form :

$$\Lambda_4^{-\sigma}(i\omega_n) = \frac{-\sigma}{4N}\sum_{\vec{q}}\frac{t(\vec{q}) <\sigma^z + \frac{1}{4}S^z>_0}{E_{1\sigma\vec{q}} - E_{2\sigma\vec{q}}}\left\{
\begin{aligned}
&\frac{E_{1\sigma\vec{q}} + \varepsilon_{0\sigma}}{i\omega_n - E_{1\sigma\vec{q}} + \sigma\mu_1}\left[f(E_{1\sigma\vec{q}}) + b(\sigma\mu_1)\right] + \\
&\frac{E_{1\sigma\vec{q}} + \varepsilon_{0\sigma}}{i\omega_n - E_{1\sigma\vec{q}} + \sigma\mu_2}\left[f(E_{1\sigma\vec{q}}) + b(\sigma\mu_2)\right] - \\
&\frac{E_{2\sigma\vec{q}} + \varepsilon_{0\sigma}}{i\omega_n - E_{2\sigma\vec{q}} + \sigma\mu_1}\left[f(E_{2\sigma\vec{q}}) + b(\sigma\mu_1)\right] - \\
&\frac{E_{2\sigma\vec{q}} + \varepsilon_{0\sigma}}{i\omega_n - E_{2\sigma\vec{q}} + \sigma\mu_2}\left[f(E_{2\sigma\vec{q}}) + b(\sigma\mu_2)\right]
\end{aligned}
\right\}$$

$$\Delta_6^\sigma(i\omega_n) = \frac{1}{2N}\sum_{\vec{q}}\frac{t^2(\vec{q}) <F^{\sigma 0}>}{E_{1\sigma\vec{q}} - E_{2\sigma\vec{q}}}\left\{\frac{E_{1\sigma\vec{q}} + \varepsilon_{0\sigma}}{i\omega_n - E_{1\sigma\vec{q}}} - \frac{E_{2\sigma\vec{q}} + \varepsilon_{0\sigma}}{i\omega_n - E_{2\sigma\vec{q}}}\right\} <F_p^{\sigma 0} F_l^{\sigma 0}>_0 \tag{6.48}$$

The expression for Δ_5^σ is identical to one presented in Eq. (6.47) having in mind that $\delta\mu_\sigma$ and $E_{i\sigma\vec{q}}$ are determined by Eqs. (6.35) and (6.39), respectively. We will introduce $\mu_1 = \varepsilon_{\uparrow\downarrow} + \xi$, $\mu_2 = \varepsilon_{\uparrow\downarrow} - \xi$. Since the parameters μ_i are finite at $\tilde{H} \to 0$, the product $<\sigma^z + \frac{1}{4}S^z>_0 b(\sigma\mu_i) \to 0$ and thus the contribution $\Lambda_4^{-\sigma}(i\omega_n)$ can be neglected.

To find the final expressions for diagrams, the value of $\Lambda_4^\sigma(i\omega_n)$ should be multiplied by $G_{0\sigma}(i\omega_n)$ and Δ_5^σ, Δ_6^σ by $G_{0\sigma}(i\omega_n)^2$. Then self-energy $\sum_\sigma(i\omega_n)$ is written as

$$\sum_\sigma(i\omega_n) = <F^{\sigma 0}> G_{0\sigma}(i\omega_n) + \Lambda_4^\sigma(i\omega_n)G_{0\sigma}(i\omega_n) + (\Delta_5^\sigma + \Delta_6^\sigma(i\omega_n))G_{0\sigma}(i\omega_n)^2 \qquad (6.49)$$

Using the Larkin equation [91] the total Green function $\mathsf{G}_\sigma(i\omega_n,\vec{k})$ can be easily found:

$$\mathsf{G}_\sigma(i\omega_n,\vec{k}) = \frac{\sum_\sigma(i\omega_n)}{1 - \beta t(\vec{k})\sum_\sigma(i\omega_n)} \qquad (6.50)$$

In the DE model ($\xi = 0$) this formula is essentially simplified:

$$\mathsf{G}_\sigma(i\omega_n,\vec{k}) = \frac{1}{\beta}\frac{<F^{\sigma 0}> + \Lambda_4^\sigma(i\omega_n)}{i\omega_n - \omega_{\sigma\vec{k}}}, \qquad (6.51)$$

where $\omega_{\sigma\vec{k}} = -\varepsilon_{0\sigma} - \frac{1}{4}\delta\mu_{-\sigma} + \left(<F^{\sigma 0}> + \Lambda_4^\sigma(i\omega_n)\right)t(\vec{k}) + \dfrac{\Delta_6^\sigma(i\omega_n)}{\beta<F^{\sigma 0}>}$.

To deduce Eq. (6.51) we have used a linear expansion of small parameters. Realizing in Eqs. (6.50) and (6.51) an analytical continuation $i\omega_n \to \omega + i\delta$ we obtain retarded Green's function whose poles determine the $\Omega(\vec{k})$ spectrum of excitations. Imaginary part of $\mathsf{G}_\sigma(i\omega_n,\vec{k})$ determines the spectral density being proportional to $\delta(\omega - \Omega(\vec{k}))$ for coherent excitations.

The spectral density of an incoherent spectrum describing the relaxation processes is of principal interest. After analytical continuation $i\omega_n \to \omega + i\delta$ using Eqs. (6.47) and (6.48) one can evaluate the nonzero imaginary parts of $\Lambda_4^\sigma(\Omega(\vec{k}))$ and $\Delta_6^\sigma(\Omega(\vec{k}))$. Corresponding formulae are given in Appendix (Eqs. (6.60) and (6.61)). $\sum_\sigma{}'(\omega)$ and $\sum_\sigma{}''(\omega)$ correspond to real and imaginary parts of self-energy $\sum_\sigma(\omega)$, respectively. Let us write the imaginary part $\mathrm{Im}(\mathsf{G}_\sigma(i\omega_n,\vec{k}))$ of the otal Green function as

$$\mathrm{Im}(\mathsf{G}_\sigma(\omega + i\delta,\vec{k})) = \frac{\sum_\sigma{}''(\omega)}{\left(1 - \beta t(\vec{k})\sum_\sigma{}'(\omega)\right)^2 + \left(\beta t(\vec{k})\sum_\sigma{}''(\omega)\right)^2} \qquad (6.52)$$

In the case of incoherent excitations, the spectral density $R_\sigma(\omega,\vec{k}) = -2\beta\,\mathrm{Im}(\mathsf{G}_\sigma(\omega + i\delta,\vec{k}))$ will be different from zero over a certain frequency interval in which the electron density of state $D_C(x)$ has also nonzero value.

As noted above, the pole singularity of Eq. (6.50) allows to find the dispersion law for the excitation spectrum :

$$t(\vec{k}) = t_{0k} = \mathrm{Re}\left(\frac{1}{\beta\sum_\sigma(\Omega(\vec{k}))}\right) = \frac{1}{\beta}\frac{\sum_\sigma{}'(\Omega(\vec{k}))}{\left[\sum_\sigma{}'(\Omega(\vec{k}))\right]^2 + \left[\sum_\sigma{}''(\Omega(\vec{k}))\right]^2} \qquad (6.53)$$

It is easy to check that derivative $\dfrac{dR_\sigma(\omega,\vec{k})}{dt(\vec{k})}$ is zero at $t(\vec{k}) = t_{0k}$. Thus, the extremal points of the spectral density as a function of the hopping integral $t(\vec{k})$ determine t_{0k} corresponding to the resonance

frequency $\Omega(\vec{k})$. On the other hand, the positions of sharp peaks at the frequency curve determine excitations closely related to the coherent ones when the imaginary part of the self energy is small.

In Fig. 6.8a,b frequency dependences of imaginary parts of $\Lambda_4^\sigma(\omega)$ and $\Delta_6^\sigma(\omega)$ as well as the spectral density of an incoherent spectrum for up- and down-spin bands are shown for $\xi = 0$, $T = 0$ and $n = 0.8$. The peaks of $R_\sigma(\omega,\vec{k})$ appear near frequencies at which imaginary parts of $\Lambda_4^\sigma(\omega)$ and $\Delta_6^\sigma(\omega)$ diagrams tend to zero. Negative values of the spectral density in a narrow frequency interval indicate that because of the smallness of the imaginary part the diagrams of the higher order for an effective radius of the interaction are to be accounted for. It should be emphasized that in the given theory $R_\sigma(-\tilde{\mu},\vec{k}) = 0$.

In the CPA method [67], the spectral density is nonzero at the Fermi level that is a serious defect since in this case the Luttinger theorem [21] for the Fermi liquid is violated. In our case, such a problem does not arise because the spectral density of incoherent excitations tends to zero near the Fermi level at $\omega \sim -\tilde{\mu}$.

Fig. 6.9 displays the frequency dependence of the spectral density $R_\sigma(\omega,\vec{k})$ in the approximation (6.31) for an effective line at $n = 0.8$, $\xi/W = 0.03$ and $t(\mathbf{q})/W = 1/3$. The curves 1 and 2 correspond to up- and down-spin bands at low temperature ($T/W = 0.005$) and curve 3 to the PM-2 phase. It is seen that very sharp peaks, characteristic for coherent polaron excitations, are only in the PM-2 phase (see inset in Fig. 6.9). Therefore, polarons are involved in the conductivity above the temperature T_C and enhance it. Unfortunately, the value $\rho(T)$ near T_C (in the PM phase) does not exceed a few mOhm·cm that is inconsistent with the experiment. Seemingly, near the phase transition the vertex corrections in the Green's function start to play an important role. This problem is very complicated and demands a special consideration.

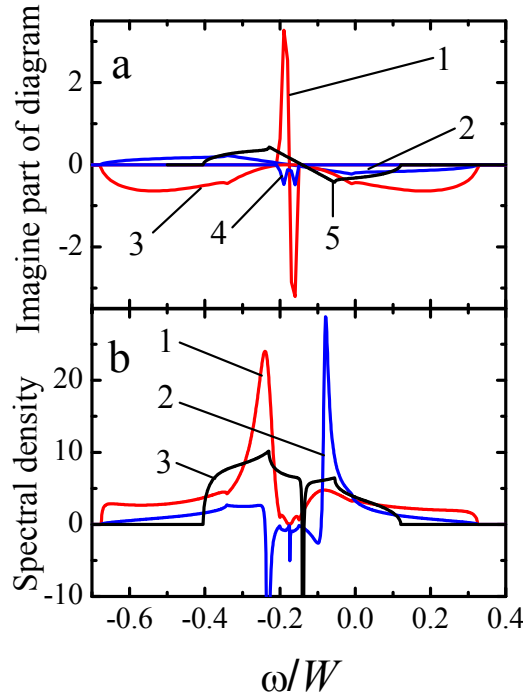*Fig. 6.8.* At $n = 0.8$, $\xi = 0$ and $T = 0$: a) the imaginary parts of diagrams $\Lambda_4^\sigma(\omega)$ (curves 1 and 2) and $\Delta_6^\sigma(\omega)$ (curves 3 and 4) for up- and down-spin bands, respectively. The curve 5 corresponds to $\Lambda_4^\sigma(\omega)$ in the PM phase; b) spectral density as a function of frequency for up- and down-spin bands and the PM phase (curves 1–3, respectively) at $t(\vec{q})/W = -0.1$
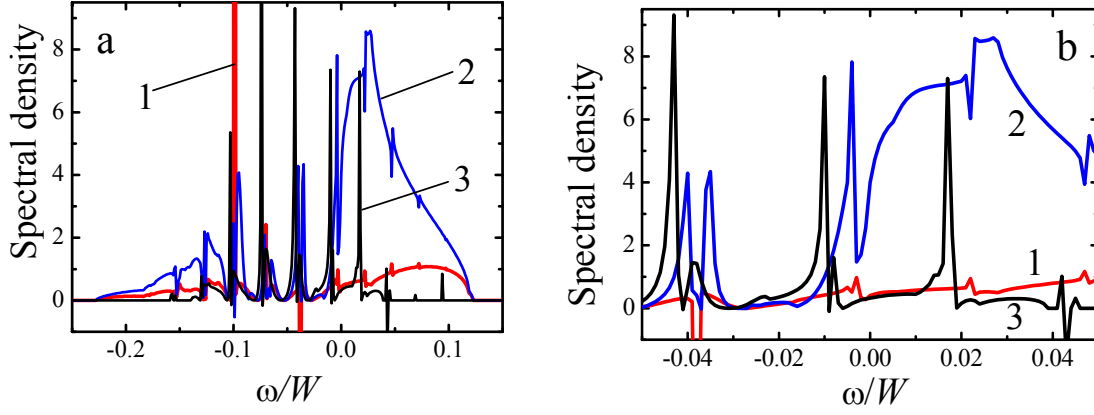
Fig. 6.9. (a) Spectral density versus frequency obtained using the first approximation (Eq. (6.31)) at $\xi = 0.03$, $t(\vec{q})/W = 1/3$, $n = 0.8$ and $T/W = 0.005$ for up- and down-spin bands (curves 1 and 2, respectively) and for the PM phase at $T/W = 0.01228$ (curve 3). (b) The same plot near zero frequency on an enlarged scale

The second approximation (Eqs. (6.35), (6.39) and (6.48)) is applicable to describe magnetoresistive effect. One will suppose that in the excitations spectrum a gap of the order of a small polaron binding energy ξ is formed at $T \sim T_C$. Using Eqs. (6.35), (6.39) and (6.48) we obtain a ~ 30% reduction of the T_C at $\xi/W = 0.2$. The chemical potential lies in the middle of the forbidden band. In Fig. 6.10 spectral densities as a function of frequency for up- and down-spin bands at $T/W = 0.015$ and for the PM phase at $T/W = 0.0172$ are shown at $\xi/W = 0.2$, $n = 0.8$ and $t(\mathbf{q})/W = 0.1$. This correlates with results obtained in [83, 67].
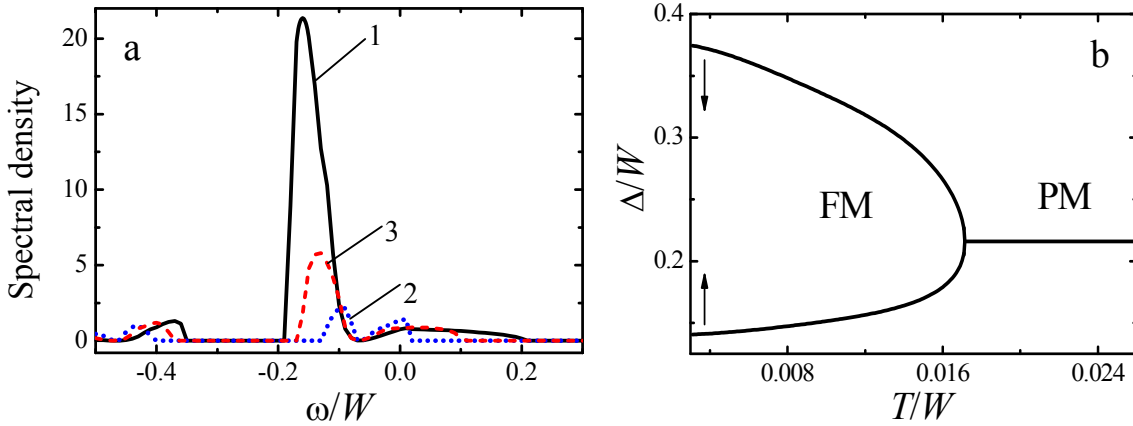
Fig. 6.10. Spectral density versus frequency using the second approximation (Eq. (6.35)) for an effective line of the electron-phonon interaction for up- and down-spin bands (curves 1 and 2, respectively, at $T/W = 0.015$) and for the PM-2 phase ($T/W = 0.0172$) at $\xi = 0.2$, $t(\vec{q})/W = 0.1$, $n = 0.8$. (b) temperature dependences of the quasigap Δ for up-, down-spin bands and the PM-2 phase

The difference is that in the CPA method a quasigap occurs at $g/W \approx 0.15$ and the nonzero spectral density at the Fermi level is increased with increasing temperature. Fig. 6.10b illustrates the temperature dependence of a gap for up- and down-spin bands. In this approximation a gap in the PM phase near the phase transition does not depend practically on temperature.

The expression for conductivity $\sigma(T)$ of the s.c. lattice obtained on basis of the above results using the Kubo formula in the bubble approximation [37] has the form:

$$\sigma(T) = \frac{e^2}{3a\pi\hbar N}\sum_{\vec{k}\sigma}\Phi_\sigma(t(\vec{k}))t(\vec{k}),$$ (6.54)

he $\Phi_\sigma(t(\vec{q}))$ function is related to the spectral density by the following differential equation:

$$\frac{d\Phi_\sigma(t(\vec{k}))}{d(t(\vec{k}))} = \left[R_\sigma(\omega,\vec{k})\right]^2$$ (6.55)

Since the imaginary part of Green's function (Eq. (6.52)) is a simple function of $t(k)$ parameter the integration of the squared spectral density in Eq. (6.55) presents no problem. Here we will not derivate a sufficiently complicated expression for $\Phi_\sigma(t(\vec{k}))$.

In Fig. 6.11 the resistivity versus band filling, $\rho(n)$, in FM and PM-2 phases (curves 1 and 2, respectively) are shown at $T = 0$ and $\xi = 0$. Curve 3 in Fig. 6.11 shows the dependence $\rho(n)$ in the PM phase calculated by the CPA method [37]. It is seen from Fig. 6.11 that the CPA method gives the minimal $\rho(n)$ value of the order of 1 mOhm·cm. In our case, the $\rho(n)$ resistivity in PM-2 and FM phases is rather smaller near their lower borders at $n \geq n_0$ (n_0 is equal to 0.116 and 0.588 for PM-2 и FM phases, respectively). According to the experimental data in the work [92], in $La_{1-x}Sr_xMnO_3$ the residuary resistance at $x \sim 0.3$ is essentially smaller than 1 mOhm·cm. For $n \rightarrow 1$ the $\rho(n)$ resistivity in the FM phase is abruptly increased as in the CPA method. However, for a dielectric state ($\mathbf{n} = 1$) the higher-order diagrams must be taken into account.
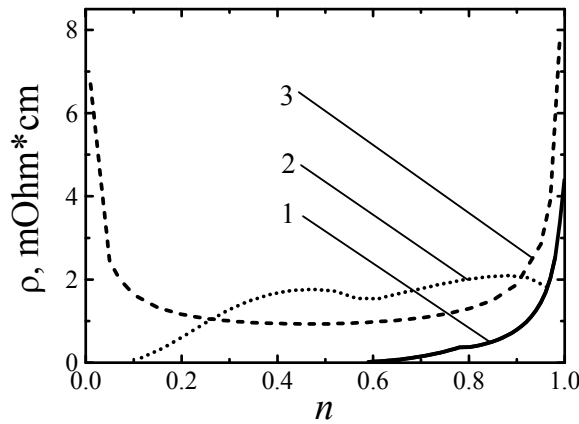
Fig. 6.11. Resistivity $\rho(n)$ in the DE model for FM and PM-2 phases (curves 1 and 2) at $T = 0$ and $h = 0$. The curve 3 is obtained using the coherent potential approximation (CPA) [37]

Fig. 6.12a shows the temperature dependence of the resistivity at $n = 0.8$ without electron-phonon coupling. Unlike the CPA method, a sufficiently abrupt growth of resistivity near the phase transition with increasing T is seen. In Fig. 6.12b the temperature dependences of imaginary parts of $\Lambda_4^\sigma(\omega)$ and $\Delta_6^\sigma(\omega)$ at $\omega = 0$ are shown. A sharp increase of some of them near T_C reflects essential strengthening of scattering processes in the range of the phase transition. In the PM phase the resistivity is weakly dependent on temperature, and its maximal value does not exceed several mOhm·cm as it was observed in [37]. The authors of [83, 86, 67] pointed out that it is the characteristic property of systems with a dominant DE as $La_{1-x}Sr_xMnO_3$ manganites. In

La$_{1-x}$Ca$_x$MnO$_3$ compounds, the polaron dynamics becomes important because of stronger electron-phonon coupling.

In Fig. 6.13, the influence of a weak electron-phonon interaction on $\rho(T)$ dependence calculated within the first approximation (6.31) for an effective line at $n = 0.8$ is shown. Indeed, above T_C large polarons take part in conductivity enhancing it with increasing temperature. However, the resistivity falls off with increasing polaron binding energy ξ. The discrepancy between calculated and experimental values of the maximum resistivity is due to the influence of vertex corrections in current correlators ignored in the bubble approximation.
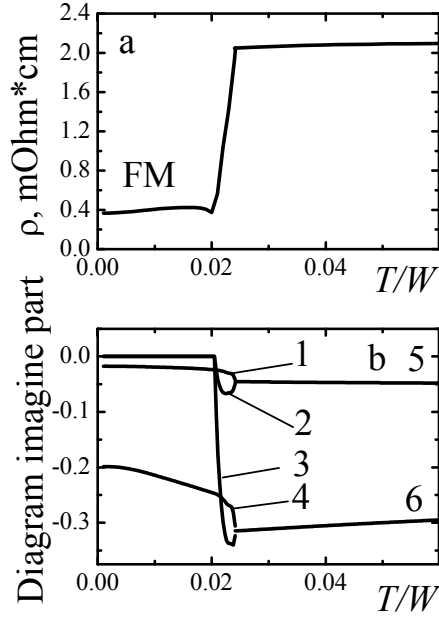
Fig. 6.12. In the DE model the $\rho(T)$ dependences (a) and imaginary parts of $\Delta_6^\sigma(\omega)$ and $\Lambda_4^\sigma(\omega)$ (b) diagrams at $n = 0.8$ and $\omega = 0$ (curves 1, 3 and 2, 4 for up- and down-spin band, respectively). The curves 5 and 6 are the same plots for $\Delta_6^\sigma(\omega)$ and $\Lambda_4^\sigma(\omega)$ in the PM-2 phase
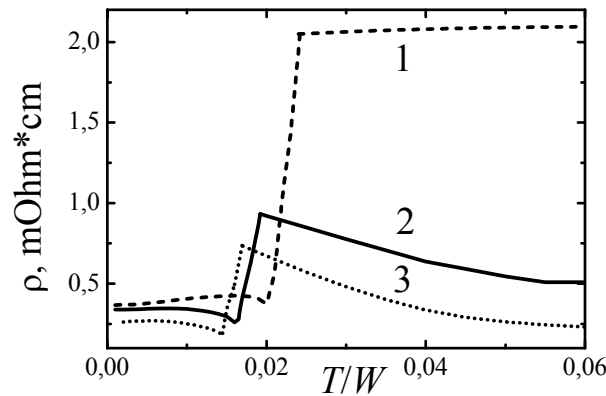
Fig. 6.13. Effect of the weak electron-phonon interaction on $\rho(T)$ at $n = 0.8$ and $h = 0$ for the polaron binding energy ξ/W: 0, 0.003 and 0.005 (curves 1-3, respectively)

Let us apply the second approximation (Eqs. (6.34)-(6.35)) to find the contribution of Δ_5^σ diagram in the spectral density $R_\sigma(\omega,\vec{k})$ calculated using Eq. (6.51) and taking into account that

in this approximation the contribution of $\Lambda_4^\sigma(\omega)$ diagram is equal to zero. It is seen from Fig. 6.14 that $\rho(T)$ correlates well with the experimental maximum resistivity near the phase transition as in the case of $La_{1-x}Ca_xMnO_3$. At high temperatures, the chemical potential abruptly decreases providing zero spectral density. It points to limited usefulness of this approximation in resistivity calculations.

In Fig. 6.14 the $\rho(T)$ curves for different magnetic fields, h, at $n = 0.8$ and $\xi/W = 0.2$ are shown. The values of both h and superexchange, $J(0)$, were chosen as in Fig. 6.7. In Fig. 6.14 one can see that the resistivity peak decreases and shifts towards higher fields with increasing applied magnetic fields. This agrees with the experimental data for the same values of h.
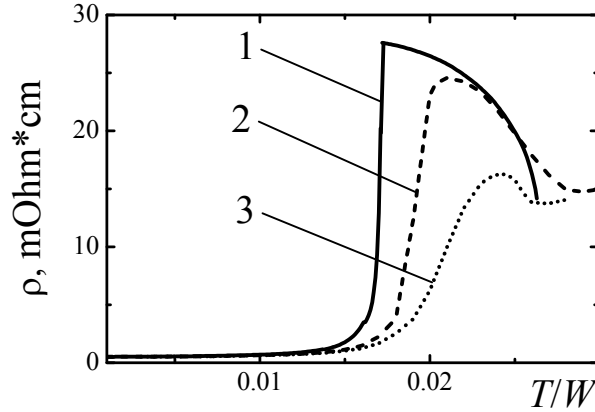
Fig. 6.14. Temperature dependence of resistivity obtained using the second approximation (Eq. (6.35)) with account of the electron-phonon interaction at $\xi/W = 0.2$, $n = 0.8$ and $h = 0$, $J(0) = 0$ (curve 1) and at $J(0)/W = 0.00215$, $h/W = 0.0001$ and 0.0006 (curves 2 and 3, respectively). The spectral density was calculated using Eq. (6.51)

Note that in [83, 86, 67, 93] h values obtained for the same reduction of ρ were five times larger than those in the experiment. The shift of the spectral density $R_\sigma(\omega,\vec{k})$ peak (Eq. (6.53)) versus $t(\vec{k})$ to the electron band edge as well as at $t_{0k} \geq 3$ is the main reason of the sharp increase of resistivity. In this case, the $\Phi_\sigma(t(\vec{k}))t(\vec{k})$ function (Eq. (6.54)) becomes almost antisymmetric.

6.7. Conclusions

Diagram techniques were proposed and developed taking into account quantum fluctuations of electron and ion spins in the model of a narrow-band Hubbard's magnet with strong Hund's rule coupling. On the basis of separated out self-consistent field in the DE model with electron-phonon coupling the equations for both magnetization and chemical potential were obtained. Quantum fluctuations of electron and ion spins were shown to reduce the Curie temperature at approximately 30 %. In the pure DE model the obtained concentration dependence of T_C in units of the bandwidth W well coincides with a similar result in the CPA method. The analysis of the temperature dependence of conductivity in the framework of a considered model shows that the $\rho(T)$ dependence rapidly drops with decreasing temperature below T_C (as for, as in $La_{1-x}Sr_xMnO_3$ with an optimal Sr content). This is due to enforcing the scattering effects near the phase transition. In the CPA theory the minimal value $\rho_0 \sim 1$ mOhm·cm was obtained for the PM phase at $T = 0$. The residual resistivity

$\rho_0 \ll 1$ mOhm·cm was found experimentally for some perovskite manganites. Our calculations agree well with this experimental result near the critical band filling with $n_0 \sim 0.116$ and 0.588 for PM-2 и FM phases, respectively The estimates of the influence of electron-phonon coupling on the magnetic structure, ordering temperature, spectral and transport properties using two approximations for the effective line of the interaction was made. Using the first approximation having regard to a few polaron bands with a quasigap near the Fermi level, a strong effect of the electron-phonon interaction on T_C as well as on the magnetization was revealed. Analysis of the spectral density shows the presence of pronounced polaron peaks in the PM-2 phase responsible for the growth of conductivity above T_C with increasing temperature. The resistivity falls off with increasing polaron binding energy ξ. Such unusual behavior of $\rho(T)$ is due to a miscalculation neglecting the influence of vertex corrections in the two-particle Green's function. Using the second approximation the effective line of two polaron bands with a gap of the order of the polaron binding energy was accounted. The influence of the ξ parameter on both T_C and magnetization was found to be essentially weaker than it is observed in the CPA method. This approximation describes well the temperature dependence of resistivity near the FM-PM phase transition as well as the influence of the applied magnetic field on the magnetoresistive effect.

6.8. Appendix

Annihilation operators are expressed as

$$c_\uparrow = L^{9,1} + \frac{\sqrt{3}}{2} L^{10,2} + \frac{1}{\sqrt{2}} L^{11,3} + \frac{1}{2} L^{12,4}$$

$$c_\downarrow = \frac{1}{2} L^{9,2} + \frac{1}{\sqrt{2}} L^{10,3} + \frac{\sqrt{3}}{2} L^{11,4} + L^{12,5}$$

(6.56)

To obtain similar formulae for electron creation operators, the Hermitian conjugate of (6.56) was performed. Since we used the wave functions of a model space in which $|\varphi_6\rangle, |\varphi_7\rangle$ and $|\varphi_8\rangle$ functions of orthogonal add-ins are excluded, the equality $c^+ c + c c^+ = 1$ fails for Fermi operators. However, under this consideration it is not important because the Wick's theorem is applied directly to Hubbard's operators for which the Fermi or Bose origin does not break down.

The operators of electron n and hole p numbers have the form:

$$\hat{n} = L^{1,1} + L^{2,2} + L^{3,3} + L^{4,4} + L^{5,5}$$

$$\hat{p} = L^{9,9} + L^{10,10} + L^{11,11} + L^{12,12}$$

(6.57)

In this case $p + n = 1$. The operators of electron n_σ and hole p_σ numbers with spin σ are determined as follows:

$$\hat{n}_\uparrow = L^{1,1} + \frac{3}{4} L^{2,2} + \frac{1}{2} L^{3,3} + \frac{1}{4} L^{4,4}$$

$$\hat{n}_\downarrow = \frac{1}{4} L^{2,2} + \frac{1}{2} L^{3,3} + \frac{3}{4} L^{4,4} + L^{5,5}$$

$$\hat{p}_\uparrow = L^{9,9} + \frac{3}{4} L^{10,10} + \frac{1}{2} L^{11,11} + \frac{1}{4} L^{12,12}$$

$$\hat{p}_\downarrow = \frac{1}{4} L^{9,9} + \frac{1}{2} L^{10,10} + \frac{3}{4} L^{11,11} + L^{12,12}$$

(6.58)

The next relations take place:

$$\hat{n}_\uparrow + \hat{n}_\downarrow = \hat{n}, \ \hat{p}_\uparrow + \hat{p}_\downarrow = \frac{5}{4}(1-\hat{n}),$$

$$\hat{n}_\uparrow - \hat{n}_\downarrow = 2\sigma^z$$

$$\hat{p}_\uparrow - \hat{p}_\downarrow = \frac{1}{2}S_0^z \qquad (6.59)$$

The z-projection of spin operator S^z in the truncated basis of t$_{2g}$ and e$_g$ electrons is expressed as

$$S^z = \frac{3}{2}(L^{1,1} - L^{5,5} + L^{9,9} - L^{12,12}) + \frac{3}{4}(L^{2,2} - L^{4,4}) + \frac{1}{2}(L^{10,10} - L^{11,11})$$

Imaginary parts of $\Lambda_4^\sigma(\omega)$ and $\Delta_6^\sigma(\omega)$ functions after analytic continuation to the real axis $i\omega_n \to \omega + i\delta$ are written in the form:

a) approximation (6.31) with formulae (6.47) for $\Lambda_4^\sigma(\omega)$ and $\Delta_6^\sigma(\omega)$:

$$\mathrm{Im}(\Lambda_4^\sigma(\omega)) = -\frac{3\pi\sigma b(\varepsilon_{-\sigma\sigma}) < \sigma^z + \frac{1}{4}S^z >_0}{W < F^{-\sigma 0} >^2} \sum_{m=-\infty}^{\infty} (\Omega_m(\omega) + \varepsilon_{0-\sigma}) \frac{P_0\varphi_{00}}{P_{-\sigma}\varphi_{m-\sigma}} D_C\left(\frac{6(\Omega_m(\omega) + \varepsilon_{0-\sigma})}{< F^{-\sigma 0} > P_{-\sigma}\varphi_{m-\sigma}W}\right),$$

(6.60)

where $\Omega_m(\omega) = \omega + \varepsilon_{0-\sigma} + m\omega_0$.

$$\frac{1}{\beta}\mathrm{Im}\left(\Delta_6^\sigma(\omega)\right) = -\frac{6\pi m(\tilde{\mu})}{W < F^{\sigma 0} >^2} \sum_{m=-\infty}^{\infty} (\Omega_m(\omega) + \varepsilon_{0\sigma})^2 \frac{1}{\left(P_\sigma\varphi_{m\sigma}\right)^2} D_C\left(\frac{6(\Omega_m(\omega) + \varepsilon_{0\sigma})}{< F^{-\sigma 0} > P_\sigma\varphi_{m\sigma}}\right) \quad (6.61)$$

б) approximation (6.34) – (6.35) with (6.48) for $\Delta_6^\sigma(\Omega)$:

$$\frac{1}{\beta}\mathrm{Im}\left(\Delta_6^\sigma(\omega)\right) = -\frac{6\pi m(\tilde{\mu})\left[(\omega + \varepsilon_{0\sigma})^2 - \xi^2\right]^2}{W < F^{\sigma 0} >^2 (\omega + \varepsilon_{0\sigma})^2} D_C\left(6\frac{(\omega + \varepsilon_{0\sigma})^2 - \xi^2}{W < F^{\sigma 0} > (\omega + \varepsilon_{0\sigma})}\right) \qquad (6.62)$$

135

7. RESISTIVE SWITCHING EFFECTS IN OXIDE-BASED HETEROSTRUCTURES

7.1. Introduction

Considerable efforts are nowadays devoted to developing the next generation of memory devices capable of overcoming the downscaling limitations of actual flash memories. In particular, resistive random access memories (ReRAM) based on cells with nanoscale metal/transition-metal oxide/metal setups are perspective candidates, exhibiting fast read/erase operations with very promising characteristics for high-density integration [94]. Their operation relies on the resistive switching phenomenon, a reversible change of the resistance between two well-defined magnitudes, high (HR) and low (LR) resistance ones, which is stimulated by applied electric pulses. The switching HR-to-LR effect is named bipolar when voltages of different polarities are controlling related transitions. In general, the bipolar cells exhibit better stability than unipolar ones. Even more, such devices based on binary transition-metal oxides usually demonstrate high compatibility with the traditional integration and retention times of more than 10^6 s. A large variety of binary oxides has been explored for ReRAM applications and the most popular of them is titanium dioxide TiO_2 [95]. Since the first physical example of a solid-state memristive device in the paper [96], these compounds have become a target of many recent studies. At the same time, we can conclude that despite the fact that several physical mechanisms based on the resistive switching effect have been recently proposed, all ingredients involved in this phenomenon have not yet been fully understood.

In this section, we discuss two issues related to the resistive switching phenomenon, the evidence of the HR-to-LR and inverse transitions at a single interface formed by a metal counter-electrode and a complex-oxide surface using oxygen-deficient yttrium-barium four-component oxide as a prototype. Together with Slovak colleagues, we have observed resistance hysteresis switching loops similar to those obtained in the case of two active interfaces [94], as will be described below. The experimental results are qualitatively reproduced by our numerical simulations built on the idea of oxygen vacancies as an origin of the discussed resistance changes. The electroforming mechanism and the degradation process in such bilayers are discussed as well. The second part of the section is dealing with a novel self-textured nanofilament technique based on the resistive-switching effect in nano-scale transition-metal oxide films. While traditional tunneling and point-contact approaches to the electron-boson interaction spectroscopy in a strong-coupled superconductor are realized *on different samples*, the novel method allows one to get related data *on the same device*. We argue that the proposed nanoscale methodology provides a simple and promising way for studying an interaction responsible for Cooper pairing in superconducting materials.

7.2. Electromigration effect in YBCO thin films

Oxygen-deficient yttrium-barium copper oxide with the general formula $YBa_2Cu_3O_{7-c}$ ($0 < c < 1$) was the first material found to become superconducting above 77 K, the boiling temperature of liquid nitrogen. Whereas $YBa_2Cu_3O_7$ is a well-defined chemical compound with a specific structure and stoichiometry, the structure and physical characteristics of cuprates with less than seven oxygen atoms per formula unit strongly depend on the value of c, the oxygen

vacancies content representing availability of empty lattice sites, which might be occupied by a migrating atom. The YBa$_2$Cu$_3$O$_{7-c}$ (YBCO) compounds are generally considered to be quasi-two-dimensional materials with electrons moving within weakly coupled copper-oxide (CuO$_2$) layers. Their electronic properties strongly depend on the number of charge carriers put into the CuO$_2$ planes. For low-carrier concentration (underdoped regime), when $c \leq 1$, the materials are insulating. The doping is achieved by adding oxygen atoms, which introduce positively charged carriers (`holes') into the CuO$_2$ planes where the superconductivity is believed to originate and for a high-carrier concentration (overdoped regime) the YBa$_2$Cu$_3$O$_{7-c}$ compounds are metallic. In some in-between states they become superconducting with a maximal critical temperature T_c for the optimum doping [97]. The YBCO films studied by us just belonged to the latter regime.

High-T_c superconductivity models are mainly based on the assumption that the introduced carriers are distributed uniformly, thus leading to an electronically homogeneous system as in conventional metals. However, now there is growing evidence for the presence of multiple phases with boundaries which are functions of temperature, doping, and magnetic field [98]. For example, scanning tunneling spectroscopy has revealed a strong spatial modulation of the local density-of-states spectrum in Bi-based cuprates and the superconducting energy gap that varies on surprisingly short-length scale of a few crystalline unit cells [99]. In order to extend the imaging of the spatial inhomogeneity from nanometer- to meso-scale and from the sample surface to its bulk, the authors of the recent paper [100] performed scanning micro X-ray diffraction measurements from 280 to 85 K on a single-layer cuprate HgBa$_2$CuO$_{4+y}$ at optimum doping ($y = 0.12$), with T_c about 95 K. Their results provided further evidence for the universality of a mesoscale phase separation even in the most optimized superconducting cuprates.

Analyzing prior results for the charge distribution pattern, we can see that the high-T_c materials are very sensitive to local variations in the doping level on nano- and micrometer scales. The intricate scale-free pattern formation is set by a delicate balance among disorder, interactions, and material anisotropy, leading to a fractal nature of the cluster pattern [101]. Following the task to probe different intermediate lengths between the nanometer and macroscopic scales [101] our first goal was to fill this gap and to reveal the charge distribution pattern at the scale of about 100 nm.

As was suggested in [101] and [102], the disordered charge distribution can give rise to hysteretic and memory phenomena in response to external inputs. Our next aim was just to study such effects in current-voltage characteristics of optimally doped YBCO layers in the normal state. Up to now, two (from the first sight, mutually exclusive) electric-field-effect mechanisms have been proposed. The first one, fundamentally electronic, is based on a conventional approach that takes into account the Coulomb interaction of an applied field with mobile current carriers [103]. It is very fast, symmetric with respect to the bias polarity and is expected to manifest itself in the enhancement or depletion of the number of charge carriers within a few near-surface atomic layers [103]. The second mechanism [104] is related to the direct interaction of oxygen ions with an applied electric field that causes their significant rearrangement due to a comparatively small oxygen migration energy and high density of vacancies within the oxygen sublattice in the optimally doping state. Such a process is characterized by a slower time constant and can be unequal in magnitude at positive and negative voltage biases of the same absolute values [104]. To choose between the two mechanisms of field-induced changes in normal-state cuprates is an experimental task. Existing data cannot uniquely support any explanation since some evidences support direct doping of superconducting CuO$_2$ planes by electric-field induced mobile charges [105] whereas others favor the oxygen-diffusion scenario [106]. In the following, we provide some new arguments to show that the latter picture is the basic phenomenon governing normal-state transport characteristics of a contact formed by a metal tip with

the YBCO optimally-doped film. At the same time, we stress that the effect of itinerant holes is very important since it can strongly influence hysteretic phenomena in such structures changing the resistance-switching voltage-bias polarity comparing to that observed in related bilayer samples, see, e.g., [107]. Below we argue that such radical modifications in optimally-doped YBCO films can arise due to the electromigration effect [108] that reveals itself in momentum transfer from current carriers moving in the applied electric field to the ions which make up the lattice of the material (the so-called "current-carrier wind"). Therefore, the last purpose of this work is to realize this effect experimentally and to develop a minimalist model able to shed some light on the nature of double-valued transport characteristics in heterostructures based on normal-state YBCO films.

Experiments provided in several laboratories have revealed that the charge conduction in the LR state is highly inhomogeneous and, in fact, is determined by one-dimensional paths associated with enhanced conduction channels. Such paths are created artificially by an initial application of strong electric fields bringing the oxide close to its breakdown. Thus, we assume that the electric transport is dominated by a single conductive path that is embedded within an insulating host. The next important feature of the model is the decisive role of oxygen vacancies in transition-metal oxides whose *local* resistivity is dramatically controlled by the *local* oxygen stoichiometry and we hope that the form of this dependence is not crucial for our results. The last assumption related an active region near the oxide surface where the main switching events take place. We suppose that it is a near-surface area in the yttrium-barium cuprate sample.

Hole-wind effect. Oxygen vacancies, intrinsic to perovskite oxides, play a major role in electronic and magnetic properties of the strongly correlated systems. Our interpretation of resistance modulations in contacts formed by a metallic counter-electrode and a YBCO film is based on the assumption that these processes are caused by the migration of oxygen vacancies and, as a result, formation or dissolution of more or less conductive regions near the tip-YBCO interface depending on the voltage-bias polarity.

Let us notice that, in contrast to binary oxides [96], an optimally doped YBCO compound is a conductor where charge carriers are holes rather than electrons in ordinary metals. In a conductor, an applied electric field E strongly impacts ionized migrating atoms with a net charge $q_{net} = Z_{net}e$ (e is the elementary charge) that appears to be the result of incomplete screening of the ion charge by electrons. In ordinary metals $q_{net} > 0$ (q_{net} is negative in the case of oxygen ions) and due to the direct electric field acting on the defect $F_1 = q_{net}E$ positively charged ions should move to the cathode. However, in some cases they are migrating in the opposite direction forming hillocks at the anode [109]. This finding led to the conclusion that in metals there is also another driving force $F_2 = q_{wind}E$ occurred due to momentum transfer from current carriers to a defect toward their flow under the field E (the so-called "charge wind") [108]. As was shown in [110], the sign of Z_{wind} depends on the character of the electron spectrum, i.e., on the electron dispersion law. To illustrate this, the author [110] considered a complicated model of a metal consisting of electron and hole bands with a quadratic dispersion law. He found that electrons and holes produce forces that drag the defect in opposite directions. In metals in which the "hole wind" predominates, it will be dragged by the current towards the cathode, whereas in electronic metals the itinerant electrons involve ions in their motion towards the anode. If to speak about negative oxygen ions, it means that the electric field applied to the YBCO hole-conducting film will exert a force F_2 on them in the direction opposite to their flow under the direct force F_1. Because of shielding, the latter force can be quite small when the density of charge carriers is high. Hence, the momentum exchange between the conducting electrons colliding with oxygen ions may change the direction of their flow to the opposite one.

The charge-wind effect is essentially nonlinear and occurs only above certain critical value of an external bias [111]. We can estimate an upper bound of the force F_2 by the product of the maximal value of the momentum transfer $2mv_F$ (m is an effective charge mass and v_F is the Fermi velocity) and the rate of hole-defect collisions equal to JA/e, where $J = \sigma E$ is the current density, σ is the local electrical conductance, and A is the scattering cross section for this process. We assume that the upper bound of the linear-response ballistic regime $F_2 \leq 2mv_F JA/e$ is valid for high-voltage biases in our experiments and hence we may introduce an effective valence Z^* for mobile oxygen vacancies in the following form

$$Z^* = Z_{net} - 2mv_F\sigma A. \tag{7.1}$$

As larger is the local concentration of itinerant holes, as smaller is the net valence $Z_{net} > 0$ and as larger is the impact of the second term in Eq. (7.1). The sign of Z^* depends on the balance between the two terms which in turn may radically vary from one point to another due to the strong inhomogeneity of the local surface conductivity in YBCO samples.

Space-charge effects in YBCO film with a free surface. To characterize the initial state of such YBCO film, we are referring to previous experiments with planar Ag/YBCO bilayer junctions demonstrated hysteretic behavior as well [112, 113]. Low-voltage differential conductance $G(V) = dI(V)/dV$ in LR and HR states was measured at 4.2 K when the c-axis oriented cuprate films were superconducting. At voltages $|V|$ of the order of the YBCO gap parameter, the LR state usually exhibited clear gap-induced features in $G(V)$ curves typical for a metal-insulator-metal junction between a normal counter-electrode and a superconductor with dominant elastic tunneling contribution, whereas, in the HR state, a quasi-linear growth of the differential conductance with a very weak fine structure in the gap region was observed. It means that in the first case a narrow poorly conducting region was formed with a barrier height high enough to allow only quantum-tunneling processes and a width so thin that the charge transmissions were only elastic. The superconducting gap features almost disappeared in the HR state and the differential conductance $G(V)$ grew rapidly with $|V|$ quasi-linearly $G(V) \propto |V|$. Such changes in $G(V)$ can be understood as an effect of the increased barrier width when inelastic tunneling processes across the insulating layer become dominant. Note that a prerequisite for a quasi-linear conductance increase, a nearly constant density of bosonic excitations created in the charge energy-loss transmissions, is well satisfied in complex transition-metal oxides, at least, for phonons [114].

What is the origin of the poor-conducting region that is adjacent to the metal-cuprate interface and why its strength slowly increases in time in as-prepared metal-YBCO bilayers as was found in [115]? Is it the result of a technological factor or it has more fundamental grounds? To answer the questions, we assume that cuprates in the normal state may be regarded as quasiparticle insulators [116] with holes, the current carriers in optimally doped YBCO samples, localized at the ion sites and moving by hopping between them [117]. Next, following [117], we explain the existence of a space-charge region near the metal-YBCO interface by a theory proposed by Frenkel for ionic solids. It comes from the fact that in the bulk of a polar crystal, the condition of charge neutrality $\rho \equiv 0$ constrains individual point defects (vacancies, in our case) to have stoichiometric ratios whereas near a surface, those with a lower formation energy would predominate. Spatial distributions of the charged defects lead to a potential difference between the bulk and the free surface in equilibrium. In the case of YBCO films, it can appear also during

the film fabrication process when the vacancies may be quenched at high temperatures when ionic mobility is high enough to maintain equilibrium.

For the sake of simplicity, we shall limit ourselves to a one-dimensional approximation for a substrate-cuprate-metal trilayer with interfaces at $x = 0$ between the cuprate film and the substrate and $x = d$ between YBCO and a metal counter-electrode. Letting the electrical potential equal zero at $x = d$, we can calculate its value $\varphi_0 = \varphi(x \to 0)$ from the neutrality condition. To derive it, we assume that point-defect formation energies do not change radically within the YBCO metallic phase and take them from Table I in [117] where corresponding energies were computed for the $YBa_2Cu_3O_7$ compound. Following the related procedure described in [117], we have found that the bulk potential $\varphi_0 = 0.19$ V at 300 K. Thus, at room temperature in equilibrium (even without external electric fields) there is an initial electric potential gradient $E_{in}(x) = -d\varphi_{in}(x)/dx$ inside the YBCO film in the direction normal to its surface. In typical metals, the depth of this sheath is given by the Thomas-Fermi screening length scale that is negligibly small due to the field screening by itinerant electrons. Usually, it is believed that in the optimally doped YBCO compound, the major changes of the electric potential are concentrated in one-two crystal cells near the free surface as well [103].

However, these arguments do not take into account the fact that the initial field $E_{in}(x)$ may lead to displacement of charged defects, most mobile of which are oxygen vacancies. The field is comparatively weak and the hole-wind effect is supposedly below related threshold value and, hence, $Z_{in}^* = Z_{net} > 0$. The force $F(x) = Z * eE(x)$ generates a drift flow of vacancies $J_{drift}(x) = c(x)v_E(x)$ where the drift velocity $v_E(x) = \mu F(x)$ with $\mu = D/(k_B T)$, the ion mobility and D, the diffusion constant. Besides it, there is a diffusion flow proportional to the gradient of the vacancies concentration, $J_{dif}(x) = -D(dc(x)/dx)$. In the stationary state, the total flux vanishes $J_{in}(x) \equiv 0$. Thus, the equilibrium distribution of oxygen vacancies $c_{in}(x)$ in a cuprate film with a free surface should satisfy the equation

$$\frac{dc_{in}(x)}{dx} = \frac{Z_{net}ec_{in}(x)}{k_B T}E_{in}(x) \tag{7.2}$$

that can be integrated using the boundary value of the potential $\varphi_0 = 0.19$ V and that of the vacancies concentration $c_0 \approx 0.24$ in an optimally doped YBCO film. Therefore, we get

$$c_{in}(x) = 0.24 \exp\left(\frac{Z_{net}e(\varphi_0 - \varphi_{in}(x))}{k_B T}\right). \tag{7.3}$$

It follows from Eq. (7.3) that, at the optimal doping, the concentration of oxygen vacancies starts from $c_{in}(x \to 0) = 0.24$ in the YBCO-film deepness and approaches the value $c_{in}(d) = 0.24 \exp(Z_{net}e\varphi_0/k_B T)$ at the YBCO-metal interface. For $Z_{net} \approx 0.2$ and higher $c_{in}(d) \approx 1$. In this case, near the YBCO-metal interface there is a sheath of an insulating YBCO compound with a huge Debye length at room temperature (see Table II in [117]). In contrast to the standard approach, assuming full screening of the surface charge on scales of the order of the YBCO lattice parameter, the analysis above shows that a large part of the bulk near the boundary will be affected by the internal electric field. As a result, the concentration of oxygen vacancies, and, consequently, the properties of the material are very heterogeneous as they approach the free cuprate surface, near which there is a thin layer of an underdoped metal-oxide compound $YBa_2Cu_3O_{7-c}$ with $c \le 1$ which, in turn, is an antiferromagnetic insulator.

The near-surface high-resistance region is just a 'natural' abnormally wide and low potential barrier that often appears on the YBCO surface and has been revealed in tunneling experiments with superconducting cuprates [113, 118]. The barrier strength can noticeably change in time [115]. Indeed, as-prepared cuprate films immediately after deposition are in a metastable state and oxygen-ion diffusion, which takes place in perovskite oxides even at low temperatures due to their specific structural features [119], causes temporal modifications of the near-interface oxygen content resulting in its outdiffusion and, hence, in the continuous increase of the contact resistance like that observed in [115] or in decrease in dielectric constant with a time scale of 180 seconds in capacitive measurements [120]. We believe that these temporal processes are associated not with the imperfection of the samples but rather with the redistribution of oxygen ions. The presence of an adjacent to the surface region, depleted of oxygen, can explain the detection of two or more energy gaps in the tunneling characteristics of yttrium-barium cuprate [118], unusual linear differential conductance-vs-voltage relation [113] which apparently may arise from inelastic electron tunneling through an antiferromagnetic dielectric interlayer as well as charge carrier redistribution in cuprate thin-film multilayers over an anomalously large distance [121].

Memristive-like effects in transport characteristics of metal counter-electrode–YBCO thin film contacts. Experiments with YBCO films can provide important information concerning the nature of the hysteretic phenomenon in *I-V* characteristics of the contacts based on complex transition-metal oxides. The prior discussion shows that the YBCO film can be conditionally divided into two parts, an active one from $x = \tilde{d}$ to $x = d$ where the man changes of the local resistivity take part and the rest that can be regarded as a reservoir for vacancies that come in and out under the influence of a periodically varying external bias and only slightly modify its metallic resistance $R_0 \approx \text{const}$. The local resistance within the film active part can be found using an approximate one-to-one relation between the homogeneous *c*-axis-oriented YBCO film resistivity ρ and its oxygen stoichiometry $\rho(c) = \rho_0 f(c)$ with $f(c) = \exp(5c)$ [122] that allows quantitative modeling of the effect. This formula is valid for $0.2 < c < 0.7$ (see Fig. 7.5 in [122]) but we extrapolate it up to $c \leq 1$, thus, underestimating the contribution of high-resistivity regions into the total contact resistance $R(t) = R_0 + \int_{\tilde{d}}^{d} \rho(x,t)dx$. The local resistivity-to-vacancy concentration correspondence $\rho(x,t) = \rho_0 f(c(x,t))$ makes it possible to calculate the contact resistance knowing the vacancy concentration $c(x,t)$ in time and space domains. Imitating our experiments, we consider an ac voltage-bias source $V(t)$ applied to the YBCO layer with mobile oxygen vacancies that generates the ac current $I(t)$ and at the same time modifies the film conductance $G(t)$ due to changes in the spatially dependent profile $c(x,t)$. As a result, it leads to a double-valued dependence of the current $I(t) = G(t)V(t)$ on the voltage bias applied.

The aim of this subsection is to show that we are just dealing with a voltage-controlled memristive system whose current-vs-voltage (the input-vs-the output) characteristic is defined by the equation $I(t) = G(z,V,t)V(t)$ where $G(z,V,t)$ is the generalized response function, z is the set of variables describing the internal state of the system, whose evolution is defined by an equation $\dfrac{dz}{dt} = f(z,V,t)$ [123]. Below we demonstrate that in our case the parameter z introduced in the theory of memristive systems is just the vacancy concentration $c(x,t)$.

The key relation describing the oxygen subsystem is the conventional mass balance (continuity) equation for $c(x,t)$, a consequence of the conservation of the number of vacancies

$$\frac{\partial c(x,t)}{\partial t} + \frac{\partial J(x,t)}{\partial x} = 0 \,. \tag{7.4}$$

Note that in our model approach the total number of oxygen vacancies in the region $\tilde{d} < x < d$ is not conserved since a part of them arrives and leaves the metallic part of the YBCO film. In the equation (7.4) the total vacancy flux $J(x,t) = J_{\mathrm{dif}}(x,t) + J_{\mathrm{drift}}(x,t)$. Using relations given above we obtain

$$J(x,t) = -D\frac{\partial c(x,t)}{\partial x} + \frac{Dq*c(x,t)}{k_{\mathrm{B}}T}E(x,t)\,, \tag{7.5}$$

where $E(x,t) = \rho(x,t)I(t)$. Notice that at comparatively high voltage biases $q*V \gg k_{\mathrm{B}}T$ the diffusion term in (7.5) is small comparing to the drift one and, thus, may be neglected. Physically, it means that at such high voltages which are of most interest to us the drift of oxygen vacancies in the external field is a dominating factor. Combining equations. (7.4) and (7.5), we get the following nonlinear partial differential equation for the oxygen vacancies concentration $c(x,t)$

$$\frac{\partial c(x,t)}{\partial t} + \frac{Dq*\rho(x,t)}{k_{\mathrm{B}}T}\frac{\partial c(x,t)}{\partial x}\frac{V(t)}{R(t)} + \frac{Dq*c(x,t)}{k_{\mathrm{B}}T}\frac{\partial \rho(x,t)}{\partial x}\frac{V(t)}{R(t)} = 0\,. \tag{7.6}$$

This equation should be solved together with the appropriate initial vacancies distribution $c_{\mathrm{in}}(x)$ and respected boundary conditions. For a fixed ratio of resistances R_0/ρ_0, we get a single dimensionless control parameter $\beta = Dq*t_0V_0/(k_{\mathrm{B}}Td^2)$, V_0 and t_0 are the amplitude and period of the input voltage bias, that determines the hysteretic behavior of the current-voltage characteristics.

In Figs 7.1 and 7.2 below we demonstrate our simulations of the current-voltage curves for two different cases, namely, that for the low mobile-charge concentration when $q* > 0$ and that for the high charge concentration when the hole wind becomes an effective factor for vacancies movement and, as a result $q* < 0$. From the figures we can conclude that the hole-wind presence really changes the bias polarities for LR-to-HR and HR-to-LR switchings in the studied contacts.

Fig. 7.1. Calculated current-voltage characteristic of the metal-YBCO contact for the positive parameter $\beta = 0.5$ (no influence of the hole wind or it is negligibly small). The left and right insets demonstrate spatial modification of the oxygen-vacancy concentration and temporal changes of the voltage bias applied as well as the YBCO-film conductance in the time domain, respectively. The arrows show direction of $I(t)$ changes
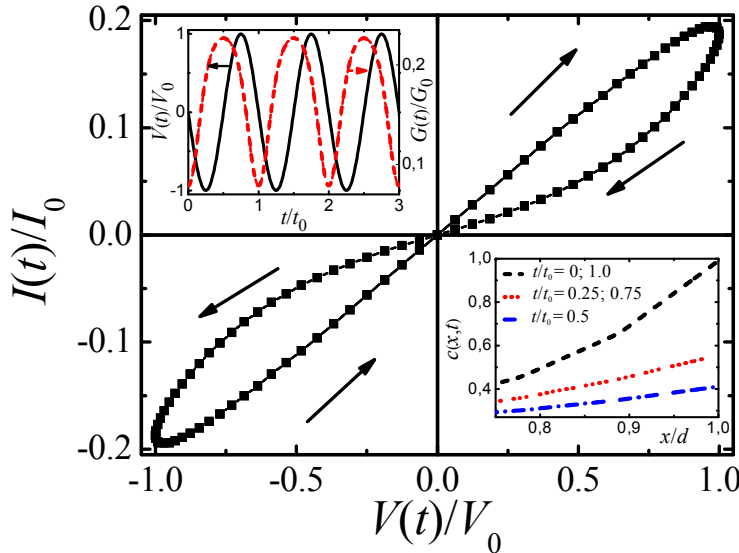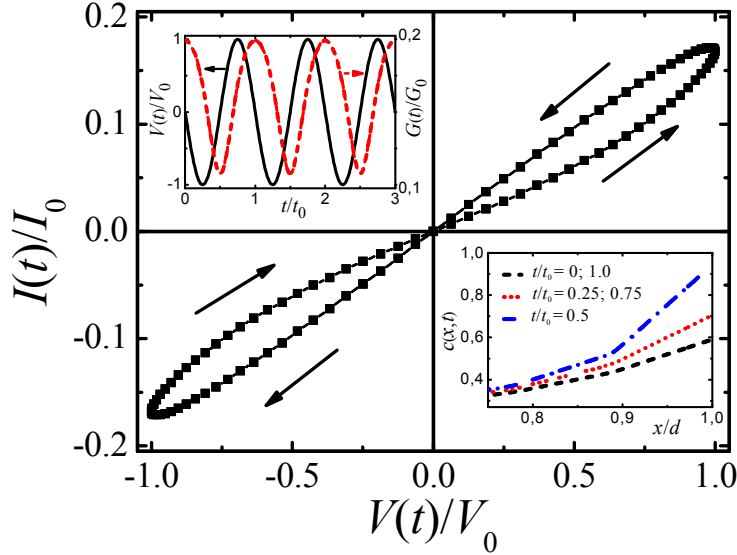
142

Fig. 7.2. Calculated current-voltage characteristic of the metal-YBCO contact for the negative parameter $\beta = -0.1$ (an effect of the hole wind). The left and right insets demonstrate the spatial modification of the oxygen-vacancy concentration and temporal changes of the voltage bias applied and the YBCO-film conductance in the time domain, respectively. The arrows show direction of $I(t)$ changes

Frequency dependence of the memristive-like transport characteristics of metal counter-electrode–YBCO thin film contacts. Let us now discuss the frequency f dependence of the double-valued current-voltage characteristics of memristive structures formed by a metal counter-electrode and a complex transition-metal oxide film. Our theoretical model is based on the assumption of the diffusion of oxygen vacancies, the local concentration of which completely determines electrical characteristics of the metal-oxide compound. It is important to know how the response of the system depends on the vacancy-subsystem relaxation in the time domain that will be characterized below with a characteristic relaxation time τ. Therefore, we have an additional term in the right side of Eq. (7.6) that now reads as

$$\frac{\partial c(x',t')}{\partial t'} + \beta \frac{\partial}{\partial x'}\left(c(x',t')\rho'(x',t')\right)I(t') = -\frac{c(x,t)-c_{in}(x)}{\tau'}, \qquad (7.7)$$

where $\tau' = \tau f$ and $c_{in}(x)$ describes the initial state of the vacancy subsystem.

The frequency f impacts not only the alternating current $I(t)$ period but also the parameter β which is inversely proportional to the frequency of the alternating current through the contact of the metal injector with the cuprate. Fig. 7.3 demonstrates the effect of the current source frequency f on current-voltage curves of the contact formed by a normal-metal emitter with an yttrium-barium oxide film. Numerical calculations have been performed using the formula (7.7) with a parameter $\beta(f) = \beta(f_0)/(f/f_0)$, where the value of $\beta(f_0)$ was set equal to 0.05. In Fig. 7.3 we neglected the effects of the vacancy subsystem relaxation to the initial state (their impact on the hysteresis curves is discussed below). As one would expect, with increasing frequency f, the ratio of the maximum contact resistance R_{off} to its minimum value R_{on} drops, see the inset in Fig. 7.3. It means that the operating frequency range of the memristor under discussion is substantially limited. For the range expansion, it is necessary to increase the parameter β, i.e., to enhance the diffusion coefficient of oxygen vacancies D and to decrease the thickness d of the complex-oxide film.

143

Let us now discuss the role of relaxation effects in the structure under discussion, i.e. an effect of finite τ values. Corresponding results shown in Fig. 7.4 demonstrate a weak influence of relaxation processes on the memristor characteristics even in the case when τ changes by several orders of magnitude. The relaxation becomes essential only when the time τ is comparable with the period of the alternating current through the contact. However, even in this case, after several current periods, a state stable in time with a clearly defined resistance period is achieved. This conclusion is of practical importance for the design of new elements of binary non-volatile memory.
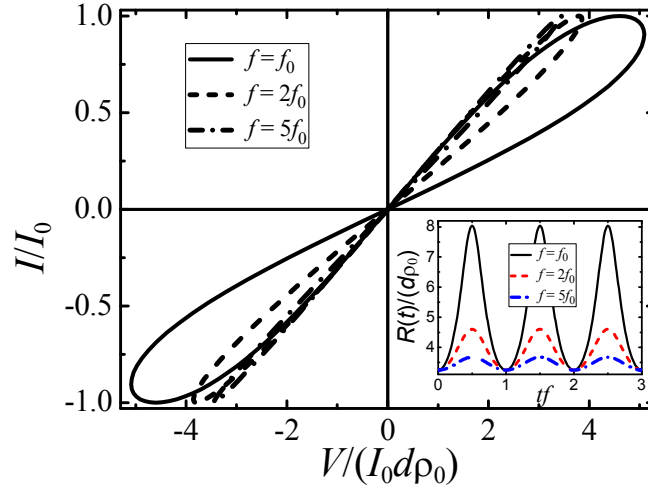
Fig. 7.3. Effect of a current source frequency f on current-voltage characteristics of a contact formed by a metal with a YBCO film, parameters $\beta(f_0) = 0.05$, $\tilde{d} = 0.75d$, $\tau \to \infty$, resistance R_0 is assumed to be negligibly small, $c_{in}(x) = 0.2 + 0.5x^5$ which corresponds to the experimental data [124]. The inset demonstrates temporal dependence of the contact resistance for three frequencies
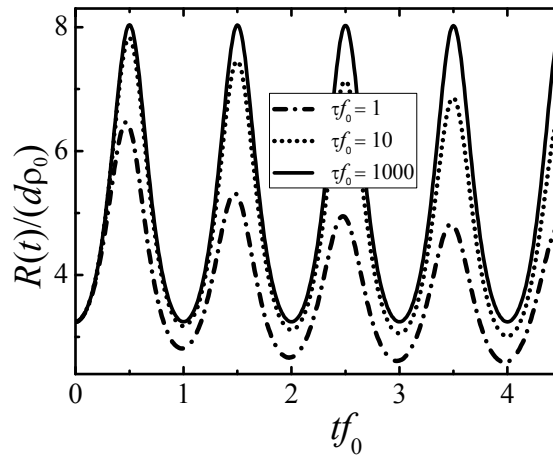
Fig. 7.4. Effect of a finite relaxation time τ on the temporal dependence of the resistance of a contact between a metal and YBCO film for a fixed ac frequency $f = f_0$

Therefore, with increasing frequency of the alternating current passed through a given contact, the ratio of its maximum resistance to the minimum value decreases, while the influence

of the vacancy-subsystem relaxation to the initial state is not significant in the case when the characteristic relaxation time substantially exceeds the period of the alternating current.

__Comparison of experimental data and numerical simulations of transport characteristics of metal counter-electrode–YBCO thin film contacts__ [124]. In the joint paper [124] we have compared measured at room temperatures current-voltage characteristics of YBCO/TiN and YBCO/PtIr junctions with our numerical calculations. Commercially available *c*-axis oriented epitaxial 400 nm-thick YBCO films on LaAlO₃ substrates with a normal-to-superconductor transition at 89 K have been studied. AFM topography was investigated with the Scanning Probe Microscope Solver P47-PRO from the NT-MDT Company. Local conductivity measurements were performed in the scanning spreading resistance microscopy (SSRM) mode. Current-voltage (*I–V*) characteristics were recorded using the SSRM setup with conductive 35-nm diameter TiN-coated AFM tips. In this mode, the tip-sample distance was well controlled and the tip was always in direct contact with the sample without penetrating its surface. The SSRM results have been compared with our scanning tunneling microscopy (STM) data that were acquired with a PtIr tip whose diameter was supposed to be less than that of TiN-coated AFM tips since the PtIr tip was obtained by mechanical cut of the wire. In the STM measurements, the controlling factor was the current across the tip-sample junction but not the distance between them. The voltage bias was swept from –10 V to +10 V up and down via a piecewise linear modulation protocol. The measurement took about 2 seconds. In the previous studies of bipolar resistive switchings in large (µm-scale) planar Ag-YBCO junctions [107, 112] a transition from a HR to a LR state was observed when a *negative* (with respect to the counter-electrode) potential was applied to oxide films. Now, surprisingly, an inverse situation in all SSRM measurements was revealed, namely, after applying high negative voltages the sample remained in the HR state until it was transformed into the LR one by high *positive* voltage biases applied to the YBCO film. On the other hand, the YBCO-STM tip junctions exhibited ambiguous behavior. In this case, switching polarity varied from point to point and depended on the STM-tip position during the measurement of a particular current-voltage characteristic.

Thus, in all SSRM measurements and a number of the STM experiments, the YBCO thin film became more conductive and switched to the LR state when it was biased positively. After application of negative biases, the YBCO near-surface region transferred back to the HR state with characteristics close to those in the initial state. These results are in apparent contradiction with the previous studies of bipolar resistive switchings in planar junctions with YBCO films [107, 112, 125] as well as with [126] but can be well understood within the hole-wind hypothesis.

Resuming the experimental part of the joint work, the main result of our Ref. [124] was confirmation of a strong inhomogeneity in the spatial charge distribution even in the most optimized YBCO thin layers at the nano- and sub-micrometer scale. The STM measurements clearly showed a broad distribution of the local conductance along the film surface and probably within its nearest neighborhood. The SSRM data obtained with a tip of the larger diameter is already the result of the averaging over an area where the local conductance variations are important. In this case, the dominant contribution to the current would arise from regions of the highest conductance and that is why all *I-V* curves measured in the SSRM mode have demonstrated opposite, to the previous experiments on planar metal counter-electrode–YBCO bilayers, voltage-bias polarity of the switching effect. The question arises why the data for bilayers where the averaging was, at least, at the micrometer scale have not followed this tendency. In our opinion, it is the result of small current densities across the bilayer interface due to its comparatively higher resistance when the hole-wind effect is strongly suppressed.

7.3. Spectroscopy setup based on a resistive-switching effect in a binary oxide interlayer

Starting from pioneering works in 60s, fine structures in *electron-tunneling spectra* have been widely applied to identify fingerprints of the electron-boson interaction responsible for Cooper pairing in *superconducting (S) materials* [127]. Using the Eliashberg theory [128], very precise tunneling experiments on low-temperature superconductors have decisively confirmed the responsibility of the electron-phonon coupling for the conventional *s*-wave electron pairing. Moreover, the tunneling-spectroscopy technique applied to a lot of traditional superconductors has allowed to extract the *Eliashberg function* $\alpha^2 F(\omega)$, *the phonon excitation* spectrum $F(\omega)$ weighted by the electron-boson coupling parameter $\alpha^2(\omega)$ [127]. In high-temperature cuprates, electrons forming Cooper pairs are at the same time strongly coupled to a bosonic mode but, up to now, it is not clear if the two phenomena have any relation to each other or not, see the concerned discussion and references in the recent paper [129]. This example demonstrates the importance of reliable information about the electron-boson interaction obtained directly from spectroscopic measurements in the superconducting state and the interest in such techniques has recently revived. Below we settle this issue by analyzing a novel device based on the resistive-switching phenomenon in a nanometer-thick transition-metal-oxide interlayer which separates two films, one of which is a superconductor under investigation and the second one is a normal (N) counter-electrode.

As was mentioned above, the first well-developed methodology to study the relationship between superconductivity and electron-boson coupling was the analysis of subtle features in the differential conductance spectrum for a sandwich formed by a superconductor studied, a metallic N or S counter-electrode (CE) and an insulating (I) barrier usually formed by a nanoscale oxide interlayer which was created artificially or naturally at the surface of one of the electrodes. The nonlinear features reveal themselves in the differential conductance-versus-voltage curves due to the frequency-dependent structure of an electronic *self-energy* in the S state [128]. Since 70s another approach known as a point-contact spectroscopy has been developed [130]. In this case, a micro-constriction (c) is created by pressing a metallic tip onto an S sample. The study of such CE/c/S junctions turned out to be an important and straightforward spectroscopic means in phonon-mediated superconductors [131]. Its superconducting modification based on the Andreev backscattering phenomenon, an electron-into-hole (and inverse) transformation at a clean N/S interface [127], is known as a point-contact Andreev-reflection spectroscopy technique. The technique has been very useful for the study of energy gaps in novel superconductors, see reviews [132] and [133]. Besides gap features, Andreev retroreflection generates also an excess current, a shift of the current-voltage (*I-V*) characteristics of superconducting point contacts with respect to those in the N state. Due to the energy-dependent electron-boson interaction it exhibits observable phonon-induced nonlinearities several times larger than related N-state features, see [134].

At the beginning of 80s, a theory proposed by Blonder, Tinkham and Klapwijk (BTK) furnished a powerful tool to describe N/I/S contacts with transparency ranging from metallic to tunneling regime [135]. In this approach, the interface barrier strength is modeled with a Dirac delta potential of arbitrary amplitude. The theory, formulated in terms of Bogoliubov-de Gennes equations, provides transmission and reflection coefficients for charge carriers and has succeeded in explaining single-charge tunneling processes as well as the conversion of a quasi-particle current into a supercurrent due to the Andreev-reflection mechanism [135]. Despite a seemingly oversimplified description of the point-contact system (a step-gap function and one-dimensional transport), the BTK model often provides excellent fits to conductance spectra for innovative S materials.

Within the BTK theory, gap-induced features in the differential conductance spectrum $G(V) = dI(V)/dV$ differ considerably in the two limiting modes discussed above. In an ideal N/S bilayer and at extremely low temperatures T, $G(V)$ is twice larger than the normal-state value G_N within the gap region and above it rapidly approaches G_N (the point-contact Andreev-reflection methodology). In this approach, natural oxides or degraded surfaces of the contacting electrodes can form a low tunnel barrier controlled by a smooth adjustment of the pressure between the electrodes. For a sandwich-type tunnel N/I/S device and $T = 0$, the $G(V)$ function is zero below the gap Δ, exhibits a peak just at the gap value $V_\Delta = \Delta/e$, and is approaching G_N above it.

After the great success of the tunneling technique in the determination of superconducting parameters in *s-p* metals [127], it was faced with great difficulties in the case of transition metals and their compounds. The problems were caused mainly by two factors arising due to the fact that the tunneling experiment probes material in depth within a superconducting coherent length ξ and thus its outcome is seriously affected by junction quality. The first one is a significant oxidation of the initially clean surface which contaminates a near-barrier region of the metal layer and the second one derives from comparatively short ξ values in transition-metal compounds. Similar obstacles, clean interface requirement and need for a nanometer-scale N/S orifice, have arisen through the interpretation of the point-contact energy-gap data, see the comprehensive analysis [136]. It became clear that very often the $G(V)$ spectrum of a CE/c/S device experiences a strong influence from a finite lifetime broadening of the quasiparticle energies described by a phenomenological Dynes parameter Γ [137] which is very important for superconductors with near-surface inhomogeneities [138]. Other factors destroying an outcome are the proximity effect between a normal tip and a superconducting sample, the presence of a series resistance and so on [138]. As a result, conductance spectra often contain features which cannot be modeled within an ideal BTK approach. Further parameters have been included into the theory [133], but in this way the number of free fitting parameters, as well as the interdependence between them, increases, thus preventing the determination of unique values due to the degeneracy of fits to the conductance spectra. The tunneling CE/I/S junction looks more robust but requires a rather complicated fabrication process relating the need to create a high-quality potential barrier between the superconductor and a counter-electrode.

To overcome the problems formulated above, we need an alternative experimental *self-formed* methodology which could be regarded as an experimental realization of the BTK model. It means that the technique should be able to modify the N/S interface transparency over a wide range and thus to measure the same S sample in the two limits, for a perfect (without any barrier) contact and in a tunneling regime. Since related characteristics are expected to be qualitatively different, comparison of theoretically predicted curves with measured experimentally would provide convincing evidence of the participation (or not) of a feasible boson mode in the Cooper-pairing process. The physical phenomenon behind the proposed approach is the so-called Resistive Switching (RS) that has been ubiquitously found in simple and complex oxide-based sandwiched structures [94, 114]. Its underlying mechanism in most cases can be basically understood following the so-called conductive filament model, in which the RS process is dominated by the formation/rupture of local conducting paths connecting terminal electrodes [94]. The model is based on the assumption that sufficiently high electrical field can induce a soft dielectric breakdown in the nanoscale oxide interlayer which sets the device to a conductive (low-resistive or ON) state. There can be two different filament-formation sources, cations from the counter-electrode material drifting from anode toward cathode and oxygen vacancies whose

migration changes the film stoichiometry and leads to strong modification of the electronic conductivity at their locations. The rupture of filaments initiated by applying a reversed bias voltage dissolves them electrochemically and turns the device to a high-resistive or OFF state. Temperature behavior of the contact resistance R can serve as a simplest indirect indicator of the filament structure. Usually, in the ON state, the R–vs-T curve demonstrates a typical metallic behavior while in the OFF state it is semiconductive.

Up to now, there were only a few attempts to combine the two fundamental phenomena, the resistive-switching effect and superconductivity. In the paper [94], Nb/ZnO/Pt devices showing stable and reproducible bipolar RS behavior were fabricated. A sudden drop in resistance below the critical temperature T_c of niobium was associated with the onset of the superconductivity in Nb. It was concluded that precisely Nb ions diffuse into the oxide film inducing the RS effect. Similar superconducting behavior was detected [139] in an In/δ-Bi$_2$O$_3$/Au cell. In contrast to Nb/ZnO/Pt devices, the observed $T_c \sim 5.8$ K was inconsistent with the value of 4.3 K for the indium electrode but agreed well with the metallic Bi nanowire. It was concluded therefore that the RS effect in In/δ-Bi$_2$O$_3$/Au trilayers originates from the formation and rupture of a conducting filament composed of metallic Bi [139]. In the paper [140] where the authors succeeded to realize a point contact between a superconductor and a normal counter-electrode in Nb/NiO/Pt heterostructure using a metallic filament in a transition-metal oxide generated by the RS effect.

In this work, we have used a similar technique that was originally proposed in the paper [141] applying it not only for studying the gap region as in the papers [140,141] but rather for the analysis of phonon-induced features in the differential conductance-versus-voltage spectra of a superconducting material, see also our joint publication [142]. We show that the pre-formation procedure typical for the RS devices causes tough disorder in the S electrode strongly suppressing and blurring gap-induced features in the conductance spectra while the phonon-induced nonlinearities, although small in size, remain almost untouched. Even more, we have been able to reveal the phonon-induced structure simultaneously in two limits for small and medium N/S interface transparences. To demonstrate the advantages of our approach, we have applied it to niobium, a conventional transition-metal superconductor, and magnesium diboride. The latter metal is characterized by two conducting electron groups which belong to σ- and π-bands with a dissimilar topology, see below. Changing the weighting factors w for the two contributions to a charge transport, we were able to obtain satisfactory agreement of calculated curves with the experimental ones.

Modification of the conventional BTK approach. Phonon-mediated pairing interaction in a single-band superconductor is described by the isotropic Eliashberg function $\alpha^2 F(\omega)$ that determines the complex gap parameter $\Delta(E)$ as a function of the real energy E [127]. Our modification of the standard BTK formulas [135] consists in the following. First, we replaced a constant gap value Δ_0 with a function $\Delta(E)$ in order to take into account the phonon spectrum structure and, second, we introduced a constant imaginary part of the electron energy $E \rightarrow E + i\Gamma$ where Γ is determined by the sample fabrication conditions and is varied with temperature. Such a replacement can be justified by taking into account inelastic-scattering [143] or proximity-induced [15] processes leading to a finite electron lifetime with a fixed energy E in a superconductor $\tilde{\Delta}(E) = \Delta(E) / (1 + i\Gamma / E)$. The modification is important only in the gap region since, as we show below, the experimentally obtained Dynes parameter Γ is of the order of Δ_0

and at energies corresponding to phonon excitations $\omega_{ph} \gg \Delta_0$ its impact is vanishing (also since the imaginary part $\text{Im}\,\Delta(\omega_{ph})$ of the gap parameter caused by phonon-induced damping becomes very large [127]). The potential barrier in the BTK approach is represented by a repulsive potential $U_0\delta(x)$ located at the N/S interface that enters into the calculations through the dimensionless parameter $Z = U_0/(\hbar v_F)$ where v_F is the Fermi energy. Resuming, for a single-band superconductor like niobium we have three fitting parameters, Δ_0, Γ, and Z.

In the case of magnesium diboride, we have two intra- and two inter-band electron-phonon spectral functions $\alpha^2 F_{ij}(\omega)$ where $i, j = \sigma, \pi$ and the Coulomb pseudopotential matrix μ_{ij}^* forming the basic input for the two-band Eliashberg theory [144, 145]. According to most calculations for magnesium diboride the $\alpha^2 F_{ij}(\omega)$ functions are dominated by the optical boron bond-stretching E_{2g} phonon branch of around 60 – 70 meV [145]. We have used calculated in the paper [145] Eliashberg functions to obtain complex gap parameters $\Delta_{\sigma,\pi}(E)$ in MgB2 as functions of the real energy E. Next, we introduced $\Delta_{\sigma,\pi}(E)$ into the BTK expressions and obtained the phonon-induced structure in the normalized conductance for the ballistic regime at any Z value which defines the barrier transmission and reflection normal-state probabilities $D_N = 1/(1+Z^2)$ and $R_N = Z^2/(1+Z^2)$. Our figure of merit is a relative deviation of the differential conductance $G(V)$ from its normal magnitude $g(V) = [G(V) - G_N]/G_N$. We expect that the oxygen-vacancies filament generated in the ON state of the Al2O3/TiO2 oxide interlayer realizes a direct contact with the MgB2 surface of a very small diameter d and thus the current is flowing in a clean regime. The differential conductance $G(V)$ spectrum can be found in the same way as it was explained above for a single-band superconductor. Therefore, for a two-band magnesium diboride the number of the fitting parameters increases up to seven, two energy gaps Δ_σ and Δ_π, two barrier strengths Z_σ and Z_π, two smearing Dynes parameters Γ_σ and Γ_π, and a weighting factor $w_\sigma < 1$ ($w_\pi = 1 - w_\sigma$).

The general formula taking into account self-energy effects in the superconducting order parameter can be written in the form similar to that proposed in the papers [146, 132]:

$$g(V) = \frac{1 + D_N |\gamma(eV)|^2 - R_N |\gamma^2(eV)|^2 - |1 - R_N\gamma^2(eV)|^2}{|1 - R_N\gamma^2(eV)|^2},$$

(7.8)

where $\gamma(E) = \dfrac{\Delta(eV)}{eV + \sqrt{(eV)^2 - \Delta^2(eV)}}$. Below we shall discuss tunneling and point-contact limits. For a tunneling junction with $D_N \ll 1$ the relative deviation of the differential conductance $G_{tun}(V)$ from its normal magnitude G_N reads as

$$g_{tun}(V) = \frac{G_{tun}(V) - G_N}{G_N} = \text{Re}\left[\frac{eV}{\sqrt{(eV)^2 - \Delta^2(eV)}}\right] - 1 \approx \frac{\text{Re}\left[\Delta^2(eV)\right]}{2(eV)^2}.$$

(7.9)

For a ballistic point contact with $D_N = 1$ we get

$$g_{pc}(V) = \frac{G_{pc}(V) - G_N}{G_N} = \left|\frac{\Delta(eV)}{eV + \sqrt{(eV)^2 - \Delta^2(eV)}}\right|^2 \approx \frac{\text{Re}\left[\Delta^2(eV)\right]}{4(eV)^2} + \frac{\left[\text{Im}\,\Delta(eV)\right]^2}{2(eV)^2}.$$

(7.10)

Thus the difference between the two limiting cases equals to $\left[\operatorname{Im}\Delta(eV)/(2eV)\right]^2$.

In Fig. 7.5 we demonstrate the effect of the barrier strength on $g_{pc}(V)$ and $g_{tun}(V)$ curves for π- and σ-bands. Note that the energy gap in the π-band Δ_π is three times less than that in the σ-band Δ_σ, thus phonon-induced effects which are proportional to the gap squared, see Eqs. (7.9) and (7.10), differ by an order of magnitude. At voltages between 40 and 50 meV, the difference between point-contact and tunneling results is of the factor of 2 due to different denominators, compare Eqs. (7.9) and (7.10). At voltages about $\tilde{V}_{\sigma,\pi} \approx \Delta_{\sigma,\pi} + E_{2g}$ corresponding to E_{2g} phonons, the $g(V)$ curve changes its sign and subsequently decreases due to the strong enhancement of the imaginary part of the gap parameter. At last, let us estimate the values of the two contributions at $V \approx \tilde{V}_{\sigma,\pi}$ when real and imaginary parts of the complex order parameter nearly coincide: $g_{tun}(\tilde{V}) \approx 0$ while $g_{pc}(\tilde{V})$ is roughly about 0.003 for the π-band and about 0.03 for the σ-band.

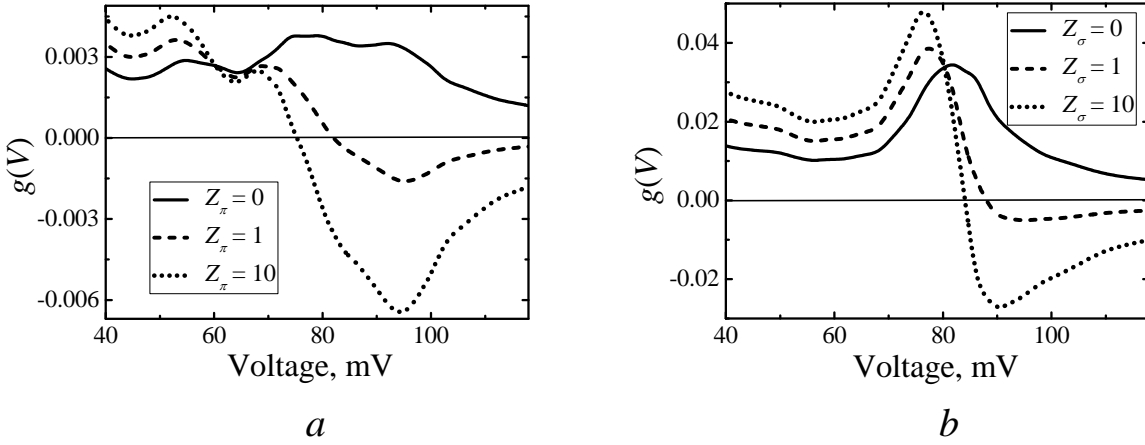*Fig. 7.5.* Theoretical estimates for phonon-induced effects in MgB$_2$-based samples. Figures *a* and *b* demonstrate π- and σ-band contributions to relative deviations of the differential conductance spectra dI/dV-vs-V from the normal-state value for three magnitudes of the barrier strength Z, temperature $T = 0$, $\Delta_\pi = 2.7$ meV, $\Gamma_\pi = 0.5$ meV, $\Delta_\sigma = 7.2$ meV, $\Gamma_\sigma = 1.5$ meV

Nb-based device in an ON state. The aim of this part of the work has been to develop and to verify the new technique for creating direct point contact between a normal counter-electrode and a superconducting transition-metal layer. Niobium was chosen as the metal of interest because its phonon spectrum and the Eliashberg function $\alpha^2 F(\omega)$ have been previously investigated experimentally by proximity electron tunneling and point-contact spectroscopy methods [147, 140]. The earlier tunneling-probe studies of superconducting Nb have revealed two basic problems strongly influencing the outcomes, see the related discussion in the paper [147]. First, the samples should be of a high quality since the tunneling technique probes only about a coherence length into the material (~ 40 nm). Second, there should be a good insulating barrier for tunneling through. Unfortunately, niobium does not produce a native oxide barrier of sufficient quality for good tunneling measurements. It was proposed [147] to apply proximity S/Al/Al$_2$O$_3$/CE structures where the thickness of the normal Al interlayer was of several

nanometers, i.e., much less than the coherence length. In this case, the cleanliness of the initially prepared S surface can be preserved by depositing the Al film in situ and the excellent properties of thermally grown Al-oxide barriers lead to spectra of a high quality needed for determination of the Eliashberg function after some complication of the standard reconstruction procedure [147]. Point contacts with single-crystalline Nb samples were obtained by [134] using the shear technique. The contacts were shown to be dirty with the elastic mean-free path much shorter than the inelastic length. In the superconducting state, they revealed a fine structure at energies close to characteristic phonon energies of Nb. A pronounced feature at ~ 16 meV corresponded to transversely polarized phonons whereas a much weaker nonlinearity at 22-24 meV originated from longitudinal phonons of Nb in good agreement with the tunneling data [146, 134]. The features disappeared in the normal state and hence were definitely related to the presence of the energy-dependent superconducting gap parameter.

Below we compare our theoretical expectations with experimental data obtained by Slovak colleagues [141]. The studied Nb/Al/Al$_2$O$_3$/TiO$_2$/Pt devices have not revealed convincing phonon-induced singularities in the OFF state and we present only experimental conductance spectra for a low-resistive state. The main panel of Fig. 7.6 demonstrates comparison of the measured $G(V)$ characteristics with calculated ones. In the latter case, we have used the $\alpha^2 F(\omega)$ function obtained in the work [147]. The left inset shows a small decrease of the gap value $\Delta_0(T)$ with temperature whereas the right one demonstrates a general agreement between our experimental phonon structure.
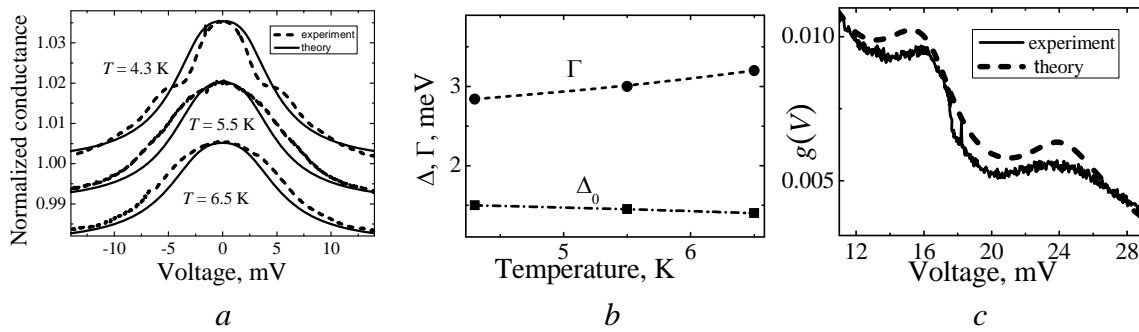

Fig. 7.6. Main panel: Differential conductance traces *dI/dV*-vs-*V* normalized to the normal-state value for a Nb/Al/Al$_2$O$_3$/TiO$_2$/Pt sample with a TiO$_2$ barrier in the low-resistance state. The curves were recorded at three indicated temperatures. Numerical calculations have been performed for the energy gap value $\Delta(4.2 \text{ K}) = 1.5$ meV, the barrier strength $Z = 0.24$ and the smearing Dynes parameter $\Gamma(4.2 \text{ K}) = 2.8$ meV. For clarity, the curves are shifted (except the upper one) in the conductance scale taking the high voltage value as a reference point. Left inset: Temperature effect on the gap value (circles) and the Dynes parameter (squares) extracted from the curves shown in the main panel. Right inset: Comparison of the experimental phonon-induced structure measured at 4.2 K with the calculated one as it is described above

MgB$_2$-based devices in ON and OFF states. Nonlinearities in the measured conductance spectra of MgB$_2$/Al/Al$_2$O$_3$/TiO$_2$/Pt devices were revealed in a low-voltage region reflecting the presence of two MgB$_2$ energy gaps below 20 mV (see the main panel in Fig. 7.7) and in a high-frequency region from 60 to 110 mV probably related to phonon features (see the right inset in

Fig. 7.7). The main panel in Fig. 7.7 demonstrates good agreement of representative conductance-vs-voltage curves measured at different temperatures with those predicted by the BTK theory for a single π-band in MgB₂ with a significant inelastic scattering impact, see above.
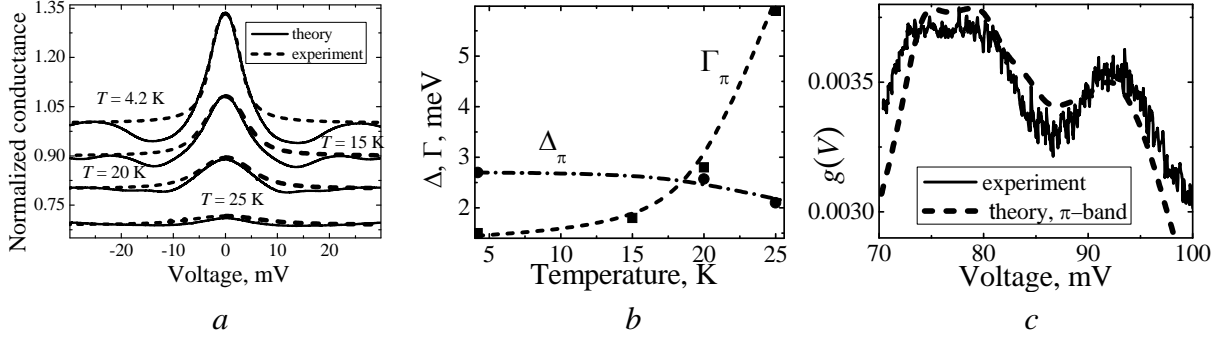

Fig. 7.7. (a): Differential conductance traces *dI/dV*-vs-*V* normalized to the normal-state value for a MgB₂/Al/Al₂O₃/TiO₂/Pt sample with a TiO₂ barrier in the low-resistance state. The curves were recorded at four indicated temperatures. Numerical calculations have been performed within a single π-band model ($w_\pi = 1$, $w_\sigma = 0$) for the energy gap value $\Delta_\pi(4.2\ \mathrm{K}) = 2.7$ meV, the barrier strength $Z = 0$ and the smearing Dynes parameter $\Gamma(4.2\ \mathrm{K}) = 1.45$ meV. For clarity, the curves are shifted (except the upper one) in the conductance scale taking the high voltage value as a reference point. (b): Temperature effect on the π-band gap (circles) and the Dynes parameter (squares) extracted from the curves shown in the main panel. The $\Delta_\pi(T)$ and $\Gamma_\pi(T)$ dependences are compared with the temperature behavior of the π-band gap predicted by [144] (the dashed-dotted curve) and the empirical result $a + bT^6$ found in [149], respectively. (c): Comparison of the experimental phonon-induced structure measured at 4.2 K with the calculated one

Our Γ_σ and Γ_π parameters found from the fitting procedure for a gap region were less than the respected gap values at lowest temperatures and rapidly increased approaching the critical temperature. Such temperature behavior agrees with that found [149]. Using angle-resolved photoemission data for the high-T_c superconductor Bi₂Sr₂CaCu₂O₈ the authors of this work revealed that a single-particle scattering rate Γ is *T*-independent in the normal state and very rapidly decreases below T_c perfectly fitting to the form $a + bT^6$, see the left inset in Fig. 7.7. According to [149] it means that electron-electron interactions are responsible for the non-zero Γ parameter. As was explained above, in our case the broadening Γ is mainly caused by the initial electroforming process creating pair-breaking scattering processes in the contact area.

Limiting us to the low-voltage region, we should note that well-pronounced (although smeared comparing with the ideal one) gap structure was observed only in the low-resistance regime, most probably, due to the lower quality of the interface and, as a result, a comparatively large parameter Γ in the tunneling-like case when the conductance curves do not exhibit clear signs of the gap peak. The same statement about the quality of the interface was drawn in the tunneling study of MgB₂/native oxide/Pb devices [150] where it was concluded that the fine structure is smeared out in junctions with large values of the product $R_N A$ (*A* is the cross-sectional area, $R_N = 1/G_N$) due to thicker barriers and strong interface scattering.
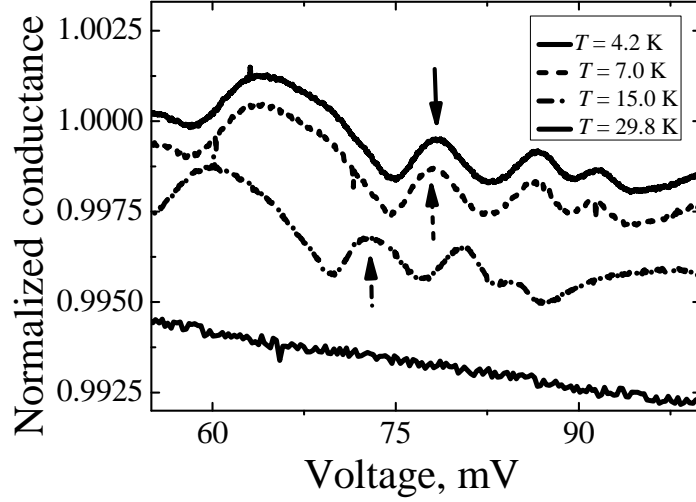
Fig. 7.8. Temperature effect on the fine structure in the conductance spectra of a MgB$_2$/Al/Al$_2$O$_3$/TiO$_2$/Pt sample with a TiO$_2$ barrier in the low-resistance state Note the shift of the peak related to the phonon-induced structure in the σ-band with increasing temperature as well as missing spectroscopic features on approaching T_c

In contrast, we have detected nonlinear phonon-induced structure at voltage biases corresponding to the crystal-lattice vibrations not only in the ON-state curves but also in high-resistance traces. Temperature dependencies of the conductance spectra were used to separate effects of the superconducting origin from those occurring also in the normal state. As an example, Fig. 7.8 exhibits a clear indication of its relationship to superconductivity, the temperature dependence of the high-voltage fine structure in the differential conductance curves for a MgB$_2$/Al/Al$_2$O$_3$/TiO$_2$/Pt sample with a TiO$_2$ barrier in the low-resistance state. We can see a shift of the feature at $e\tilde{V}(T) \approx \Delta_\sigma(T) + E_{2g}$ to the left due to the reduction of the gap $\Delta_\sigma(T)$ with increasing temperature, its suppression due to the decreasing ratio of the gap to the characteristic phonon energy and, finally, complete disappearance without any signs of a phonon-induced structure above T_c.
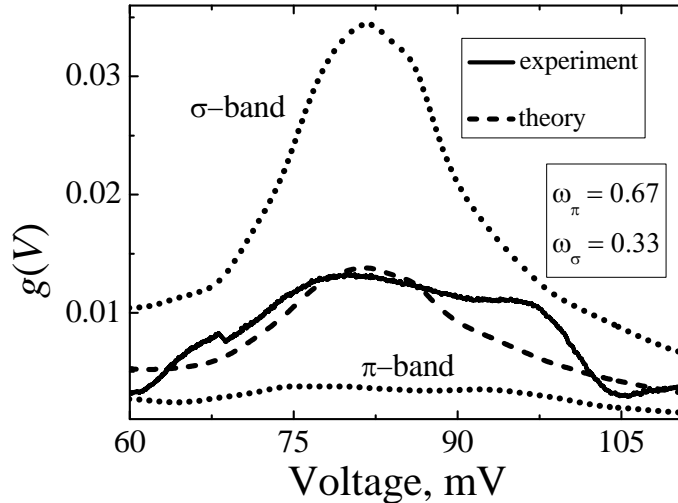

Fig. 7.9. Fine phonon-induced structure in the $g(V)$ characteristic of MgB$_2$/Al/Al$_2$O$_3$/TiO$_2$/Pt sample with a TiO$_2$ barrier in the low-resistance state. Dotted curves demonstrate theoretical estimates for π- and σ-band inputs in the point-contact regime when a barrier between the MgB$_2$ layer and a counter-electrode is expected to vanish, $Z = 0$, $T = 0$, $\Delta_\pi = 2.7$ meV, $\Gamma_\pi = 0.7$ meV, $\Delta_\sigma = 7.2$ meV, $\Gamma_\sigma = 1.5$ meV. The sum of the contributions with the ratio of weighting factors $w_\pi/w_\sigma \approx 2$ shown by a dashed curve is compared with the experimental result measured at 4.2 K

153

Typical example of the $G(V)$ curve measured at 4.2 K which revealed the presence of the only π-band is exhibited in the right inset in Fig. 7.7 where it is compared with the numerical result for a π-band contribution to the conductance spectrum of an ideal ON contact ($Z = 0$) shown in Fig. 7.1a. As was mentioned above, our junctions repeatedly demonstrated a π-band phonon-induced structure shown, in particular, in the inset in Fig. 7.5. At the same time, there were junctions with a σ-band contribution as well. Conductance spectra for two representative MgB$_2$/Al/Al$_2$O$_3$/TiO$_2$/Pt samples with a TiO$_2$ barrier in low- and high-resistance states are given in Figs. 7.9 and 7.10, respectively. They are compared with theoretical characteristics calculated for two extreme cases, the absence of any scattering at the interface with a MgB$_2$ sample and the tunneling barrier. The energy gap values were fixed to $\Delta_\pi = 2.7$ meV and $\Delta_\sigma = 7.2$ meV and three fitting parameters have been used, Γ_π, Γ_σ, a weighting factor w_π. The resulting $g(V)$ characteristic reads as $g(V) = w_\pi g_\pi(V) + w_\sigma g_\sigma(V)$ with $w_\pi = 1 - w_\sigma$.

The general shape and amplitudes of dI/dV-vs-V traces reasonably agree each with other. It should be emphasized that the experimental curves comprise much fine structure than the calculated ones. Apparently, it is due to the fact that the real phonon spectrum of magnesium diboride [151] contains more small details comparing to the electron-phonon function used in the calculations.
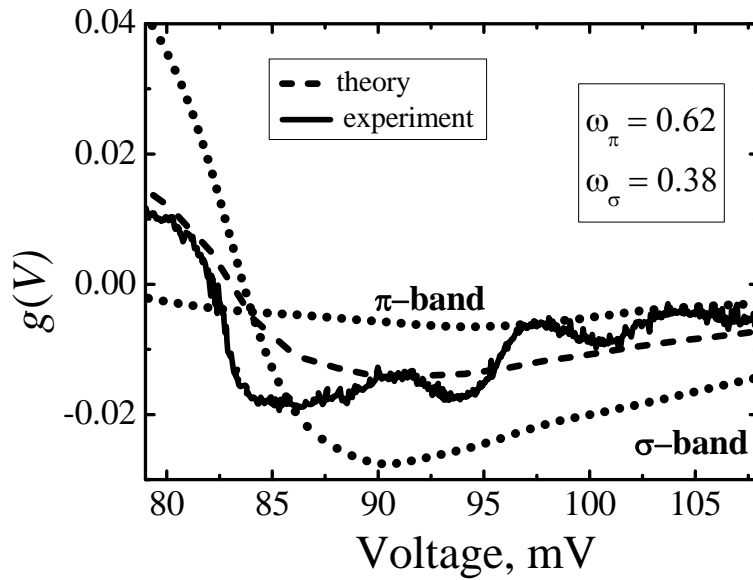

Fig. 7.10. Fine phonon-induced structure in the $g(V)$ characteristic of MgB$_2$/Al/Al$_2$O$_3$/TiO$_2$/Pt sample with a TiO$_2$ barrier in the high-resistance state. Dotted curves demonstrate theoretical estimates for π- and σ-band inputs in the tunneling-like regime with a barrier between the MgB$_2$ layer and a counter-electrode characterized by parameters $Z_\pi = Z_\sigma = 8$, $T = 0$, $\Delta_\pi = 2.7$ meV, $\Gamma_\pi = 0.3$ meV, $\Delta_\sigma = 7.2$ meV, $\Gamma_\sigma = 1.1$ meV. The sum of the contributions with the ratio of weighting factors $w_\pi/w_\sigma \approx 1.6$ shown by a dashed curve is compared with the experimental spectrum measured at 4.2 K

Finalizing this chapter, we would like to stress again that ionic transport-related phenomena are of primary importance in energy transformation and storage devices, such as solid oxide fuel cells or batteries. Traditionally, the main issue that hindered a wide spread of solid-state electrochemical devices is the slow ionic conduction and the reduced number of families of materials with pure ionic conductivity able to play the role of the electrolyte. The

ionic conductivity has been typically controlled by doping the oxides with aliovalent cations, which naturally creates charged defects to maintain the electroneutrality, Nonetheless, limitations came across in terms of materials instability, reactivity and defect interactions when trying to implement and operate these ionic conductors in real devices. By using interface-dominated materials, like thin films or nanoscale filaments, both the concentration of charge carriers and their mobility can be modified. Engineering nanostructures can allow tuning the changes and to maximize their impact on the ionic conduction. An example of such engineering efforts can be a novel self-formed nanofilament technique based on the resistive-switching effect in binary transition-metal oxide films that can be applied for the study of electron-boson interaction spectra in strong-coupled superconductors. We have proved above that the superconductor/nanoscale transition-metal oxide/counter-electrode junction with a controllable interface transparency allows, in principle, to measure conductance characteristics in two modes, a point-contact regime with a vanishing interface barrier and a tunneling one.

References

1. Mott N. F., Peierls R. Discussion of the paper by de Boer and Verwey. *Proc. Phys. Soc*. 1937. V. 49. P. 72–73.

2. Imada M., Fujimori A., Tokura Y. Metal-insulator transitions. *Rev. Mod. Phys*. 1998. V. 70. P. 1039–1263.

3. Bednorz J. G., Müller K. A. Possible high T_c superconductivity in the Ba-La-Cu-O system. *Z. Phys. B*. 1986. V. 64. P. 189–193.

4. Ohtomo A., Muller D. A., Grazul J. L., Hwang H. Y. Artificial charge-modulation in atomic-scale perovskite titanate superlattices. *Nature*. 2002. V. 419. P. 378–380.

5. Zubko P., Gariglio S., Gabay M., Ghosez P., Triscone J.M. Interface physics in complex oxide heterostructures. *Annu. Rev. Condens. Matter. Phys*. 2011. V. 2. P. 141–165.

6. Hwang H. Y., Iwasa Y., Kawasaki M., Keimer B., Nagaosa N., Tokura Y. Emergent phenomena at oxide interfaces. *Nature Mater*. 2012. V. 11. P. 103–113.

7. Chakhalian J., Freeland J. W., Millis A. J., Panagopoulos C., Rondinelli J. M. Emergent properties in plane view: Strong correlations at oxide interfaces. *Rev. Mod. Phys*. 2014. V. 86. P. 1189–1202.

8. Žutić I, Matos-Abiague A, Scharf B, Dery H, Belashchenko K. Proximitized materials. *Mater Today*. 2019. V. 22. P. 85–107.

9. Chen Z-G, Han G, Yang L, Cheng L, Zou J. Nanostructured thermoelectric materials: Current research and future challenge. *Prog. Nat. Sci.-Mater*. 2012. V. 22. P. 535–549.

10. Abrikosov A.A., Gor'kov L.P., Dzyaloshinskii I.Ye. Quantum field theoretical methods in statistical physics. Pergamon Press: Oxford. 1965. 365 pp.

11. Chandrasekhar V. Introduction to the quasiclassical theory of superconductivity for diffusive proximity-coupled systems. In: The physics of superconductors. V.2. Springer-Verlag. 2004.

12. Devizorova Zh., Mironov S. Spin-valve effect in superconductor/ferromagnet/ ferromagnet and ferromagnet/superconductor/ferromagnet structures of atomic thickness. *Phys. Rev. B*. 2017. V. 95. ID 144514.

13. Ouassou J. A., Pal A., Blamire M., Eschrig M., Linder J. Triplet Cooper pairs induced in diffusive *s*-wave superconductors interfaced with strongly spin-polarized magnetic insulators or half-metallic ferromagnets. *Scientific Reports*. 2017. V. 16. P. 1932.

14. Gennes P. G. Boundary effects in superconductors. *Rev. Mod. Phys*. 1964. V. 36. P. 225–237.

15. McMillan W. L. Tunneling model of the superconducting proximity effect. *Phys.Rev*. 1968. V. 175. P. 537–542.

16. Gor'kov L. P. On the energy spectrum of superconductors. *Sov. Phys. JETP*. 1958. V.34. P. 505–508.

17. Eliashberg G. M. Temperature Green's functions for electrons in a superconductor. *Sov. Phys. JETP*. 1961. V. 12. P. 1000–1002.

18. Eilenberger G. Transformation of Gorkov's equations for type II superconductors into transport-like. *Z. Phys*. 1968. V. 214. P. 195–213.

19. Mahan G. D. Many particle physics. Plenum: New York. 1990. 793 pp.

20. Bardeen J. Schrieffer J. Recent development in superconductivity. In: Progress in low temperature physics. Chapter VI. North-Holland Publishing Company: Amsterdam. 1961. 170 pp.

21.   Luttinger J. M., Ward J. C. Ground-state energy of a many-fermion system II. *Phys. Rev.* 1960. V. 118. P. 1417–1427.

22.   Meservey R. Schwartz B. B. Equilibrium properties: comparison of experimental results with predictions of the BCS Theory. In book: Superconductivity. V. 1, edited by Parks R.D. Marcell Dekker: New York. 1969. 664 pp.

23.   Guéron S., Pothier H., Birge N. O., Esteve D., Devoret M. H. Superconductivity proximity effect probed on a mesoscopic length scale. *Phys. Rev. Lett.* 1996. V. 77. P. 3025–3028.

24.   Hubbard J. Electron correlations in narrow energy bands. *Proc. Roy. Soc. Lond. A.* 1963. V. 276. P. 238–257.

25.   Hubbard J. Electron correlations in narrow energy bands III. An improved solution. *Proc. Roy. Soc. Lond. A.* 1964. V. 281. P. 401–419.

26.   Izyumov Yu.A. Strongly correlated electrons: the *t-J* model. *Physics-Uspekhi.* 1997. V. 167, P. 445–476.

27.   Rozenberg M. J., Kotliar G., Zhang X. Y. Mott-Hubbard transition in infinite dimensions. II. *Phys. Rev. B.* 1994. V. 49. ID 10181.

28.   Mott N.F. Metal-insulator transitions. London: Taylor & Francis. 1990.

29.   Brinkman W. F., Rice T. M. Electron-hole liquids in semiconductors. *Phys. Rev. B.* 1973. V. 7. ID 1508.

30.   Zaitsev R. O. The Mott transition in the many-dimensional Hubbard model. *Sov. Phys. JETP.* 1978. V. 48. P. 1193–1199.

31.   Izyumov Yu. A., Skryabin Yu. N. Statistical mechanics of the magnetically ordered systems. Moscow: Nauka. 1987.

32.   Zubov E. E. High-temperature superconductivity and normal state in the Holstein-t-J model. *Physica C.* 2014. V. 497. P. 67-76.

33.   Morita T., Horiguchi T. Calculation of the lattice green's function for the bcc, fcc, and rectangular lattices. *J. Math. Phys.* 1971. V. 12. P. 986–992.

34.   Joyce G.S. On the simple cubic lattice Green function. *Phil. Trans. R. Soc. Lond. A.* 1973. V. 273. P. 583–610.

35.   Morita T., Horiguchi T. Convergence of the arithmetic-geometric mean procedure for the complex variables and the calcultion of the complete elliptic integrals with complex modulus. *Numer. Math.* 1973. V. 20. P. 425–430.

36.   Kalashnikov O. K., Fradkin E. S. Application of the spectral density method to systems with a pair interaction. *Teoreticheskaya i Matematicheskaya Fizika.* 1970. V. 5. P. 417–438.

37.   Edwards D. M. Green A. C. M. Kubo K. Electronic structure and resistivity of the double exchange model. *J. Phys.: Condens. Matter.* 1999. V. 11. P. 2791–2808.

38.   Schrieffer J. R., Brooks J. S. Eds. Handbook of high-temperature superconductivity. Theory and experiment. Springer: New York. 2007. 627 pp.

39.   Zhang W. Photoemission spectroscopy on high temperature superconductor. Springer-Verlag: Berlin, Heidelberg. 2013. 139 pp.

40.   Bhattacharya R. N., Paranthaman M. P. Eds. High temperature superconductors. Wiley-VCH. 2010. 227 pp.

41.   Pickett W. E. Electronic structure of the high-temperature oxide superconductors. *Rev. Mod. Phys.* 1989. V. 61. ID 433.

42.   Anisimov V., Izyumov Yu. Electronic structure of strongly correlated materials. Springer: Heidelberg. 2010. 288 pp.

43.   Verga S., Knigavko A., Marsiglio F. Inversion of angle-resolved photoemission measurements in high-T_c cuprates. *Phys. Rev. B*. 2003. V. 67. ID 054503.

44.   Sandvik A. W., Scalapino D. J., Bickers N. E. Effect of an electron-phonon interaction on the one-electron spectral weight of a d-wave superconductor. *Phys. Rev. B*. 2004. V. 69. ID 094523.

45.   Zhao L., Wang J., Shi J., Zhang W., Liu H., Meng J., Liu G., Dong X., Zhang J., Lu W., Wang G., Zhu Y., Wang X., Peng Q., Wang Z., Zhang S., Yang F., Chen C., Xu Z., Zhou X. J. Quantitative determination of Eliashberg function and evidence of strong electron coupling with multiple phonon modes in heavily overdoped $(Bi,Pb)_2Sr_2CuO_{6+\delta}$. *Phys. Rev. B*. 2011. V. 83. ID 184515.

46.   Valla T., Fedorov A. V., Johnson P. D., Wells B. O., Hulbert S. L., Li Q., Gu G. D., Koshizuka N. Evidence for quantum critical behavior in the optimally doped cuprate Bi(2)Sr(2)CaCu(2)O(8+delta). *Science*. 1999. V. 285. P. 2110–2113.

47.   Bogdanov P. V., Lanzara A., Kellar S. A., Zhou X. J., Lu E. D., Zheng W. J., Gu G., Shimoyama J.-I., Kishio K., Ikeda H., Yoshizaki R., Hussain Z., Shen Z.X. Evidence for an energy scale for quasiparticle dispersion in $Bi_2Sr_2CaCu_2O_8$. *Phys. Rev. Lett.* 2000. V. 85. ID 2581.

48.   Xie B. P., Yang K., Shen D. W., Zhao J. F., Ou H.W., Wei J., Gu S. Y., Arita M., Qiao S., Namatame H., Taniguchi M., Kaneko N., Eisaki H., Tsuei K. D., Cheng C.M., Vobornik I., Fujii J., Rossi G., Yang Z. Q., Feng D. L. High-energy scale revival and giant kink in the dispersion of a cuprate superconductor. *Phys. Rev. Lett.* 2007. V. 98. ID 147001.

49.   Brinkman W. F., Rice T. M. Single-particle excitations in magnetic insulators. *Phys. Rev. B*. 1970. V. 2. ID 1324.

50.   Zubov E. E., Dyakonov V. P., Szymczak H. Diagrammatic method for the theory of magnetic and resistive properties of manganites. *J. Phys.: Condens.Matter*. 2006. V. 18. ID 6699.

51.   Kulič M. L. Interplay of electron-phonon interaction and strong correlations: the possible way to high-temperature superconductivity. *Phys. Reports*. 2000. V. 338. P. 1–264.

52.   Lang I. G., Firsov Yu. A. Kinetic theory of semiconductors with low mobility. *Zh. Exp. Teor. Fiz.* 1962. V. 43. P. 1843–1860 (*Sov.Phys.JETP*. 1962. V. 16. P. 1301–1312).

53.   Migdal A. B. Interaction between electrons and lattice vibrations in a normal metal. *Zh. Exp. Teor. Fiz.* 1958, V. 7. P. 996–1001.

54.   Abramowitz M., Stegun C. A. (Eds.). Handbook of mathematical functions with formulas, graphs, and mathematical tables. Dover: New York, 1972. 1046 pp.

55.   Gil A., Koepf W. Segura J. Computing the real zeros of hypergeometric functions. *Numerical Algorithms*. 2004. V. 36. P. 113–134.

56.   Morita T., Horiguchi T. Calculation of the lattice Green's function for the bcc, fcc, and rectangular lattices. *J. Math. Phys.* 1971. V. 12, ID 986.

57.   Zubov E. E. The ground state of a weakly doped narrow-band Hubbard magnet. *Theoretical and Mathematical Physics*. 1995. V. 105. P. 1442–1452.

58.   Ideta S., Yoshida T., Hashimoto M., Fujimori A., Anzai H., Ino A., Arita M., Namatame H., Taniguchi M., Takashima K., Kojima K. M., Uchida S. Effect of electron-phonon coupling in the APRES spectra of the tri-layer cuprate $Bi_2Sr_2Ca_2Cu_3O_{10+\delta}$. *J. Phys.: Conf. Ser.* 2013. V. 428. P. 012039-1-5.

59.   Uchida S. Forefront in the elucidation of the mechanism of high-temperature superconductivity. *Jpn. Journ. App. Phys.* 2012. V. 51. ID 010002.

60. Gros C., Joynt R., Rice T. M. Antiferromagnetic correlations in almost-localized Fermi liquids. *Phys. Rev B*. 1987. V. 36. ID 381.

61. Baskaran G., Zou Z., Anderson P. W. The resonating valence bond state and high-Tc superconductivity - A mean field theory. *Sol. St. Comm*. 1987. V. 63. P. 973–976.

62. Ciuchi S., Pascuale F., Fratini S., Feinberg D. Dynamical mean-field theory of the small polaron. *Phys. Rev. B*. 1997. V. 56. ID 4494.

63. Alexandrov A., Ranninger J. Bipolaronic superconductivity. *Phys. Rev. B*. 1981. V. 24. ID 1164.

64. Izyumov Yu. A., Letfulov B. M., Shipitsyn E. V., Bartkowiak M., Chao K. A. Theory of strongly correlated electron systems on the basis of a diagrammatic technique for Hubbard operators. *Phys. Rev. B*. 1992. V. 46. ID 15697.

65. Zubov E. E. Effective self-consistent field and phase transitions in the *t-J* model. *Physics Solid State*. 2009. V. 51. P. 106–112.

66. Myronova S. F., Zubov E. E. Effective field and spin-wave excitation in a narrow-band Hubbard magnet. *JMMM*. 2007. V. 316. P. e724-e727.

67. Edwards D. M. Ferromagnetism and electron-phonon coupling in the manganites. *Adv. Phys*. 2002. V. 51. P. 1259–1318.

68. Cyrot M. On high superconductivity in La_2CuO_4 type compounds. *Solid Sate Commun*. 1983. V. 62. P. 821–823.

69. Mott N. F., Davis E. A. Electronic processes in non-crystalline materials. Clarendon Press: Oxford. 1971. 662 pp.

70. Beenakker C. W. Random-matrix theory of quantum transport. *Rev. Mod. Phys*. 1997. V. 69. P. 731-808.

71. Ryndyk D.A. Theory of quantum transport at nanoscale. Springer Ser. In Sol. State. V. 184. Dresden. 2016. 246 pp.

72. Свистунов В. М., Белоголовский М. А. Туннельная спектроскопия квазичастичных возбуждений в металлах. Киев: Наук. думка. 1986. 152 с.

73. Matsubara T. A new approach to quantum-statistical mechanics. *Progr. Theor. Phys*. 1955. V. 14. P. 351–378.

74. Kubo R. Statistical-mechanical theory of irreversible processes. *J. Phys. Soc. Jpn*. 1957. V. 12. P. 570–586.

75. Barone A., Paterno G. Physics and applications of the Josephson effect. John Wiley & Sons: New York. 1982. 529 pp.

76. Biedenharn L. C., Louck J. D. Angular momentum in quantum physics. Theory and Application. Addison-Wesley: Massachusetts. 1981. 299 pp.

77. Landauer R. Electrical resistance of disordered one-dimensional lattice. *Phil. Mag*. 1970. V. 21. P. 863–867.

78. Zubov E. E. Nonlinear transport theory in the metal with tunnel barrier. *Phil. Mag*. 2018. V. 98. P. 329–344.

79. Anderson P. W., Hasegawa H., Considerations on double exchange. *Phys. Rev*. 1955. V. 100. ID 675.

80. Gennes P. G. Effects of double exchange in magnetic crystals. *Phys. Rev*. 1960. V. 118. ID 141.

81. Kubo K. A., Ohata N. Quantum theory of double exchange. *J. Phys. Soc. Jpn*. 1972. V. 33. P. 21–32.

82. Furukawa N. Transport properties of the Kondo lattice model in the limit S=∞ and D=∞. *J. Phys. Soc. Jpn.* 1994. V. 6. P. 3214–3217.

83. Green A. C. M. Many-body CPA for the Holstein double-exchange model. *Phys. Rev. B.* 2001. V. 63. ID 205110.

84. Zubov E. E. Low-temperature thermodynamics of magnetically ordered states of a narrow-band Hubbard magnetic material. *Fiz. Nizk. Temp.* 1993. V. 19. P. 274-283.

85. Zubov E. E., Dyakonov V. P., Szymczak H. Noncollinear claster ferromagnetism in lanthnum-manganite perovskites with excess of manganese. *J. Exp. Theor. Phys.* 2002. V. 95. P. 1044-1055.

86. Millis A. J., Mueller R., Shraiman B. I. Fermi-liquid-to-polaron crossover. II. Double exchange and the physics of colossal magnetoresistance. *Phys. Rev. B.* 1996. V. 54. ID 5405.

87. Yang D. H. Y., Wang Y. L. Green's-function diagrammatic technique for complicated level systems. Phys. Rev. B. 1974. V. 10. ID 4714.

88. Holstein T. Studies of polaron motion. Part II. The "small" polaron. *Ann. Phys.* 1959. V. 8. P. 343–389.

89. Jonker G. H., Van Santen J. H. Ferromagnetic compounds of manganese with perovskite structure. *Physica.* 1950. V. 16. P. 337–349. Magnetic compounds with perovskite structure III. Ferromagnetic compounds of cobalt. 1953. V. 19. P. 120–130.

90. Moussa F., Hennion M., Rodriguez-Carvajal J., Moudden H., Pinsard L., Revcolevschi A. Spin waves in the antiferromagnet perovskite $LaMnO_3$: A neutron-scattering study. *Phys.Rev.B.* 1996. V. 54. P. 15149–15155.

91. Larkin A. I. Passage of particles through a plasma. *Sov.Phys. JETP.* 1959. V. 37. P. 186-191.

92. Urushibara A., Moritomo Y., Arima T., Asamitsu A., Kido G., Tokura Y. Insulator-metal transition and giant magnetoresistance in $La_{1-x}Sr_xMnO_3$. *Phys. Rev. B.* 1995. V. 51. ID 14103.

93. Alexandrov A. S., Bratkovsky A. M. The essential interactions in oxides and spectral weight transfer in doped manganites. *J. Phys.: Condens. Matter.* 1999. V. 11. ID 1989.

94. Zhu X. J., Shang J., Li R.W. Resistive switching effects in oxide sandwiched structures. *Front. Mater. Sci.* 2012. V. 6. P. 183–206.

95. Hoskins B. D., Adam G. C., Strelcov E., Zhitenev N., Kolmakov A., Strukov D. B., McClelland J. J. Stateful characterization of resistive switching TiO_2 with electron beam induced currents. *Nat. Commun.* 2017. V. 8. ID 1972.

96. Strukov D.B., Snider G.S., Stewart D.R., Williams R.S. The fourth circuit element. *Nature.* 2008. V. 453. P. 80–83.

97. Chu C. W., Deng L. Z., Lv B. Hole-doped cuprate high temperature superconductors. *Physica C.* 2015. V. 514. P. 290–313.

98. Kemper J. B., Vafek O., Betts J. B., Balakirev F. F., Hardy W. N., Liang R., Bonn D. A., Boebinger G. S. Thermodynamic signature of a magnetic-field-driven phase transition within the superconducting state of an underdoped cuprate. *Nature Phys.* 2016. V. 12. P. 47–51.

99. Pan S. H., O'Neal J. P., Badzey R. L., Chamon C., Ding H., Engelbrecht J. R., Wang Z., Eisaki H., Uchida S., Guptak A. K., Ng K. W., Hudson E. W., Lang K. M., Davis J. C.

Microscopic electronic inhomogeneity in the high-T_c superconductor $Bi_2Sr_2CaCu_2O_{8+x}$. *Nature*. 2001. V. 413. P. 282–285.

100. Campi G., Bianconi A., Poccia N., Bianconi G., Barba L., Arrighetti G., Innocenti D., Karpinski J., Zhigadlo N. D., Kazakov S. M., Burghammer M., Zimmermann M., Sprung M., Ricci A. Inhomogeneity of charge-density-wave order and quenched disorder in a high-Tc superconductor. *Nature*. 2015. V. 525. P. 359–362.

101. Carlson E. W. Charge topology in superconductors. *Nature*. 2015. V. 525. P. 329–330.

102. Carlson E. W., Liu S., Phillabaum B., Dahmen K. A. Decoding spatial complexity in strongly correlated electronic systems. *J. Supercond. Nov. Magn*. 2015. V. 28. P. 1237–1243.

103. Ahn C.H., Bhattacharya A., Ventra M., Eckstein J.N., Frisbie C.D., Gershenson M.E., Goldman A.M., Inoue I.H., Mannhart J., Millis A.J., Morpurgo A.F., Natelson D., Triscone J.M. Electrostatic modification of novel materials. *Rev. Mod. Phys*. 2006. V. 78. P. 1185–1212.

104. Chandrasekhar N., Valls O. T., Goldman A. M. Mechanism for electric field effects observed in $YBa_2Cu_3O_{7-x}$ films. *Phys-1. Rev. Lett*. 1993. V. 71. P. 1079082.

105. Saluzzo M., Ghiringhelli G., Cezar J. C., Brookes N. B., De Luca G. M., Fracassi F., Vaglio R. Indirect electric field doping of the CuO_2 planes of the cuprate $NdBa_2Cu_3O_7$ superconductor. *Phys. Rev. Lett*. 2008. V. 100. ID 056810.

106. Tulina N. A. Colossal electroresistance and electron instability in strongly correlated electron systems. *Phys. Usp*. 2007. V. 50. P. 1171–1178.

107. Plecenik A., Tomasek M., Plecenik T., Truchly M., Noskovic J., Zahoran M., Roch T., Belogolovskii M., Spankova M., Chromik S., Kus P. Studies of resistance switching effects in metal/$YBa_2Cu_3O_{7-x}$ interface junctions. *Appl. Surf. Sci*. 2010. V. 256. P. 5684–5687.

108. Lienig J. Introduction to electromigration-aware physical design. *Proceedings of the ACM International Symposium on Physical Design*. San Jose, 2006. P. 39–46.

109. Ho P. S., Kwok T. Electromigration in metals. *Rep. Prog. Phys*. 1989. V. 52. P. 301–348.

110. Fiks V. B. Drag and inhibition of mobile defects in metals by conduction electrons – The role of the law of electron dispersion. *Zh. Eksp. Teor. Fiz*. 1981. V. 80. P. 1539–1542.

111. Ralls K. S., Ralph D. C., Buhrman R. A. Individual-defect electromigration in metal nanobridges. *Phys. Rev. B*. 1989. V. 40. P. 11561–11570.

112. Plecenik T., Tomášek M., Belogolovskii M., Truchly M., Gregor M., Noskovič J., Zahoran M., Roch T., Boylo I., Španková M., Chromik Š., Kúš P., Plecenik A. Effect of crystallographic anisotropy on the resistance switching phenomenon in perovskites. *J. Appl. Phys*. 2012. V. 111. ID 056106.

113. Plecenik A., Grajcar M., Seidel P., Benacka S. Investigation of HTS surface properties by tunneling spectroscopy. *Studies of High Temperature Superconductors*. Nova Science Publishers. New York, 1996. V. 20. P. 75–123.

114. Belogolovskii M. Interface resistive switching effects in bulk manganites *Cent. Eur. J. Phys*. 2009. V. 7. P. 304–309.

115. Grajcar M., Plecenik A., Darula M., Beňačka Š. Surface degradation of $YBa_2Cu_3O_{7-\delta}$ observed by means of contact resistance measurement. *Solid State Commun*. 1992. V. 81. P. 191–194.

116. Emery V. J., Kivelson S. A. Superconductivity in bad metals. *Phys. Rev. Lett*. 1995. V. 74. ID 3253.

117. Su H., Welch D. O. The effects of space charge, dopants, and strain fields on surfaces and grain boundaries in YBCO compounds. *Supercond. Sci. Technol.* 2005. V. 18. P. 24–34.

118. Kirtley J. R. Tunneling measurements of the energy gap in high-Tc superconductors. *Int. J. Mod. Phys. B.* 1990. V. 4. P. 201–237.

119. Inoue S., Kawai M., Ichikawa N., Kageyama H., Paulus W., Shimakawa Y. Anisotropic oxygen diffusion at low temperature in perovskite-structure iron oxides. *Nature Chem.* 2010. V. 2. P. 213–217.

120. Larkins Jr. G. L., Lu Q., Jones W. K., Kennedy R. J., Chern G. Surface degradation and aging in $YBa_2Cu_3O_{7-x}$ ceramics. *Physica C.* 1991. V. 173. P. 201-207.

121. Jin K., Bach P., Zhang X. H., Grupel U., Zohar E., Diamant I., Dagan Y., Smadici S., Abbamonte P., Greene R. L. Anomalous enhancement of the superconducting transition temperature of electron-doped $La_{2-x}Ce_xCuO_4$ and $Pr_{2-x}Ce_xCuO_4$ cuprate heterostructures. *Phys. Rev. B.* 2011. V. 83. ID 060511(R).

122. Yamamoto K., Lairson B. M., Bravman J. C., Geballe T. H. Oxidation kinetics of $YBa_2Cu_3O_{7-x}$ thin films in the presence of atomic oxygen and molecular oxygen by in situ resistivity measurements. *J. Appl. Phys.* 1991. V. 69. ID 7189.

123. Di Ventra M., Pershin Y. V., Chua L. O. Circuit elements with memory: memristors, memcapacitors, and meminductors. *Proc. IEEE.* 2009. V. 97. P. 1717–1724.

124. Truchly M., Plecenik T., Zhitlukhina E., Belogolovskii M., Dvoranova M., Kus P., Plecenik A. Inverse polarity of the resistive switching effect and strong inhomogeneity in nanoscale YBCO-metal contacts. *J. Appl. Phys.* 2016. V. 120. ID 185302.

125. Tomasek M., Plecenik T., Truchly M., Noskovic J., Roch T., Zahoran M., Chromik S., Spankova M., Kus P., Plecenik A. Temperature dependence of the resistance switching effect studied on the metal/$YBa_2Cu_3O_{6+x}$ planar junctions. *J. Vac. Sci. Technol. B.* 2011. V. 29. ID 01AD04.

126. Acha C. Electric pulse-induced resistive switching in ceramic $YBa_2Cu_3O_{7-\delta}$/Au interfaces. *Physica B.* 2009. V. 404. P. 2746–2748.

127. Wolf E. L. Principles of electron tunneling spectroscopy: Second Edition. Oxford University Press: Oxford. 2011. 593 pp.

128. Schrieffer J. R. Theory of superconductivity. Benjamin: New York. 1964. 282 pp.

129. Miller T. L., Zhang W., Ma J., Eisaki H., Moore J. E., Lanzara A. Interplay of superconductivity and bosonic coupling in the peak-dip-hump structure of $Bi_2Sr_2CaCu_2O_{8+\delta}$. 2018. *Phys. Rev. B.* V. 97. ID 134517.

130. Naidyuk Yu. G., Yanson I. K. Point-contact spectroscopy. Springer. 2005. 297 pp.

131. Khotkevich A. V., Yanson I. K. Atlas of point contact spectra of electron-phonon interactions in metals. Springer. 1995. 168 pp.

132. Daghero D., Gonnelli R. S. Probing multiband superconductivity by point-contact spectroscopy. *Supercomd. Sci. Technol.* 2010. V. 23. ID 043001.

133. Daghero D., Tortello M., Ummarino G. A., Gonnelli R. S. Directional point-contact Andreev-reflection spectroscopy of Fe-based superconductors: Fermi surface topology, gap symmetry, and electron–boson interaction. *Rep. Prog. Phys.* 2011. V. 74. ID 124509.

134. Yanson I.K., Bobrov N.L., Rybal'chenko L.F., Fisun V.V. Spectroscopy of phonons in dirty superconducting contacts. *Sov. J. Low. Temp. Phys.* 1983. V. 9. P. 596–603.

135. Blonder G. E., Tinkham M., Klapwijk T. M. Transition from metallic to tunneling regimes in superconducting microconstrictions: Excess current, charge imbalance, and supercurrent conversion. *Phys. Rev. B.* 1982. V. 25. P. 4515–4532.

136. Baltz V., Naylor A.D., Seemann K. M., Elder W., Sheen S., Westerholt K., Zabel H., Burnell G., Marrows C. H., Hickey B. J. Conductance features in point contact Andreev reflection spectra. *J. Phys. Condens. Matter.* 2009. V. 21. ID 095701.

137. Dynes R. C., Narayanamurti V., Garno J. P. Direct measurement of quasiparticle-lifetime broadening in a strong-coupled superconductor. *Phys. Rev. Lett.* 1978. V. 41. P. 1509–1512.

138. Tsindlekht M. I., Genkin V. M., Leviev G. I., Felner I., Yuli O., Asulin I., Millo O., Belogolovskii M. A., Shitsevalova N. Yu. Linear and nonlinear low-frequency electrodynamics of surface superconducting states in an yttrium hexaboride single crystal. *Phys. Rev. B.* 2008. V. 78. ID 024522.

139. Koza J. A., Bohannan E. W., Switzer J. A. Superconducting filaments formed during nonvolatile resistance switching in electrodeposited δ-Bi(2)O(3). *ACS Nano.* 2013. V. 7. P. 9940–9946.

140. Hwang I., Lee K., Jin H., Choi S., Jung E., Park B. H., Lee S. A new simple method for point contact Andreev reflection. *Nanoscale.* 2015. V. 7. P. 8531–8535.

141. Dvoranová M., Plecenik T., Moško M., Vidiš M., Gregor M, Roch T., Grančič B., Satrapinskyy L., Kúš P., Plecenik A. Point contact spectroscopy of superconductors via nanometer scale point contacts formed by resistive switching. *AIP Adv.* 2018. V. 8. ID 125217.

142. Zhitlukhina E., Dvoranová M., Plecenik T., Gregor M., Belogolovskii M., Plecenik A. Electron–boson coupling in superconductors studied by a self-formed nanoilament device. *Appl. Nanosci.* 2019. DOI: 10.1007/s13204-019-01082-6.

143. Herman F., Hlubina R. Microscopic interpretation of the Dynes formula for the tunneling density of states. *Phys. Rev. B.* 2016. V. 94. ID 144508.

144. Brinkman A., Golubov A. A., Rogalla H., Dolgov O. V., Kortus J., Kong Y., Jepsen O., Andersen O. K. Multiband model for tunneling in MgB2 junctions. *Phys. Rev. B.* 2002. V. 65. ID 180517.

145. Dolgov O. V., Gonnelli R. S., Ummarino G. A., Golubov A. A., Shulga S. V., Kortus J. Extraction of the electron-phonon interaction from tunneling data in the multigap superconductor MgB2. *Phys. Rev. B.* 2003. V. 68. ID 132503.

146. Kashiwaya S., Tanaka Y., Koyanagi M., Kajimura K. Theory for tunneling spectroscopy of anisotropic superconductors. *Phys. Rev. B.* 1996. V. 53. P. 2667–2676.

147. Wolf E. L., Zasadzinski J., Osmun J. W. Proximity electron tunneling spectroscopy I. Experiments on Nb. *J. Low. Temp. Phys.* 1980. V. 40. P. 19–50.

148. Robinson B., Geballe T. H., Rowell J.M. Tunneling study of niobium using aluminum-aluminum oxide niobium junctions. In: Superconductivity in *d-* and *f-*band Metals. Ed. Douglass D.H. Plenum Press: New York. 1976. P. 381–386.

149. Norman M. R., Randeria M., Ding H., Campuzano J. C. Phenomenology of the low-energy spectral function in high-T_c superconductors. *Phys. Rev. B.* 1998. V. 57. ID R11093.

150. Chen K., Dai W., Zhuang C. G., Li Q., Carabello S., Lambert J. G., Mlack J. T., Ramos R. C., Xi X. X. Momentum-dependent multiple gaps in magnesium diboride probed by electron tunnelling spectroscopy. *Nature Commun.* 2012. V. 3. ID 619.

151. Takasaki T., Ekino T., Gabovich A. M., Sugimoto A., Yamanaka S., Akimitsu J. Tunneling spectroscopy of novel layered superconductors: MgB2, Li0.48(THF)XHfNCl and related substances. In: Superconductivity: Theory, Materials and Applications. Ed. Romanovskií V. R. Nova Science: Hauppauge. 2012. P. 1–110.